Vibrationally and Rotationally Inelastic Scattering of Methane from Ni(111)

THÈSE N^{O} 8563 (2018)

PRÉSENTÉE LE 27 AVRIL 2018

À LA FACULTÉ DES SCIENCES DE BASE
LABORATOIRE DE CHIMIE PHYSIQUE MOLÉCULAIRE
PROGRAMME DOCTORAL EN CHIMIE ET GÉNIE CHIMIQUE

ÉCOLE POLYTECHNIQUE FÉDÉRALE DE LAUSANNE

POUR L'OBTENTION DU GRADE DE DOCTEUR ÈS SCIENCES

PAR

Jörn WERDECKER

acceptée sur proposition du jury:

Dr A.-S. Chauvin, présidente du jury
Prof. R. Beck, Prof. A. Wodtke, directeurs de thèse
Prof. D. J. Auerbach, rapporteur
Prof. F. F. Crim, rapporteur
Dr W. Harbich, rapporteur

ÉCOLE POLYTECHNIQUE
FÉDÉRALE DE LAUSANNE
Suisse
2018

Abstract

This thesis presents a quantum-state-resolved molecular beam study of the non-reactive scattering of methane (CH_4) from a Ni(111) surface. It is one of the first experimental investigations in which the internal quantum state distribution of a polyatomic molecule is measured after surface scattering.

The quantum state populations of scattered CH_4 were probed by selective rovibrational excitation using a high-power continuous-wave (cw) infrared (IR) laser in combination with a cryogenic bolometer. This technique is introduced as "Bolometric detection with Infrared Laser Tagging" (BILT) and its experimental realization is described in detail. Example data illustrates the capabilities and the performance of the method.

Scattering experiments were conducted in a near-specular geometry at grazing incidence ($\theta_i = 65°$) and exit angles ($\theta_f = 70°$). The surface temperature was in all cases 673 K. Two aspects of the scattering dynamics of CH_4 at Ni(111) were investigated.

First, the fate of initial vibrational energy in the gas-surface encounter between CH_4 and Ni(111) was studied in a state-to-state scattering experiment. Here, incident CH_4 was prepared with one quantum of the anti-symmetric C–H stretch vibration (ν_3) and in rotational state $J = 1$ by coherent IR pumping. The results include the first observation of vibrational energy redistribution in the direct scattering of a molecule from a surface. Specifically, a portion of the CH_4 molecules, which were initially in the ν_3 state, were detected in the symmetric C–H stretch state (ν_1) after scattering. The probability for this vibrationally inelastic process is about 40 % compared to the vibrationally elastic process in which CH_4 remains in the initially prepared ν_3 state. This branching ratio is insensitive to changes in incidence kinetic energy in the range 100–370 meV. Rotational excitation is in all cases significant, where molecules that underwent $\nu_3 \rightarrow \nu_1$ conversion carry away an increased amount of rotational energy. The results are discussed in the context of previously observed mode-specific reactivity in this gas-surface system.

Second, the rotational excitation of scattered CH_4 in its vibrational ground state was investigated. The scattering is likewise direct and the final rotational state distributions

are non-Boltzmann, revealing a propensity for scattering into low-J states. Extended analysis of the rotational-state-resolved angular distributions and the Doppler-broadened absorption profiles suggest that, at low incidence kinetic energies, rotational excitation is dominated by energy transfer from the surface, *i.e.* phonon annihilation. This conclusion is supported by classical scattering simulations, which recover the rotational excitation at low incidence kinetic energies. However, they strongly overestimate the efficiency of translational-to-rotational energy transfer.

The highly detailed scattering data obtained in this work can serve as stringent test of multi-dimensional dynamical models of this prototypical gas-surface reaction, thereby paving the way toward a predictive understanding of heterogeneous catalysis. This work also proves that BILT detection using state-of-the-art IR light sources is sufficiently sensitive to enable state-to-state surface scattering experiments on polyatomic molecules, opening the possibility to study their dynamics at surfaces with unprecedented detail.

Keywords: Methane, Ni(111), molecular beam, surface scattering, inelastic scattering, quantum-state-resolved detection, bolometer, infrared spectroscopy, vibrational energy redistribution, rotational excitation.

Zusammenfassung

Diese Doktorarbeit präsentiert eine quantenzustandsaufgelöste Molekularstrahl-Studie der nicht-reaktiven Streuung von Methan (CH_4) an einer Ni(111) Oberfläche. Sie stellt eine der ersten experimentellen Untersuchungen dar, in welcher die internen Zustandsverteilungen eines mehratomigen Moleküls nach der Streuung an einer Oberfläche gemessen wurden.

Die Bevölkerungen der Quantenzustände der gestreuten CH_4 Moleküle wurde ermittelt mithilfe von rotations- und schwingungs-selektiver Anregung durch einen leistungsstarken kontinuierlichen Infrarot-Laser in Kombination mit einem kryogenischen Bolometer. Diese Technik wird als "Bolometric detection with Infrared Laser Tagging" (BILT) eingeführt und ihre experimentelle Realisierung im Detail beschrieben. Beispieldaten dienen zur Veranschaulichung der Möglichkeiten und der Leistungsfähigkeit der Methode.

Die Streuexperimente wurden durchgeführt in fast-spekulärer Geometrie unter Einfalls- und Streuwinkeln von jeweils $\theta_i = 65°$ und $\theta_f = 70°$. Die Oberflächentemperatur betrug in allen Fällen 673 K. Zwei Aspekte der Streudynamik von CH_4 an Ni(111) wurden untersucht.

Zuerst wurde das Schicksal der Schwingungsenergie studiert wenn anfänglich schwingungsangeregtes CH_4 auf Ni(111) trifft. Hierbei wurden die einfallenden CH_4 Moleküle mit einem Quant der anti-symmetrischen C–H Streckschwingung (ν_3) und im Rotationszustand $J = 1$ mittels kohärentem Infrarotpumpen präpariert. Die Ergebnisse beinhalten die erste Beobachtung von Schwingungsenergieumverteilung in der direkten Streuung eines Moleküls an einer Oberfläche. Genauer gesagt, ein Teil der CH_4 Moleküle, die ursprünglich in ν_3 waren, wurden mit einem Quantum der symmetrischen Streckschwingung ν_1 detektiert. Die Wahrscheinlichkeit dieses schwingungsinelastischen Prozesses beträgt etwa 40 % im Vergleich zum schwingselastischen Prozess, bei dem CH_4 im ursprüngliche präparierten ν_3 Zustand verharrt. Dieses Verhältnis ist unempfindlich gegenüber Änderungen in der kinetischen Einfallsenergie im Bereich von 100–370 meV. Rotationsanregung ist in allen Fällen signifikant, wobei Moleküle, welche

$\nu_3 \rightarrow \nu_1$ Konversion untergehen, einen erhöhten Betrag an Rotationsenergie davontragen. Die Ergebnisse werden im Kontext der in diesem Gas-Oberflächen-System bereits zuvor beobachteten modenspezifischen Reaktivität diskutiert.

Als zweites wurde die Rotationsanregung von gestreutem CH_4 im Schwingungsgrundzustand untersucht. Die Streuung ist gleichfalls direkt und die sich ergebenden Rotationsverteilungen sind nicht-Boltzmann-verteilt, wobei sie eine Neigung zur Bevölkerung von niedrigen J-Zuständen aufzeigen. Eine genauere Analyse der rotationszustandsaufgelösten Winkelverteilungen und der Doppler-verbreiterten Absorptionslinien weist darauf hin, dass die Rotationsanregung bei niedrigen Einfallsenergien durch Energietransfer von der Oberfläche, d.h. durch Phononenvernichtung, dominiert wird. Diese Schlussfolgerung wird durch klassische Streusimulationen erhärtet, welche die Rotationsanregung bei niedrigen Einfallsenergien reproduziert. Allerdings überschätzen sie die Effizienz des Energietransfers von Translation zu Rotation stark.

Die hoch-detaillierten Streudaten, die in dieser Arbeit gewonnen wurden, können der stringenten Beurteilung von mehrdimensionalen dynamischen Modellen dieser Gas-Oberflächenreaktion dienen und damit den Weg für ein vorhersagendes Verständnis der heterogenen Katalyse ebnen. Diese Arbeit zeigt zudem, dass BILT-Detektion bei Verwendung von modernsten IR Lichtquellen empfindlich genug ist, um zustands-zu-zustandsaufgelöste Oberflächenstreuexperimente an mehratomigen Molekülen zu ermöglichen, was die Studie ihrer Dynamik mit zuvor ungekannter Präzision erlaubt.

Schlüsselbegriffe: Methan, Ni(111), Molekularstrahl, Oberflächenstreuung, inelastische Streuung, quantenzustandsaufgelöste Detektion, Bolometer, Infrarotspektroskopie, Schwingungsenergieumverteilung, Rotationsanregung.

Table of Contents

List of abbreviations

AC ..... Alternating current
ADC ..... Analog-to-digital converter
AES ..... Auger electron spectroscopy
AIMD ..... *Ab initio* molecular dynamics
BOA ..... Born-Oppenheimer approximation
BILT ..... Bolometric detection with IR laser tagging
cw ..... continuous-wave
DAC ..... Digital-to-analog converter
DAQ ..... Data acquisition (National Instruments hardware)
DC ..... Direct current
DFT ..... Density functional theory
DOF ..... Degree of freedom
FPI ..... Fabry-Pérot interferometer
FSR ..... Free spectral range
FWHM ..... Full width at half maximum
HAS ..... Helium atom scattering
HeNe ..... Helium-neon laser
HV ..... High voltage
IR ..... Infrared
IVR ..... Intramolecular vibrational energy redistribution
LEED ..... Low energy electron diffraction
MCS ..... Multichannel scaler
MEP ..... Minimum energy path
NEP ..... Noise-equivalent power
OPO ..... Optical parametric oscillator
PES ..... Potential energy surface
PID ..... Proportional-integral-differential (controller)
PZT ..... Lead zirconate titanate (piezoelectric material)
QMS ..... Quadrupole mass spectrometer
RAP ..... Rapid adiabatic passage
REMPI ..... Resonantly enhanced multiphoton ionization (spectroscopy)
RMS ..... Root mean square
RPH ..... Reaction path Hamiltonian
S/N ..... Signal-to-noise ratio
TD ..... Trapping followed by desorption
TOF ..... Time-of-flight
TS ..... Transition state
UHV ..... Ultra-high vacuum
VI ..... Virtual instrument (LabVIEW^{TM})

1 Introduction

1.1 Motivation

The variety of dynamical processes that occur when molecules interact with solid surfaces are of fundamental interest because they constitute the complex chemical reaction mechanisms found in heterogeneous catalysis[1]. The dissociation of methane (CH_4) on nickel surfaces is known to be the rate-limiting step in the steam-reforming reaction, which is the principal industrial process for the generation of molecular hydrogen from natural gas and water[2]. Considering that an activation barrier of about 90 kJ/mol separates the gas-phase CH_4 from the dissociation product, which is surface-bound methyl (CH_3), it is no surprise that this process is run in reactors under high-temperature and high-pressure conditions. Because processes such as this one consume a considerable fraction of our total energy production, any insights that could lead to their optimization, as for instance through the development of better catalysts, are highly valuable.

Gaining a microscopic understanding of chemical reactions is the goal of our research field, chemical reaction dynamics. The relevance to industrial applications is one reason why a number of research groups have over the years strived to obtain a predictive understanding of methane dissociation on transition metals, both from an experimental and theoretical standpoint[3–5]. The second reason why it has become such an important model system for reaction dynamics studies, is its favorable system size. Methane, with its five atoms, is small enough to be tractable by high-level quantum chemical calculations. Yet, at the same time, it offers the opportunity to investigate phenomena that cannot occur in diatomic molecules, such as mode-specificity, bond-selectivity, and intramolecular vibrational energy redistribution (IVR)[6].

In past years, the experimental study of methane's interaction with transition metal surfaces focused on determining reactivities, *i.e.* reaction probabilities, where incident

methane molecules were prepared with varying amounts of kinetic and vibrational energy, and in different vibrational modes. This gave insight into how the molecule can acquire the energy that it needs to overcome the activation barrier and to form a specific product. Theoretical modeling established a picture of vibrational energy flow within the reaction complex, explaining how this initial energy is channeled into the reaction coordinate. Knowledge of the fate of this initial energy, and of vibrational energy in particular, is at the heart of understanding the overall reaction dynamics. These information can be provided by a state-to-state scattering experiment, which both prepares the incoming molecule in one specific state and analyzes the states of the scattered species. Unfortunately, and for reasons that I will discuss below, realizing this type of experiment for polyatomic molecules is very challenging, which has prevented progress in this area up to the present day.

In this work, I used a cryogenic bolometer in combination with state-selective infrared laser excitation to probe the quantum state distribution of CH_4 after scattering from a Ni(111) surface in order to elucidate the fate of initial translational and vibrational energy. The results will be helpful in benchmarking current and future theoretical modeling of this prototypical gas-surface system.

1.2 Basic notions of gas-surface reaction dynamics

1.2.1 Molecule-surface interactions

This section introduces the common language that has been established in the field of gas-surface dynamics to describe the different process occurring at this interface.

To understand the dynamics of molecules at surfaces, we need to consider the forces acting on them, which are due to electrostatic and van der Waals interactions. The simplest model that describes the interaction between a general molecule A–B and a metal surface was proposed[7] by Lennard-Jones back in 1932. In his model, the interaction energy V is a function of only one coordinate, namely the molecule-surface distance z. This is shown in Figure 1.1, where the lower black curve represents the potential energy of the molecule A–B and the upper black curve that of the dissociated molecule A+B. As we shall see shortly, this model oversimplifies the situation, in particular for somewhat larger molecules such as CH_4. Yet, it is still useful for visualizing the basic processes and interactions. At relatively large molecule-surface distances z (several Å), attractive van der Waals interaction dominates and gives rise to a shallow potential energy minimum at a distance z_p. Molecules which find themselves held in this minimum are said to be *physisorbed* (binding energy $\sim 50-500\,\mathrm{meV/atom}$). Any process that leads to the

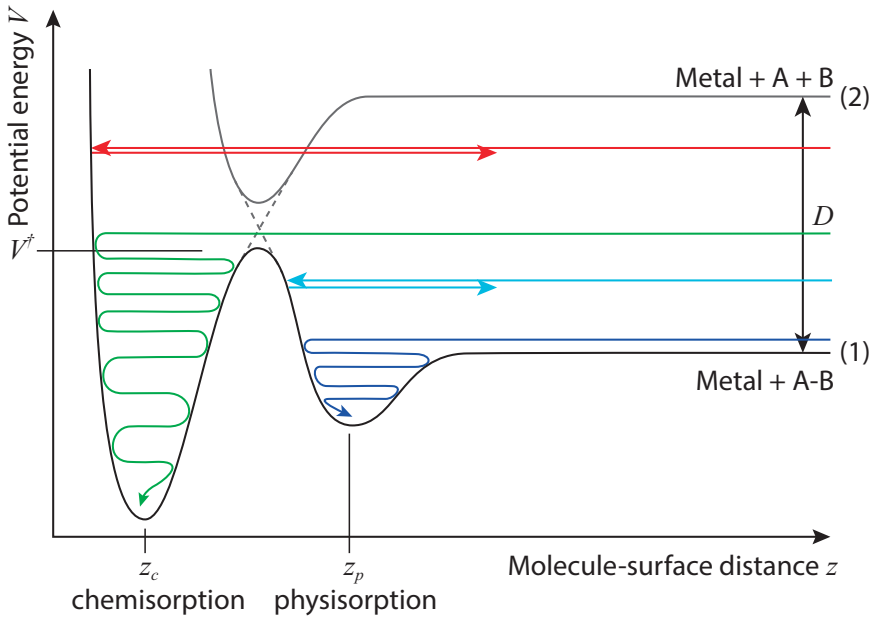

Figure 1.1 One-dimensional potential energy diagram after Lennard-Jones, describing the physisorption and dissociative chemisorption of a general molecule A–B on a surface. The physisorption well depth is shown highly exaggerated for the sake of clarity. Shown in color are different types of trajectories that a molecule can follow. See text for details.

"capturing" of a molecule in such a potential energy well is referred to as *adsorption* or *sticking*. When a molecule adsorbs only for a short time (compared to the time duration over which we observe the system), we speak of this molecule as being *trapped*. A trapped molecule will again leave the surface at a later time through a process which is called *desorption*.

At shorter distances, the electron orbitals of metal and molecule will start to overlap, giving rise to repulsion or attraction. This more "chemical interaction" can be strong enough so that a chemical bond may be formed between surface and molecule, which in turn may weaken an intramolecular bond up to the point where it breaks. A molecule that can be considered to have a chemical bond with the surface is called *chemisorbed* (binding energy $\sim 1-10\,\mathrm{eV/atom}$).

The Lennard-Jones model describes the breaking of the intramolecular bond as an avoided curve crossing of the molecular potential energy curve (1) and the curve that correspond to the dissociated molecule (2), where D is the dissociation energy in the gas-phase. The potential energy local maximum between the physisorbed and chemisorbed states is called *activation barrier*, since a molecule must be activated with at least an amount $V^\dagger$ of energy in order to overcome the barrier and be able to react.

The force that acts on the molecule in the vicinity of the surface is given by the gradient of the potential energy curve (1), $F = -\mathrm{d}V/\mathrm{d}z$. Shown in Figure 1.1 are four different types of trajectories describing the possible dynamics that an incoming molecule can follow during the encounter with the surface. The vertical offset of these trajectories at large z corresponds to the molecule's initial kinetic energy. When this energy is low (dark blue curve), the molecule is repelled by the activation barrier. If it looses enough energy during the collision, for instance by exciting vibrations of surface atoms (*phonons*), it becomes trapped in the physisorption well. At slightly higher energies (light blue curve), the molecule might just be reflected from the barrier, causing it to fly back into the gas-phase. It is said to have undergone *direct scattering*. If the energy after the collision is the same as before, we speak of the scattering as being *elastic* and otherwise as being *inelastic*. At even higher energies (green curve), the molecule may be able to directly overcome the barrier and chemisorb (*direct dissociative adsorption*). Not shown is the case when a molecule can overcome the activation barrier after it became physisorbed. This is known as *precursor mediated chemisorption*.

At very high energies (red curve), the molecule is again reflected back into the gas-phase due to the strong repulsion, which occurs at shorter distances than the chemisorption well location z_c. This last example, however, presents us with an apparent dilemma. We know from many experiments that the chemisorption probability typically does not decrease even when the initial energy of the molecule greatly exceeds the activation barrier height. We thus have to ask ourselves how all of this excess energy can be dissipated. One can estimate the fraction of energy that is dissipated by phonons using the hard-cube model[8,9], which dates back to the work of Baule[10]. He modeled the collision of a surface atom and molecule as that of two hard spheres with the masses M and m, respectively. The hard-cube model makes the further assumption that the surface is structureless, *i.e.* it resembles a hard-cube. The relative kinetic energy loss $\Delta E/E_i$ experienced by the incoming projectile in this binary collision with the surface is given by

$$\frac{\Delta E}{E_i} = \frac{4mM}{(m+M)^2}\,, \tag{1.1}$$

where E_i is the incidence kinetic energy normal to the surface. For CH_4 ($m = 16\,\mathrm{u}$) and nickel ($M = 58.7\,\mathrm{u}$), we find a value of $\Delta E/E_i = 0.67$. So how does the molecule loose the remaining $\approx 32\,\%$ of its kinetic energy in order to become adsorbed? The dilemma is resolved by taking into account the remaining *degrees of freedom* (DOFs), that is, the remaining atomic coordinates, of the molecule. A general molecule with N number of

atoms has $3N$ degrees of freedom, of which $3N-6$ correspond to the intramolecular vibrations ($3N-5$ in case of a linear molecule). It is these motions plus the molecular rotation that can store the excess energy. Moreover, for the molecule to dissociate, the activation energy must be channeled into that particular coordinate, which corresponds to the stretching of the very bond that will eventually break. This special coordinate is called the *reaction coordinate*.

1.2.2 Potential energy surfaces

In reality, the potential energy of a molecule is a function of $3N$ coordinates. In the case of a diatomic molecule these are the three space-coordinates of the center of mass $\{x, y, z\}$, the interatomic bond distance (r), and two angles that describe the polar (φ) and azimuthal (ϑ) orientation of the bond with respect to the surface. The $3N$-dimensional potential energy function V is referred to as the *potential energy surface* (PES). Due to its multi-dimensionality, the PES can usually not be visualized. However, Eyring and M. Polanyi found a way to represent the PES in a simplified way: we have seen that a more realistic representation of the molecule-surface interaction compared to the Lennard-Jones model should include at least one more coordinate, namely the intramolecular bond length. Consider a diatomic molecule with a fixed orientation with respect to the surface. Here, the potential energy is now a function of two coordinates and typically represented by contours in what is called an elbow-plot[11]. Figure 1.2 displays four examples. This establishes the picture of a potential energy "landscape", where the state of the molecule, *i.e.* its distance from the surface r_{AB} and its bond length r_{BC} is represented by a point on the PES. The forces acting on the atoms are given by the gradient of the PES and they govern the classical molecular dynamics. That is, the point on the PES, which describes the nuclear configuration, will move under the influence of those forces just like a ball would move on a hilly landscape under the influence of gravity. This representation is ubiquitous in physical chemistry, because it recasts the picture of a complex multi-dimensional PES into a two-dimensional picture, which allows visualizing the dynamics in an intuitive way.

J. Polanyi has proposed[12] a set of rules that relate the shape of the PES to the energy consumption of a reaction and the energy disposal in the final products. He realized that a key point of the PES is the location of the *transition state* in relation to the entrance and exit vallies. The transition state (TS) is the saddle point that separates reactants from products. Consider, for instance, the top left PES in Figure 1.2. Here, the TS is located more toward the entrance valley, which is the bottom right corner (small r_{BC} indicates the presence of a strong B–C bond.) That is, the structure at the TS resembles the original

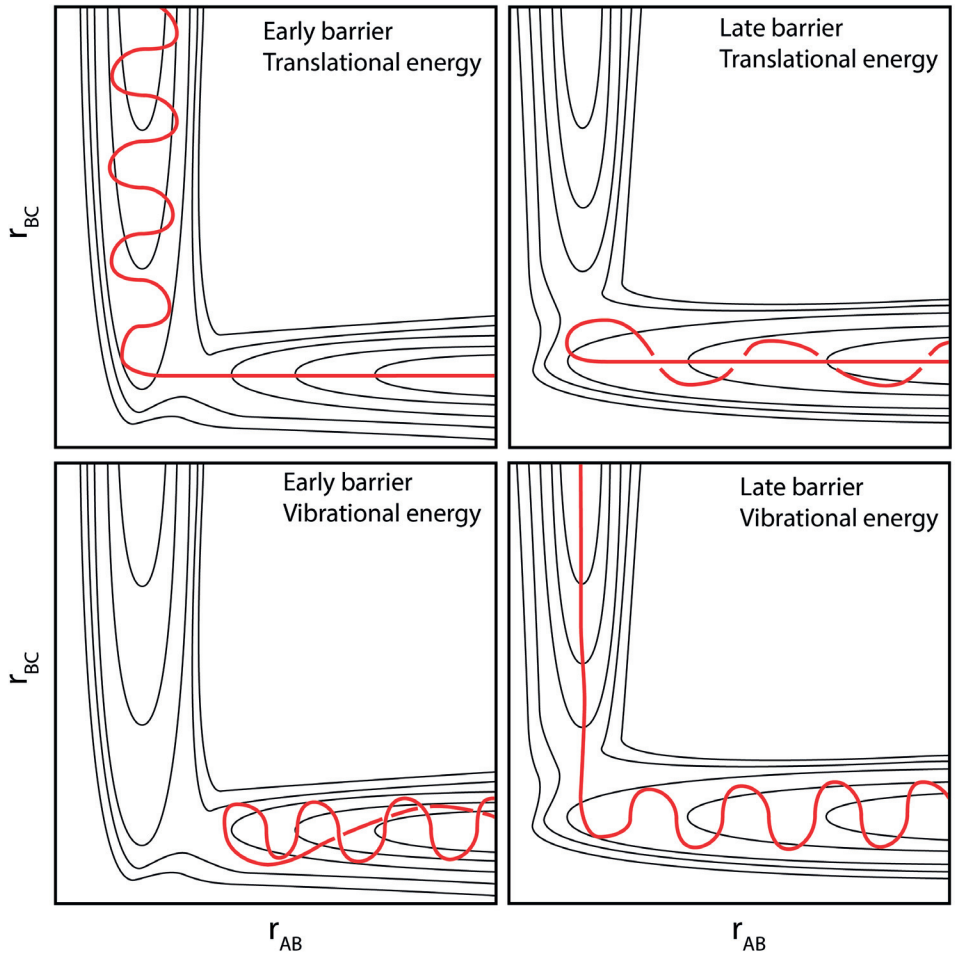

Figure 1.2 Schematic potential energy surface for a general reaction A + BC → AB + C. Reproduced with permission from Ref. [4].

molecule more than the final reaction product A–B. In order to overcome the barrier, which leads up to the TS, incident kinetic energy is most effective, because the minimum energy path (MEP) is parallel to the r_{AB} coordinate. Once the molecule has overcome the barrier, the energy that is released in forming the product is converted into vibration of the A–B bond because of the PES gradient, which now has to be in the direction of r_{BC}. Conversely, initial vibrational energy is ineffective in promoting the reaction since the MEP has no component along the r_{BC} coordinate. A system with a TS located in the entrance channel is said to have an early barrier while a system with a late barrier is one

in which the TS is located in the exit channel. This is shown in the two panels on the right hand side of Figure 1.2. Here, the situation reverses and initial vibrational energy is now more effective in promoting the reaction than translational energy Moreover, the products carry away the excess energy in the form of translational rather than vibrational energy. Polanyi's rules originally aimed at describing the reaction of a diatomic molecule with an atom in the gas phase. However, in a qualitative way, they can be generalized to reactions of polyatomic molecules and molecule-surface reaction.

The two-dimensional PES in Figure 1.2 illustrate how the gradient of the PES couples translational and vibrational degrees of freedom, thereby enabling initial kinetic energy to flow into the reaction coordinate. Similarly, the different vibrations present in polyatomic molecules can be coupled to each other by gradients along different vibrational coordinates. Energy, which is initially localized in one particular vibrational mode can thus start to "flow" into other modes during the surface encounter. This establishes a classical picture of intramolecular vibrational energy flow.

Thus far, I have assumed that the molecule-surface interaction is a function of only the nuclear coordinates. In principle, the system is composed of nuclei and electrons and the potential energy should depend on the coordinates of all particles. The picture of a single potential energy surface governing the dynamics, finds justification in the Born-Oppenheimer approximation (BOA)[13,14]. It is founded on the notion that the nuclei can be considered static on the very short time-scales of the electron motion. This allows the molecular wavefunction to be separated into two parts that describe the electron and the nuclear motions, respectively. The multi-dimensional PES is constructed by solving the electronic structure problem for a number of nuclear configurations.

Solving the electronic structure problem with chemical accuracy using *ab initio* quantum chemical calculations remains a great challenge, notwithstanding the rapid advances in computational capability. This is particularly true in the field of surface chemistry because of the large number of electronic and nuclear degrees of freedom, which constitute even the simplest systems. Approximations that go beyond the BOA are therefore indispensable. They often come in the form of reduced dimensionality or use of semi-empirical methods. Tackling the electronic structure problem using high-level wavefunction methods is still far from feasible in the realm of surface chemistry. Instead, energies are calculated using density functional theory (DFT), most often employing exchange correlation functionals at the generalized gradient approximation (GGA) level. Recently, potentials obtained by neural network fitting of a comparably low number of selected DFT points have shown great promise in terms of fidelity and reduction in computing time[15–18]. Once the PES is found, quasi-classical trajectory or quantum

mechanical wavepacket calculations are performed to obtain the actual dynamics. *Ab initio* molecular dynamics (AIMD) is an approach that avoids beforehand calculation of the entire PES [19]. Instead, quasi-classical simulations are performed where the potential energy is calculated "on-the-fly" using DFT, taking into account all dimensions. This allows including the DOF of the surface atoms explicitly [20].

1.2.3 Vibrational mode representations and eigenstates

In the previous section, I have discussed the vibrational dynamics within the framework of classical mechanics. Here, the different vibrational coordinates are coupled by gradients of the PES, which correspond to the anharmonicities that we know from the normal mode description of molecular vibrations (cf. Refs. [21, 22]). However, in order to understand the role of vibrational excitation in the interaction of CH_4 with solids, we have to consider the quantum mechanical nature of molecular vibrations. All vibrational states below the molecule's dissociation limit are discrete, well-separated molecular eigenstates. The types of experiments, which we concern ourselves with in this thesis, typically prepare such eigenstates and it is important to point out that they are static [23], a fact that appears to stand in stark contrast to the dynamic picture presented above. So how can we talk about the flow of vibrational energy and IVR if there is no time-dependence?

The molecular (rotation)-vibration eigenstates ψ_n are the solutions to the eigenvalue problem posed by the time-dependent Schrödinger equation,

$$\hat{H}\Psi(t) = i\hbar\frac{\partial\Psi}{\partial t} = E_n\psi_n \mathrm{e}^{-iE_nt/\hbar}\,, \tag{1.2}$$

where E_n is the energy eigenvalue belonging to ψ_n, $\hat{H}$ is the (time-independent) molecular Hamiltonian, and $\hbar$ is Planck's constant divided by 2π. We note that all relevant expectation values and the probability distribution, $\Psi^*\Psi$, are time-independent.

As long as vibrational excitation is low compared to the dissociation energy and the molecule in an isolated environment, we can assume the intramolecular potential to be harmonic. This enables us to divide the vibrational motions into normal modes, and the eigenstates of the molecular Hamiltonian (the zero-order states) will correspond to these normal modes. Any initial excitation of one of the normal modes will remain contained in the same mode. However, as the degree of vibrational excitation increases or the molecule approaches a reaction partner, *e.g.* a surface, anharmonic terms or terms describing the molecule-surface interaction will become important. This leads to the breakdown of the harmonic approximation. Eventually, a bond may be broken, highlighting the fact that the excitation can no longer correspond to our initial normal

modes. The classical picture, which is dynamic, can be brought into agreement with the static quantum mechanical picture by recognizing that the initial excitations are then no longer eigenstates of the Hamiltonian, because the latter has evolved in time as the molecule approached a transition state, for instance. The initial state, however, can be expressed as a superposition of the instantaneous eigenstates at any time t,

$$\Psi(t=0) = \sum_i c_i \psi_i \,, \tag{1.3}$$

where c_i is a mixing coefficient with $c_i \equiv \langle \psi_i | \Psi(t=0) \rangle$. The time-evolution of this initial state is then given by

$$\Psi(t) = \sum_i c_i \psi \mathrm{e}^{-iE_i t/\hbar} \,. \tag{1.4}$$

This state *does* exhibit a time-dependence and it is this dephasing of the initial state that is the quantum mechanical equivalent of what we have previously recognized as vibrational energy flow, or IVR.

1.2.4 Experimental methods

The goal in the field of chemical reaction dynamics is to obtain a *predictive* understanding of the dynamic processes that take part in a chemical reaction. In order to improve and to validate the computed PES and the dynamical calculations that are run on them, detailed dynamical data from well-defined experiments are required. It is the task of the experimentalist to design experiments, which can gather as much information about the characteristics of the PES as possible. We follow the reductionist approach to this problem, that is, we aim to eliminate or at least reduce the degree of averaging over initial and final conditions, which would otherwise obscure the subtle effects that we want to observe.

Since several decades, experimentalists use molecular beams to study the interaction of atoms and molecules with each other[11,24] or with interfaces[25–27]. A molecular beam is a directed stream of gas that propagates through vacuum until reaching the collision partner. It provides an ideal environment for studying reaction dynamics at a single collision level because molecules, once the beam is formed, are isolated and undergo no further collisions before they reach the target. Furthermore, the kinetic and internal energy of molecules in the beam can be, to some degree, tuned independently. Supersonic molecular beams have proven particularly useful because they prepare molecules with a well-defined speed and force them into occupying only few, low-lying internal states.

This avoids many of the averaging effects coming from different initial speeds and dispersed quantum state populations, which would otherwise obscure details in the product distributions. In the field of gas-surface reaction dynamics, molecular beams are combined with surface science techniques to define the initial conditions of the incoming molecules and of the surface with as much control as possible.

An experiment that prepares the incoming molecule in one quantum state at a time and then probes the reaction products in all possible quantum states is among the most powerful tools that we have at our disposal. Initial state selection can be achieved using optical methods employing lasers or by using electric or magnetic fields[28,29]. State-selective detection typically uses particularly sensitive methods of laser spectroscopy, as I will discuss below. In this work, I present such a *state-to-state* scattering study, where methane molecules are prepared in a molecular beam, collided with a clean well-defined Ni(111) surface and the quantum states of the scattered molecules analyzed. From these quantum-state-resolved scattering distributions, we can infer certain features of the PES, and the highly detailed data are valuable for benchmarking the dynamical simulations and their underlying PES[30].

1.3 Dynamics of CH_4 on surfaces

Owing to its significance as a model system, a large body of work dealing with the chemisorption of CH_4 on metal surfaces has accumulated over the past decades. Since this topic was reviewed only very recently and by multiple authors[3,5,31], I will not go into much details here. Most experimental insight into this prototypical reaction has come from quantum-state-resolved reactivity measurements[5]. Here, molecular beams of methane or its isotopologues are prepared in particular rovibrationally excited states using IR pumping. Then, the composition and the amount of surface-bound reaction products are analyzed by surface science techniques. By exciting different vibrations, one can determine their relative effectiveness in promoting the reaction and infer about certain details of the PES as well as about the influence of IVR.

Briefly speaking, CH_4 dissociation on Ni(111) is classified as a system with a later barrier. The reaction is promoted both by incidence translational and vibrational energy[32,33]. Mode-specific reactivity was first reported[34] by Beck *et al.* in 2003. Here, the reactivity of the molecule depends not simply on its total energy content but also on the particular vibrational mode that was excited. The authors showed that excitation of the nearly isoenergetic $2\nu_6$ and $\nu_1 + \nu_6$ vibrations of CH_2D_2 give rise to vastly different sticking coefficients on Ni(100), where the latter mode promotes reactivity five times more strongly. Later, mode-specificity was also demonstrated[35] for CH_4 on the same

surface, where one quantum of symmetric C–H stretch excitation (ν_1) is up to one order of magnitude more effective in promoting reaction than the anti-symmetric C–H stretch vibration (ν_3), although the two modes are nearly isoenergetic as well. This might seem somewhat surprising at first because there is no individual bond in the tetrahedral CH_4 molecule that can be singled out by the excitation. Instead, all C–H bonds carry the same vibrational amplitude. Since then, more systems were discovered that show mode specificity. Hundt *et al.* were able to show[36] that, within the same vibrational mode, different vibrational symmetries can affect reactivity as well. Despite the fact that IVR is evidently not complete on the time-scale of the reaction, the pronounced difference in the reactivities of $CH_4(\nu_1)$ and $CH_4(\nu_3)$ suggests that surface-induced IVR must play some role in that the initial normal modes must evolve into localized excitations during the surface encounter. This was indeed predicted[37] by Halonen *et al.* on the basis of a vibrationally adiabatic model, which simulated the normal mode evolution as a function of surface distance.

Additionally, the dissociation of deuterated isotopologues of methane was found to be bond-selective in many cases. The first report of bond-selectivity was given by Killelea *et al.*, who discovered[38] that vibrational excitation of the C–H stretch vibration in CHD_3 caused preferential breaking of this bond on Ni(111). In the following years, several other isotopologue-surface systems have been identified, which exhibit similar behavior[39].

Yoder *et al.* studied[40,41] methane reactivity also in dependence of angular momentum alignment. Here, IR laser pumping prepared vibrationally excited CH_4 or CHD_3 with the vibrational transition dipole moment aligned either parallel or perpendicular to the surface. For both molecules, the reactivity is found to be highest when the vibrational amplitude is aligned parallel to the surface.

All these experimental results clearly show that IVR is not complete on the time-scale of the molecule-surface collision under hyperthermal molecular beam conditions. CH_4 dissociation on metal surfaces, therefore, cannot be described accurately by statistical rate theories. Despite the staggering detail in the available state-resolved reactivity data, some questions remain unanswered because these measurements can only reveal the behavior of those molecules that actually react. For example, one might ask why only a maximum of about 10 % of all methane molecules can react even when their combined internal and kinetic energies greatly exceed the reaction barrier height[33]. Two possible explanations come to mind. First, fast vibrational quenching might lead to a loss of internal energy before the transitions state is reached. Such a loss mechanism would probably have to involve coupling to the electron-hole pairs of the metal since

methane's vibrational frequencies are high compared to typical phonon frequencies. Electronically non-adiabatic behavior has so far never been observed for polyatomic molecules at surfaces and the fact that BOA-based models can nowadays quantitatively reproduce the reactivity data renders a strong influence of electron-hole pair excitation unlikely. Notwithstanding, experiment was up to now unable to clarify to what extent electronically non-adiabatic process play a role in methane dissociation. The second explanation assumes that the reactivity is limited by transition state accessibility. That is, energy from the initial normal modes or the translational DOF cannot be channeled efficiently enough into the reaction coordinate. If we could detect those molecules with quantum state resolution that scattered non-reactively, we would be able to find answers to some of these questions. More specifically, it should be possible to map out the coupling of vibrational modes, both among each other and to electron-hole pairs, by pre-exciting molecules in well-defined initial states and detecting all the different vibrational states after scattering.

Several surface scattering studies on methane have been reported over the years. However, only one of them, conducted by Miller and co-workers, resolved the quantum state distribution of the scattered CH_4. I will discuss it further below. Other scattering studies on a variety of metal surfaces and on LiF(001) were reported in the past and are summarized in van Reijzen's thesis[42]. Only one very recent study, reported[43] by Al Taleb and Farías, is of immediate relevance to this work and should there be mentioned explicitly. These authors observed, for the first time, quantum coherent diffraction of CH_4 from a transition metal, here Ni(111). They recorded the intensity of a CH_4 molecular beam that scattered along the $\langle 11\overline{2}\rangle$ direction for three incidence kinetic energies between 69 and 109 meV using a mass spectrometer. By rotating the surface, they were able to resolve clear diffraction peaks in the angular distributions at all E_i, indicating that the scattering is direct. In addition to this, they observe rotationally induced diffraction (RID) peaks. These are peaks that appear close to the elastic diffraction features and stem from the conversion of incidence translational into rotational ($T \rightarrow R$) energy. The accompanying loss of momentum normal to the surface gives rise to the slight deflection from the elastic feature. In that sense, the authors detected scattered CH_4 with resolving the rotational states. It should be noted that such diffraction patterns are only visible at low surface temperatures ($T_S \approx 100\,K$) where Debye-Waller attenuation is greatly reduced. Interestingly, in the same paper, the authors report that no diffraction pattern is observed from graphene-covered Ni(111), which they attribute to trapping-desorption being the dominant scattering channel.

1.4 Surface scattering of polyatomic molecules

1.4.1 Previous work

It should have become clear through the preceding discussion that there is a lack of molecular beam scattering studies, which also resolve the post-scattering state distributions of methane. This, however, is true for polyatomic molecules in general and all the more remarkable when considering the vast body of work that is available for diatomic molecules[25,44–46]. I will briefly review the few cases for which quantum-state-resolved data was obtained for polyatomics scattering from surfaces.

The earliest experiments, which were conducted with surfaces prepared under well-defined conditions, that is, in ultra-high vacuum (UHV), are those reported by Merrill and co-workers. They studied the vibrational relaxation of CO_2 in collisions with various polycrystalline metal surfaces[47,48] as well as LiF(001)[49]. A pulsed infrared (IR) laser excited the bulb CO_2 gas that was admitted to the UHV chamber and a fast IR detector measured the time-decay of the fluorescence signal in the 4.3 μm spectral region. They found varying degrees of vibrational accommodation, but in all cases relaxation was attributed to the fraction of molecules that became temporarily trapped on the surface, which led to their deactivation.

The first study, which employed a molecular beam, a single crystal metal surface prepared in UHV and state selective product detection, was performed[50,51] by Bruce Kay *et al.* These authors detected ammonia scattering from Au(111) in the vibrational ground state or excited states of the ν_2 "umbrella" mode using rotationally-resolved (2+1)-REMPI spectroscopy. The study in Ref. [51] has become a classic example for translational-to-vibrational ($T \rightarrow V$) energy transfer. Here, the vibrational excitation of NH_3 was found to increase with incident beam energy, exciting up to three quanta of vibration. Interestingly, the translational energy onset at which each of these states starts to become populated correlates perfectly with the energy required to excite the corresponding number of vibrational quanta. The authors concluded that the excitation is due to efficient $T \rightarrow V$ energy transfer. The surface temperature, by contrast, has no effect on the excitation probability, leading to the conclusion that the scattering occurs *via* a direct mechanism. In Ref. [50] the same authors studied the rotationally inelastic scattering of NH_3 from the same surface and found a propensity for excitation of low-K states, *i.e.* a preference for rotation about an axis perpendicular to the figure axis.

In the late 1990s, Miller and co-workers performed molecular beam scattering of C_2H_2[52–54] and CH_4[55] from LiF(001). Although they did not investigate scattering from a metal, their studies are of great relevance because we use their experimental

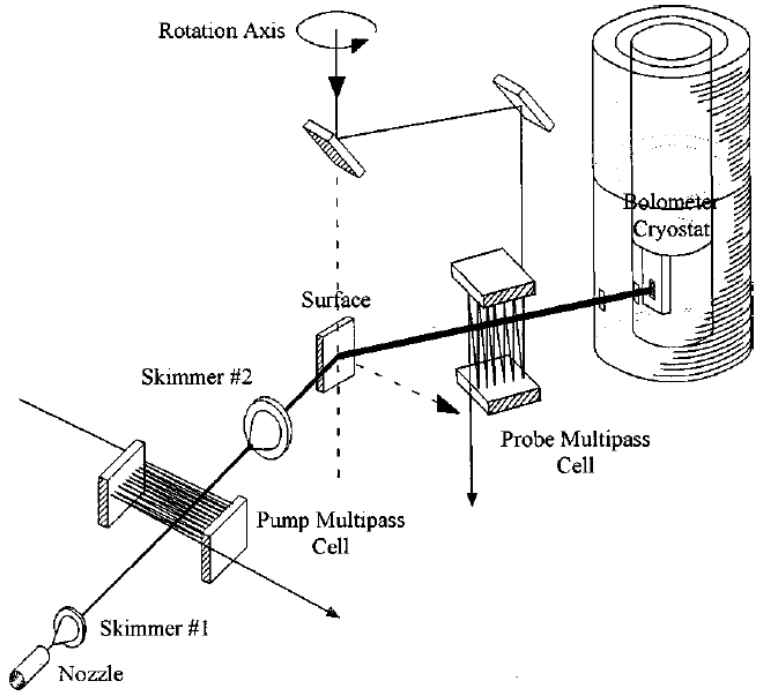

Figure 1.3 Schematic diagram of the experimental setup used by the Miller group for molecular beam-surface scattering of CH_4. Reproduced with permission from Ref. [53].

design as a guide for our scattering experiments. They were the first ones to report beam-surface scattering with product detection based on IR spectroscopy, which was made possible by combining a tunable IR laser with a cryogenic bolometer. Figure 1.3 shows a schematic of their experimental setup. A continuous molecular beam was generated by expanding the gas of interest through a small nozzle into vacuum. The beam could be state-prepared in a specific rovibrationally excited state using IR laser excitation in a multipass cell. A bolometer detector placed at an angle θ_f with respect to the surface normal sampled the scattered molecules. On their way to the detector, the molecules were interrogated by a modulated IR laser that selectively excited them, which in combination with the bolometer allowed the determination of their quantum state populations. I will highlight the principle of this detection technique in more detail in the next section.

The Miller group was able to resolve individual rotational states of the vibrational ground states of scattered C_2H_2 and CH_4. By measuring the Doppler shifts in the scattered beam, they also determined the final speed distributions. For scattered C_2H_2 incident in the vibrational ground state, the authors found that rotational excitation does not further increase when the normal component of the incidence kinetic energy,

$E_n = E_i \cos\theta_i^2$, is increased beyond $\sim 60\,\text{meV}$. They interpreted this behavior as being due to the excitation of low-energy bending vibrations that take up the additional energy. However, they were not able to detect these states. Furthermore, they studied the vibrational relaxation probability in acetylene, which they initially prepared in the anti-symmetric C–H stretch state. They found that direct scattering from LiF(001) is vibrationally elastic, while quenching of the vibrational excitation takes place for molecules that underwent trapping followed by desorption. Surprisingly, they found no signs of rotational rainbow scattering for neither C_2H_2 nor CH_4. This phenomenon is frequently observed in direct collisions of diatomics with surfaces[56–62] and comes from an orientation dependent translation-to-rotation energy transfer. The authors suggested so-called "chattering" collisions and orientation-dependent excitation of low-lying bend-vibrations as possible explanations for this absence.

Perkins and Nesbitt have studied the scattering of CO_2 from liquid surfaces using IR laser absorption spectroscopy. They were able to distinguish direct scattering from trapping-desorption by analyzing the rotational distributions and the Doppler-broadened absorption profiles. Furthermore they investigated the stereodynamics, finding a propensity for "top-spin" rotational excitation, which increases strongly as a function of J-state[63].

Later, Golibrzuch *et al.* employed a newly developed (1+2)-REMPI scheme for performing state-to-state scattering of acetylene from Au(111)[64]. They found that rotational rainbow scattering has a negligible role in the overall rotational excitation and that vibrational excitation of one or two quanta of the *trans*-bend vibration increases with E_i. Similar to the observations made by Kay *et al.*, the authors interpret this as a signature of mechanical, *i.e.* electronically adiabatic, $T \rightarrow V$ energy transfer.

Very recently, the same group reported[65] a new (1+1')-REMPI scheme that allows rotational-state-resolved detection of formaldehyde. They probed[66,67] the rotational states after scattering from Au(111) and found, for the first time in the case of a non-linear polyatomic molecule, a high-J rotational rainbow and a propensity for rotation about the figure axis in the fraction of molecules that underwent impulsive scattering. Their results further suggest that the molecule's affinity for rotational excitation aids in converting and storing incidence translational energy. This efficient energy removal mechanism enhances the trapping-probability when E_i is above 0.5 eV.

1.4.2 Quantum-state-selective detection

Collisions between molecules and surfaces typically generate scattered products, which are widely dispersed in space, quantum states, and in the case of pulsed experiments

also in time. The resulting low fluxes per quantum state call for detection techniques with extremely high sensitivities and it should not surprise that Resonantly Enhanced Multiphoton Ionization (REMPI) spectroscopy has become and still is the method of choice for experimentalists working in the field. Apart from its unmatched sensitivity, the straight forward integration of a REMPI detector into a UHV environment, makes the technique particularly attractive for surface scattering. These advantages generally outweigh the complications that electronic spectroscopy can bring in terms of spectral complexity and conversion of intensities to populations.

While well-characterized ionization schemes are available for numerous atoms, diatomic molecules and small radicals, the situation is much different in the realm of polyatomic molecules for which only few sufficiently sensitive and rotationally resolved REMPI schemes are known[50,51]. Despite more recent efforts by the Wodtke group[64–67] towards the development of such schemes for beam-surface scattering applications, the lack of applicable REMPI schemes is still the primary reason for the scarcity of such studies with polyatomics. In particular, no REMPI scheme has yet been reported for CH_4.

The advantages of using a bolometer in combination with a narrow-band tunable IR laser to perform spectroscopic measurements in a molecular beam have been explored first in the pioneering work of Gough, Miller and Scoles[68]. A molecular beam impinging on a cryogenic bolometer gives up its translational and internal energy, which this thermal detector sees as a DC signal. When molecules in the beam are excited ("tagged") by a modulated laser beam, the additional internal energy is registered as an AC signal, which is selectively amplified and gives a measure of the excited population. This bolometric method has also been referred to as optothermal spectroscopy in the past.

The use of IR light as a spectroscopic probe provides immediate rovibrational state resolution and makes it universally applicable. Even weaker IR-active transitions can be addressed by the use of multipass arrangements or optical enhancement cavities.

The method has been used extensively for high-resolution spectroscopy in molecular beams, most notably in the seminal work of R. E. Miller. Ettinger et al. introduced[69] the method to molecular beam-surface scattering in their investigation of the rotationally inelastic scattering of HF from LiF(100). However, its potential for studying the scattering of polyatomics remained unused until Miller and co-workers published a series of papers on the scattering of acetylene and methane from the same surface[52–55].

Despite the advantages, certain practical limitations have hindered the implementation of optothermal detection for beam-surface scattering. Incorporating a bolometer into a UHV system is challenging due to the large size of the detector, which on one hand

should be placed as close as possible to the surface and on the other hand must not block the incoming beam. There are also problems with the UHV compatibility of bolometers as they typically contain materials that cannot undergo the usual baking procedures required to achieve UHV conditions. This problem is reflected in the fact that all surface scattering studies have been performed on rather inert LiF(100) which is easily cleaned by heating and is more forgiving towards imperfect UHV conditions compared to most metal surfaces.

Another aspect, which rendered application of the technique difficult, was the limited choice of appropriate IR light sources. Typical semiconductor bolometers have slow time responses, requiring lasers that operate in continuous-wave (cw) mode. For a long time, mostly F-center lasers were used because they offered cw operation and tunability but they provided only low power. This presents a serious drawback since optothermal detection attains its highest signal-to-noise ratio when the transferred population is maximized. Exceptions were cases where the wavelengths of molecular absorption lines coincided with emission lines from readily available cw lasers. One example is the HF chemical laser, which was used to study HF scattering in crossed beams with rare gases[70] and from the LiF(100) surface[69].

Since the last surface scattering experiments by Miller and co-workers, widely tunable narrow-band continuous-wave mid-IR light sources based on optical parametric oscillators (OPOs) have emerged and rapidly found their way into physical chemistry laboratories[71]. Their high brightness and coherence has enabled sophisticated laser pumping schemes exploiting the adiabatic following method[72]. Specifically, rapid adiabatic passage (RAP) can achieve almost complete population inversion in favorable cases[73]. The enhanced excitation efficiencies achieved with these lasers provide a substantial improvement for reactant state preparation[74] but also for product detection using the bolometric method. They are key to the successful implementation of state-to-state scattering of polyatomics in this work.

1.5 Objective and outline of this thesis

Starting with the Ph.D. work[42] of van Reijzen, we upgraded an existing molecular beam-surface science apparatus for achieving state-selective detection of scattered polyatomic molecules. Following R. E. Miller's work, we added a cryogenic bolometer and combined it with the OPO light sources available in our laboratory.

Building on the initial results obtained by van Reijzen, I extended the experiments to molecular beams with higher energies. Moreover, I implemented precision frequency scanning in order to determine the absorption line profiles of the scattered molecules,

which yields information on their final speeds. With these tools at hand, I studied the fate of initial vibrational energy and the rotationally inelastic scattering of CH_4 from Ni(111).

The remainder of this thesis is organized as follows: Chapter 2 describes the molecular beam-surface scattering apparatus and the IR laser setups that were used for optical state-preparation in the incident beam as well as for state-selective tagging of scattered molecules before their detection by a cryogenic bolometer.

In chapter 3, I will elaborate on the details of our laser tagging technique. Selected results from our scattering experiments serve to illustrate the basic principle and the capabilities of the method. This chapter also includes a discussion of the relevant aspects of methane's IR spectroscopy.

The following chapter 4 presents a state-to-state scattering study, where incident CH_4 was prepared with one quantum of the anti-symmetric C–H stretch vibration and in the rotational state $J = 1$ before scattering from a Ni(111) surface. The final scattering distributions were resolved by vibrational and rotational quantum state as well as, partially, by angle and speed. These results elucidate the fate of vibrational energy in the direct molecule-surface collision.

In chapter 5, I present results concerning the rotationally inelastic scattering of CH_4 in its vibrational ground state. Measurements of the final rotational state distributions were performed as a function of incident translational energy and combined with an extended analysis of the rotational-state-resolved angular distributions and Doppler-broadened absorption profiles. Classical scattering simulations are presented, which serve to aid the interpretation of the experimental findings.

In the final chapter, I will summarize the results and give future directions for experimental improvements as well as suggestions for decisive experiments that can help to further elucidate the dynamics of methane at surfaces.

References

[1] K. W. Kolasinski, *Surface Science: Foundations of Catalysis and Nanoscience* (John Wiley & Sons, Ltd, Chichester, 2012).

[2] I. Chorkendorff and J. W. Niemantsverdriet, *Concepts of Modern Catalysis and Kinetics* (Wiley-VCH, Weinheim, 2003).

[3] L. Juurlink, D. Killelea, and A. Utz, Prog. Surf. Sci. **84**, 69 (2009).

[4] H. Chadwick and R. D. Beck, Chem. Soc. Rev. **45**, 3576 (2016).

[5] H. Chadwick and R. D. Beck, Annu. Rev. Phys. Chem. **68**, 39 (2017).

[6] D. R. Killelea and A. L. Utz, Phys. Chem. Chem. Phys. **15**, 20545 (2013).

[7] J. E. Lennard-Jones, Trans. Faraday Soc. **28**, 333 (1932).

[8] R. M. Logan and R. E. Stickney, J. Chem. Phys. **44**, 195 (1966).

[9] E. K. Grimmelmann, J. C. Tully, and M. J. Cardillo, J. Chem. Phys. **72**, 1039 (1980).

[10] B. Baule, Ann. Phys. **349**, 145 (1914).

[11] M. Brouard and C. Vallance, eds., *Tutorials in molecular reaction dynamics* (Royal Society of Chemistry, Cambridge, 2012).

[12] J. C. Polanyi, Acc. Chem. Res. **5**, 161 (1972).

[13] M. Born and R. Oppenheimer, Ann. Phys. **84**, 0457 (1927).

[14] J. C. Tully, Theor. Chem. Acc. **103**, 173 (2000).

[15] J. Behler and M. Parrinello, Phys. Rev. Lett. **98**, 146401 (2007).

[16] J. Behler, J. Chem. Phys. **145**, 170901 (2016).

[17] K. Shakouri, J. Behler, J. Meyer, and G.-J. Kroes, J. Phys. Chem. Lett. **8**, 2131 (2017).

[18] Q. Liu, X. Zhou, L. Zhou, Y. Zhang, X. Luo, H. Guo, and B. Jiang, J. Phys. Chem. C **122**, 1761 (2018).

[19] F. Nattino, H. Ueta, H. Chadwick, M. E. van Reijzen, R. D. Beck, B. Jackson, M. C. van Hemert, and G.-J. Kroes, J. Phys. Chem. Lett. **5**, 1294 (2014).

[20] G.-J. Kroes, Phys. Chem. Chem. Phys. **14**, 14966 (2012).

[21] G. Herzberg, *Infrared and Raman spectra of polyatomic molecules*, Molecular spectra and molecular structure, Vol. 2 (Krieger, Malabar, Florida, 1991).

[22] E. B. Wilson, J. C. Decius, and P. C. Cross, *Molecular vibrations: the theory of infrared and Raman vibrational spectra* (Dover Publications, New York, 1980).

[23] D. J. Nesbitt and R. W. Field, J. Phys. Chem. **100**, 12735 (1996).

[24] Giacinto Scoles, ed., *Atomic and molecular beam methods, Vol. 1* (Oxford University Press, New York, 1988).

[25] J. Barker and D. Auerbach, Surf. Sci. Rep. **4**, 1 (1984).

[26] A. W. Kleyn, Chem. Soc. Rev. **32**, 87 (2003).

[27] L. Vattuone, G. Bracco, M. Smerieri, L. Savio, and M. Rocca, in *Dynamics of Gas-Surface Interactions*, Springer Series in Surface Sciences, Vol. 50, edited by R. Díez Muiño and H. F. Busnengo (Springer, Berlin and Heidelberg, 2013) pp. 1–23.
[28] G. O. Sitz, Rep. Prog. Phys. **65**, 1165 (2002).
[29] S. Y. Van De Meerakker, H. L. Bethlem, and G. Meijer, Nature Phys. **4**, 595 (2008).
[30] K. Golibrzuch, N. Bartels, D. J. Auerbach, and A. M. Wodtke, Annu. Rev. Phys. Chem. **66**, 399 (2015).
[31] A. C. Luntz and R. D. Beck, J. Vac. Sci. Technol. A **35**, 05C201 (2017).
[32] L. B. F. Juurlink, P. R. McCabe, R. R. Smith, C. L. DiCologero, and A. L. Utz, Phys. Rev. Lett. **83**, 868 (1999).
[33] R. R. Smith, D. Killelea, D. F. DelSesto, and A. L. Utz, Science **304**, 992 (2004).
[34] R. D. Beck, P. Maroni, D. C. Papageorgopoulos, T. T. Dang, M. P. Schmid, and T. R. Rizzo, Science **302**, 98 (2003).
[35] P. Maroni, D. C. Papageorgopoulos, M. Sacchi, T. T. Dang, R. D. Beck, and T. R. Rizzo, Phys. Rev. Lett. **94**, 246104 (2005).
[36] P. M. Hundt, M. E. van Reijzen, H. Ueta, and R. D. Beck, J. Phys. Chem. Lett. **5**, 1963 (2014).
[37] L. Halonen, S. L. Bernasek, and D. J. Nesbitt, J. Chem. Phys. **115**, 5611 (2001).
[38] D. R. Killelea, V. L. Campbell, N. S. Shuman, and A. L. Utz, Science **319**, 790 (2008).
[39] L. Chen, H. Ueta, R. Bisson, and R. D. Beck, Farad. Discuss. **157**, 285 (2012).
[40] B. L. Yoder, R. Bisson, and R. D. Beck, Science **329**, 553 (2010).
[41] B. L. Yoder, R. Bisson, P. Morten Hundt, and R. D. Beck, J. Chem. Phys. **135**, 224703 (2011).
[42] M. E. van Reijzen, *State-to-state scattering of CH_4 from Ni(111) and Gr/Ni(111)*, Ph.D. thesis, École polytechnique fédérale de Lausanne, Lausanne (2016).
[43] A. Al Taleb and D. Farías, Phys. Chem. Chem. Phys. **19**, 21267 (2017).
[44] M. C. Lin and G. Ertl, Annu. Rev. Phys. Chem. **37**, 587 (1986).
[45] A. Wodtke, D. Matsiev, and D. Auerbach, Prog. Surf. Sci. **83**, 167 (2008).
[46] L. Vattuone, L. Savio, F. Pirani, D. Cappelletti, M. Okada, and M. Rocca, Prog. Surf. Sci. **85**, 92 (2010).
[47] J. Misewich, C. N. Plum, G. Blyholder, P. L. Houston, and R. P. Merrill, J. Chem. Phys. **78**, 4245 (1983).
[48] J. Misewich, P. L. Houston, and R. P. Merrill, J. Chem. Phys. **82**, 1577 (1985).
[49] J. S. Hamers, P. L. Houston, and R. P. Merrill, J. Chem. Phys. **92**, 5661 (1990).
[50] B. D. Kay, T. D. Raymond, and M. E. Coltrin, Phys. Rev. Lett. **59**, 2792 (1987).
[51] B. D. Kay, T. D. Raymond, and M. E. Coltrin, Phys. Rev. B **36**, 6695 (1987).

[52] T. W. Francisco, N. Camillone III, and R. E. Miller, Phys. Rev. Lett. **77**, 1402 (1996).
[53] A. C. Wight and R. E. Miller, J. Chem. Phys. **109**, 8626 (1998).
[54] A. C. Wight, M. Penno, and R. E. Miller, J. Chem. Phys. **111**, 8622 (1999).
[55] A. C. Wight and R. E. Miller, J. Chem. Phys. **109**, 1976 (1998).
[56] R. Schinke, J. Chem. Phys. **76**, 2352 (1982).
[57] R. Elber and R. B. Gerber, J. Chem. Phys. **79**, 4087 (1983).
[58] H. Voges and R. Schinke, Chem. Phys. Lett. **95**, 221 (1983).
[59] R. B. Gerber, Chem. Rev. **87**, 29 (1987).
[60] A. W. Kleyn and T. C. M. Horn, Phys. Rep. **199**, 191 (1991).
[61] M. A. Hines and R. N. Zare, J. Chem. Phys. **98**, 9134 (1993).
[62] A. Kleyn, Prog. Surf. Sci. **54**, 407 (1997).
[63] B. G. Perkins and D. J. Nesbitt, Proc. Natl. Acad. Sci. **105**, 12684 (2008).
[64] K. Golibrzuch, J. H. Baraban, P. R. Shirhatti, J. Werdecker, C. Bartels, and A. M. Wodtke, Z. Phys. Chem. **229**, 1929 (2015).
[65] G. B. Park, B. C. Krüger, S. Meyer, A. M. Wodtke, and T. Schäfer, Phys. Chem. Chem. Phys. **18**, 22355 (2016).
[66] B. C. Krüger, G. B. Park, S. Meyer, R. J. V. Wagner, A. M. Wodtke, and T. Schäfer, Phys. Chem. Chem. Phys. **19**, 19896 (2017).
[67] G. B. Park, B. C. Krüger, S. Meyer, A. Kandratsenka, A. M. Wodtke, and T. Schäfer, Phys. Chem. Chem. Phys. **19**, 19904 (2017).
[68] T. E. Gough, R. E. Miller, and G. Scoles, Appl. Phys. Lett. **30**, 338 (1977).
[69] D. Ettinger, K. Honma, M. Keil, and J. Polanyi, Chem. Phys. Lett. **87**, 413 (1982).
[70] L. J. Rawluk, Y. B. Fan, Y. Apelblat, and M. Keil, J. Chem. Phys. **94**, 4205 (1991).
[71] M. Vainio and L. Halonen, Phys. Chem. Chem. Phys. **18**, 4266 (2016).
[72] N. V. Vitanov, T. Halfmann, B. W. Shore, and K. Bergmann, Annu. Rev. Phys. Chem. **52**, 763 (2001).
[73] H. Chadwick, P. M. Hundt, M. E. van Reijzen, B. L. Yoder, and R. D. Beck, J. Chem. Phys. **140**, 034321 (2014).
[74] H. Pan, S. Mondal, C.-H. Yang, and K. Liu, J. Chem. Phys. **147**, 013928 (2017).

2 Experimental setup

2.1 Overview

The experiments presented in this thesis aim at the determination of the quantum state populations of CH_4 molecules after they scattered from a well-defined Ni(111) single crystal surface. The experimental approach is based on the pioneering work of Ettinger *et al.*[1] and Miller and co-workers[2], combining a molecular beam with IR laser spectroscopy and bolometric detection.

Figure 2.1 presents the overall view of the experimental apparatus. A molecular beam is generated by supersonic jet expansion of CH_4 gas, which accelerates the molecules to a well-defined kinetic energy. It moreover cools their internal degrees of freedom leaving only few quantum states populated. The cold and collision-free molecular beam environment provides well-defined initial conditions before the molecules are collided with the target surface. It also lends itself to further quantum state preparation using optical pumping techniques. The molecular beam source (bottom left part of the figure) is coupled to a surface science chamber that contains the target surface and which is where the beam-surface scattering takes place. The ultra-high vacuum in this chamber ensures surface cleanliness during the experiments. It is, moreover, equipped with tools for surface preparation and analysis as well as a quadrupole mass spectrometer (QMS). The latter is used for performing time-of-flight (TOF) measurements, which yield the velocity distribution of the incoming molecular beam. Here, the surface is moved out of the beam path so that the chopped molecular beam enters directly into the QMS ionizer. The UHV chamber also houses a cryogenic bolometer for detecting the molecular beam after it has scattered from the surface.

The bolometric molecular beam detection is made quantum-state-specific by selective rovibrational excitation of scattered molecules before they reach the bolometer using a modulated (chopped) tunable mid-IR light source. The rovibrational energy, which is added by the optical excitation, induces a measurable increase of bolometer signal

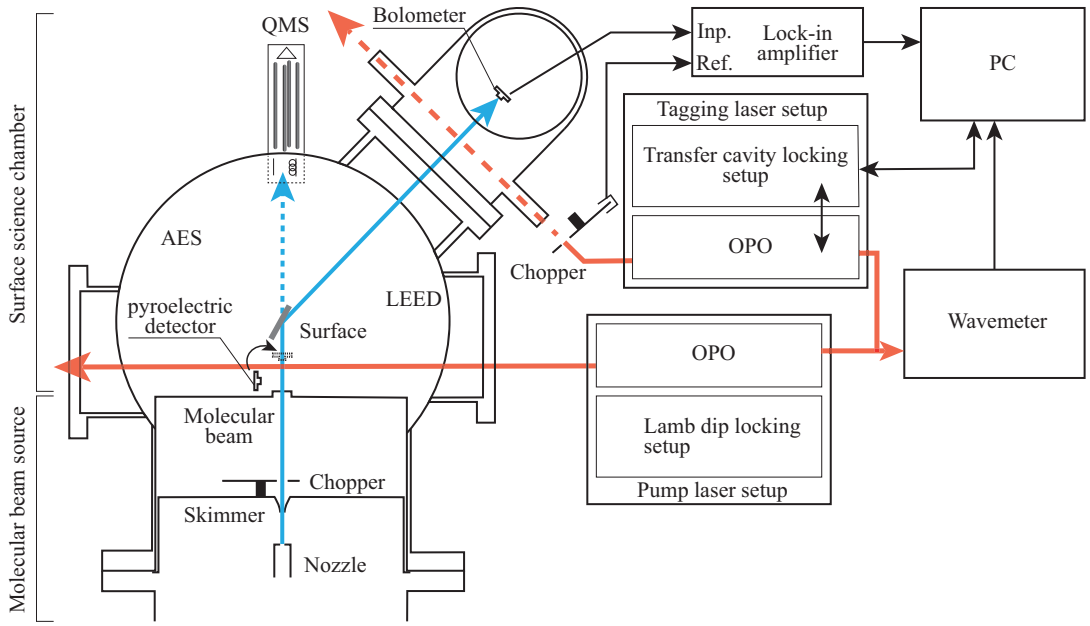

Figure 2.1 Overall schematic of the experimental apparatus. In the shown configuration, the continuous incident molecular beam is rovibratonally excited by a first continuous IR laser before scattering from the target surface. The scattered molecules are subsequently detected by a cryogenic bolometer after selective excitation by a second chopped IR laser.

that is selectively detected using a lock-in amplifier. This signal gives a direct measure of the population in the quantum state from which the excitation occurred. To increase the detection efficiency, we exploit coherent excitation through rapid adiabatic passage, maximizing the transferred population. Optionally, RAP is also used excite the incoming molecular beam, employing a second IR laser, in order to study the scattering dynamics of vibrationally excited CH_4. A room-temperature pyroelectric detector, which can be moved into the incoming molecular beam path, allows monitoring of the optical pumping efficiency.

Overall, the experimental apparatus can be divided into six parts, which I will describe in more detail in the remainder of this chapter:

- A continuous molecular beam source with a heatable nozzle,
- a UHV chamber featuring tools for surface manipulation, preparation and analysis,
- a time-of-flight setup for molecular beam speed characterization,
- a cryogenic bolometer for the detection of scattered products,
- a cw-IR laser setup for state-selective excitation of scattered molecules with a

transfer cavity setup for frequency stabilization and precision scanning,

- and optionally, a second cw-IR laser setup for state preparation of the incoming molecular beam with frequency stabilization by Lamb dip-locking.

2.2 Molecular beam-surface science apparatus

The vacuum apparatus, which combines a UHV surface science chamber with a triply differentially pumped molecular beam sources, has originally been built for performing state-resolved beam-surface reactivity measurements. Figure 2.2 shows a schematic section view of the vacuum apparatus. It has been described in detail in a previous publication[3] and in the Ph.D. theses of Schmid[4] and Maroni[5]. In the following, I will discuss the relevant features of this apparatus and focus on the changes that have been made in order to allow for the state-selective detection of scattered molecules.

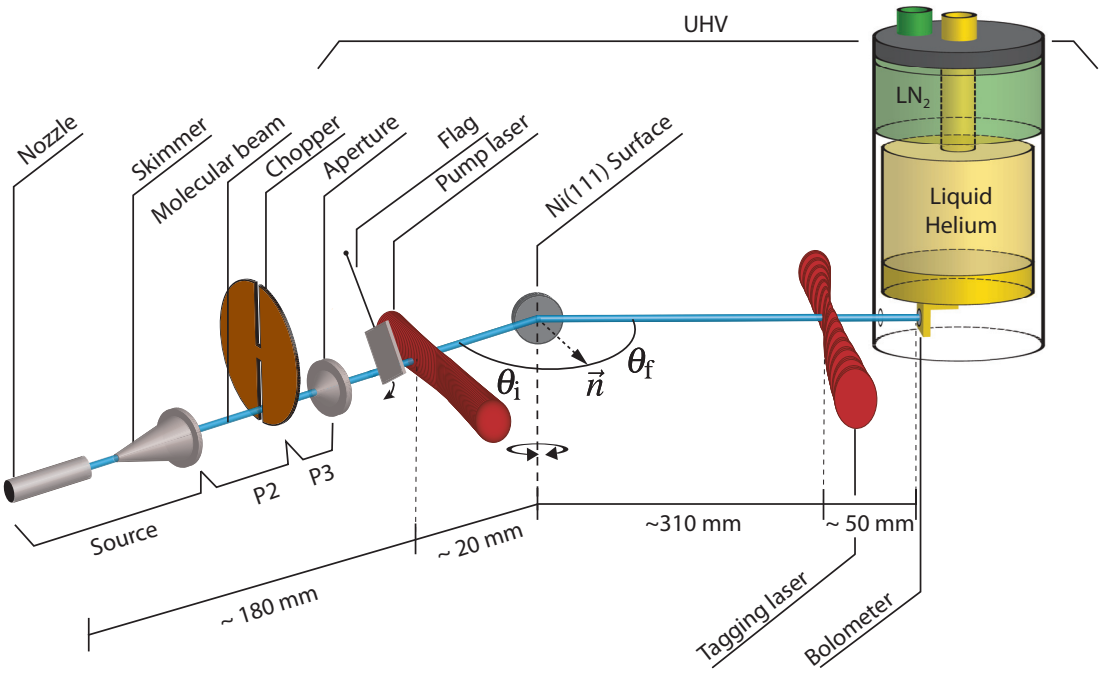

Figure 2.2 Schematic diagram of the molecular beam-surface science apparatus. P2 and P3 denote second and third differentially pumped stages, respectively. Not shown is the valve separating these two stages, the quadrupole mass spectrometer used for time-of-flight measurements and the pyroelectric detector used for determining the amount of vibrational energy added to incoming beam by IR pumping. The angle between incident molecular beam and bolometer measures $\theta_i + \theta_f = 135\ ^\circ$. The surface can be rotated about an axis perpendicular to the scattering plane.

2.2.1 Molecular beam source

The molecular beam source (Model MSC-9800, Thermionics Inc.) consists of three differentially pumped stages (Figure 2.2). Table 2.1 compiles the specifications of the used high-vacuum pumps and the typical vacuum conditions in all stages. A continuous supersonic jet is generated in the first chamber (source chamber) by expanding neat CH_4 or CH_4 seeded in helium gas through a 30 µm diameter Inconel nozzle. The molecular beam is formed by a 1 mm diameter skimmer (Beam Dynamics, Model 1), which samples the core of the expansion. The nozzle is mounted on a three-axis manipulator, which allows optimizing the nozzle position with respect to the skimmer opening, thereby maximizing the gas flow into the first differential pumping stage. Moreover, the nozzle can be heated by resistive DC heating in order to increase the beam speed. Temperature control of the nozzle is achieved by measuring the nozzle temperature close to the orifice with a *K*-type thermocouple and adjusting the heating current *via* a proportional-integral-differential (PID) feedback loop. A detailed description of the nozzle design can be found in Li Chen's thesis[6]. The source chamber is pumped by a 1300 L/s turbomolecular pump that keeps the pressure below $1 \cdot 10^{-3}$ mbar when the beam is operating.

After passing through the skimmer, the molecular beam enters the second differentially pumped stage. Here, a chopper wheel is used to generate short beam pulses for TOF measurements. The chopper wheel has a pair of opposing 2 mm wide slits that transmit the beam. A regulated brush-less DC synchronous motor (Maxon Motors) rotates the wheel and a position encoder with 2048 steps allows precise control of the motor speed between 0.5 and 200 Hz as well as positioning in a given orientation to allow the continuous beam to pass. The duty cycle of the chopper wheel is 1%. An optocoupler is mounted 180° from the molecular beam path. It registers the passing of the second chopper slit while the first slit clears the beam path. The optocoupler signal is used for triggering the TOF measurements.

The exit of the second differentially pumped stage can be closed by an O-ring-sealed separation valve that is manually actuated *via* a rotary motion feedthrough. The valve can be used to isolate the source region including the second stage, which allows venting of the source chamber without breaking vacuum in the UHV chamber. After the beam passed through the third stage, it is collimated by a cone-shaped aperture with a diameter of 1 mm before it finally enters into the UHV chamber.

2.2.1.1 Molecular beam speed characterization

Supersonic expansion occurs when a gas escapes from a high-pressure region with stagnation pressure p_{stag} into vacuum through an orifice whose diameter is much larger

Table 2.1 Typical vacuum conditions in the molecular beam-surface science apparatus and specifications of the high vacuum pumps, where S_p is the nominal pumping speed for nitrogen, f_{rot} is the rotation speed of the turbomolecular pump, and p_{base} is the base pressure under no load conditions. (*) The base pressure reaches $< 10^{-10}$ mbar when the bolometer is operating at cryogenic temperatures.

Stage	Pump model	S_p / L · s^{-1}	f_{rot} / Hz	p_{base} / mbar	
Source	Edwards STP A1303C	1300	542	$1 \cdot 10^{-8}$	
2nd differential	Edwards STP H451C	450	800	$7 \cdot 10^{-9}$	
3rd differential	Edwards STP 603C	650	583	$1 \cdot 10^{-10}$	
UHV	Pfeiffer TMU 1000 P	880	655	$1 \cdot 10^{-9}$	(*)

than the mean free path of the gas molecules at the initial pressure. During the expansion, the random thermal motion of the molecules is converted into directed mass flow in which the final flow velocity exceeds the local speed of sound $a = \sqrt{\gamma k_B T_{stag}/m}$, where k_B is the Boltzmann constant, T_{stag} is the temperature of the gas before the expansion, m is the molecular mass, and $\gamma = C_p/C_v$ is the ratio of the heat capacities at constant pressure and volume.

The theoretical description of supersonic expansions is well-documented[7] and has been outlined in previous Ph.D. theses[5,6]. Briefly, the terminal velocity of the supersonic jet is given by

$$v_\infty = \sqrt{\frac{2k_B}{\langle m \rangle} \frac{\langle \gamma \rangle}{\langle \gamma \rangle - 1} T_{stag}}\,, \tag{2.1}$$

where $\langle m \rangle = \sum_i X_i m_i$ is the average molecular mass of a gas mixture composed of i constituents and their molar fractions X_i, and $\langle \gamma \rangle = \sum_i X_i \gamma_i$ is the average ratio of heat capacities C_p/C_v. The velocity distribution of a supersonic molecular beam can be described by a flux-weighted Maxwell-Boltzmann distribution that is shifted by the stream velocity v_0,

$$f(v) \propto v^3 \exp\left[-\frac{m}{2k_B T_{||}}(v - v_0)^2\right], \tag{2.2}$$

with the translational temperature $T_{||}$ along the molecular beam axis. We determine the speed distribution of the molecular beam by performing time-of-flight measurements. Here, the beam is chopped by a mechanical chopper with low duty cycle into short pulses, which then travel towards a mass-selective detector with a fast time response. For this purpose, a QMS with an electron bombardment ionizer is installed in the UHV chamber

facing directly the incoming molecular beam.

The quadrupole mass analyzer transmits only ions of a given mass-to-charge ratio m/z while all other ions are deflected from the spectrometer axis. The selected ions are detected by the channeltron of the QMS and the ion signals amplified by a fast pre-amplifier with a gain of 100. The so-produced voltage pulses are sent to a multichannel scaler (Turbo-MCS, Ortec) which counts and stores the number the ion pulses according to their time delay with respect to a reference trigger. Here, the time is measured from the moment that one of the chopper slits lets the beam pass through while the second slit triggers the optocoupler which at that point sends the "open" signal that serves as the reference trigger for the MCS. For TOF measurements, the chopper is rotated at a rate of 200 revolutions/s, which gives a beam modulation of 400 Hz. The MCS acquisition is configured such that only every other signal from the optocoupler triggers the pulse counting. In this way, it always the same slit that triggers the optocoupler while the other slit lets the beam pass. This avoids artifacts in the final arrival time distribution that come from the fact that the two slits are not positioned at exactly 180° from each other. The final arrival time distribution is accumulated over many repeated chopper cycles.

The calibration for the TOF setup has been well described[5] by Maroni and is not repeated here. During my Ph.D. work, I have rewritten his original MATLAB script that extracts the speed distribution from the arrival time distribution in order to keep the script compatible with current and future versions of the software package (see appendix A). Since the mathematical treatment did not change compared to the ealier implementation, I will not go into much further details here. Briefly, the TOF analysis takes care of the deconvolution of the time-of-arrival distribution with the chopper gating function, applies the appropriate Jacobian transformation from time to velocity space and the necessary corrections for the various time delays occurring in the data acquisition.

2.2.2 Surface science chamber

Surface scattering takes place in the main surface science chamber. This UHV chamber is also equipped with instruments for basic surface preparation and characterization comprising an ion sputter gun (Omicron, ISE 10), an Auger electron spectrometer (AES) (Omicron) with cylindrical mirror analyzer (CMA 150), and a low energy electron diffraction (LEED) spectrometer (Omicron SPECTRALEED). The quadrupole mass spectrometer (Model HAL 301/3FPIC, Hiden Analytics) used for TOF measurements is mounted on a port aligner at the end of the chamber that is facing the molecular beam entrance. The QMS is also used for residual gas analysis and CH_4 flux monitoring during experiments. Two cold cathode ionization gauges are installed for total pressure

monitoring.

The most important alteration, which has been made to the surface science chamber, is the addition of a cryogenic bolometer for the detection of the scattered molecular beam. I will describe the bolometer itself in section 2.3 while its incorporation into the UHV chamber has been discussed in van Reijzen's thesis[8]. Briefly, the bolometer is mounted in an elbow-like extension to the main chamber. The opening aperture of the bolometer faces the surface sample and makes a fixed angle of 135° with the incident molecular beam. Molecular beam axis, target surface, and bolometer lie in the same plane and the surface-to-detector distance measures about 36 cm. Scattering angular distributions are obtained by rotating the surface about an axis perpendicular to the scattering plane.

Optical access for IR light is provided in two locations. Two differentially pumped CaF_2 windows with 50 mm diameter are mounted on opposite sides of the main chamber such that an IR laser can perpendicularly intersect the incoming molecular beam. This access is used for state preparation of the beam by IR pumping. For the state-selective detection of scattered molecules, IR excitation has to take place before the bolometer. Two differentially pumped CaF_2 windows similar to the ones mounted on the main chamber are located in the extension housing of the bolometer and provide optical access about 25 mm upstream of the detector entrance aperture and about 50 mm before the bolometer sensing element. Also here, the laser beam crosses the scattered molecules in a perpendicular geometry. Due to spatial constraints, the exit window is not mounted directly opposite to the entrance window. Instead, a 45° gold mirror is mounted at the far side, reflecting the laser beam towards the exit CaF_2 window, which assumes a Brewster angle orientation to reduce light back-reflection into the chamber. Thereby, the magnitude of scattered light, which the bolometer detects, is reduced.

The UHV surface science chamber is pumped by a 880 L/s turbomolecular pump (see Table 2.1), which is backed by a dry scroll pump. Previously, the chamber has proven to provide a UHV environment with a base pressure below $1 \cdot 10^{-10}$ mbar after baking. Unfortunately, the addition of the bolometer has deteriorated the base pressure to $1 \cdot 10^{-9}$ mbar affecting the cleanliness of the surface sample. This can be traced back to two main causes: first, the bolometer manufacturer used some materials in its construction that are not UHV compatible. We found that the amount of hydrocarbon vapors, which before were negligible, increased substantially after installing the detector. We believe that certain adhesive materials used in the liquid nitrogen cooled radiation shield are mostly responsible for this contamination. Second, the assembly of the sensitive element uses non-bakable adhesive and varnish rendering a bake-out above 60 °C impossible. However, the outgassing rate of hydrocarbons and the partial pressure of residual water

are greatly reduced when the bolometer is cooled down. In particular, the large liquid nitrogen cooled radiation shields provided efficient cryopumping. After about two hours of cooling, the base pressure in the UHV chamber drops below $1 \cdot 10^{-10}$ mbar. Despite this, the amount of hydrocarbon vapor is still high enough to cause carbon contamination on the reactive nickel surface within about 1 h. This can be remedied by keeping the temperature of the nickel crystal above ~600 K. Due to the enhanced carbon solubility in the bulk Ni at this elevated temperature[9], no permanent carbon build-up occurs because any surface carbon immediately dissolves in the bulk. Nonetheless, the vacuum quality in the current setup is a serious drawback and limits scattering studies to surface temperatures above 600 K. This leads, for instance, to strong Debye-Waller attenuation in the scattering angular distributions.

Additionally, the chamber contains an inert beam flag made from mica, which is located right after the entrance of the molecular beam. The flag is mounted on a metal arm that attaches to the rotation axle of a UHV-compatible stepper motor (Arun Microelectronics). Rotation of the stepper motor moves the flag in and out of the incoming molecular beam. The motor controller is interfaced with a PC *via* RS232 and can be remotely operated using a custom LabVIEW™ program. Initially integrated into the chamber for molecular beam reflectivity measurements with the King and Wells method, the flag is used in scattering experiments to block the beam when the scattered light contribution to the bolometer signal is to be measured.

The chamber is also equipped with a pyroelectric detector (ELTEC, 406M70-o), which is used to detect the incoming molecular beam, determine its rovibrational state populations, and quantify the IR pumping efficiency. Note that the detector differs from the one used initially by Yoder[10]. The new detector has a square sensor area with an edge length of 3.5 mm. It therefore subtends the entire molecular beam when positioned accurately. The detector is mounted on a swivel arm that allows its rotation in and out of the molecular beam axis. In the "on-axis" position, the detector assumes roughly the same position as the surface would. The pyroelectric detector operates at room temperature and is thus many orders of magnitude less sensitive compared to the cryogenic bolometer. Its sensitivity is, however, still high enough for application in the direct molecular beam. Similarly to our cryogenic bolometer, the pyroelectric detector is a thermal detector that responds to the kinetic and internal energy that a molecular beam deposits on it. An important difference is that molecules do not permanently stick to the pyroelectric element but leave it with a certain kinetic and internal energy, which are determined by the temperature of the detector and the degree to which the molecules have accommodated to it. Since it is based on the pyroelectric effect present in certain

materials, only a *change* of the detector temperature generates a voltage signal[11]. The signal is lock-in detected after amplification by a home-built amplifier.

2.2.2.1 Sample mounting, surface preparation and characterization

The left panel of Figure 2.3 shows a photograph of the sample mounting inside the UHV chamber. The sample holder is located at the end of the probe of a vertical four-axis manipulator (Thermionics, FM series), which allows translational motion in the x, y and z directions, as well as rotation about the vertical (z) axis through a doubly differentially pumped rotary flange (Thermionics, RNN series). The plane spanned by x and y defines the scattering plane. To allow for sample cooling, the holder consists of a liquid nitrogen dewar made of copper. A continuous flow of liquid nitrogen from a pressurized container feeds the dewar during operation.

The crystal is affixed to an exchangeable sample platen (Thermionics, STLC-TTC) that is shown in the right panel of Figure 2.3. Sample changing is possible without breaking vacuum by means of a load-lock chamber and a magnetically coupled rotary-linear sample transfer arm (Thermionics, FLRE series). The platen is held on the sample holder by clamps, which lock into position by a rotation of the platen. A thin tantalum

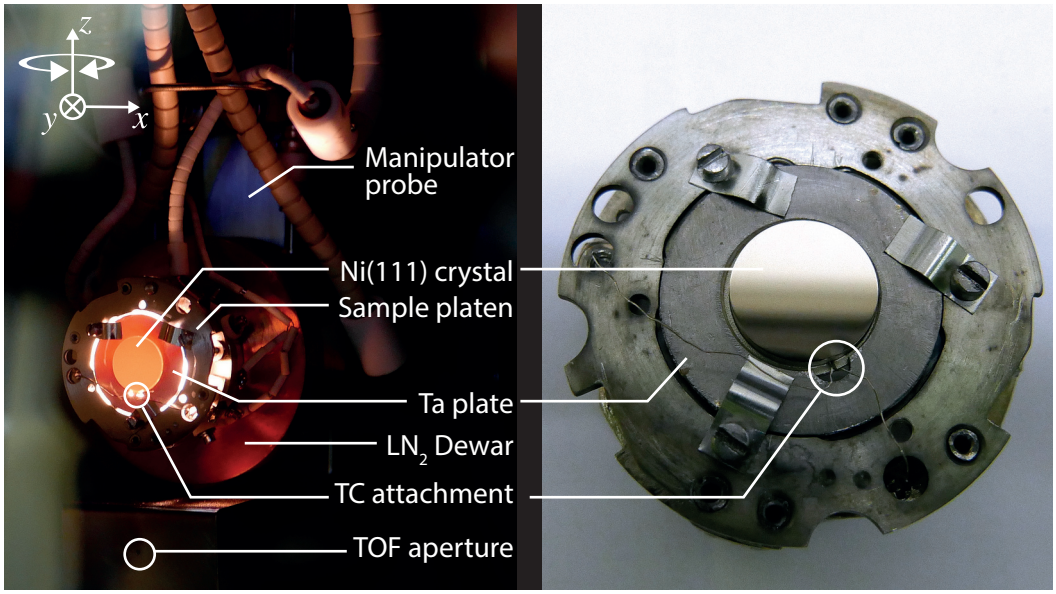

Figure 2.3 Left: Photograph of the sample holder with a Ni(111) crystal mounted in the sample platen and glowing at 973 K. TC denotes the *K*-type thermocouple, which is inserted into a small hole in the side of the crystal. The Ta plate has a cut-out at the attachment point, where escaping light from the filament behind the crystal can be seen. The scattering plane is the x, y-plane. Right: Sample platen with mounted Ni(111) crystal. The cut-out in the Ta plate, where the thermocouple attaches, is nicely visible.

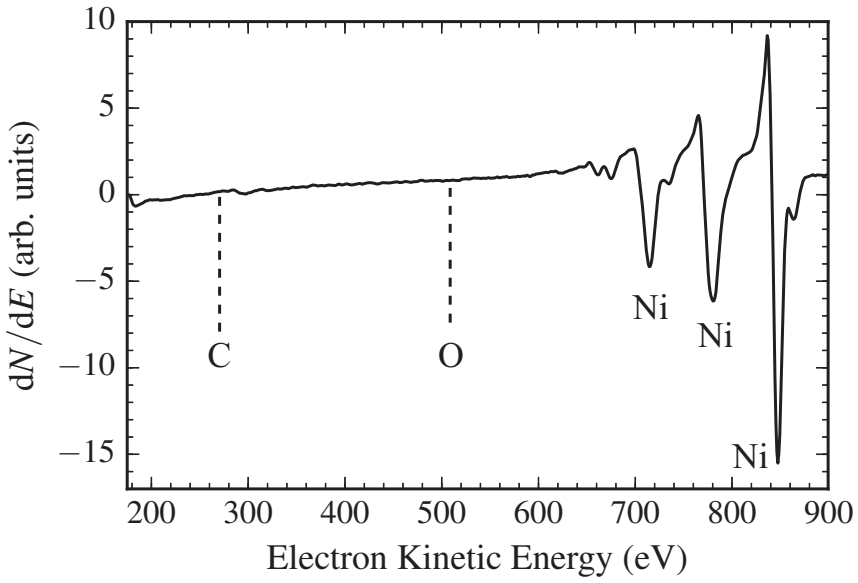

Figure 2.4 Auger electron spectrum of the clean Ni(111) surface.

(Ta) adapter plate holds the crystal in place.

The surface temperature is measured by a *K*-type thermocouple, which is inserted into a small blind hole that has been spark-eroded into the side of the crystal. Heating of the surface is done radiatively or by means electron bombardment heating. Electrons are emitted from a hot filament located behind the crystal and accelerated towards the back side of the electrically grounded sample by the negative bias voltage ($\sim 1\,\mathrm{kV}$) of the filament. The heating rate can be controlled *via* the filament heating current and bias voltage. A PID-controller (Omron, E5AK) adjusts these parameters to keep a constant set point temperature. The temperature stability is typically within 1 K.

The Ni(111) surface sample was a circular single crystal (Surface Preparation Laboratory, Leiden) with a diameter of 10 mm and 2 mm thickness. It was cleaned each day before scattering experiments by sputtering for 5 min with 1 keV Ar^+ ions at grazing incidence with an argon pressure of $5 \cdot 10^{-7}$ mbar. Sputtering was followed by annealing for 5 min at 700 °C. We verified the cleanliness of the surface using Auger electron spectroscopy (AES). Figure 2.4 displays a typical Auger electron spectrum of the clean Ni(111) surface. The resonances above 650 eV are due to LMM transitions of nickel, the most intense one located at 848 eV, using the convention of stating the energy at the local minimum of the $\mathrm{d}N/\mathrm{d}E$ curve. The two most frequent contaminants, carbon (C) and oxygen (O) exhibit KLL transitions at 273 and 510 eV, respectively. The slight curvature in the spectrum around 300 eV is a well-known diffraction feature coming from the scattering of the low-energy electrons on the Ni(111) surface and is not an indication for

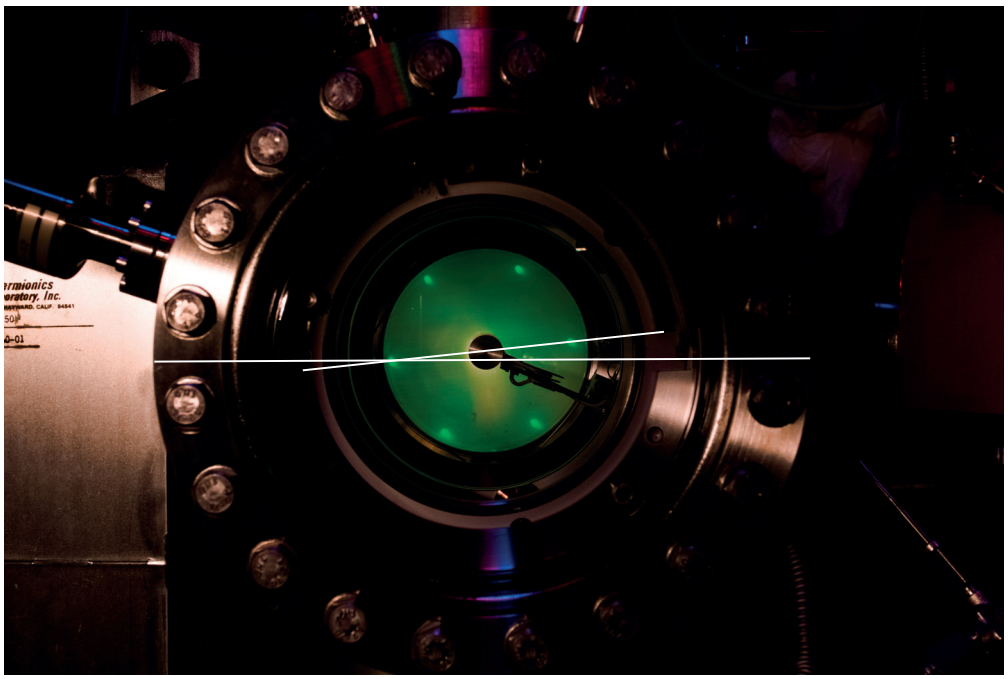

Figure 2.5 LEED image of the Ni(111) sample at an electron energy of 67 eV. The surface was heated to 673 K during the exposure of the image. To avoid distortions of the image, the bias voltage of the heating filament was switched off so that the sample was heated radiatively.

a carbon contamination[12].

The azimuthal orientation of the crystal was determined by inspection of the LEED pattern of which Figure 2.5 shows a photograph. I imported the photo into a vector graphics editor (Adobe Illustrator^{TM}) and determined the misalignment of a row of diffraction spots with respect to the molecular beam direction. The latter is indicated by two markings on both sides of the viewport flange. The horizontal white line in Figure 2.5 indicates this direction. The angle between this line and the indicated row of spots was 5.8°. Thus, the surface was oriented such that the scattering plane was at an angle of 5.8° with respect to the $\langle 11\bar{2} \rangle$ crystallographic direction that corresponds to the direction of next-nearest neighbors. Note that the LEED spots of the (111) face of an fcc lattice are rotated by 30° with respect to the real-space atomic positions.

2.3 Cryogenic bolometer

The detector is a doped silicon bolometer (Infrared Laboratories Inc.), which operates at ~ 1.6 K. The bolometer is mounted to a liquid helium cryostat and the assembly is surrounded by a liquid nitrogen cooled radiation shield except for a 4 mm diameter opening, which allows molecules to reach the bolometer. I will discuss the operation principle of semiconductor bolometers in chapter 3. Briefly speaking, any small temperature rise due to an influx of heat onto the bolometer causes a drop in its electrical resistance, which can be measured. To increase the effective detection area, the bolometer is bonded to the backside of a 4 mm diameter synthetic diamond disk. When molecules strike the diamond or overlayers of previously adsorbed molecules, they stick and transfer their kinetic and internal energy to the diamond substrate and eventually to the bolometer. The diamond is highly transparent for visible and IR light and gold coated on the backside to reflect light before it can reach the bolometer. Low sensitivity towards IR light is important because scattered IR laser light is an unwanted thermal load on the bolometer and, if the laser amplitude is modulated as in most of our tagging experiments, gives rise to a bolometer signal that cannot be filtered out by phase-sensitive amplification.

The liquid helium cryostat (Model HDL5, Infrared Laboratories) has a capacity of 2.4 L allowing for nearly 24 hours of continuous operation. Since methane does not desorb at the operating temperature, a layer of methane ice builds on the bolometer. This lowers the heat transfer rate from the adsorbate to the actual bolometer, which degrades its sensitivity as I will discuss in chapter 3. However, we found these adverse effects to be tolerable under the low flux conditions of our current surface scattering experiments. Specifically, we did not observe a significant drop in bolometer sensitivity even after ~ 8 h of continued exposure to the scattered molecular beam of CH_4. Eventually, we have to allow the bolometer to warm up in order to desorb the condensed species and recover the original properties. Note that hydrogen cannot be used as a seed gas under specular or close-to-specular scattering conditions due to the very high flux of hydrogen coming from the zeroth order diffraction peak, which leads to excessive condensation and sensitivity degradation. Likewise, the specular diffraction of a helium beam can lower the sensitivity, which in contrast to H_2 is only a temporary effect since helium does not solidify on the bolometer.

The entire bolometer assembly is housed in an elbow-shaped vacuum chamber, which attaches to the main UHV chamber of the molecular beam-surface science apparatus. A more detailed description of the bolometer incorporation into the existing apparatus can be found in van Reijzen's thesis[8].

We determined the sensitivity of the bolometer by detecting an effusive methane

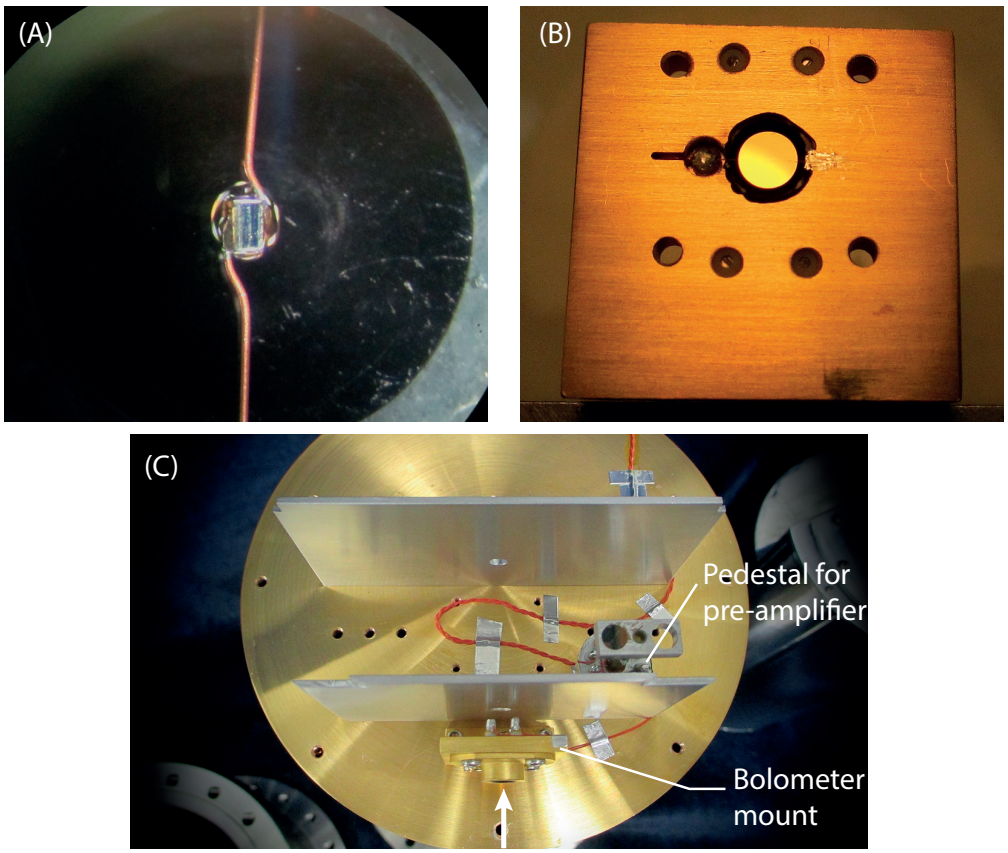

Figure 2.6 Photographs of the bolometer at different stages of assembly. (A) Bolometer element (center) bonded to the back of the diamond disk with two leads for electrical connection. (B) View of the bolometer mounting from the backside. The bolometer is suspended by two thin electrical wires from the copper mounting block, which attaches to the liquid helium cryostat. (C) View of the bolometer assembly from the bottom. The big circular gold plated surface is the cold work surface, which is also the bottom of the liquid helium dewar. The bolometer is mounted to on an L-shaped copper holder that is attached to the cold surface. The pre-amplifier stage is mounted on a pedestal to reduce thermal contact with the helium bath. The arrow indicates the direction that the molecular beam travels in our experiments. Photos are courtesy of Infrared Laboratories, Inc.

beam of known flux. By mounting the bolometer in line with the molecular beam, about 65 cm away from the skimmer orifice, it could be exposed either to the direct supersonic beam or an effusive beam of molecules from the source chamber. The flux of the direct supersonic molecular beam was high enough to cause a rapid drop in sensitivity during a time that was on the order of a few minutes due to the creation of a macroscopic layer of methane ice on the bolometer. By backfilling the source chamber of our molecular beam source with CH_4, we generated an effusive beam whose flux was low enough to not

deteriorate the detector sensitivity even over the course of several hours of exposure. For a known backing pressure, temperature of the chamber walls, and geometry, the flux of the effusive beam onto the detector can be calculated[8]. Taking into account the thermal energy of methane molecules in the effusive beam plus their adsorption energy,[(a)] we estimate that the Noise-equivalent power (NEP) after lock-in amplification is on the order of 10^{-13} W Hz$^{-1/2}$. This means that when using laser tagging, where each molecules contributes $\nu \sim 3000$ cm^{-1} of rovibrational energy to the signal, a number of

$$N_\mathrm{d} = \frac{\mathrm{NEP}}{hc\nu}\sqrt{\mathrm{Hz}} \approx 2 \cdot 10^6 \ \frac{\text{molecules}}{\mathrm{s}} \tag{2.3}$$

are required to adsorb on the bolometer to reach a signal-to-noise ratio (S/N) of one with an integration time of 0.5 s, since the bandwidth of a signal is given by $\Delta f = 1/(2\Delta t)$, where Δt is the integration time (Nyquist sampling theorem). Given the detector area of $A_\mathrm{d} = 0.126$ cm^2, the flux of molecules that can be detected under the same conditions amounts to

$$F_\mathrm{d} = \frac{N_\mathrm{d}}{A_\mathrm{d}} \approx 1 \cdot 10^7 \ \frac{\text{molecules}}{\mathrm{s} \cdot \mathrm{cm}^2} \ . \tag{2.4}$$

The quoted NEP and responsivity of the bolometer is $6.3 \cdot 10^{-14}\,\mathrm{W/Hz^{1/2}}$ and $5.8 \cdot 10^5$ V/W, respectively. Mounted in the scattering position, at a distance $r_\mathrm{d} = 36$ cm from the surface, the detector subtends a solid angle of

$$\Omega_\mathrm{d} = \frac{A_\mathrm{d}}{r_\mathrm{d}^2} = 9.7 \cdot 10^{-5} \ \mathrm{sr} \ . \tag{2.5}$$

The main amplifier stage for the bolometer signal is mounted directly onto a vacuum electrical feedthrough. The amplifier offers two gain settings, 200 and 1000-fold amplification. Since our detection scheme involves modulated laser excitation or a chopped molecular beam, the signal output of the bolometer amplifier is AC-coupled by default. Figure 2.7 shows a power spectrum of the bolometer output at a gain of 200, where no external load was incident on the bolometer except for the background radiation coming from the room temperature vacuum chamber. The spectrum was obtained by digitizing the bolometer output using a data acquisition card with a dynamic range of 16 bits over

[(a)] Note that in the quoted thesis the thermal energy of the methane molecules was taken to be equal to $5k_\mathrm{B}T$. Due to the fact that methane vibrations are relatively high in frequency, one can however not assume that they will be populated at room temperature. Hence, a thermal energy comprised only of kinetic and rotational energy, which amounts to $2k_\mathrm{B}T + 3/2\,k_\mathrm{B}T$ should be assumed. The adsorption energy was initially not taken into account, partially compensating for the previous error. I have assumed the adsorption energy to be equal to the enthalpy of sublimation of 9.7 kJ/mol found in the literature[13].

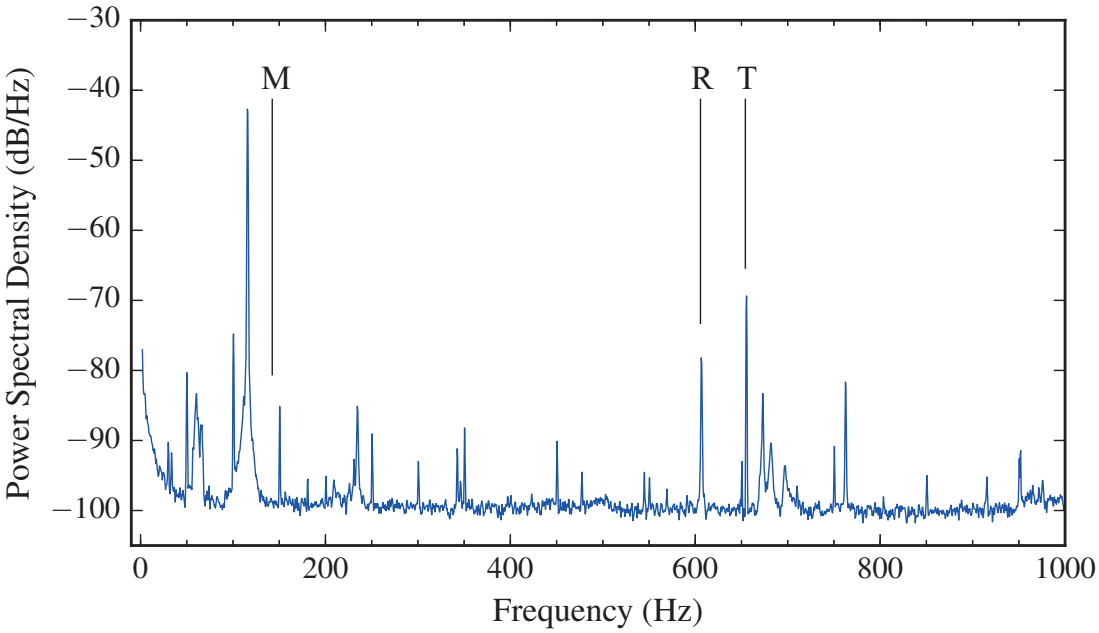

Figure 2.7 Typical noise spectrum of the bolometer output. The black vertical lines depict three distinguished frequencies. M: Modulation frequency used for molecular beam detection and tagging; R: strong mechanical resonance; T: UHV turbo pump rotation frequency.

a full range of (−5)–5 V. The digitized waveform was processed by built-in LabVIEW routines that use fast Fourier transformation to yield the power spectral density in dB/Hz. As expected for a very sensitive thermal detector, the bolometer picks up parasitic signals from a wide range of sources including turbo pumps, light sources, sample heaters, etc. It is therefore critical to choose a modulation frequency where unwanted signals are minimized. Among the low-noise regions found in the spectrum, we chose 142 Hz for modulating our experiment. It is marked in Figure 2.7 with "M". While the use of higher modulation frequencies is possible, they lead to a decrease in bolometer responsivity, as I will show in section 3.2

Nicely visible in Figure 2.7 is also the $1/f$ noise in the low-frequency part of the spectrum. The $1/f$ noise typically increases over the course of hours. This is most likely connected to uncorrelated phase transitions occurring in the adsorbate layer that forms on the bolometer. Furthermore, there are a number of sharp peaks, most of which are due to microphonic noise pickup. One particularly important example is the resonance "R" at 603 Hz. When this resonance is mechanically excited, the bolometer signal exhibits a strong response, which can even saturate the amplifier. While the excitation of this resonance is not particularly strong in Figure 2.7, we observed that it can be efficiently

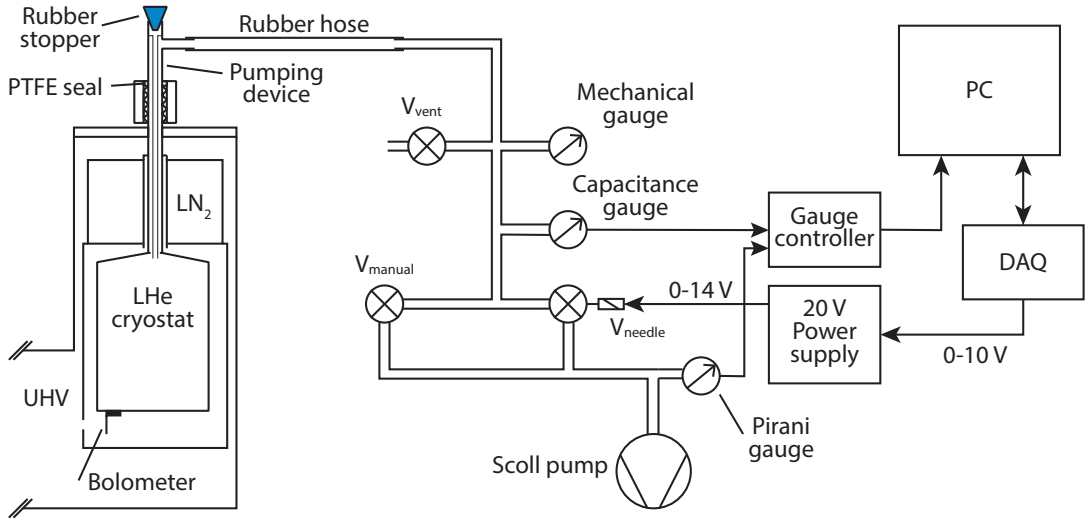

Figure 2.8 Schematic drawing of the pumping setup for evaporative cooling of the liquid helium cyrostat. V_{manual} and V_{needle} are manually and solenoid actuated valves, respectively. V_{needle} is remotely adjusted by a voltage-controlled power supply. V_{vent} is a manual valve that allows venting of the setup to atmospheric pressure. The pumping device features a thin tube that extends into the liquid helium dewar below the neck of the filling tube, thereby providing an escape path for overpressure release in case the neck clogs. A rubber stopper seals the tube from atmospheric pressure and pops off in case of overpressure.

excited by the rotation of the UHV turbo pump "T" under certain conditions that we were not able to define exactly. We suspect that the filling level of the liquid helium dewar plays a role in the coupling efficiency of the turbo rotation to the bolometer resonance. In some cases, it is possible to remedy the excessive noise by lowering the rotation speed of the pump, shifting the driving frequency away from resonance.

Operation of the bolometer at 1.6 K instead of 4.2 K increases the sensitivity substantially (typically by about three orders of magnitude). Furthermore, helium is in its superfluid phase (Helium II) at 1.6 K, which avoids additional microphonic noise coming from the boiling of helium. The final operating temperature is reached by successively lowering the pressure over the helium bath using a scroll pump (10 m^3/h) until a steady state is reached where the pumping speed equals the helium evaporation rate. A schematic view of the pumping setup is presented in Figure 2.8. The pressure over the helium bath is monitored with a capacitance gauge and registered by a computer. Using the definition[14] of the ITS-90 international temperature scale, we convert the helium partial pressure into absolute temperature (see also appendix B). A solenoid actuated needle valve limits the pumping rate during the first stage of the pump-down process to avoid

excessive helium boil-off while a second manual valve with larger conductance remains closed initially. The needle valve is driven by a voltage-controlled 20 V power supply, which in turn receives its control voltage from a digital-analog converter (DAC) of a data acquisition card (Model NI 6115 PCI, National Instruments). A custom LabVIEW^{TM} program automatically adjusts the valve's conductance *via* a PID control loop to keep a pump-down rate of 0.5 mbar/s until a pressure of ~ 300 mbar is reached. In the following, the manual valve is opened manually. The phase transition to superfluidity occurs[15] at a pressure of $p_\lambda = 50.6$ mbar and a temperature of $T_\lambda = 2.1768\,\mathrm{K}$. At that point the pressure above the helium bath stays constant for about one minute due to the liquid's infinite heat capacity. After the phase transition, we allow the bolometer to reach its final temperature. We verify that the operating point is reached by observing the signal generated by a chopped molecular beam scattering from the surface sample and ensuring that the signal intensity no longer changes with time.

2.4 Laser setup

2.4.1 Overview

The experiments presented in this thesis require generation of tunable light in the mid-IR spectral regime around 3.3 μm for the excitation of methane's C–H stretch vibration. We use two single–mode OPOs operating in continuous-wave mode delivering > 1 W of widely tunable light at this wavelength. One of the OPOs, hereafter called "Pump OPO", can be used to excite the incoming molecular beam while the second one, (the "Tagging OPO"), excites scattered methane into a selected rovibrationally excited state, which in combination with bolometric molecular beam detection enables state-selective detection of CH_4, as I will detail in chapter 3.

Since excited state lifetimes are on the order of milliseconds in the infrared, the natural linewidths of rovibrational transitions are usually negligible compared to the instrumental laser linewidth, which in the case of our OPOs is $1.0 \pm 0.5\,\mathrm{MHz}$. Even in well-collimated molecular beams, Doppler broadening is typically dominating but in our case does not exceed 10 MHz (FWHM). As I will show below, the transitions observed in both incoming and scattered molecular beam can be as narrow as 2.5 MHz. Therefore, active stabilization of the OPO wavelength within 1 MHz is necessary in order to keep it resonant with the molecular transition during the entire course of the experiment. The frequency stabilization mechanisms, which we have implemented and optimized over the years, are integral parts of the entire experimental setup. Their installation and operation presents a major effort in the realization of our scattering experiments.

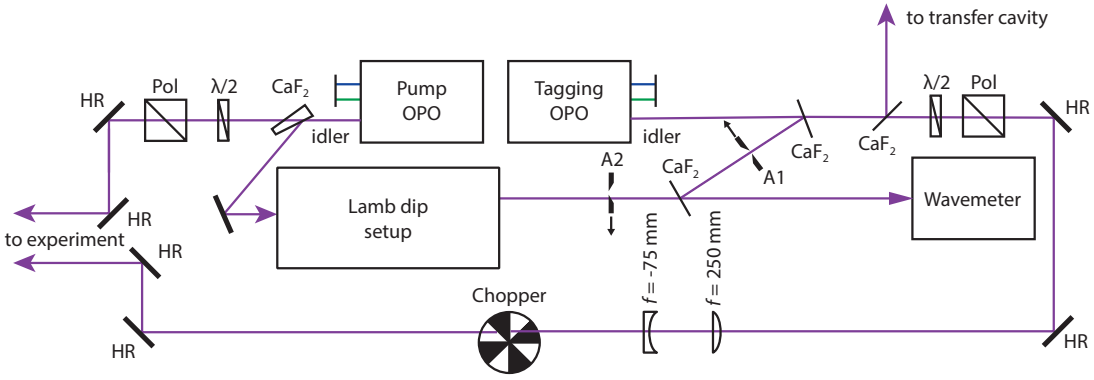

Figure 2.9 Overview of the optical layout. Elements labeled CaF_2 are calcium fluoride windows or wedges used to reflect small portions of the beam intensity.

Previously, Bruce Yoder has implemented a stabilization mechanism based on locking of the laser frequency to a Doppler-free saturation feature (Lamb dip) that is detect in a room-temperature static gas cell[10]. While this approach is very robust and provides absolute wavelength stabilization, it is only applicable to fundamental transitions, because only the vibrational ground state is sufficiently populated at ambient temperature. To overcome this limitation and be able to lock on hot-band transitions, which originate from vibrationally excited levels, we have built a second stabilization setup, a so-called transfer cavity, which I will describe in section 2.4.4. However, we still use the Lamb dip technique when we want to state-prepare the incident molecular beam *via* a fundamental transition due to its simplicity and ease of use.

An overview of the optical layout is presented in Figure 2.9. Here and in the following, highly reflective mirrors (HR) are typically gold mirrors on copper or silica substrate. Small portions of the idler output from both OPOs are split off from the main beams and sent to the frequency stabilization setups and to a wavelength-meter (Model 621 B, Bristol Instruments) used for monitoring the absolute frequency. Note that the accuracy of the wavemeter is on the order of 70 MHz and thus not a suitable reference for frequency stabilization. The wavemeter can only monitor the wavelength of one OPO at a time, so we manually switch between the two beams by blocking one of them using movable apertures. Depending on the alignment of the IR beam into the wavemeter, the measured wavelengths exhibit a systematic offset. Absolute wavelengths reported in this thesis are either quoted values from the HITRAN database[16] or the measured wavelength after it was corrected by subtracting the offset. I determined the latter by measuring the wavelength of some other transition (typically in the ν_3 fundamental band) and referencing to HITRAN. Both main idler beams pass a broadband half-waveplate

($\lambda/2$) and a polarizing beamsplitter (both ALPHALAS). The waveplates are mounted on computer-controlled rotational mounts (Model PRM1/MZ8, Thorlabs) allowing quasi-continuous attenuation of the beam intensities. The diverging idler beam of the Tagging OPO is reduced in diameter by a telescope before going the scattering experiment. The Tagging OPO beam can be modulated by a fast spinning chopper wheel (Model 3501, New Focus) with 50 % duty cycle. Further details of the optical layout for the individual experiments will be given where appropriate.

2.4.2 Light sources

Up to now, there are no lasers that can deliver continuous light with powers of 1 W or more in the 3.3 µm range directly, that is by lasing on a transition between two states with the corresponding energy gap. Thus, one makes use of parametric processes in optically non-linear materials, allowing the generation of new wavelengths by converting a part of the light from readily available lasers. An optical parametric oscillator is a light source which, like lasers, consists of an optical resonator, but by contrast achieves optical gain by parametric amplification instead of stimulated emission. Parametric amplification can be observed in optically nonlinear crystalline materials, which exhibit a nonvanishing second order susceptibility ($\chi^{(2)}$). This nonlinearity enables the interaction between three light waves, which can have three distinct frequencies, the so-called pump, signal and idler waves. The interaction converts photons of the incident pump wave of frequency ω_{pump} into two photons of lower frequency. The newly generated wave that is resonant in the OPO cavity is the signal wave with frequency ω_{signal} and the remaining idler wave has the frequency ω_{idler}. The amplification process obeys conservation of photon energy,

$$\omega_{\text{pump}} = \omega_{\text{signal}} + \omega_{\text{idler}} \,, \tag{2.6}$$

as well as conservation of momentum. Since different wavelengths generally have different propagation speeds inside the nonlinear medium, the newly generated partial waves run out of phase and cannot add up to a macroscopic wave. Efficient amplification is only achieved when the phase relation between the waves retains fixed along the entire interaction path inside the nonlinear medium. This phase-matching condition dictates which frequencies can be generated for a given pump frequency, light polarization, propagation direction, crystal orientation and temperature. The frequencies ω_{signal} and ω_{idler} depend parametrically on these factors, which enables the wide range tuning capabilities of OPOs. The interested reader is referred to a very recent perspective article[17] (and

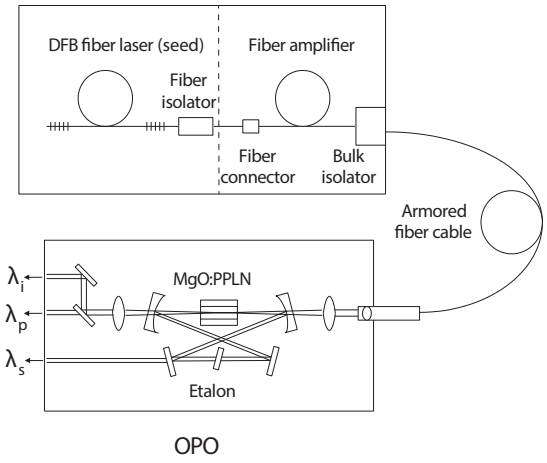

Figure 2.10 Schematic of the Argos 2400 SF tunable mid-IR light source. A DFB fiber laser seeds a high-power fiber amplifier providing the pump wavelength λ_p. Inside the OPO, signal (λ_s) and idler (λ_i) beams are generated and coupled out of the resonator. The Pump OPO has its seed laser and amplifier installed in separate units, indicated by the dashed line. Drawing provided by Lockheed Martin Aculight and modified.

references therein) that gives a good introduction to the general operating principle of mid-IR OPOs and reviews their application possibilities in molecular spectroscopy.

The IR light sources used in this work are two cw single–mode OPOs (Aculight, Argos 2400 SF, module C). Their idler outputs deliver tunable mid-IR light ranging from 3.2 to 3.9 μm with an instantaneous linewidth of less than 1 MHz. A schematic of the OPO system is shown in Figure 2.10. One major improvement over previously available OPOs lies in the use of a singly-resonant OPO cavity. That is, only the signal wave is resonant inside the OPO cavity, which significantly simplifies tuning since no wavelength-selecting elements for the idler wave are required. Instead, the idler frequency can be tuned by varying the pump wavelength, which is made possible by the use of state-of-the-art fiber lasers and amplifiers.

A detailed description of the operation principle, layout and tuning characteristics of these singly-resonant OPOs can be found in Refs. [18] and [19]. Briefly, each OPO is pumped by a fiber laser system consisting of a fiber amplifier (IPG Photonics) that is pumped by laser diodes and seeded by a distributed feedback (DFB) fiber laser with a linewidth of < 100 kHz. The pump wavelength is centered at 1064 nm and generated by emission in the Yb-doped fibers. The amplified light is transmitted to the OPO through a polarization preserving armored fiber cable and coupled into the OPO cavity. The nonlinear medium is a periodically-poled lithium niobate (PPLN) crystal. This material is fabricated with birefringent domains of alternating orientation. The periodicity of

Table 2.2 Relevant characteristics of the OPO mid-IR light sources used in this work.

	Tagging OPO	Pump OPO
Module designation	C	
Pump wavelength	1064 nm	
Beam quality	TEM_{00}	
Idler polarization	horizontal	
Maximum pump power	15 W	20 W
Typical pump power	9 W	20 W
Typical idler power	~0.8 W	~2.5 W
Piezo tuning voltage range	0–(+90) V	0–(+150) V
Seed laser tuning range	~50 GHz (1.7 cm^{-1})	~100 GHz (3.4 cm^{-1})

the domains is chosen such that quasi-phase matching (QPM) is achieved. Here, even though the phase-matching condition is not fulfilled exactly, the reversal of the nonlinear coefficient leads to a rephasing of the partial waves and highly efficient wavelength conversion without beam walk-off. Moreover, the crystal is engineered with a "fan-out" structure. That is, the domain periodicity varies across the crystal and allows achieving of QPM for a wide wavelength range with the same crystal. For tuning, the crystal only needs to be translated in the direction of changing periodicity. An intra-cavity etalon with a free spectral range of 400 GHz ($\approx 13\,cm^{-1}$) is installed to select a particular cavity mode ensuring single-mode operation. OPO cavity and crystal are heated and separately temperature-controlled. The three different colors are coupled out of the cavity and the pump and signal beams are immediately guided into beam dumps. Only the idler wave was used in the experiments presented in this thesis.

The two Argos systems in our laboratory have all of the aforementioned features in common, but differ in a few other aspects. The older system (Tagging OPO) has a fiber amplifier with a maximum output power of 15 W and the amplifier and seed laser are housed in the same unit. By contrast, the newer system (Pump OPO) operates with a pump power of 20 W and has a separate seed laser which also offers a wider tuning range. Table 2.2 gives an overview of the relevant characteristics of the two systems.

Wavelength tuning of the idler output of these OPOs is achieved by three mechanisms, which provide different levels tuning:

1. Translation of the nonlinear crystal perpendicular to the beam axis provides coarse tuning in steps of $\approx 12\,cm^{-1}$ corresponding to the free spectral range of the etalon.
2. Tuning with intermediate accuracy is achieved by tilting the intra-cavity etalon *via* a galvanometer. Tuning by this method occurs with mode-hops of $\approx 1\,cm^{-1}$. Tilt

of the etalon by ±1° covers its entire free spectral range.

3. Fine tuning of the idler frequency is provided by tuning of the pump frequency, which according to Equation 2.6 simultaneously changes the idler frequency. The pump frequency is altered by applying strain to the fiber resonator of the seed laser using a built-in piezo electric element (PZT). This tuning method is in principle mode-hop-free, unlike the former two methods. The seed laser of the Pump OPO has a long-stroke piezo installed, which offers ~ 100 GHz of tuning with a piezo voltage range of 0–150 V, while the one of the Tagging OPO has a piezo for 0–90 V, providing ~ 50 GHz of tuning.

Note that the idler wavelength may also be varied by crystal or seed laser temperature tuning, but we did not make use of these mechanisms in the present work.

Despite the robust layout and the temperature control of the OPOs, active drift compensation is required to keep the frequency resonant with the narrow absorption lines found in molecular beams. Active stabilization of the idler frequency in a singly-resonant OPO is achieved by changing the frequency of the pump beam *via* the seed laser frequency to exactly compensate the frequency drift of the idler output. We use two different methods for determining the frequency drift and the necessary compensation. I will discuss both of them in the following sections.

2.4.3 Lamb dip locking

Stabilization of a laser's frequency to an absorption peak detected in an ordinary gas cell is a tempting idea, in particular if the same transition can be used as the one that is to be excited in the molecular beam. However, absorption lines of molecules in a thermal, isotropic environment are affected by Doppler broadening. The full width at half maximum (FWHM) of a Doppler-broadened absorption profile is about 280 MHz for ν_3 fundamental transitions of CH_4. Stabilization to the maximum of a Doppler-broadened absorption line is not sufficiently accurate for IR pumping in a molecular beam, where one encounters linewidths of less than 10 MHz. Fortunately, a Doppler-free absorption feature can be generated in an otherwise Doppler broadened line shape by exploiting saturation effects. A Lamb dip is a saturation hole burnt into the center of a Doppler-broadened absorption line by pumping molecules to an excited state with an intense laser beam. The characteristic Lamb dip can be detected by retro-reflecting the beam in itself and measuring the transmitted light intensity as shown in Figure 2.11. Locking of the laser frequency to a Lamb dip provides a convenient and robust means of stabilizing the absolute laser frequency. A detailed description of the method is given in the thesis of Yoder[10], so I will only briefly outline its practical realization and application in the

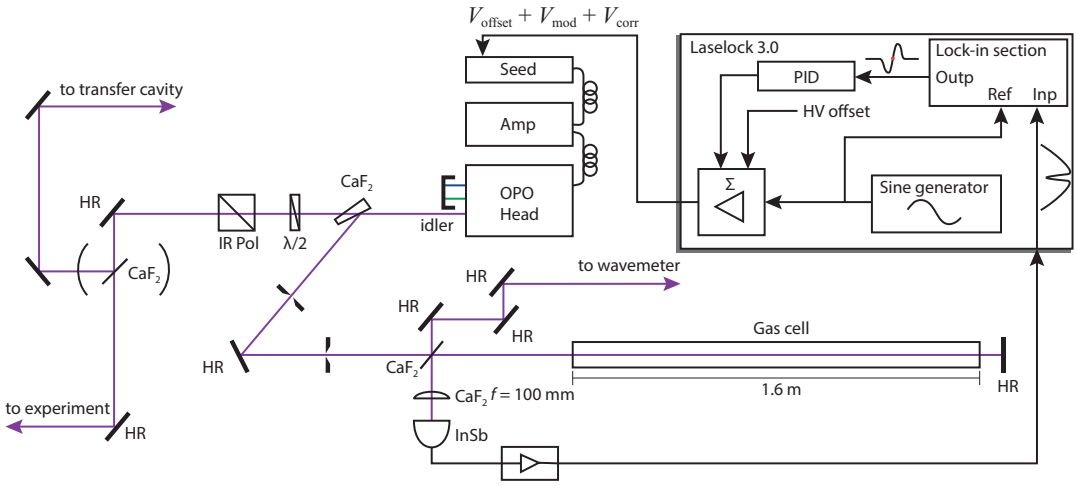

Figure 2.11 Optical layout for the stabilization of the Pump OPO to a Lamb dip of a fundamental transition detected in a static gas cell. Shown is also a simplified schematic of the electronic stabilization circuit. See text for details.

present case.

Figure 2.11 shows the optical layout for Lamb dip locking of the Pump OPO frequency. Reflection from a CaF_2 wedge splits off a small portion of the idler beam power, typically about 100 mW, which is sent to a CaF_2 window that acts as a beam splitter. The transmitted beam is retro-reflected by a highly reflective mirror after passing through a 1.6 m long gas cell with CaF_2 windows. The beam passes the cell twice and the CaF_2 window reflects a small portion of the retro-reflected beam which is then detected by a liquid nitrogen cooled InSb photodiode (Judson, J10D-M204-R01M-30). The absorption cell is filled with typically 20–50 µbar of the gas of interest. Higher pressures increase the absorption but decrease the relative amplitude of the Lamb dip because collisional deactivation of the rovibrationally excited state competes with the IR pumping rate. Figure 2.12 shows the Doppler-broadened absorption profile of the $R(0)$ transition of the anti-symmetric stretch (ν_3) fundamental of CH_4 located[16] at 3028.752 260 cm^{-1}. It was obtained by recording the photodiode signal while the laser frequency was scanned over the transition using a linear voltage ramp applied to the seed laser piezo. The laser beam had a power of 80 mW before entering the gas cell with a beam diameter of about 3 mm. A 16-bit (±10 V) analog-to-digital converter (ADC, National Instruments, Model USB-6002) digitized the photodiode signal with a sampling rate of 25 ksamples/s. The trace in Figure 2.12 contains 3786 samples. A nonlinear baseline was removed by subtracting a background recorded with no CH_4 gas present in the cell. The frequency axis was calibrated by matching the observed Doppler linewidth to the expected linewidth

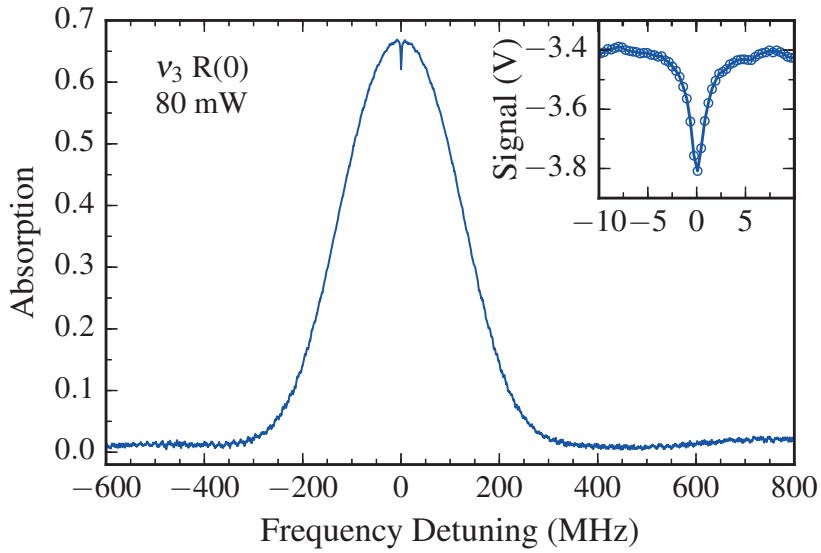

Figure 2.12 Doppler-broadened line profile of the R(0) transition of the antisymmetric stretch (ν_3) fundamental of CH_4. The Lamb dip is clearly visible in the line center. The profile was recorded in the 1.6 m long gas cell with 80 mW of IR power. The time axis was converted into frequency by matching the observed linewidth with the expected Doppler width at room temperature. A nonlinear baseline was removed by subtracting a background recorded with no CH_4 gas present in the cell. Inset: Magnification of the Lamb dip given as raw photodiode signal.

$\delta\nu_{\text{Doppler}}$ of 281 MHz, which can be calculated according to

$$\delta\nu_{\text{Doppler}} = \frac{2\nu_0}{c}\sqrt{\frac{2RT\ln 2}{M}}\,, \tag{2.7}$$

where ν_0 is the center frequency, R is the gas constant, $T = 300$ K is the gas temperature and $M = 16$ amu is the molecular mass of CH_4. The inset shows a magnification of the Lamb dip in terms of raw photodiode signal. A Lorentzian fit to the dip yields a homogeneuous linewidth of 2.0 MHz. We shall see below that the observed Doppler-broadened line shape is actually wider than the calculated 281 MHz.

To understand the occurrence of a Lamb dip, we consider a monochromatic laser beam that travels in the z direction through a thermal ensemble of molecules. Due to their Maxwell-Boltzmann velocity distribution $f(v_z)\,\mathrm{d}v_z$ along the laser propagation direction, the absorption profile of a particular transition is Doppler-broadened around the center frequency ω_0. Molecules that belong to a velocity class v_z can absorb the laser light only

when their Doppler shift $\Delta\omega$ which is given by

$$\Delta\omega = \frac{\omega_0}{c} v_z \,, \tag{2.8}$$

and where c is the speed of light, exactly compensates the detuning of the laser from the center frequency. If the laser is detuned from ω_0 by $\Delta\omega_\mathrm{L}$, molecules of the velocity class $v_z = +c \cdot \Delta\omega_\mathrm{L}/\omega_0$ will contribute to the absorption during the first pass, while during the second pass those belonging to the velocity class $v_z = -c \cdot \Delta\omega_\mathrm{L}/\omega_0$ will contribute, due to the reversal of the light propagation direction. The situation is different when the laser is tuned exactly to ω_0, because molecules of the same velocity class ($v_z = 0$) can absorb the light during both passes. If the laser is intense enough to excite a significant fraction of molecules, the IR absorption will be partially bleached due to the depopulation of the lower level. For molecules with $v_z = 0$, this effect is enhanced because they are exposed to a twice higher light intensity since they interact with both the incoming and the reflected beam. The drop in absorption intensity around the line center is caused by this enhanced saturation. See Refs. [11] and [20] for a quantitative description of the Lamb dip generation.

Active frequency stabilization is accomplished by a commercial stabilization electronics unit (Laselock 3.0, TEM Messtechnik GmbH). A simplified schematic diagram of the circuitry is shown in Figure 2.11. First, the laser is tuned to the center frequency of a transition, overlapping with the Lamp dip, by manually adjusting the high voltage (HV) offset V_offset of the Laselock, which is applied to the tuning piezo of the seed laser. Then, a small sine-wave modulation voltage $V_\mathrm{mod}(\sin\omega_\mathrm{mod}t)$ is added to the offset voltage, generating a small frequency dither (< 2 MHz at a rate of 8.5 kHz) around the center frequency. The resulting signal is detected by the photodiode and processed by the Laselock after pre-amplification. Here, a lock-in amplifier detects the AC component of the photodiode signal at the modulation frequency, thus producing the first derivative of the Lamb dip signal waveform. It is used as error signal for the stabilization because any frequency excursion of the carrier wave from the center frequency to either side yields a non-zero derivative value with opposite signs. A PID regulation circuit processes the error signal and generates a correction voltage V_corr, which is added to the HV offset to drive the frequency back to the center where the derivative signal is zero. The so-achieved frequency "lock" stabilizes the idler frequency to within less than 1.2 MHz for many hours as shown by Yoder[10].

2.4.4 Transfer cavity stabilization

While Lamb dip locking provides robust absolute wavelength stabilization over the course of hours and can be realized with a relatively simple experimental setup, it comes with some limitations. For instance, large transition dipole moments or high laser intensities are required to burn a sufficient saturation hole into the lower level population. An even more critical factor is given by the fact that the lower levels must be populated in a gas cell at room temperature. This limits the applicability of the Lamb dip technique to fundamental transitions. In our scattering experiments, however, we also wish to address higher vibrational states. Even if we were to heat the gas cell, it would be quite difficult to sufficiently populate excited vibrational states because of the high frequency vibrations of CH_4. Moreover, Lamb dip locking does not provide the possibility of controlled wavelength tuning. The ability of performing such scans can give information about the transitions' Doppler linewidths, which in turn can be used to determine the speed distributions of molecules in a molecular beam[7,21].

A transfer cavity provides an alternative means of stabilizing a lasers's frequency. It utilizes a Fabry-Pérot cavity to transfer the wavelength stability of an intrinsically stable reference laser to the target laser. Figure 2.13 shows a schematic of the transfer cavity used in this work and illustrates its working principle. A small portion of the OPO idler beam is aligned through a scanning Fabry-Pérot interferometer (FPI) along with a commercially available temperature-stabilized helium-neon (HeNe) laser. The cavity length is scanned by applying a linear voltage ramp to a piezo electric actuator (PZT) that suspends one of the cavity end mirrors. The two laser beams are transmitted by the cavity whenever the conditions for constructive interference are satisfied. For a confocal FPI with off-axis excitation, this condition reads[11]

$$4n(\lambda)L = m\lambda\,, \tag{2.9}$$

where λ is the wavelength, $n(\lambda)$ is the refractive index of the intra-cavity medium, L is the cavity length, and m an integer taking the values $m = 0, 1, 2, \ldots$. The two wavelengths are separated after the cavity by a germanium window, detected by photodiodes and the signal registered by a computer. Scanning of the cavity length gives rise to a set of periodic transmission fringes for each laser as shown in the top right graph. Each fringe corresponds to a cavity mode numbered m and k for IR and HeNe, respectively,

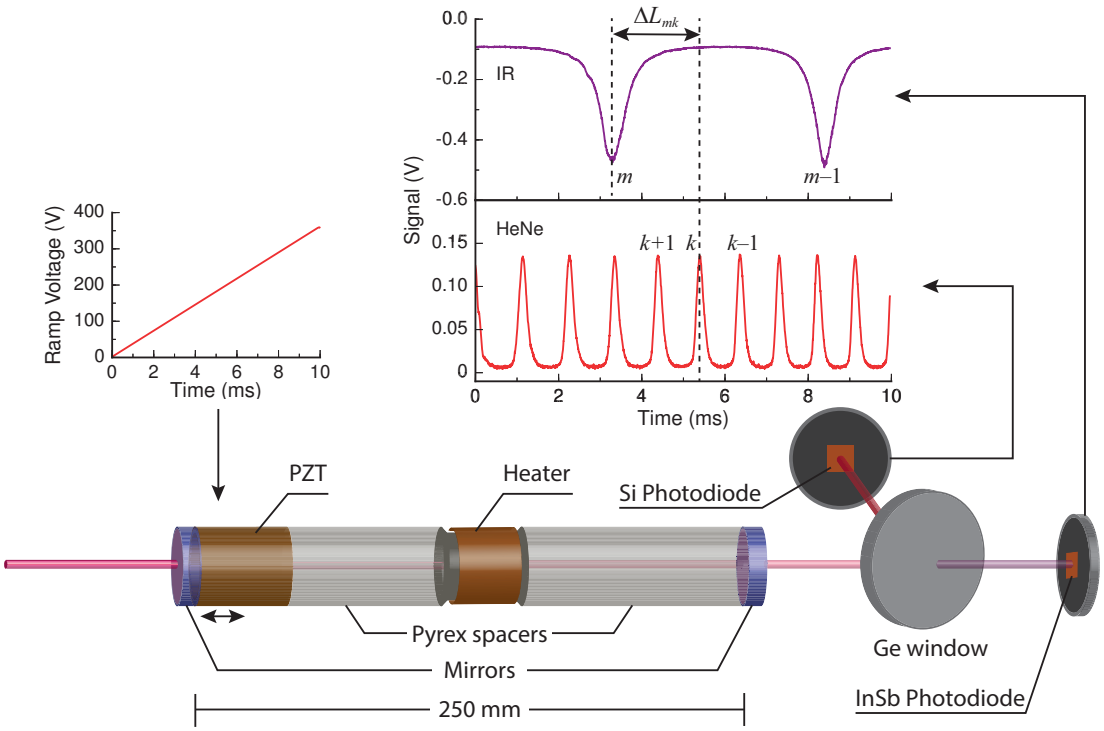

Figure 2.13 Schematic drawing of the transfer cavity illustrating its working principle. The IR target laser is aligned through a 250 mms long confocal Fabry-Pérot cavity along with the 632.8 nm output from a stable HeNe reference laser. The cavity length is scanned by periodically applying a voltage ramp to a piezo eletric actuator (PZT) on which one of the cavity end mirrors is mounted. The beams are separated after the cavity by a germanium window and detected by photodetectors. A shift in the relative position of an IR transmission fringe with respect to a chosen HeNe fringe indicates a drift in IR frequency.

satisfying the relations

$$4n(\lambda_{\mathrm{IR}})l_m = m\lambda_{\mathrm{IR}} \tag{2.10}$$

$$4n(\lambda_{\mathrm{HeNe}})l_k = k\lambda_{\mathrm{HeNe}}\ . \tag{2.11}$$

Here, l_m and l_k are the cavity lengths at which cavity mode m and k are excited by the IR and HeNe, respectively. It is now obvious that the IR wavelength is stabilized when one controls λ_{IR} in such a way that its transmission fringe m maintains the same relative distance $\Delta L_{mk} = l_m - l_k$ to a chosen HeNe fringe k. In other words, the HeNe laser acts as a ruler measuring the cavity length and the IR laser is in turn referenced to the cavity length.

While the IR laser could also be stabilized to an intrinsically stable FPI without

an additional reference laser, the transfer cavity approach has several advantages. The optical path length $n(\lambda)l$ in a reference FPI has to be extremely stable to reach MHz precision, which requires the use of ultra-low expansion materials and typically the FPI has to be placed inside a vacuum container and carefully temperature-regulated. In a transfer cavity, the absolute stability comes from the HeNe laser rather than the cavity itself, which greatly relaxes the requirements on its design. Such a cavity can operate in air and, in principle, without temperature stabilization, although the latter proves useful in practice. The reference laser that is required for the transfer cavity is furthermore commercially available for a price of not more than 3000 CHF.

Other authors have reported alternative stabilization techniques for the same type of mid-IR light sources. Pan *et al.* used[22] locking to a commercially available reference FPI for stabilizing their Argos OPO system. However, their solution requires frequency doubling of the OPO idler output and subsequent shifting which is achieved using two electro-optic modulators. These additional steps make their method complicated and expensive compared to the transfer cavity approach. Moreover, the locking procedure in their case is rather involved and frequency scanning possibilities are limited. Finally, we note that optical frequency combs have been used[23,24] for referencing. Despite their extreme spectral resolution, the current high cost (> 250 kCHF) of these devices presents a major hurdle for most laboratories. The two orders of magnitude lower cost of our transfer cavity setup can be seen as one of its main advantages.

Several different implementations of the transfer cavity have been reported over the years[25–31]. In the most straightforward version, as demonstrated[25] in the original work of Nesbitt and co-workers, the cavity length is locked to a transmission maximum of the reference laser and the target laser is then locked to a transmission maximum in the stabilized cavity. A severe limitation of this method is that the target laser can only be stabilized to frequencies where it is resonant with the cavity, that is, in frequency intervals given by the free spectral range (FSR) of the interferometer. Our setup employs the same cavity layout as the one reported by Nesbitt and co-workers, but digital signal processing is used to achieve stabilization and scanning with quasi-continuous frequency coverage, similar to the version described[31] by Kwolek *et al.* In his thesis work, van Reijzen implemented[8] a first version of the current transfer cavity setup. I have subsequently improved it by programming a new stabilization algorithm and implementing continuous frequency scanning, which I will describe further below.

2.4.4.1 Optical layout and data acquisition

The FPI was built by Dr. Bradford Perkins during a three months visit at EPFL and consists of two pyrex tubes, which are separated by a metal spacer tube, as shown in Figure 2.13. A likewise tube-shaped piezo electric actuator (PZT) is bonded to one of the pyrex tubes holding one of the cavity end mirrors. The second mirror is mounted directly to the other pyrex tube. The piezo contracts by about 3.7 nm per Volt applied. Both mirrors are custom-coated (BMV Optical Technologies) and highly reflective ($R > 0.95$) for the HeNe (632.8 nm) and IR wavelengths. They are spherical mirrors with radius $R = 250\,\text{mm}$ and placed at a distance $L = R$, which means that their focal points $f = R/2$ coincide in the center of the confocal cavity. The corresponding free spectral range, *i.e.* the frequency separation of two adjacent cavity modes, is given by

$$\text{FSR} = \frac{c}{4L} = 299.8\ \text{MHz}\ . \tag{2.12}$$

The ratio of the FSR over the (FWHM) bandwidth of the cavity resonances depends on the miror reflectivity and is called finesse of the cavity and is about 10.5 for the HeNe wavelength and about 4.6 for the IR. Note that the finesse varies across the full OPO tuning range as the reflectivity of the mirrors is not constant throughout. The metal spacer in the cavity center is wrapped with a heater foil (Minco) and its temperature measured by a *K*-type thermocouple that processed by a LabVIEW$^{\text{TM}}$ program *via* a thermocouple (USB-TC01, National Instruments) readout. The program includes PID-loop control of the temperature which is typically held at 30.0 °C. Because the cavity temperature is measured directly at the metal spacer, the actual temperature of the entire cavity is only slightly above room temperature. The slightly elevated temperature is nonetheless sufficient to stabilize the cavity length against the daily changes in the laboratory temperature, which can be as high as 2 °C in our laboratory (CH G0 528). Moreover, the cavity is housed in a box made from PMMA as indicated by the rectangle in Figure 2.14 to further reduce environmental influences. I will address the residual effects of ambient condition changes on the cavity performance at the end of this chapter.

Figure 2.14 shows the optical layout of the transfer cavity setup. The reference laser is a polarization-stabilized HeNe laser (Melles Griot, 05-STP-911) operating at 632.8 nm with a quoted stability of ±1 MHz over a period of 8 hours. Its horizontally polarized output passes a Faraday isolator (Thorlabs, IO-2D-633-VLP), which also rotates the polarization by 45°. A polarizing beam splitter cube reflects about half of the intensity, which is sent to a second transfer cavity, which I have built for use with a different OPO module and which is not presented here because it was used for experiments not

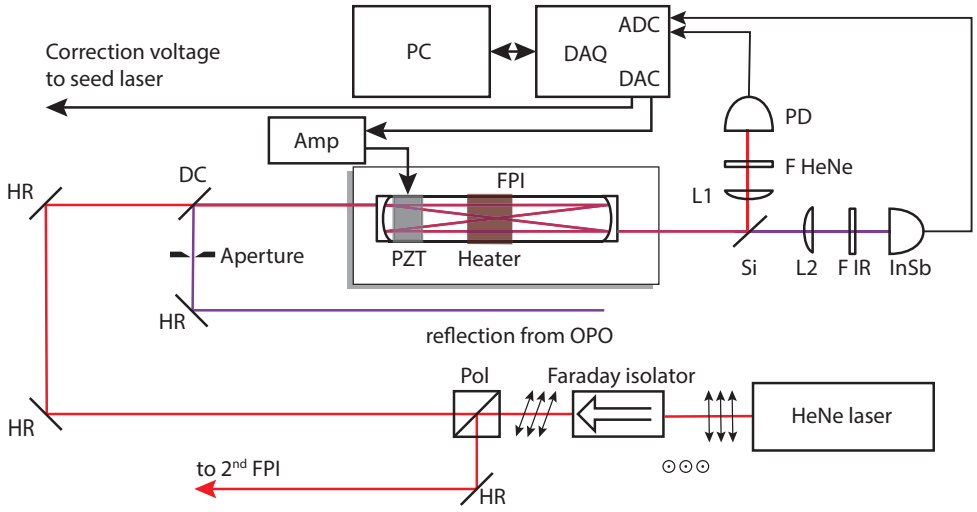

Figure 2.14 Optical layout of the transfer cavity setup and simplified illustration of the circuitry not showing the cavity temperature stabilization.

described in this thesis. The transmitted intensity is directed to the cavity used in this work and overlapped with a reflected beam from the OPO (< 10 mW) by a dichroic mirror. The beams are aligned through the FPI in an off-axis (bow-tie) configuration. A germanium (Ge) windows separates the beams after the cavity. IR and HeNe beams are then focused by a $f = 100$ mm focal length CaF_2 and glass lens, respectively. The HeNe beam is detected by a silicon photodiode (Thorlabs, PDA 55) and the IR beam by a DC-coupled liquid nitrogen cooled InSb photodiode (Judson, J10D-M204-R01M-30). A HeNe laser line filter and an IR transmissive filter are placed in the front of the corresponding photodetectors.

A simplified view of the data acquisition and circuitry is shown in Figure 2.14. A data acquisition card (DAQ, USB-6211, National Instruments) is used to acquire the signals from the two photodetectors, generate a triangle waveform that drives the cavity piezo, and likewise generate the correction voltage that is sent to the OPO's seed laser. The piezo driving voltage is a $0-6$ V V peak-to-peak triangle wave, which is generated by a 16-bit DAC and subsequently amplified by a factor of 60 using a high-voltage amplifier (Piezomaster, VP7210-600). The resulting $0-360$ V ramp scans the cavity length by about 1.4 µm (see also Figure 2.15). Each photodiode signal is digitized with 16-bit resolution at a sampling rate of 6 kilosamples per second (at 50 Hz repetition rate). Since the ADC inputs are multiplexed, the sampling rate has to be reduced for higher repetition rates. Generation of the triangle wave and acquisition of the detector signals are hardware-synchronized. From the full waveforms, only the part corresponding to the

rising slope of the piezo voltage is further processed by a custom LabVIEW program, which analyzes the fringe positions of HeNe and IR and derives an error signal that is applied to the OPO's seed laser to keep the relative fringe positions and thus the IR frequency constant. The error signal is translated into a voltage by the DAC of the DAQ-card and sent to a home-built summing amplifier, which adds the correction voltage to an HV offset for manual frequency tuning and, optionally, to a modulation voltage. The 0–75 V offset is generated by a piezo driver (Model MDT694A, Thorlabs) with 16-bit resolution and can be adjusted *via* a precision 10-turn potentiometer. The summed voltage is then applied to the seed laser piezo.

2.4.4.2 Frequency calibration

We wish to use the cavity not only for stabilization but also for precise scanning of the OPO idler frequency, *i.e.* as a relative frequency standard. Once locked, the frequency of the target laser can be systematically varied by changing the set-point of ΔL_{mk}. We now have to convert the change in ΔL_{mk} into a frequency detuning $\Delta\nu$ in MHz. Using Equation 2.9 we find for the frequency change of the cavity resonance with varying cavity length,

$$\frac{\mathrm{d}\nu}{\mathrm{d}L} = \frac{\mathrm{d}\lambda}{\mathrm{d}L}\frac{\mathrm{d}\nu}{\mathrm{d}\lambda} = -\frac{c}{L\lambda} \,. \tag{2.13}$$

For small frequency changes $\Delta\nu$, we can integrate Equation 2.13, which yields

$$\Delta\nu = -\frac{c}{L\lambda}\Delta(\Delta L_{mk}) \,, \tag{2.14}$$

where the negative sign indicates that an increase in IR-to-HeNe-peak distance ΔL_{mk} corresponds to a decrease in frequency. To obtain a frequency scale, we have to determine the piezo response, that is, the expansion (in this case contraction) as a function of applied voltage. This calibration is done in the following way: The HeNe signal is recorded and stored while the cavity is periodically scanned at the desired repetition rate (here 50 Hz). The HeNe fringe positions are converted to the corresponding cavity length change and plotted against piezo voltage. From Equation 2.12 we know that the cavity length difference between two adjacent fringes is $L_k - L_{k+1} = \lambda_{\mathrm{HeNe}}/4$. The obtained calibration curve is shown in Figure 2.15. A second order polynomial function is sufficient to describe the contraction as a function of piezo voltage V,

$$f_{\mathrm{calib}}(V) = \sum_{i=0}^{2} a_i V^i \,. \tag{2.15}$$

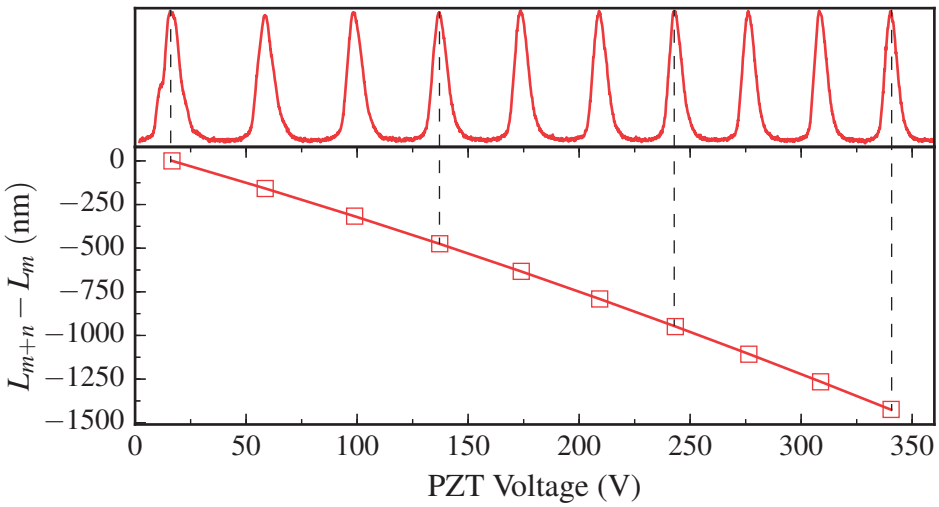

Figure 2.15 Calibration of the transfer cavity at a repetition rate of 50 Hz.

By combining the calibration function and Equation 2.13, we find

$$\mathrm{d}\nu = -\frac{c}{L\lambda}\left(\frac{\mathrm{d}L}{\mathrm{d}V}\right)\mathrm{d}V = -\frac{c}{L\lambda}f'_{\mathrm{calib}}(V)\mathrm{d}V\ . \tag{2.16}$$

Since the changes in wavelength and cavity length are very small compared to their absolute values, we can move these factors in front of the integral. Integration then yields the conversion formula

$$\Delta\nu = -\frac{c}{L\lambda}\int_{V_0}^{V} f'_{\mathrm{calib}}(V)\mathrm{d}V \tag{2.17}$$

$$= -\frac{c}{L\lambda}\left[F_{\mathrm{calib}}(V) - F_{\mathrm{calib}}(V_0)\right]\ , \tag{2.18}$$

where V_0 is the initial fringe position at the moment the laser was locked and $F_{\mathrm{calib}}(V)$ is the anti-derivative of $f'_{\mathrm{calib}}(V)$,

$$F_{\mathrm{calib}}(V) = \sum_{i=1}^{2} a_i V^i\ . \tag{2.19}$$

Considering that $F_{\mathrm{calib}}(V) < 1$, because the piezo contracts, we find that an increase in IR frequency shifts the IR peak to the right (towards higher driving voltage). In practice, we first convert the piezo voltage scale to cavity length change using $\Delta L(V) = F_{\mathrm{calib}}(V) - F_{\mathrm{calib}}(0)$. Then, Equation 2.13 is used to convert a change in IR-HeNe peak distance into a frequency detuning.

2.4.4.3 Digital data processing and interfacing

Processing of the photodiode signals is done using a custom LabVIEW^{TM} program running on a desktop PC, which interfaces the DAQ-card. The data analysis algorithm is a completely new implementation compared to the one described in the thesis of van Reijzen[8]. It now allows for continuous IR frequency scanning rather than just stabilization. During the first iteration, the program performs a peak picking routine for both IR and HeNe waveforms in order to find the fringe positions. It then fits a Gaussian to one HeNe peak (preferably located in the center of the cavity piezo range) during every iteration, thereby increasing the accuracy. The same is done for the IR waveform but here either one or two fringes are fitted with Gaussians depending on how many IR fringes appear within the piezo scan range. I found that with the present computer hardware, on-the-fly fitting and stabilization is possible for repetition rates up to at least 150 Hz. Once the IR and HeNe peak positions are known, the stabilization loop may be activated. Upon activation, the initial relative position of IR and HeNe ($\Delta L_{mk}(0)$) is stored and taken as the set-point for stabilization. During each subsequent program iteration, the positions of IR and HeNe are determined and sent to a PID-loop that generates an error signal when the relative IR fringe position changes.

Figure 2.16 presents a view of the program's graphical user interface (GUI). The HeNe and IR waveforms can be seen in blue in panels (a) and (b), respectively, along with the Gaussian fits in red. We can see that two IR fringes were captured within the cavity piezo scan range at that time. The program fits both of these peaks with Gaussians but uses only one of them (here fringe number 1) to determine the frequency drift. The IR frequency is controlled by changing the set-point ΔL_{mk}, which will move the IR fringes to the left or the right. It is clear that this detuning is limited by the available piezo range. To overcome this and enable continuous scanning, I implemented an algorithm, which can switch stabilization from one IR fringe to an adjacent one. Consider what happens to fringe number (1) in Figure 2.16 when the set-point is made more negative. The fringe will move towards the lower end of the piezo range and eventually disappear. Before this happens, the algorithm will switch the PID control to fringe (2), whose relative position with respect to the HeNe will then be the new setpoint. When the setpoint is further lowered, which moves fringe (2) further to the left, a new fringe will appear from the right hand side and take over as reference once fringe (2) is about to disappear, and so on. In this way, continuous scanning is possible. A more detailed description of the software implementation for the use with LabVIEW^{TM} can be found in appendix C.

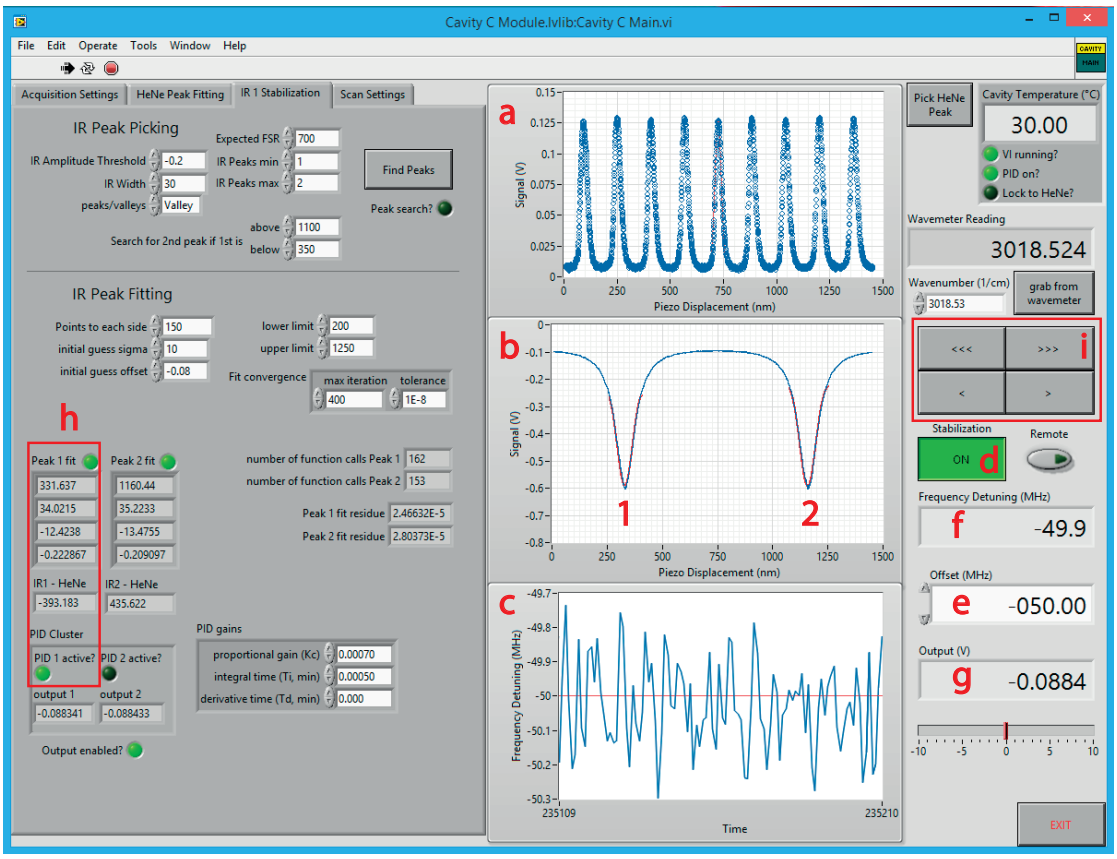

Figure 2.16 Screenshot of the graphical user interface for controlling the transfer cavity. The following essential elements are highlighted: (a) and (b) HeNe and IR transmission patterns, respectively. The red curves are Gaussian fits used to determine the peak centers; (c) measured frequency detuning (blue) of the IR with respect to the initial lock point. The red line shows the current frequency offset from the initial set-point defined in input (e); (d) toggle button to switch on/off frequency locking; (g) correction voltage output; (h): fitting parameters for IR peak (1) and offset with respect to the fitted HeNe peak. Currently, the IR is stabilized using peak (1). Should peak (1) drift out of the acquisition window to the left, the PID will switch to peak (2) for continued stabilization; (i): buttons to activate frequency scanning (forwards, backward at two different scan rates).

2.4.4.4 Performance

I will now demonstrate the performance of the transfer cavity, starting with its scanning capability. All data shown in this section have been obtained with the Pump OPO, which was either locked to the cavity or the Lamb dip for the purpose of comparison. First, we have to ensure that the frequency calibration presented in section 2.4.4.2 is correct. This can be done by scanning the laser frequency over an absorption profile of known width, for instance a Doppler-broadened line measured in a gas cell of known

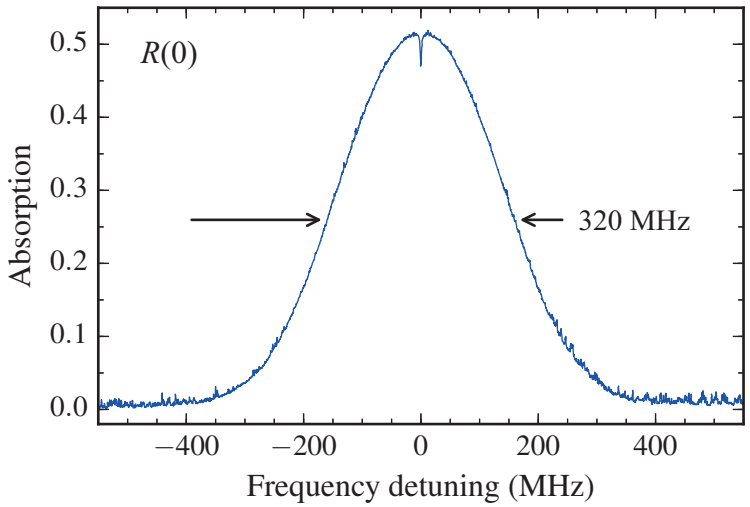

Figure 2.17 . Spectral scan of the ν_3 $R(0)$ transition detected in a 1.6 m-long static gas cell under Lamb dip (retro-reflecting) conditions using transfer cavity scanning. The pressure of CH_4 was about 30 µbar and the laser power ~ 80 mW. The scan rate was 0.5 MHz.

temperature. We can then compare the expected linewidth to the one obtained using the cavity frequency scale. Figure 2.17 shows a spectral scan over methane's ν_3 $R(0)$ transition at 3028.752 260 cm^{-1} obtained by monitoring the photodiode signal from the Lamb dip cell (see Figure 2.11). The latter was filled with about 30 µbar of CH_4 gas and the laser beam had a power of ~ 80 mW before entering the Lamb dip cell. The scan was carried out with a scan rate of 0.5 MHz/s. The photodiode signal was corrected for systematic laser power variations and slightly smoothed by convolution with a 1 MHz wide boxcar window. The measured width of the transition is 320 MHz (FWHM). This has to be compared to the expected value of 281 MHz for the purely Doppler-broadened absorption profile, obtained by evaluating Equation 2.7. I found the linewidth to depend on the methane pressure in the gas cell, as shown in Figure 2.18. This behavior seems surprising at first since the self-broadening coefficient of this transition is only γ_{self} = 4.9 kHz/µbar (FWHM)[16]. Pressure-broadening should therefore contribute less than 200 kHz to the line width. The observed pressure dependence most likely comes from a saturation effect due to the extreme spectral brightness of the OPO. As the laser beam travels through the 3.2 m of CH_4 atmosphere its intensity drops significantly due to absorption. With the laser intensity that enters the gas cell, the molecular transition is easily saturated, meaning that the probability of exciting a molecule is maximized (equal to 0.5). Further along the absorption path, the laser intensity and also the saturation

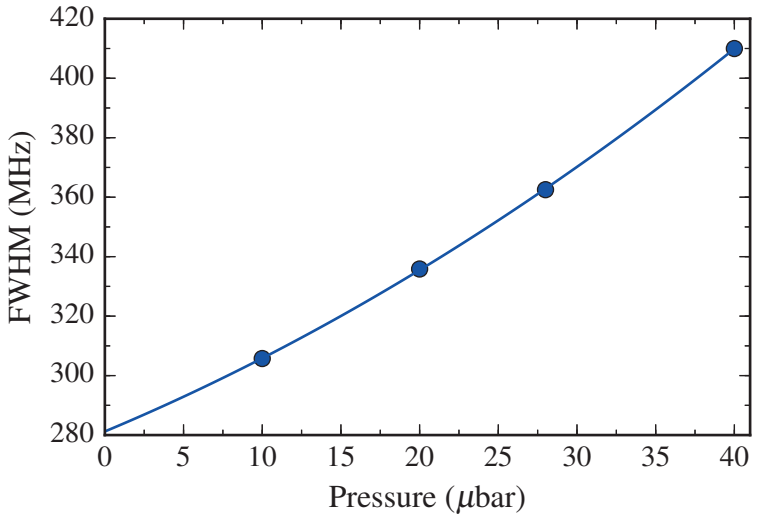

Figure 2.18 . Measured line width (FWHM) of the Doppler-broadened ν_3 $R(0)$ transition as a function of CH_4 pressure. The absorption profiles were measured with reduced laser power (< 1 mW). The solid line is a fit to the data points using a second order polynomial function. The intercept with the vertical axis is at 281 MHz, agreement with the expected Doppler width of the transition.

parameter $S(\omega)$, which describes the degree of saturation[11], drop significantly. It is important to realize that $S(\omega)$, when integrated along the absorption path, depends on the number of molecules that can absorb at the frequency ω. The more molecules that contribute to absorption, the more rapidly the light intensity will drop and the integrated saturation coefficient will decrease. This leads to stronger saturation in the wings of the Gaussian absorption profile, where less molecules are in resonance with the laser compared to the line center. For this reason, the absorption profile is significantly broader than what can be expected when the laser intensity is so high that it can be considered constant throughout the absorbing medium[11]. In the latter case, saturation only contributes to the broadening of the *homogeneuous* line width as molecules of all velocity classes (except those with $v_z \approx 0$) experience the same degree of saturation. It is now also clear, that the pressure in the cell must have an effect on the saturated line width. While the exact functional dependence of linewidth on pressure is not immediately clear, the aforementioned broadening effect on the heterogeneous linewidth must become more pronounced with increasing pressure. To remove the pressure dependent contribution to the linewidth, I fitted a second order polynomial function to the data points in Figure 2.18. While the exact functional dependence was not quite clear, the chosen function with three adjustable parameters was the lowest order polynomial that gave an acceptable fit. The

intercept with the vertical axis gives a linewidth of 281 MHz, in perfect agreement with the expected value for pure Doppler broadening. The remaining broadening mechanisms are transit-time broadening and power broadening, which are expected[10] to be on the order of 200 kHz and $\leq$ 1 MHz, respectively. We can therefore conclude that the frequency calibration of the cavity is accurate to within less than 5%.

In the following, I will show that the transfer cavity is able to stabilize the OPO frequency with a reliability that is at least as good as that of the Lamb dip technique. Yoder has shown[10] in his thesis that the Lamb dip can stabilize the idler frequency to within 1.2 MHz. One way of assessing the frequency stability is to monitor the amount of transferred population when the OPO excites a molecular beam. Here, the chopped OPO was set up to excite CH_4 molecules in the $v = 0,\ J = 0$ state after they scattered off the Ni(111) surface and before they were detected by the cryogenic bolometer, (see chapter 3). Figure 2.19 displays the lock-in-detected bolometer signal due to the vibrationally excited molecules impinging on the bolometer after the OPO has excited the ν_3 $R(0)$ transition. The signal is a direct measure of the transferred population. During the first 12 minutes, the OPO was locked to the Lamb dip. Afterwards, the lock was switched off, which caused the frequency to drift off-resonance and the signal dropped to the baseline value, which is due to scattered light and not related to laser excitation. After 16 minutes, the laser was locked to the cavity. We can see that the amount of added rovibrational energy reaches at least the same value as with the Lamb dip technique. What would happen if the laser was not stable but instead suffered excursions from the center frequency? We shall distinguish these frequency excursions by the time scale on which they occur. In case of those that occur on a time scale longer than the time resolution of the experiment, we will speak of frequency drift. Short-term fluctuations, on the other hand, occur on time scales shorter or comparable to the experimental time resolution. The signal shown in Figure 2.19 has been recorded with a lock-in time constant of 300 ms, which is the limiting time constant in this experiment. The linewidth of the transition in the molecular beam under the given conditions (with excitation by rapid adiabatic passage) is about 7 MHz (FWHM). If there was frequency drift by more than $\sim$ 2 MHz, the amount of transferred population would be expected to decrease, leading to a drop in the signal amplitude over time. This is not observed, which means that the cavity successfully prevents frequency drift. If frequency excursions of more than $\sim$ 2 MHz would occur on a timescale shorter than 300 ms, we would measure a stable signal, due to experimental averaging. However, its amplitude would be lower compared to when the Lamb dip method was used. The result indicates that the short-term frequency stability with cavity locking is at least as good as with the Lamb dip

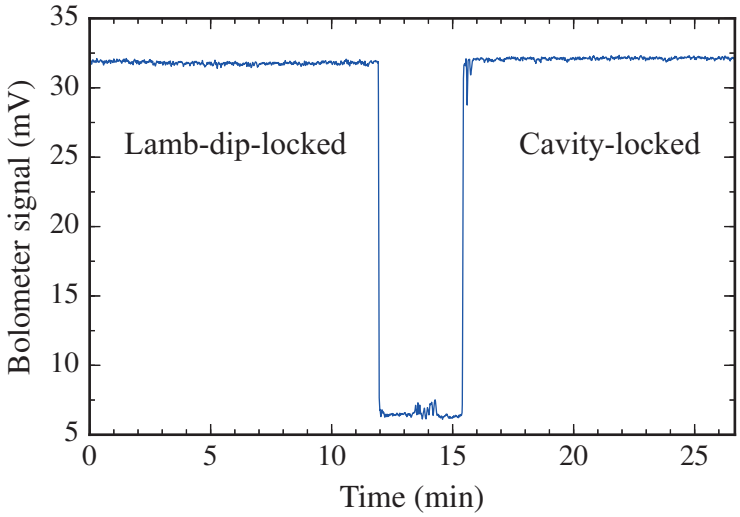

Figure 2.19 Comparison of the frequency stability of the OPO idler using the Lamb dip technique and the transfer cavity. The bolometer signal is generated by scattering a CH_4 molecular beam off Ni(111) and tagging scattered molecules in $v = 0$, $J = 0$ *via* the ν_3 $R(0)$ transition. The signal is a measure of the number of molecules excited by the OPO. See text for details.

method, *i.e.* better than 1.2 MHz.

Note that the long term frequency stability is ultimately limited by the environmental influences on the optical dispersion inside the cavity, that is, changes in the refractive indexes of air, $n(\lambda_{\mathrm{HeNe}})$ and $n(\lambda_{\mathrm{IR}})$. Since the wavelengths of the two lasers are vastly different, the change in the refractive indexes for the two wavelengths with temperature, pressure and air composition is generally different. A variation in any of these parameters hence results in different changes of the optical path lengths in the cavity. Since the IR laser stabilization aims to keep the relative path difference constant, this leads to a detuning effect. We can estimate the environmental influences on the frequency stability by letting

$$\frac{\Delta(\Delta L_{mk})}{\Delta\alpha} = \frac{\partial l_m}{\partial\alpha} - \frac{\partial l_k}{\partial\alpha}\,, \tag{2.20}$$

where $\Delta(\Delta L_{mk})$ is the change in relative fringe position induced by a change in an environmental parameter α. Using the chain rule of differentiation, we find

$$\frac{\Delta(\Delta L_{mk})}{\Delta\alpha} = \frac{\partial n(\lambda_{\mathrm{HeNe}})}{\partial\alpha}\frac{l_k}{n(\lambda_{\mathrm{HeNe}})} - \frac{\partial n(\lambda_{\mathrm{IR}})}{\partial\alpha}\frac{l_m}{n(\lambda_{\mathrm{IR}})} \tag{2.21}$$

$$\approx L\left[\frac{\partial n(\lambda_{\mathrm{HeNe}})}{\partial\alpha}\frac{1}{n(\lambda_{\mathrm{HeNe}})} - \frac{\partial n(\lambda_{\mathrm{IR}})}{\partial\alpha}\frac{1}{n(\lambda_{\mathrm{IR}})}\right], \tag{2.22}$$

Table 2.3 Sensitivity of the IR frequency drift to changes in environmental conditions α when the IR is locked to the transfer cavity. Equation 2.23 was evaluated using the Ciddor equation[32] with $\lambda_{IR} = 3.31$ µm, $p = 101\,325$ Pa, $T = 300$ K, RH = 0.4, and $x(CO_2) = 450$ ppm.

Parameter α	$\Delta\nu/\Delta\alpha$
Pressure	−323 kHz/hPa
Temperature	1.02 MHz/K
rel. Humidity	−35 kHz/%
CO_2 concentration	172 Hz/ppm

since $l_k \approx l_m \approx L$. Using Equation 2.14, we arrive at

$$\frac{\Delta\nu}{\Delta\alpha} \approx \frac{c}{\lambda_{IR}} \left[\frac{\partial n(\lambda_{IR})}{\partial\alpha} \frac{1}{n(\lambda_{IR})} - \frac{\partial n(\lambda_{HeNe})}{\partial\alpha} \frac{1}{n(\lambda_{HeNe})} \right] . \tag{2.23}$$

I evaluated Equation 2.23 numerically for typical ambient conditions encountered in the laboratory using the Ciddor equation[32], which gives the refractive index of air as a function of pressure p, temperature T, relative humidity (RH) and CO_2 concentration $x(CO_2)$. The resulting sensitivities of the frequency drift with respect to these parameters are given in Table 2.3. It becomes clear that changes in ambient temperature have the largest effect on the frequency drift making active temperature control of the cavity beneficial. In our laboratory, the relative humidity is subject to large changes throughout the day. It may vary by up to 10 % during a typical summer day. However, we can see that this parameter has a comparibly small influence on the IR frequency drift with only −35 kHz/%.

References

[1] D. Ettinger, K. Honma, M. Keil, and J. Polanyi, Chem. Phys. Lett. **87**, 413 (1982).

[2] T. W. Francisco, N. Camillone III, and R. E. Miller, Phys. Rev. Lett. **77**, 1402 (1996).

[3] M. P. Schmid, P. Maroni, R. D. Beck, and T. R. Rizzo, Rev. Sci. Instrum. **74**, 4110 (2003).

[4] M. Schmid, *Interaction of Highly Excited Molecules with Solid Surfaces*, Ph.D. thesis, École polytechnique fédérale de Lausanne, Lausanne (2003).

[5] P. Maroni, *Bond- and Mode-Specific Reactivity of Methane on Ni(100)*, Ph.D. thesis, École polytechnique fédérale de Lausanne, Lausanne (2005).

[6] L. Chen, *Vibrationally Bond-Selective Chemisorption of Methane Isotopologues on Pt(111) Studied by Reflection Absorption Infrared Spectroscopy*, Ph.D. thesis, École polytechnique fédérale de Lausanne, Lausanne (2012).

[7] Giacinto Scoles, ed., *Atomic and molecular beam methods, Vol. 1* (Oxford University Press, New York, 1988).

[8] M. E. van Reijzen, *State-to-state scattering of CH_4 from Ni(111) and Gr/Ni(111)*, Ph.D. thesis, École polytechnique fédérale de Lausanne, Lausanne (2016).

[9] J. Lahiri, T. S Miller, A. J Ross, L. Adamska, I. I. Oleynik, and M. Batzill, New J. Phys. **13**, 025001 (2011).

[10] B. Yoder, *Steric effects in the Chemisorption of Vibrationally Excited Methane on Nickel*, Ph.D. thesis, École polytechnique fédérale de Lausanne, Lausanne (2010).

[11] W. Demtröder, *Laser Spectroscopy 1: Basic Principles* (Spinger, Berlin and Heidelberg, 2014).

[12] G. E. Becker and H. D. Hagstrum, J. Vac. Sci. Technol. **11**, 284 (1974).

[13] R. M. Stephenson and S. Malanowski, in *NIST Chemistry WebBook, NIST Standard Reference Database Number 69*, edited by P. J. Linstrom and W. G. Mallard (National Institute of Standards and Technology, Gaithersburg MD, 1987) , (retrieved January 3, 2018).

[14] H. Preston-Thomas, Metrologia **27**, 3 (1990).

[15] R. J. Donnelly and C. F. Barenghi, J. Phys. Chem. Ref. Data. **27**, 1217 (1998).

[16] I. Gordon *et al.*, J. Quant. Spectrosc. Radiat. Transf. **203**, 3 (2017).

[17] M. Vainio and L. Halonen, Phys. Chem. Chem. Phys. **18**, 4266 (2016).

[18] A. Henderson and R. Stafford, Opt. Express **14**, 767 (2006).

[19] A. M. Morrison, T. Liang, and G. E. Douberly, Rev. Sci. Instrum. **84**, 013102 (2013).

[20] W. Demtröder, *Laser Spectroscopy 2: Experimental Techniques* (Springer Berlin Heidelberg, Berlin, Heidelberg, 2015).

[21] K. Bergmann, W. Demtröder, and P. Hering, Appl. Phys. **8**, 65 (1975).

[22] H. Pan, S. Mondal, C.-H. Yang, and K. Liu, J. Chem. Phys. **147**, 013928 (2017).
[23] O. Asvany, J. Krieg, and S. Schlemmer, Rev. Sci. Instrum. **83**, 093110 (2012).
[24] A. Prehn, R. Glöckner, G. Rempe, and M. Zeppenfeld, Rev. Sci. Instrum. **88**, 033101 (2017).
[25] E. Riedle, S. H. Ashworth, J. T. Farrell, and D. J. Nesbitt, Rev. Sci. Instrum. **65**, 42 (1994).
[26] D. F. Plusquellic, O. Votava, and D. J. Nesbitt, Appl. Opt. **35**, 1464 (1996).
[27] A. Rossi, V. Biancalana, B. Mai, and L. Tomassetti, Rev. Sci. Instrum. **73**, 2544 (2002).
[28] P. Kruk, A. Noga, T. Trepka, J. Zachorowski, and W. Gawlik, Rev. Sci. Instrum. **76**, 033109 (2005).
[29] P. Bohlouli-Zanjani, K. Afrousheh, and J. D. D. Martin, Rev. Sci. Instrum. **77**, 093105 (2006).
[30] F. Rohde, M. Almendros, C. Schuck, J. Huwer, M. Hennrich, and J. Eschner, J. Phys. B: At. Mol. Phys. **43**, 115401 (2010).
[31] J. M. Kwolek, J. E. Wells, D. S. Goodman, and W. W. Smith, Rev. Sci. Instrum. **87**, 055102 (2016).
[32] P. E. Ciddor, Appl. Opt. **35**, 1566 (1996).

3 Bolometric detection of CH_4

3.1 Introduction

This chapter discusses the theory and experimental realization of bolometric molecular beam detection and its combination with selective infrared excitation for the quantum-state-resolved detection of CH_4. Experimental results obtained during the course of this thesis work serve to illustrate the underlying concepts and demonstrate the capabilities of the technique. Although only results on the quantum-state-resolved detection of methane are included, I point out that the presented method is generally applicable to all molecules possessing infrared-active transitions.

I will begin this chapter with the basic theory of cryogenic bolometers and semiconductor bolometers in particular. Then, I will discuss their use as a molecular beam detector followed by a comprehensive description of our infrared laser tagging technique. This includes a discussion of coherent IR pumping by rapid adiabatic passage. Next, I will develop the quantitative analysis for converting bolometer signal into state populations. One section is dedicated to the discussion of angular momentum polarization and how it affects our data analysis. After a brief excursion outlining the implementation of frequency modulated IR spectroscopy, I will close this chapter with a discussion of the relevant aspects of methanes's IR spectroscopy.

3.2 Theory of bolometric detection

Bolometers are detectors that convert a temperature change ΔT into an electrical signal. The most sensitive bolometers rely on the temperature dependence of the electrical resistance of a certain material. It is characterized by the resistance temperature coefficient α, which is defined as

$$\alpha = \frac{1}{R_\mathrm{B}} \left(\frac{\mathrm{d}R_\mathrm{B}}{\mathrm{d}T} \right) , \tag{3.1}$$

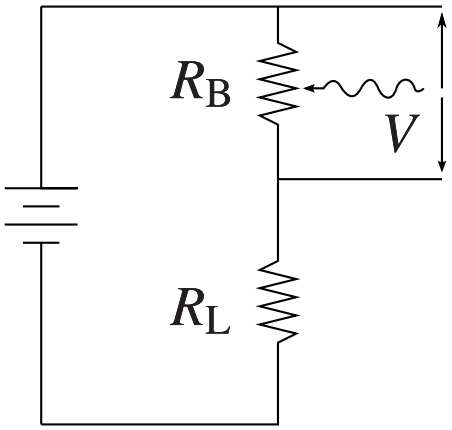

Figure 3.1 Diagram of the bolometer circuit, where R_L and R_B are the load and bolometer resistance, respectively. V is the output signal, which is sent to a pre-amplifier.

where R_B is the bolometer resistance. The largest temperature coefficients, and therefore sensitivities, are achieved with semiconductor materials whose resistance exhibits an exponential temperature dependence at cryogenic temperatures, or with superconducting materials, for which a very rapid change in resistance is observed at the superconducting transition. The bolometer used in this thesis work is a semiconductor bolometer made from doped silicon. A discussion of their conductance mechanism at cryogenic temperatures and resulting design considerations is beyond the scope this thesis. The interested reader is instead referred to the literature[1].

I will now review the quantitative description of the bolometer responsivity and time response, following the approach given in Ref. [1]. Consider the equivalent circuit for a bolometer, which is shown in Figure 3.1. In addition to the bolometer element, which is in contact with a thermostat at temperature T_0, it consists of a voltage source and a load resistor R_L, where $R_L \gg R_B$, so that the bias current can be considered constant. When a small bias voltage U_0 is applied to this circuit, the bias current

$$i = \frac{U_0}{R_L + R_B} \tag{3.2}$$

passes through the sensitive element. A temperature dependent voltage signal U can then be measured across the bolometer after pre-amplification.

The bias current i heats the bolometer from the initial temperature T_0 to a higher value T_B due to the dissipation of joule heating power $P_{bias} = R_B \cdot i^2$. The temperature rise is governed by the heat transfer equation,

$$C\left(\frac{dT}{dt}\right) + G_0(T - T_0) = i^2 \cdot R_B\,, \tag{3.3}$$

where C is the heat capacity of the bolometer and G_0 is the thermal conductivity. At equilibrium, $(\mathrm{d}T/\mathrm{d}t) = 0$, and therefore

$$G_0(T_\mathrm{B} - T_0) = i^2 \cdot R_\mathrm{B} \ . \tag{3.4}$$

We now switch on an additional input power P_A, which could come from a molecular beam hitting the bolometer surface, for instance. This causes an additional temperature rise to $T = T_\mathrm{B} + \Delta T$ and with it a change of resistance R_B and voltage U. One therefore has to modify Equation 3.3 to

$$C\left(\frac{\mathrm{d}T}{\mathrm{d}t}\right) + G_0(T - T_0) = i^2 \cdot R_\mathrm{B} + \Delta(U \cdot i) + P_\mathrm{A} \ , \tag{3.5}$$

where $\Delta(U \cdot i)$ is the change in joule heating due to the additional resistance change caused by P_A. Assuming that ΔT is small enough for the thermal conductivity to be equal to G_0, one obtains

$$\begin{aligned} G_0(T - T_0) &= G_0 \cdot \Delta T + G_0(T_\mathrm{B} - T_0) && (3.6)\\ &= G_0 \cdot \Delta T + i^2 \cdot R_\mathrm{B} \ . && (3.7) \end{aligned}$$

Inserting Equation 3.7 into Equation 3.5 yields

$$C\left(\frac{\mathrm{d}(\Delta T)}{\mathrm{d}t}\right) + G_\mathrm{E} \cdot \Delta T = P_\mathrm{A} \tag{3.8}$$

with the equivalent thermal conductivity

$$\begin{aligned} G_\mathrm{E} &= G_0 - \frac{\mathrm{d}(U \cdot i)}{\mathrm{d}T} && (3.9)\\ &= G_0 - \frac{\mathrm{d}U}{\mathrm{d}T} i - \frac{\mathrm{d}i}{\mathrm{d}T} U && (3.10)\\ &= G_0 - i^2 \cdot R_\mathrm{B} \frac{R_\mathrm{L} - R_\mathrm{B}}{R_\mathrm{L} + R_\mathrm{B}} \alpha && (3.11)\\ &\simeq G_0 - G_0(T_\mathrm{B} - T_0) \cdot \alpha \ . && (3.12) \end{aligned}$$

Note that semiconductor bolometers exhibit a drop in resistance when the temperature is increased, that is $\alpha < 0$. Equation 3.8 describes the time-dependence of the bolometer temperature change ΔT when an external power input P_A is applied. Note that for a constant P_A, the temperature rise depends only on the heat losses of the detector but not on its heat capacity. When we switch on a constant input power P_A at time $t = 0$, the

corresponding solution to Equation 3.8 reads

$$T = T_B + \frac{P_A}{G_E}\left(1 - e^{-t/\tau}\right) . \tag{3.13}$$

That is, the bolometer reaches its new equilibrium temperature with an exponentially decreasing rate with the characteristic time constant

$$\tau = \frac{C}{G_E} . \tag{3.14}$$

This illustrates that a good thermal insulation (small G_E) makes the bolometer more sensitive but also slows down its time response. The low-frequency responsivity of the bolometer $S(0)$ is defined as the voltage signal U that is generated by a temperature change $\Delta T = T - T_B$ due to a constant ($\Omega = 0$) input power P_A, and divided by the latter,

$$S(0) = \frac{U}{P_A} = \frac{i\left(\frac{dR_B}{dT}\right)\Delta T}{P_A} \tag{3.15}$$

The responsivity is normally specified in V/W. We can find the relationship between $S(0)$ and the basic bolometer properties by setting the first term on the left hand side of Equation 3.8 equal to zero and comparing to Equation 3.15, which yields

$$S(0) = i \cdot \alpha \cdot \frac{R_B}{G_E} = \frac{i \cdot \alpha \cdot R_B}{G_0 \cdot [\alpha \cdot (T_B - T_0)]} . \tag{3.16}$$

We can now rewrite Equation 3.13 in terms of the bolometer responsivity S instead of its temperature,

$$S_{rise}(t) = S(0) \cdot \left(1 - e^{-t/\tau}\right) . \tag{3.17}$$

Similarly, the bolometer response to an input signal in the form of a Dirac δ pulse is given by

$$S_{decay}(t) = S(0) \cdot \tau^{-1} \cdot \exp(-t/\tau) . \tag{3.18}$$

Figure 3.2 shows the measured decay of the raw bolometer signal after excitation by a short pulse of a helium atom beam that has scattered from a clean Ni(111) crystal. The incoming molecular beam was chopped at 142 s^{-1} with a 1% duty cycle. I fitted the tail

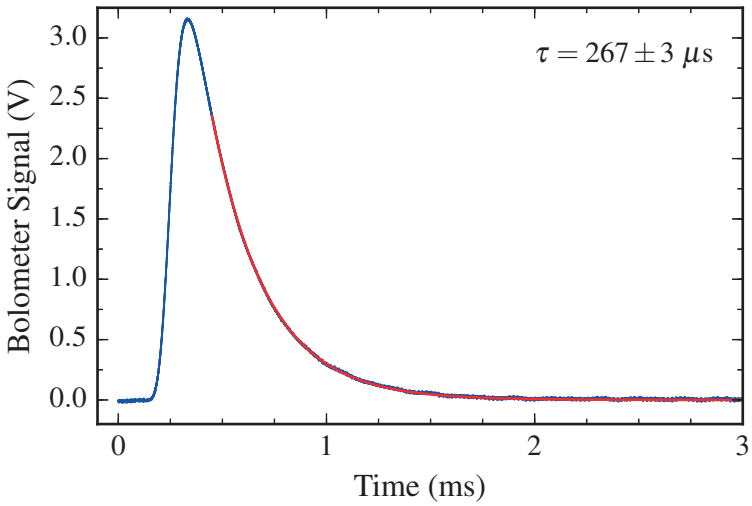

Figure 3.2 Decay of the measured raw bolometer signal (blue). The bolometer was excited by a supersonic helium beam (p_{stag} = 2 bar, T_{Nozzle} = RT) which has scattered from Ni(111). The beam was chopped before scattering at 142 s^{-1} with 1% duty cycle, corresponding to a pulse duration of 70 µs. The red curve is a fit to the data assuming a single exponential decay (see text). The resulting time constant is $\tau = 267 \pm 3$ µs.

of the decaying signal using a modified version of Equation 3.18,

$$f_{decay}(t) = f(0) \cdot \tau^{-1} \cdot \exp[-(t - t_0)/\tau] \,, \tag{3.19}$$

where $f(0)$ and t_0 are adjustable parameters. The resulting fit is shown as red line in Figure 3.2 and yields a bolometer time constant of $\tau = 267 \pm 3$ µs.

So far, we have only considered the bolometer response for a constant and a very short power input signal, respectively. In a typical experimental application however, the bolometer excitation will be modulated in order to selectively remove unwanted signal contributions. The solution of Equation 3.8 for a periodically modulated power input of the form

$$P(t) = P_0 \, [1 + \cos(\omega_{mod} t)] \tag{3.20}$$

is given by

$$T(t) = T_B + \frac{P_0 \cos(\omega_{mod} t + \phi)}{(G_E^2 + \omega_{mod}^2 C^2)^{1/2}} \,, \tag{3.21}$$

meaning that the achievable responsivity in the modulated case $S(\omega_{mod})$ is lower than

the low-frequency responsivity $S(0)$. Specifically, we have

$$S(\omega_{\mathrm{mod}}) = \frac{S(0)}{(1+\omega_{\mathrm{mod}}^2\tau^2)^{1/2}} \ . \tag{3.22}$$

Moreover, there is a dephasing between bolometer excitation and signal response, which is described by the phase factor

$$\tan\phi = \frac{\omega_{\mathrm{mod}} \cdot C}{G_{\mathrm{E}}} = \omega_{\mathrm{mod}} \cdot \tau \ . \tag{3.23}$$

We typically observe a slight change in the lock-in phase over the course of several hours of bolometer operation. It is most likely related to the the decrease in heat conductivity due to the thickening adsorbate layer on the bolometer.

The growth of amorphous adsorbate layers also affects the bolometer's responsivity, as one can see from Equation 3.22. An increase in heat capacity and a decrease in heat conductivity will always lead to a reduction of sensitivity[1,2]. When working with high fluxes of condensible gases, one thus has to anticipate this sensitivity reduction. Fortunately, the deterioration of bolometer responsivity due to adsorbates is much less pronounced for surface-scattered beams generated from neat CH_4 or mixtures with helium because the flux of condensible gas is usually low. Typically, the phase change is here on the order of 1 °/h and the decrease in bolometer responsivity is negligible for at least 8 hours of continued exposure. Based on the bolometer sensitivity reported in the previous chapter, I estimate that the influx of scattered CH_4 from a molecular beam, which only contains this gas, is on the order of 10^{14} molecules/(h·cm^2). Assuming a typical value of 10^{14} molecule/cm^2 for the density of adsorption sites, I estimate the adsorbate growth rate to be on the order of only 1 monolayer/h.

By contrast, a much more pronounced effect on the bolometer properties due to cryofrost formation is observed when a high flux of condensible gas strikes the detector. Van Reijzen has given[3] an example where the bolometer directly sampled a molecular beam of CH_4, which led to a significant reduction of $S(\omega_{\mathrm{mod}})$ over time. Here, the effect was permanent and the original properties of the bolometer could only be recovered by removing the cryofrost, which is usually done by allowing the bolometer to heat up above the desorption temperature. Other methods that involve bleeding hydrogen or oxygen gas onto the bolometer surface during molecular beam exposure have been reported in the literature[1]. Another example is the detection of a beam of methane (6%) seeded in H_2 that has scattered from Ni(111). This is shown in Figure 3.3. Here, I recorded the lock-in phase as a function of the time during which the bolometer was exposed to the scattered

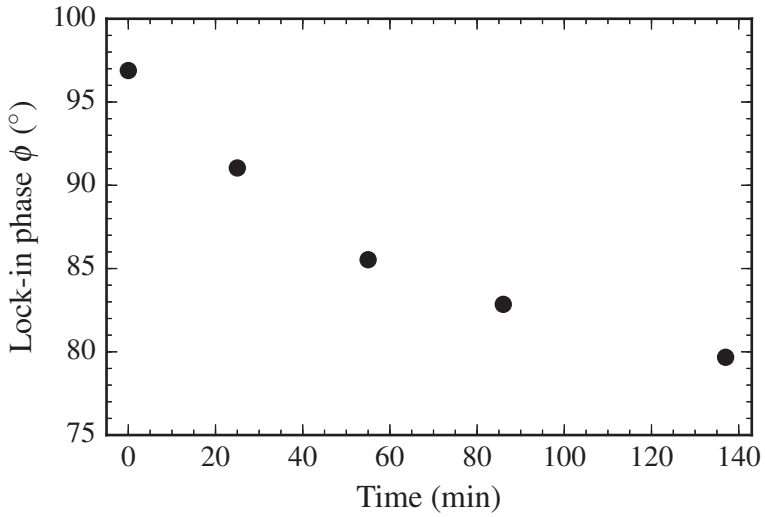

Figure 3.3 Variation of the lock-in phase ϕ during exposure of the bolometer with an H_2-seeded beam of CH_4 (6% CH_4 in H_2). The signal was obtained by exciting methane with an amplitude modulated IR laser. The change in phase angle reflects the decreasing bolometer heat conductivity, which is due to the increasing thickness of the adsorbed H_2 layer.

molecular beam. The latter was excited by an amplitude-modulated IR laser and the resulting bolometer signal analyzed by the lock-in amplifier. A molecular beam of H_2, which scatters from a clean single-crystal surface, gives rise to a very intense specular reflection. If the detector is placed to sample a part of this reflection, the bolometer element becomes rapidly covered with hydrogen ice.

3.3 Molecular beam detection

A bolometer may be used to detect a molecular beam directly without any previous laser excitation solely due to the energy that it releases upon impinging on the sensitive element. The resulting bolometer signal, however, can usually not be used as a direct measure of the number flux of molecules $F = N \cdot \langle v \rangle$, where N is the number density and $\langle v \rangle$ the average molecular velocity. The reason for this lies in the fact that the input power from the detected beam contains several contributions, whose partitioning is unknown unless additional measurements are performed or certain limiting conditions apply. More specifically, we can write the signal S_{MB} that is generated by a molecular

beam impinging on a cryogenic bolometer as

$$S_{\mathrm{MB}} = S_{\mathrm{Bolo}}\, F \cdot \Big\{ (s-1)(\beta_{\mathrm{kin}}\, E_{\mathrm{kin}} + \beta_{\mathrm{int}}\, E_{\mathrm{int}}) + s\left[E_{\mathrm{kin}} + E_{\mathrm{int}} + E_{\mathrm{ads}} - E_{\mathrm{th}}(k_{\mathrm{B}} T_{\mathrm{Bolo}})\right] \Big\}, \quad (3.24)$$

where S_{Bolo} is the bolometer responsivity and s the sticking coefficient. When the molecular beam of flux F hits the bolometer surface, a fraction of molecules s sticks permanently to the bolometer, which is held at liquid helium temperature, prohibiting subsequent desorption. These molecules transfer all their kinetic (E_{kin}) and internal energy (E_{int}) to the detector, corresponding to the second term in Equation 3.24. Additionally, they release a certain amount of adsorption energy E_{ads}. Assuming that molecules, after an induction phase where they stick on the bare bolometer, adsorb on an amorphous condensed layer constituted by their own kind, this energy can be taken equal to the negative heat of vaporization. Furthermore, we have neglected the energy that may be released by subsequent crystallization or phase transitions occurring within the adsorbate layer. The negative term $E_{\mathrm{th}}(k_{\mathrm{B}} T_{\mathrm{Bolo}})$ corresponds to the thermal energy that remains in the adsorbed molecules. It can normally be disregarded for a cryogenic bolometer since $k_{\mathrm{B}} T_{\mathrm{Bolo}}$ is on the order of 100 µeV. Lastly, the first term in Equation 3.24 represents the part of the beam that does not permanently stick to the bolometer but instead is reflected back into the gas phase. These molecules transfer only fractions β_{kin} and β_{int} of their kinetic and internal energy, respectively.

The bolometer signal S_{MB} is only an accurate measure of the number flux as long the kinetic and internal energy of the beam remain fixed. An exception is presented by a situation where the sticking coefficient is close to unity and the adsorption energy greatly exceeds the combined kinetic and internal energies. Under this condition, the bolometer may operate as a number flux detector irrespective of beam energy. For our supersonic molecular beams of CH_4 this is unfortunately not the case. We can quickly check this by comparing the relative magnitudes of the adsorption energy and typical kinetic energies of the molecular beams. We may take methane's enthalpy of sublimation[4] of 9.7 kJ/mol as an estimate for E_{ads} and a value of 9 kJ/mol for the kinetic energy, which corresponds to a rather slow beam generated by expanding neat CH_4. Adsorption and kinetic energy are therefore expected to be of comparable magnitude.

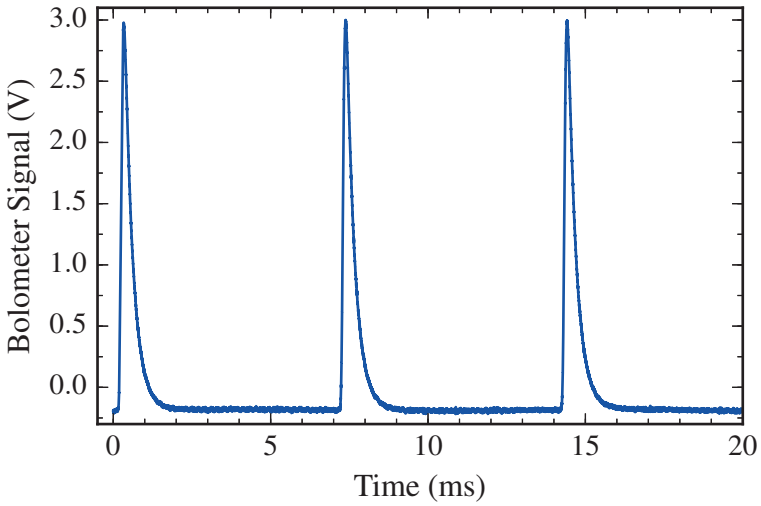

Figure 3.4 Raw bolometer signal produced by a supersonic helium beam (p_{stag} = 2 bar, T_{Nozzle} = RT) scattering from Ni(111). The beam was chopped at 142 s^{-1} and the surface temperature was 673 K.

3.3.1 Helium atom scattering

Despite the aforementioned caveats of direct bolometric detection with respect to methane beams, it still proves useful for performing helium atom scattering (HAS). The scattering of a nearly monochromatic supersonic beam of He from surfaces is an extremely sensitive, non-destructive and, because of the low projectile energy, surface-sensitive technique for the study of surface structure and orientation, corrugation and adsorbate dynamics[5]. Furthermore, highly-resolved energy analysis of the scattered He atoms can yield the dispersion of surface phonons.

Figure 3.4 shows the raw bolometer signal generated by a helium beam scattered from the Ni(111) surface under specular scattering conditions $\theta_i = \theta_f = 67.5°$. The beam was chopped before scattering at a rate of 142 s^{-1} and with a duty cycle of 1 %. Note that only the kinetic energy of the He atoms can make a contribution to the bolometer signal for a pure He beam (Equation 3.24), since helium does not permanently stick on the bolometer ($s = 0$) and no internal energy is present. The surface scattering of such light and low-energetic particles like He atoms in an atomic beam is predominantly elastic. Since their de Broglie wavelengths are on the order of some tenths to a few Ångström, we may think of the scattering as a diffraction process where most atoms are reflected elastically along the specular direction corresponding to zeroth-order diffraction. The intensity maxima in the scattering angular distributions are typically very narrow and their positions intensities allow determination of unit cell size and orientation.

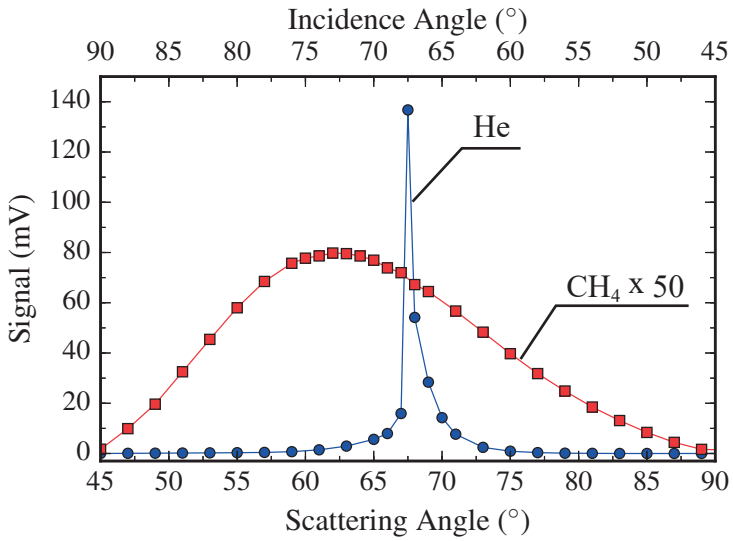

Figure 3.5 Comparison of the scattering angular distributions of a CH_4 and a helium atom beam obtained by chopping the incoming beams and lock-in detecting the bolometer signal. Both beams scattered form a 673 K hot Ni(111) surface. The beam conditions for the He beam were the same as the ones in Figure 3.4. The methane beam was generated by expanding pure CH_4 from a pressure of 3 bar and the resulting signal scaled by a factor of 50. Solid lines are meant to guide the eye.

Figure 3.5 compares the scattering angular distributions of a molecular beam of CH_4 and a helium atom beam. The beams were chopped before scattering and the bolometer signal lock-in detected with the chopper wheel's optocoupler signal as a reference. Here, we integrated the lock-in output for 15 and 9 seconds, respectively, before moving to the next angle. I used the specular helium peak as a reference for calibrating the conversion of the angular scale on the surface manipulator rotary flange to the incidence and scattering angles, and I maintain this calibration throughout this thesis. The specular helium peak is very sharp, even at the high surface temperature of $T_S = 673\,K$, and together with our AES and LEED data confirms that the surface is clean and well-ordered. HAS is extremely sensitivity toward dilute impurities on the surface. Even minute adsorbate concentrations (down to 10^{-3} monolayers) typically result in a significant decrease of the specular intensity. The CH_4 signal intensity in Figure 3.5 is scaled by a factor of 50 and therefore about two orders of magnitude lower than the He peak intensity. Note that the angular distribution obtained by chopping the molecular beam is not necessarily a faithful measure of the number flux in the case of methane, as discussed above. Moreover, it is impossible to obtain an angular distribution for molecules seeded in a carrier gas since we cannot distinguish bolometer signal coming

from the carrier gas and the gas of interest. Quantum-state-resolved detection using the tagging technique, presented in the following section, overcomes these limitations.

3.4 Bolometric detection with IR laser tagging

3.4.1 Basic principle of BILT

A bolometer detects the total incident power and is thus not state-specific by itself. However, a modulated IR laser can be used to state-specifically excite molecules before they reach the bolometer. We refer to this excitation as "tagging" because the added rovibrational energy "labels" molecules that are in one particular state. Since radiative lifetimes are on the order of milliseconds in the infrared and therefore much longer than the flight time from the excitation region to the bolometer, the tagged molecules carry the additional rovibrational energy to the bolometer, which leads to a signal increase upon their adsorption. If we now compare the bolometer signal with and without excitation, we obtain a measure of the population in the initial state.

Figure 3.6 illustrates the basic principle of our bolometric detection scheme with IR laser tagging, hereafter abbreviated BILT. In practice, we modulate the excitation by chopping the laser beam with a chopper wheel while the molecular beam operates continuously. A lock-in amplifier, which is attuned to the modulation frequency of the laser, selectively amplifies the modulated portion of the bolometer signal. This removes the non-modulated (DC) signal component and with it all other contributions apart from

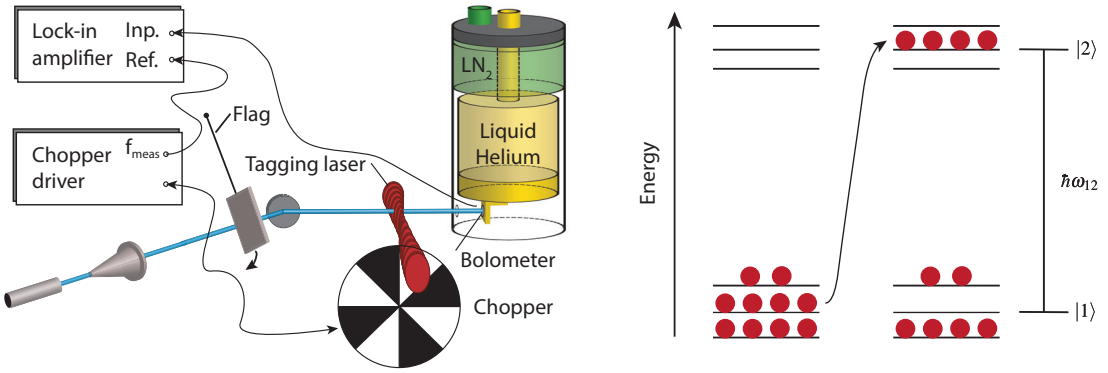

Figure 3.6 (Left) Schematic diagram illustrating the principle of our BILT technique. A continuous molecular beam that underwent surface scattering is state-specifically excited by an IR laser before impinging on the cryogenic bolometer. The additional energy of the so-tagged molecules gives an AC signal that is demodulated by a lock-in amplifier. (Right) Energy level diagram of the tagging step. The resonant IR laser moves population, represented by the spheres, from a specific lower to an empty upper level.

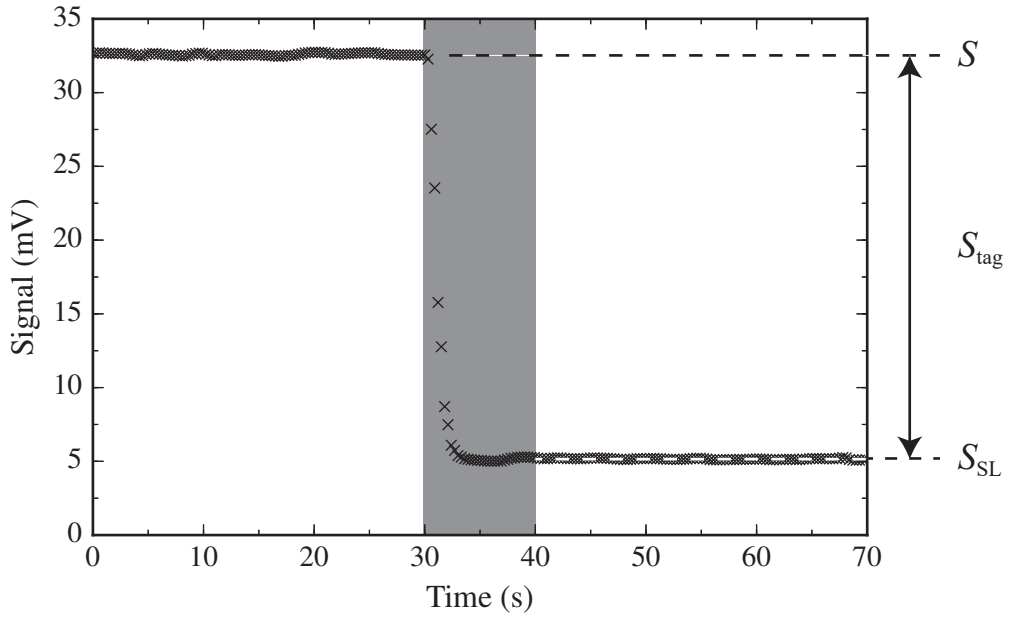

Figure 3.7 Typical signal trace from a laser tagging experiment, detecting scattered CH_4 in its $v = 0$, $J = 0$ state *via* the ν_3, $R(0)$ transition. The bolometer output was selectively amplified by a lock-in amplifier attuned to the laser chopping frequency of 142 Hz. A data point was recorded every 300 ms. After 30 s, the beam flag was moved to block the incoming molecular beam. The remaining signal S_{SL} is due to scattered IR light. The grayed area indicates the part of the trace that is ignored in the later analysis.

the rovibrational energy change induced by the tagging laser and scattered IR light that reaches the detector. In other words, the lock-in amplifier output is proportional to the bolometer signal difference between laser on and laser off.

Figure 3.7 shows a typical signal recording obtained using the BILT method. During the first 30 s of the recording, a molecular beam of CH_4, which was scattered from the Ni(111) surface, was tagged by the IR laser tuned to excite the $R(0)$ transition of the anti-symmetric C–H stretch (ν_3) fundamental band. That is, the tagging experiment detected CH_4 in its $v = 0$, $J = 0$ state. After 30 s, the incoming molecular beam was blocked by an automated beam flag resulting in a signal decrease from the initial value S because there are no more molecules that could be excited and carry the additional rovibrational energy to the detector. The signal, however, does not drop to zero but to a value S_{SL}, which is due to scattered IR light. This scattered light signal cannot be removed by lock-in amplification because it also appears at the chopping frequency. Moreover, the time that scattered light and tagged molecules take for traveling to the bolometer are in both cases very short compared to the detector time constant. This

means that the two signals appear as well under the same phase. As the total energy that molecules remove from the IR beam due to absorption is extremely small, we can assume that the scattered light contribution is the same, irrespective of whether the flag blocks the molecules or not. The difference $S_{\mathrm{tag}} = S - S_{\mathrm{SL}}$ thus gives a measure of the rovibrational energy released by the tagged molecules on the bolometer. We obtain S_{tag} by separately averaging both, flag-on and flag-off signals before performing the subtraction. We ignore the data points right after the closing of the flag, because it takes some time for the lock-in to adjust to the new value. This waiting time, which is shown as gray area in Figure 3.7, typically lasts 10 lock-in time-constants. Throughout this thesis – unless stated otherwise –, the lock-in time-constant was 300 ms, which was also the time interval between the acquisition of two data points (dwell time).

3.4.2 Conversion of bolometer signal to population

The post-scattering quantum state population reported in this thesis have been obtained by analyzing "tagging traces" similar to the one in Figure 3.7. The so-obtained background-subtracted signals S_{tag} now have to be converted to state populations. Let $|1\rangle$ and $|2\rangle$ denote the lower and upper levels of the tagging transition, respectively. The signal S_{tag} is proportional to $\Delta N_2 = N_2 - N_2(0)$, which is the net population actually promoted to the upper state $|2\rangle$ by the laser, and the energy difference between the two states $\hbar\omega_{12}$,

$$S_{\mathrm{tag}} \propto \Delta N_2 \cdot \hbar\omega_{12} \; . \tag{3.25}$$

Note that ΔN_2 and therefore S_{tag} may be negative if the upper level $|2\rangle$ was sufficiently populated in the beginning and the laser caused stimulated emission rather than absorption. In our case, the upper levels are located at least ~ 3000 cm^{-1} above the ground state. Neither thermal nor collisional energies are high enough in the current experiments to cause significant excitation of these levels, which we therefore assume to be empty. We can then relate the bolometer signal to the population of lower state N_1 by rewriting Equation 3.25 as,

$$S_{\mathrm{tag}} \propto N_1 \cdot f_{\mathrm{tag}} \cdot \hbar\omega_{12} \, , \tag{3.26}$$

where f_{tag} is the excitation probability. The product $N_1 \cdot f_{\mathrm{tag}}$ is proportional to the total number of excited molecules during the time when the laser is tuned to resonance, which is an accurate measure of the number flux if the time-averaged excitation probability is independent of velocity. Two conditions need to be met to fulfill this requirement. First,

the *instantaneous* transition probability f_{tag} needs to be independent of velocity. This can be achieved for instance using strong pumping conditions, saturating the absorption. Second, the laser beam has to be on for long enough to effectively define a surface that molecules cross on their way to the detector. We typically chop the tagging laser at a frequency of 142 Hz with a duty cycle of 0.5, corresponding to a laser-on duration of 3.5 ms. This is long compared to the time that it takes the scattered molecules to travel the 36 cm distance from the surface to the detector. Hence, the number of molecules allowed to pass through the laser while it is on is much greater than the number of molecules in the scattered beam at any instant. In other words, the tagging laser excites all scattered molecules with equal probability, irrespective of their velocity. The quantity N_1 is thus the flux-weighted population residing in lower state $|1\rangle$ if the aforementioned conditions hold. This stands in contrast to detection techniques involving pulsed excitation, which typically yield densities because the excitation probability depends here on the final scattering velocity.

We note that the bolometric technique only yields the correct state populations if the sticking probability of the probed molecules on the bolometer is independent of the state excited in the tagging transition. A comparative study of the physisorption probability of ground state and rovibrationally excited CH_4 on cryogenic Pt(111) surface has been performed in our laboratory[6]. Alongside similar studies on different molecule-surface systems, including the sticking of water on ice[7], the results suggest that rovibrational excitation has negligible effect on most molecules' physisorption probability. For an incident molecule to become physisorbed on the bolometer surface, it must loose sufficient normal kinetic energy to become trapped in the physisorption potential well. Since desorption of CH_4 from the cold bolometer environment is practically excluded and the actual bolometer substrate surface will be completely covered with adsorbed CH_4 very quickly, the relevant adsorption process is the sticking of CH_4 on methane-ice. One might further argue that the transfer of kinetic energy from the incoming molecule to an adlayer of CH_4 is more efficient than to a transition metal surface due to the smaller mass mismatch. Furthermore, we expect the methane-ice surface to be somewhat corrugated, which may aid in the loss of normal kinetic energy and facilitate sticking. Overall, we have reason to believe that the sticking probability of methane on methane-ice should be high and insensitive to rovibrational excitation, making the BILT signal an accurate measure of state populations.

3.4.3 Coherent excitation by rapid adiabatic passage

It should be clear from the previous discussion that the BILT technique greatly benefits from maximizing the degree of population transfer during the laser tagging step. Saturation of the tagging transition is desirable for at least three reasons: first, and most importantly, the BILT signal is directly proportional to the excitation probability f_{tag}. Second, saturation ensures that f_{tag} is insensitive to the velocity of the detected particles, and third, it eliminates the effect of small laser power variations on the BILT signal, thereby further increasing the signal-to-noise ratio.

Even though we are mostly interested in comparably strong IR transitions of methane, powerful lasers are needed to achieve saturation. The OPOs available in our laboratory provide the required brightness because of their narrow linewidth and high power. Moreover, their light is extraordinarily coherent, which can be exploited to overcome the limit of 50 % population transfer encountered when incoherent radiation is used. Starting with the PhD work of Bruce Yoder[8], we have used a technique known as Rapid Adiabatic Passage (RAP), which can achieve almost complete population inversion in a molecular beam.

While the full theoretical description of RAP is beyond the scope of this thesis, the present section will outline the basic concepts and the experimental realization of RAP. I will also summarize the relevant theoretical framework that is required in the analysis of the experimental data obtained in this work. The interested reader is referred to the thesis of Yoder[8] and a recent review article[9] for a more comprehensive theoretical treatment of RAP. Moreover, Chadwick *et al.* have reported[10] our implementation of RAP and how it can be modeled theoretically by solving the optical Bloch equations.

Let us first consider a case where molecules are exposed to an intense, coherent and resonant radiation field but where the conditions for RAP are not applied. Consider a two-level system with lower and upper levels $|1\rangle$ and $|2\rangle$, which are separated by an energy gap $\hbar\omega_{12}$, as depicted in Figure 3.8 (a). Let all the population be in level $|1\rangle$ ($N_1 = 1$) at time $t = 0$, while level $|2\rangle$ is empty. We now switch on a coherent light field that is resonant with the transition between these two levels, that is, its frequency is $\hbar\omega_{12}$. It is well-known[11] that the presence of this driving field will cause the population to oscillate between $|1\rangle$ and $|2\rangle$, as shown in Figure 3.8 (b). The frequency of this oscillation is given by the Rabi frequency Ω, which depends on the transition dipole moment μ_{12} and the electric field amplitude E,

$$\Omega = \frac{\mu_{12} \cdot E}{\hbar} \,. \tag{3.27}$$

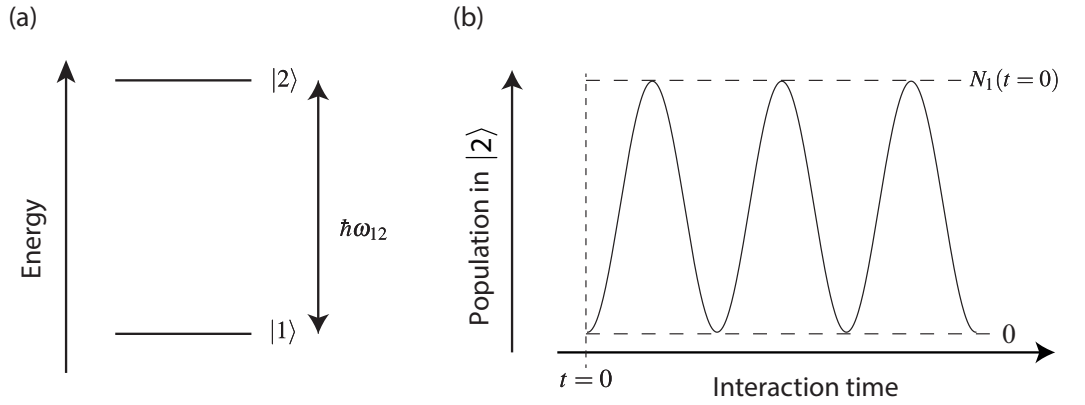

Figure 3.8 (a) Energy level diagram of a general two-level system and (b) Rabi-cycling of the state populations induced by a coherent, resonant radiation field.

Hence, the transferred population ΔN depends on the total interaction time t. A molecular beam has, despite the translational cooling during supersonic expansion, a finite velocity spread, which means that molecules spend different amounts of time in the interaction region with the excitation field that is usually a laser beam. Also, the finite collimation angle of the molecular beam gives rise to different Doppler shifts $\Delta\omega_D = \omega_{12} \cdot v_x/c$, where v_x is the molecular velocity component along the light propagation direction and $c$the speed of light. The Doppler shift lowers the Rabi frequency and amplitude of the population oscillations. The total excitation probability for an ensemble of molecules in a beam is the average of the probabilities at the end of the Rabi cycles. In most cases this average is equal to $1/2$ and, as we should expect, identical to the result when saturation in achieved by incoherent radiation.

In contrast to Rabi cycling, RAP makes use of a time-dependent detuning between laser and transition frequency, which induces adiabatic population transfer from the initial to the final state. It useful to adopt a slightly different picture of our two-level system for understanding the basic principle behind RAP. If the laser is sufficiently intense, the ground-state energy is lifted (dressed) by the photon energy $\hbar\omega$, as shown in Figure 3.9.

That is, photon and original ground state form an adiabatic state with energy $E_1 + \hbar\omega$. Let us assume that in the beginning of the interaction, the laser frequency is detuned (blue-shifted) from the transition, shifting the dressed ground state above the excited state. Now, a frequency sweep (chirp) $\Delta(t)$ is applied, which creates a curve crossing at the point where the energies of the dressed ground state and that of the excited state meet. Adiabatic following occurs if the chirp rate $|\mathrm{d}\omega/\mathrm{d}t|$ is slow compared to the maximum

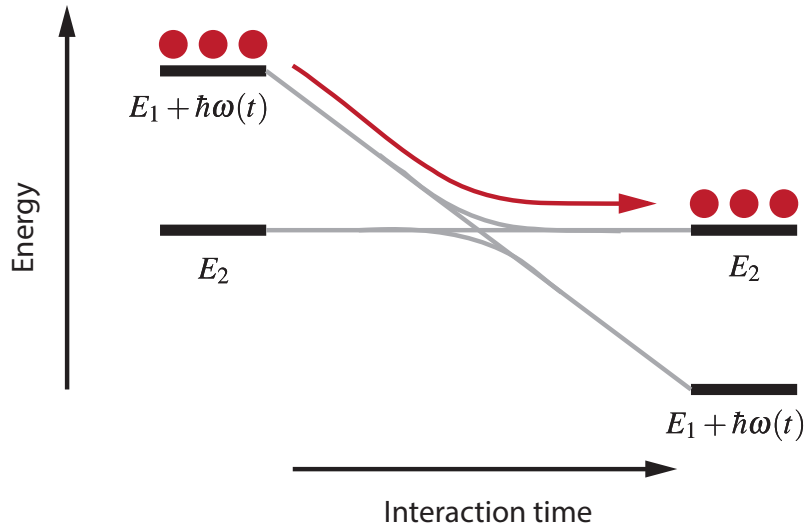

Figure 3.9 Schematic illustration of adiabatic following in a two-level system. Adapted from Ref. [8].

Rabi frequency Ω_0, that is

$$\left|\frac{\mathrm{d}\omega}{\mathrm{d}t}\right| \ll \Omega_0^2 \tag{3.28}$$

where Ω_0 is the Rabi frequency in the center of the transition $\Omega(\omega_{12})$. Equation 3.28 is therefore known as the adiabatic condition. Adiabatic following means that all population remains in the same adiabatic state. However, the adiabatic state that was initially associated with the ground state corresponds to the excited state at the end of the interaction. As a result, all population that was in $|1\rangle$ at $t = 0$ is then in $|2\rangle$, meaning that full population inversion is achieved. Note that this process is symmetric with respect to levels $|1\rangle$ and $|2\rangle$, or in other words, adiabatic following occurs for both absorption and stimulated emission. If neither level is initially empty, RAP will invert their populations.

Two more conditions need to be satisfied for RAP to occur. First, the laser intensity should only vary smoothly as the chirp is performed. We can write this condition as

$$\left|(\omega_{12}-\omega)\frac{\mathrm{d}\omega}{\mathrm{d}t}\right| \ll \left[\Omega^2 + (\omega_{12}-\omega)^2\right]^{3/2} . \tag{3.29}$$

The third condition stipulates that the total chirp should be larger than the maximum

Rabi frequency, that is,

$$\left|\frac{\mathrm{d}\omega}{\mathrm{d}t}\right| T > \Omega_0 \,, \tag{3.30}$$

where T is the transit time that it takes for molecules to cross through the radiation field. Under these conditions, the excitation probability P_{exc} of a molecule can be approximated as one minus the probability of the diabatic (curve-crossing) transition given by the Landau-Zener formula,

$$P_{\mathrm{exc}} = 1 - \exp\left(-\frac{\pi\Omega^2(\mu, E)}{2\left|\frac{\mathrm{d}\omega}{\mathrm{d}t}\right|}\right) . \tag{3.31}$$

The required frequency sweep can be readily achieved for a directed molecular beam by the Doppler tuning method. Here, the laser beam is focused in such a way that molecules experience a change in wavefront curvature as they traverse the laser field. This is shown schematically in Figure 3.10. We use a cylindrical lens to focus the beam in only one dimension. Molecules that cross the radiation field perpendicular to the light propagation direction, experience a time-dependent Doppler shift

$$\Delta_{\mathrm{D}} = \frac{\omega_{12}\, v_{\mathrm{wf}}}{c} \,, \tag{3.32}$$

where v_{wf} is the velocity component of molecules along the wavefront's surface normal. The detuning is related to the radius of wavefront curvature R and the longitudinal molecular velocity v by

$$\Delta_{\mathrm{D}}(t) = \frac{v^2 \omega_{12}\, t}{cR} \,, \tag{3.33}$$

where t is the interaction time. For a Gaussian laser beam, the radius of curvature at a distance z from the beam waist is given by

$$R(z) = z + \frac{z_{\mathrm{R}}^2}{z} \tag{3.34}$$

with the Rayleigh length z_{R},

$$z_{\mathrm{R}} = \frac{\pi w_0^2}{\lambda} \,, \tag{3.35}$$

where w_0 is the beam waist. The latter is related to the radius of the unfocused beam r

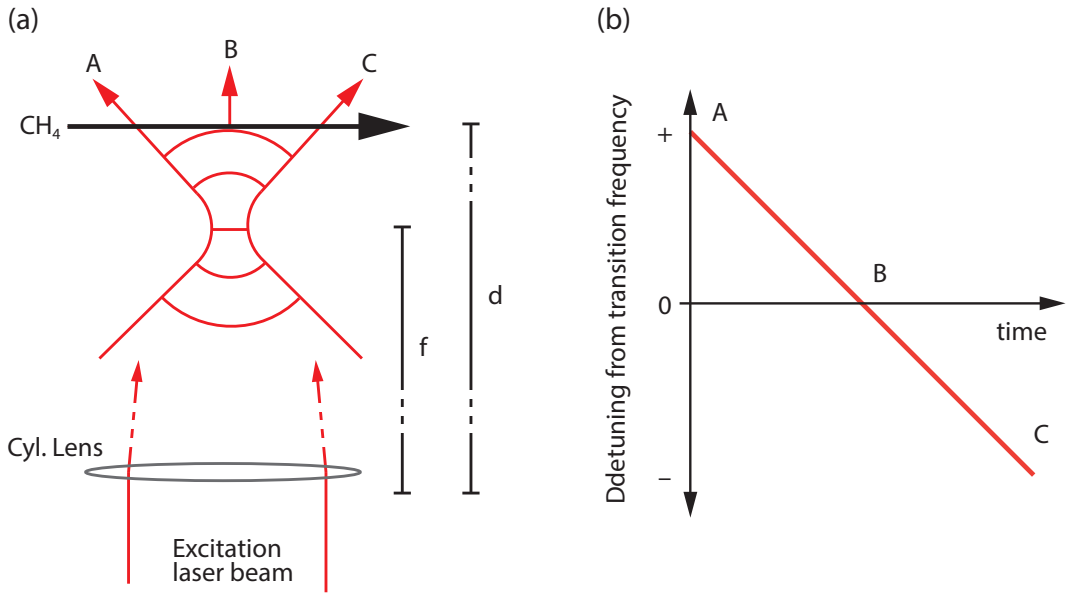

Figure 3.10 Illustration of how the frequency sweep for excitation by adiabatic following is achieved through Doppler-detuning. (a) A cylindrical lens with focal length f focuses the laser beam. The molecular beam traverses the curved wave-fronts of the laser field at a distance d from the lens. (b) Frequency detuning that molecules experience as they travel through the diverging laser beam. In the beginning, the frequency will be blue-shifted, at the center of the beam B no shift is induced and at C the frequency is red-shifted. Adapted from Ref. [8].

by

$$w_0 = \frac{\lambda f}{\pi r} \,. \tag{3.36}$$

Most tagging measurements presented in this thesis have been carried out with a $f = 25.4\,\text{cm}$ CaF_2 lens placed about 35 cm away from the molecular beam. We now estimate the RAP parameters for the ν_3 $R(0)$ transition at $\lambda = 3.302\,510\,\mu\text{m}$ to ensure that the RAP conditions are satisfied. The transition dipole moment is related[12] to the Einstein coefficient of spontaneous emission A_{21} by

$$\mu_{12}^2 = \frac{3\varepsilon_0 hc^3}{2\omega_{12}^3} A_{21} \,, \tag{3.37}$$

where ε_0 is the permittivity of free space. For this particular transition, HITRAN lists[13] an A_{21} coefficient of $25.36\,\text{s}^{-1}$, which gives a transition dipole moment of $1.8 \cdot 10^{-31}\,\text{Cm}$

or $5.4 \cdot 10^{-2}$ Debye. To estimate Ω_0, we further require the peak electric field strength, which is related to the laser intensity I (power per unit area) by

$$E_0 = \sqrt{\frac{2I}{\varepsilon_0 c}}\,, \tag{3.38}$$

which in turn is related to the laser power P by

$$I = \frac{2P}{A} = \frac{2P}{\pi w_x(z) w_y(z)}\,, \tag{3.39}$$

where A is the laser area of the laser beam, which is defined by the boundary curve where the electric field amplitude (intensity) drops to $1/\mathrm{e}$ ($1/\mathrm{e}^2$) of the peak value. The beam radius in the focused direction is given by

$$w_x(z) = w_0 \sqrt{1 + \frac{z^2}{z_\mathrm{R}^2}}\,, \tag{3.40}$$

while in the unfocused direction, $w_y(z) = w_0$. For a typical laser power of 0.8 W (Tagging OPO), a laser beam radius of $r = 1.5\,\mathrm{mm}$ and the focusing conditions mentioned above, we find a Rabi frequency of $\Omega_0 = 5.6\,\mathrm{MHz}$. The detuning rate is given by

$$\frac{\mathrm{d}\omega}{\mathrm{d}t} = \frac{v_x^2 \omega_{12}}{R(z) c}\,, \tag{3.41}$$

which for a longitudinal molecular speed of $v_x = 2000\,\mathrm{m/s}$ yields $\mathrm{d}\omega/\mathrm{d}t = 11.5\,\mathrm{MHz/\mu s}$. Therefore, the first RAP condition is easily satisfied. Yoder has shown in his thesis[8] that the second RAP condition is practically always fulfilled because of the Gaussian TEM_{00} mode of our OPO idler beam. The total detuning, given the transit time of 0.6 µs, is then $|\mathrm{d}\omega/\mathrm{d}t| \cdot T = 6.8\,\mathrm{MHz}$, satisfying the third RAP condition.

Figure 3.11 shows a comparison of the line profiles of the ν_3 $R(0)$ transition of CH_4 with and without RAP excitation detected after scattering of a molecular beam with an incidence speed of 1067 m/s. The frequency of the Pump OPO[(a)] was scanned at rates of 0.2 and 0.5 MHz/s, respectively, using the transfer cavity. I verified separately that the different scan rates had a negligible effect on the linewidth. The linewith in panel (a) observed when excitation does not proceed *via* RAP, represents the residual Doppler broadening in the scattered beam, which is due to the small molecular velocity

[(a)] Here, the Pump OPO was used to excite scattered molecules instead of the Tagging OPO. This is an exception and should not lead to further confusion in the remainder of this thesis.

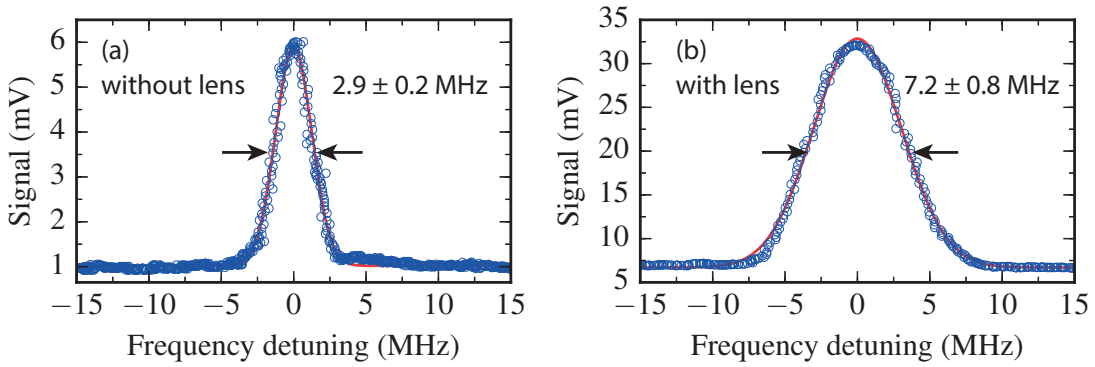

Figure 3.11 Line shape comparison of the ν_3 $R(0)$ transition detected in scattered CH_4 without (a) and with (b) a $f = 25.4\,\text{cm}$ lens in place. When the lens is installed, the frequency chirp for achieving RAP produces a significantly increased linewidth. Gaussian fits shown in red determined the linewidths. The no-lens profile was taken with reduced laser power (180 mW) and the incidence speed of the CH_4 molecular beam was 1067 m/s.

component along the laser axis. However, when the cylindrical lens is installed, the transition linewidth more than doubles. This is explained by the Doppler detuning effect coming from the curved wavefronts, which effectively broadens the laser linewidth. In this particular experiment, the unfocused beam radius was 1.8 mm. Together with the incident beam speed, we estimate a total Doppler tuning $|\mathrm{d}\omega/\mathrm{d}t| \cdot T$ of 4.2 MHz. The combined width of the Doppler-broadened profile in Figure 3.11 (a) with the expected broadening due to Doppler tuning is in good agreement with the observed linewidth in Figure 3.11 (b).

Figure 3.12 illustrates the difference in excitation efficiency between RAP and "non-RAP" saturation. Here, the ν_3 $R(0)$ transition was excited and the bolometer signal recorded as a function of the laser power. The scattered light signal was recorded separately and subtracted. The asymptote of the RAP-induced signal towards high laser powers indeed reaches about twice the value compared to when no cylindrical lens is used. Since both curves show that saturation occurs at the highest laser powers, we can conclude that RAP indeed caused complete population inversion ($f_{\text{tag}} = 1$) while in the non-focused case only a maximum of 50% of all molecules in the ν_3 $J = 0$ state were excited. Note that in the latter case, f_{tag} may be even lower than 0.5 if the residual Doppler width of the molecules is substantially larger than the laser linewidth. Only molecules with small Doppler shifts may then be excited when the laser is tuned to the center frequency. In the present case though, the Doppler width is larger than the instrumental laser linewidth by a factor of ~ 3. Because of the high peak power, the laser

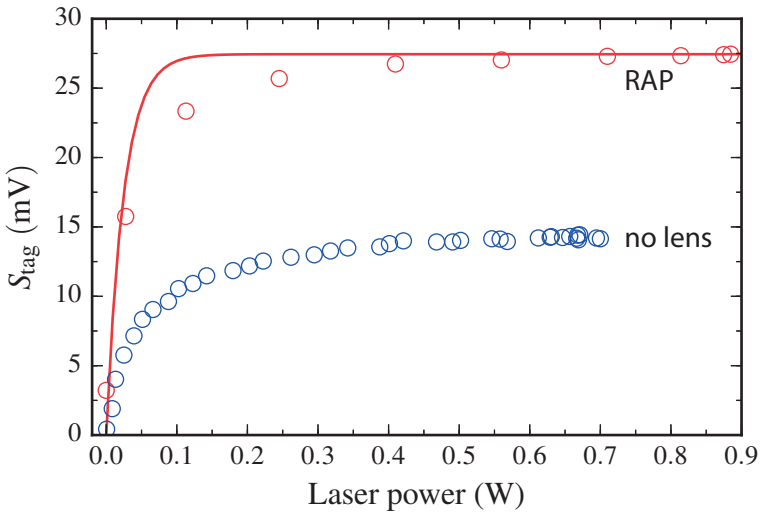

Figure 3.12 Laser power dependence of the BILT signal with (red circles) and without (blue circles) RAP excitation for the ν_3 $R(0)$ transition of CH_4. The conditions were the same as the ones in Figure 3.11 The solid lines represent the calculated fluence curve using the theoretical modeling of RAP outlined above.

power in the wings of the laser line profile is still high enough to saturate those molecules that have the largest Doppler shifts. RAP, by contrast, does not suffer from this problem because a wider distribution of velocities are "captured" as the laser frequency is swept by Doppler detuning. The solid red line in Figure 3.12 further shows the theoretically modeled power dependence for excitation *via* RAP, scaled to match the maximum signal. The model captures the initial slope well, but shows significant deviations at intermediate laser fluence. This departure from the experimental data is, however, typically most pronounced for this particular transition. For all other transitions, the Landau-Zener model performs much better, as Hundt has shown in his thesis[14]. I note in passing that one can alternatively solve the optical Bloch equations for fluence curve modeling. This was has been demonstrated[10] by Chadwick *et al.*, who were able to obtain quantitative agreement with the experimental fluence curves.

I have shown that the condition for RAP are generally fulfilled for the ν_3 $R(0)$ transition when one applies the focusing condition outlined above. However, we have encountered many situations where the RAP conditions break down and only partial population transfer is achieved. This failure can have several reasons. As shown by Yoder[8] and Hundt[14], an increase in molecular velocity v_x leads to a faster tuning rate, which may compromise condition #1. In our current scattering experiments though, another aspect is more important. So far in this thesis but also in previous PhD theses

starting with the one by Yoder, and in the paper[10] by Chadwick *et al.*, transitions starting from rotational levels with low rotational quantum numbers $J \leq 1$ have been considered since RAP was only used to prepare reactant molecules in the incoming beam, where only those levels are populated. Surface scattering, however, will produce CH_4 in much higher excited rotational states. This has a profound effect on the excitation probability because of the dependence of the transition probability on the rotational quantum number M_J, which is the projection of the angular momentum vector J onto an axis that is fixed in the laboratory frame. Even though the M_J levels for a given J are mutually degenerate, their excitation probabilities differ when polarized light is used. As I will show below, the related transition moments will always be smaller than that of the ν_3 $R(0)$ transition where only the $M_J = 0$ level is excited. As a result, we cannot assume that full population inversion is achieved for all transition.

In spite of those problems, we will anyway use RAP because excitation efficiencies are still higher compared to non-RAP saturation and adverse effects like Rabi oscillations are avoided. In order to quantitatively analyze the scattering distributions, we can measure the laser power dependence of the excitation signal and fit the obtained curve to a model based on Equation 3.31. The following section describes the measurement of these fluence curves and develops the machinery for their quantitative analysis. I note here, for completeness, that Fan *et al.* have derived[15] expressions for the laser fluence dependence for incoherent IR pumping based on a rate equation approach.

3.4.3.1 Fluence curves

Figure 3.13 provides a schematic drawing of the setup used for recording the laser fluence dependence of the BILT signal. The BILT signal is generated, as previously outlined, by chopping the tagging laser beam and lock-in amplification of the bolometer signal. A laser power meter (Model Solo-PE, gentec) monitors the laser power P_{exit} that exits the scattering apparatus after exciting the scattered molecules and the data is transferred to the main data acquisition computer. The OPO idler beam, which is initially horizontally polarized, passes a rotatable half-waveplate and then a polarizing beam splitter that transmits the horizontal polarization. Rotation of the $\lambda/2$-plate is actuated by a computer-controlled stepper motor. 90° rotation of the plane of polarization is achieved by 45° rotation of the waveplate.

During this PhD work, I automated the acquisition of the fluence curve measurement. The procedure, which is carried out by the custom LabVIEW^{TM} program, consists of the following steps:

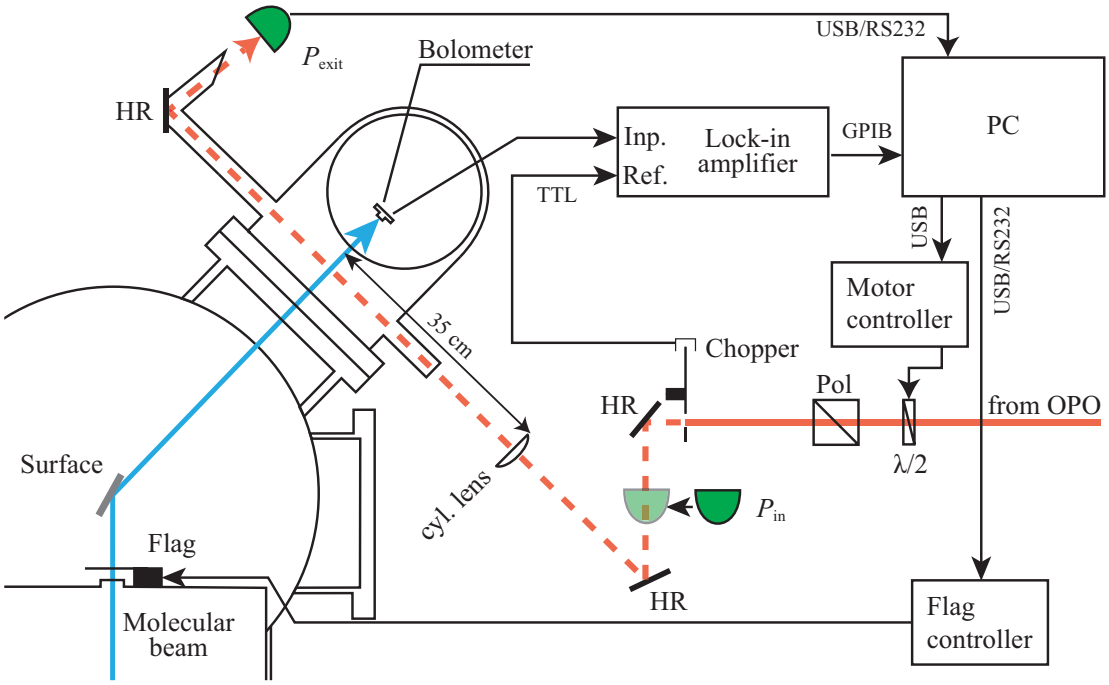

Figure 3.13 Schematic of the setup for recording laser fluence curves of the BILT signal.

1. a tagging trace similar to the one in Figure 3.7 is recorded. The beam flag is closed automatically after a specified integration time (typically 30 s).

2. After both, flag-on and flag-off signal have been determined, the program sends commands to reopen the flag and rotate the waveplate to the next angle, usually in steps of 5°. After a short waiting time the next tagging trace is recorded, an so on.

3. After the last measurement, a second power meter (Scientech) determines the peak laser power that enters the machine P_{in}. Here, the chopper is stopped in the open position and the waveplate rotated to leave the polarization unchanged.

Subsequently, I analyzed the obtained power-dependent tagging traces using a custom analysis script written in Python. The asymptote of the fluence curve towards high laser power is directly proportional to the population of the lower level if the upper level was initially empty. If the fluence curve exhibits saturation at the highest laser powers, *i.e.* the asymptote is reached, then S_{tag} at the highest power can be used directly to characterize the population of the lower level. In all other cases, the asymptote must be determined through a fit to the data. I note in passing that the population can also be determined from the initial slope of the fluence curve with knowledge of the transition dipole moment.

If only one M_J of the lower and upper tagging levels participate in the transition, as

Table 3.1 Analytical expressions for the Hönl-London factors in Equation 3.43.

Branch	Expression
R	$\lvert\langle JM, 10 \rvert (J+1)M\rangle\rvert^2 = \dfrac{(J-M+1)(J+M+1)}{(2J+1)(J+1)}$
Q	$\lvert\langle JM, 10 \rvert JM\rangle\rvert^2 = \dfrac{M^2}{J(J+1)}$
P	$\lvert\langle JM, 10 \rvert (J-1)M\rangle\rvert^2 = \dfrac{(J-M)(J+M)}{J(2J+1)}$

it is the case for the $R(0)$ transition, the Landau-Zener formula Equation 3.31 may be used as a model function to fit the experimental fluence curve,

$$S_{\text{tag}}(P) = A\left(1 - \exp^{-cP}\right), \tag{3.42}$$

which yields a function with two adjustable parameters, A and c, where A corresponds to the asymptotic BILT signal.

In general, however, we do not have a two level system. Instead, transitions occur between multiple degenerate M_J levels, which have different Rabi frequencies. This becomes evident when inspecting the dependence of the transition dipole moment on the M_J quantum number, which is given[10] by

$$\mu_{12} = \langle J_1 M_1, 10 | J_2 M_2 \rangle \sqrt{\frac{3\varepsilon_0 hc^3}{2\omega_{12}^3} A_{21}}\,, \tag{3.43}$$

where $\langle J_1 M_1, 10 | J_2 M_2 \rangle$ is a Clebsch-Gordan coefficient for a transition between two levels with rotational quantum numbers (J_1, M_1) and (J_2, M_2), respectively, induced by linearly polarized light. The Clebsch-Gordan coefficient in Equation 3.43 governs the M_J-level selection rules of the rovibrational transitions (see also section 3.5). The main selection rule reads $\Delta M = 0$ and additionally $M = 0 \nleftrightarrow M = 0$ for Q-branch transitions ($\Delta J = 0$). In the following we drop the subscript for the M_J quantum numbers for brevity. The analytical expressions for the square of the Clebsch-Gordan coefficient in Equation 3.43 (Hönl-London factors) are summarized in Table 3.1.

By combining Equations (3.43) and (3.27) and inserting into Equation 3.31, we find the M level dependent excitation probability as a function of laser power. Assuming that the population of the J_1 level is equally distributed over all M_1 levels, we can express the

overall fluence dependence as a sum over all allowed ($M_1 \leftrightarrow M_2$) transitions,

$$S_{\text{tag}}(P) = \frac{A}{g_1} \sum_{M=-J_1}^{J_1} \left[1 - \exp\left(-a|C(J_1, M, J_2)|^2 P \right) \right], \tag{3.44}$$

where $C(J_1, M, J_2)$ is the Clebsch-Gordan coefficient,

$$C(J_1, M, J_2) = \langle J_1 M, 10 | J_2 M \rangle \,, \tag{3.45}$$

and $g_1 = 2J + 1$ is the degeneracy of the lower J level. M_J takes the values $-J_1, -J_1 + 1, \ldots, J$. It is worth noting that the adjustable parameter a is proportional to A_{21}.

Figure 3.14 shows four fluences curves measured for different transitions of the $2\nu_3 \leftarrow \nu_3$ hot-band, which are the subject of chapter 4. Solid lines represent non-linear fits, where Equation 3.44 was used as fit function. As we can see, the M_J-averaged Landau-Zener formula can describe the experimental fluence data reasonably well. It is at this point instructive to discuss the different shapes of the curves in Figure 3.14.

In general, R-branch transitions are, for a given Einstein coefficient and J-level, more readily saturated than their Q-branch counterparts. Also, their curvature behaves differently as the laser power increases. For Q-branch transitions, the initial slope is rather steep but then drops rapidly. These characteristics can be understood by inspection of the Clebsch-Gordan coefficients. Figure 3.15 displays the absolute square of the coefficients as a function of J and M_J for Q-branch and R-branch transitions, respectively. We see that for the Q-branch these values, which determine the transition probabilities, exhibit a larger spread between 0 and 1 for a given J level. The M_J levels with a large coefficient contribute most to the initial slope and saturate first, whereas those levels with very low coefficients (towards lower M_J) can usually not be fully saturated. They are responsible for the non-asymptotic behavior even at the highest laser powers. In the case of R-branch transitions, the coefficients vary by not more than a factor of three among different M_J levels and hence the slope of the fluence curve changes more smoothly and asymptotic behavior is more easily reached at high laser powers compared to Q-branch transitions.

In order to enable proper fitting of the experimental fluence curves, a good power calibration is necessary. This is particularly true for the low-power regime where the slopes of the fluence curves are steep. While one could fit the fluence dependence of the tagging signal directly as a function of either of these power data sets, their use brings some problems at low laser powers because power meters often acquire changing non-zero offsets throughout the day. This leads to aberrations at low laser powers where the excitation efficiency is strongly dependent on power. The problem can be avoided by

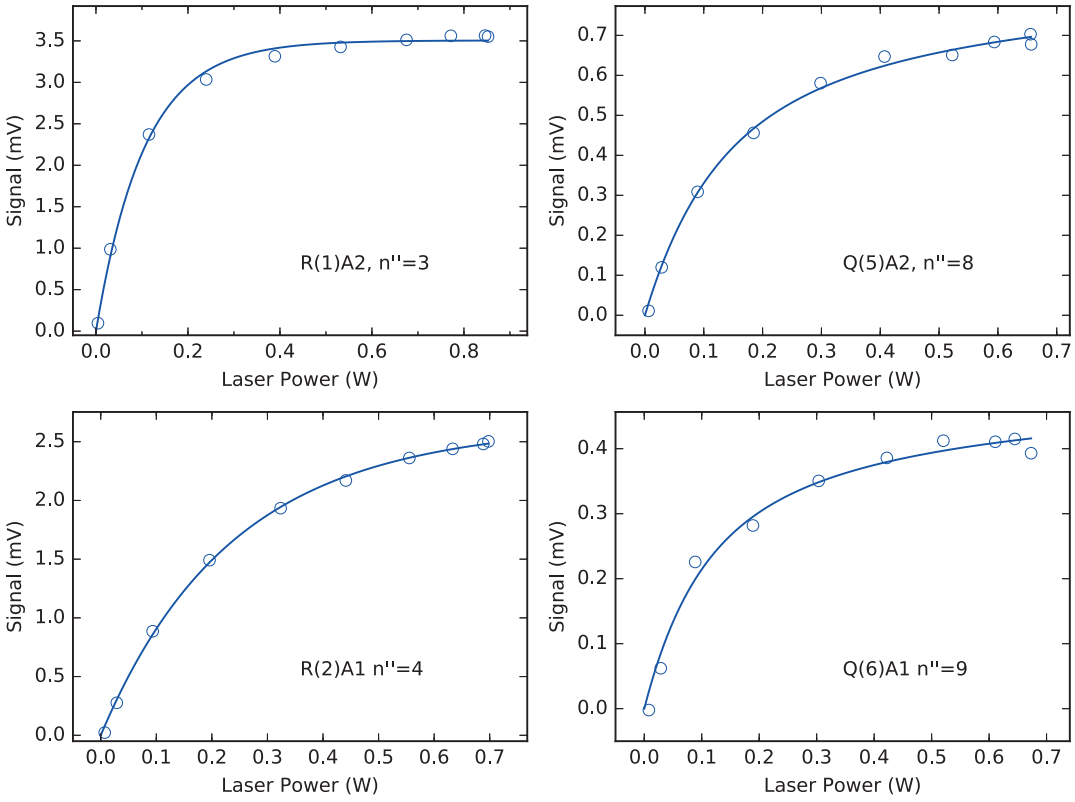

Figure 3.14 Fluence curves for different $2\nu_3 \leftarrow \nu_3$ transitions for scattered CH_4 illustrating RAP fluence curve fitting. The fits to the data points using Equation 3.44 are shown as solid lines.

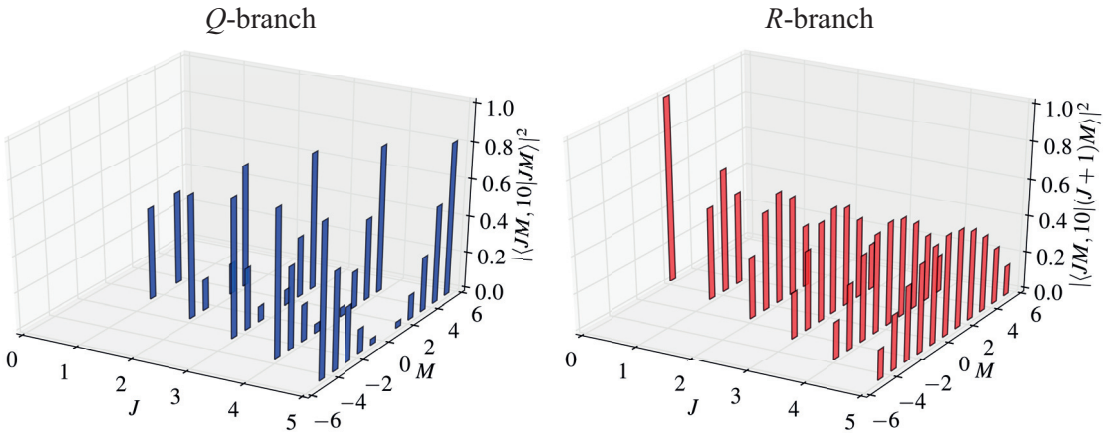

Figure 3.15 Hönl-London factors defined in Table 3.1 for Q-branch (top left panel) and R-branch (top right panel) transitions, respectively.

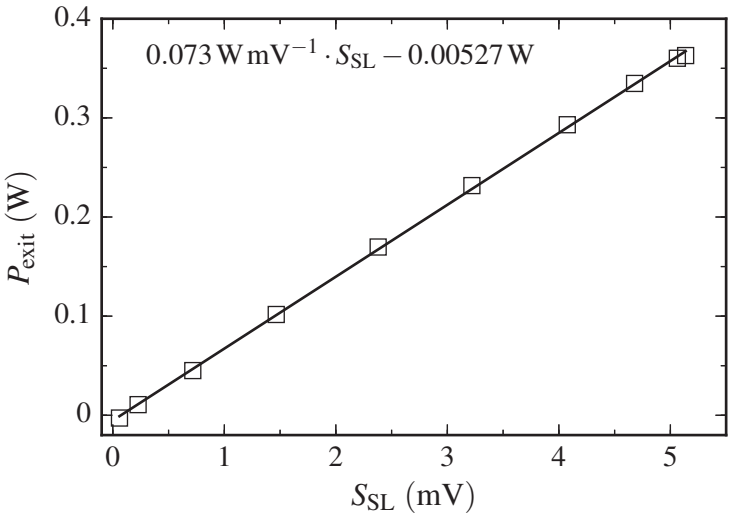

Figure 3.16 Bolometer signal corresponding only to scattered light as a function of laser power exiting the apparatus. The solid line is a linear fit to the data.

using the bolometer signal when the beam flag is closed as a measure for the power. We can assume that, without the molecular beam striking the detector, the bolometer signal S_{SL} is strictly proportional to the laser power P if the fraction of scattered light does not change, that is,

$$S_{SL} = a_{SL} P \,, \tag{3.46}$$

where a_{SL} is a constant for a given wavelength of the laser. Most importantly, the bolometer signal has no offset. We now perform the following power calibration procedure: First, we obtain a linear fit of the measured P_{exit} as a function of S_{SL},

$$P_{exit}(S_{SL}) = a_{SL}^{-1} \cdot S_{SL} + P_{offset} \,, \tag{3.47}$$

where P_{offset} is the power meter offset. Such a fit is presented in Figure 3.16, which also illustrates the linearity of the scattered light signal with laser power. The power for each angle is obtained by re-evaluating Equation 3.47 using the fitted parameter a_{SL}^{-1} but setting P_0 equal to zero. In this way, the offset of the power meter is removed. As a last step, P is scaled to match the power measured before the beam enters the machine, according to

$$P_{in}(S_{SL}) = \frac{P_{in}^{\alpha}}{P_{exit}^{\alpha}} \cdot a_{SL}^{-1} \cdot S_{SL} \,, \tag{3.48}$$

where the laser powers were measured for a given waveplate angle α, typically the one at which the transmitted power is maximized. Lastly, we plot S_{tag} against P_{in} to obtain the fluence curve.

3.4.4 Polarization considerations

In the previous discussion, I have not considered the effect of angular momentum polarization, *i.e.* alignment and orientation[16–18]. We speak of alignment when the direction of the total angular momentum vector $\vec{J}$ is preferentially along or perpendicular with respect to some reference axis but with equal probabilities in opposite direction (parallel *vs.* anti-parallel). $\vec{J}$ is said to be oriented if it has a preferred absolute direction in space with respect to a reference axis. Therefore, alignment and orientation my be imagined as the preferential directionality of double-headed and single-headed arrows, respectively. Alignment and orientation of the angular momentum $\vec{J}$ are nothing else but anisotropies in the probability distribution of the M_J magnetic quantum number, which, in the vector model describes the projection of M_J onto some reference axis that is fixed in the laboratory frame. A distribution in which all M_J are equally likely to occur is called isotropic and possesses neither alignment nor orientation. If the M_J-level distribution is anisotropic in the absolute values of M_J, we have alignment, and if the average (expectation value) of M_J is non-zero, we have orientation. Note that a system may exhibit alignment and orientation at the same time. Collisions with other molecules or in our case with a surface[19–25], but also optical excitation with polarized light[26,27], can align and/or orient the total angular momentum of molecules in space. While the degree of rotational excitation, that occurs during a collision, provides information about the *magnitude* of the anisotropy of the interaction, alignment and orientation tell us something about the *directionality* of this anisotropy. Owing to the importance of the relative movement and orientation of reactants in the understanding of chemical reactions, an entire branch of chemical dynamics research, known as stereodynamics, is devoted to this subject.

Angular momentum polarization is generally described in terms of multipole moments of the M_J distribution. A discussion of the underlying theory is beyond the scope of this thesis and the interested reader is therefore referred to the literature[16,17,28]. In this thesis work, I have not undertaken attempts to determine the angular momentum polarization of surface-scattered methane. However, we have to keep in mind that such polarization effects may have an impact on our observed infrared absorption signals since we employ polarized lasers, which in general makes the detection sensitive to polarization effects as $\vec{J}$ may exhibit a directional preference with respect to the laser polarization

direction. In other words, if a polarized laser can create an M_J-level anisotropy, then it should also be able to analyze it. In our case, the laser is linearly polarized ($J_{\text{photon}} = 1$, $M_{\text{photon}} = 0$). In the following discussion, we shall drop the J-subscript from the M quantum number. We have seen above, that the transition dipole moment for a one-photon transition between two levels with rotational quantum numbers J'' and J' depends on the angular momentum coupling strengths, which are described by the Clebsch-Gordan coefficient $\langle J''\,M'', J_{\text{photon}}\,M_{\text{photon}}|J'\,M'\rangle$, for which analytical expressions for the three possible branches are given in Table 3.1.

To understand the effect of angular momentum polarization on our absorption measurements, consider Figure 3.15. We see here that the coupling strength and thus the excitation probability strongly depends on the absolute value of M but also on the branch that we excite. Imagine a situation where we are probing an aligned sample carrying excess population in the low-M levels. If the excitation is performed in the linear absorption regime, then Q-branch excitation will underestimate the total population in the given J-level because it is more sensitive to the (less populated) levels with large M. Conversely, probing *via* the R-branch will overestimate the total population for the reversed reason. For completeness, we note that the P-branch excitation probabilities behave very similarly compared to those of the R-branch. If the laser polarization changes, the M-levels will go over into specific linear combinations of each other, giving a different M-distribution, which can again be probed. One can extract the alignment or orientation moments[(b)] from the difference in absorption between the two different polarization directions using Fano-Macek theory[16,28,29]. For example, Perkins and Nesbitt have used this approach to investigate the stereodynamics of CO_2 scattering from a liquid surface (perfluoropolyether, PFPE)[30,31].

In our BILT measurements, the effect of the aforementioned M-sensitivity on the absorption coefficient is greatly reduced because we use sufficiently high laser fluence to saturate most transitions. Thereby, we excite all population irrespective of M-level as long as the coupling coefficients are large enough to allow saturation of all $J', M' \leftarrow J''\,M''$ transitions. For high-J transitions, which have small coupling coefficients for some M-levels, we cannot assume full saturation. In this case, we will use the fluence curve analysis outlined above. However, I have assumed an isotropic M-level distribution to derive the fitting function Equation 3.44. If there was excess population in those M-levels that are difficult to excite, the fit might yield an asymptote that underestimates the

[(b)] Note that using one-photon absorption and linearly polarized radiation, only the first alignment (even) moment $A^{(2)}_{\pm q}(J)$ may be probed, while with circularly polarized light only the first orientation (odd) moment $A^{(1)}_{\pm q}(J)$ is accessible[17].

total J population because mostly the remaining, easier to excite, levels were taken into account in the fit.

An additional bias can be introduced when P- or Q-branch excitation is used. It comes from the M-level selection rules, which stipulate that the M-levels with the values $M = |J|$ and $M = 0$, respectively, cannot be excited with linearly polarized light. For a Q-branch transition, this means that if the population in $M = 0$ is higher (lower) than the M-averaged population, we would measure a lower (higher) absorption signal than if we had excited all M-levels. By contrast, if R-branch transitions are used and if saturation is complete, the measured S_{tag} accurately reflects the total J level population because all M_J level are addressed by the tagging laser. We typically correct the BILT signal for the $M = 0$ population that is missed by Q-branch excitation using

$$P_{J''}^{\mathrm{corr}} = \frac{2J''+1}{2J''} S_{Q,J''} \tag{3.49}$$

where S_Q is the BILT signal for Q-branch excitation. We can calculate the error due to excess population in $M = 0$ as

$$\frac{P_{Q,J''}^{\mathrm{corr}} - P_{R,J''}}{P_{R,J''}} = \frac{\langle p_M \rangle - p_0}{2J'' \langle p_M \rangle} , \tag{3.50}$$

where P_R is the "true" population that we would determine using the R-branch, $\langle p_R \rangle$ is the average population calculated over all M-levels, and p_0 is the population in $M = 0$. We can see here that the error is proportional to the difference between the average M-level population $\langle p_M \rangle$ and that of the $M = 0$ level, and that it furthermore decreases with J.

I will complete this discussion by considering the effect of hyperfine depolarization. Hyperfine depolarization leads to a time-dependent loss of an initial polarization $A_q^{(k)}(J;t=0)$[32]. The origin of this effect lies in unresolved hyperfine structure. The fine structure is due to a coupling of $\vec{J}$ with the total nuclear spin $\vec{I}$ to form a resultant $\vec{F}$ about which $\vec{J}$ precesses (see Refs. [16, 32] and[8] for details). As I will discuss in more detail below, the four hydrogen atoms in CH_4 carry a nuclear spin of $I_{\mathrm{H}} = 1/2$, which can couple to give a non-zero total nuclear spin I. In this work, I have performed scattering experiments on *meta*-methane, which has $I = 2$. The time-dependence of an alignment parameter is given[32] by

$$A_q^{(k)}(J;t) = G^{(k)}(t)\, A_q^{(k)}(J;t=0) , \tag{3.51}$$

with the depolarization coefficient

$$G^{(k)}(t) = \sum_{F,F'} \frac{(2F'+1)(2F+1)}{(2I+1)} \begin{Bmatrix} F' & F & k \\ J & J & I \end{Bmatrix}^2 \cdot \cos\left[(E_{F'} - E_F)\, t/\hbar\,,\right] \tag{3.52}$$

where the summation is carried out over all pairs of F-levels with $F = I + J, I + J - 1, \ldots, |I - J|$ and where the element in curly brackets is a Wigner-6j symbol. Therefore, depolarization leads to a decrease in the alignment on a timescale defined by

$$\frac{1}{\tau} = |E'_F - E_F|/\hbar\,. \tag{3.53}$$

Yoder has shown[8] that the depolarization occurs on a timescale of $\sim 15\,\mu s$ for methane in agreement with the hyperfine splittings of $50 - 100\,MHz$, which have been measured[33] by Hall and Bordé. In the absence of stray magnetic fields, however, the alignment will "rephase" periodically (quantum beats). In our experiments, an aligned ensemble of molecules may be created in the surface collision but, since the molecular beam is continuous, molecules arrive at the tagging laser with random "depolarization phase". We therefore have to use the time-averaged form of Equation 3.52, which reads

$$\langle G^{(k)} \rangle_t = \frac{1}{(2I+1)} \sum_F (2F+1) \begin{Bmatrix} F & F & k \\ J & J & I \end{Bmatrix}^2 . \tag{3.54}$$

Figure 3.17 displays the J-dependence of the time-averaged depolarization coefficient for the first even polarization moment, $\langle G^{(2)} \rangle_t$ which our experiment is in principle sensitive to. We see that for large J (compared to I), initial alignment is approximately conserved. This can be explained by the almost parallel orientation of F along J and the resultingly weak coupling to I. For low J values, however, depolarization is strong and leads to a significant reduction of alignment. Note that $G^{(k)}$ is equal to zero for $J = 0$ since neither alignment nor orientation can exist for this state.

To summarize this discussion, we have seen that BILT detection *via* R-branch excitation under saturating conditions directly yields a signal that is a measure of the total population of a rotational state with quantum number J. When we tag by exciting the Q-branch, we have to correct for the missing $M = 0$ population, which introduces an error that scales inversely proportional with J. At low J, where this error might be large, we do not expect a strong deviation of the $M = 0$ population from the M-averaged value, because hyperfine depolarization helps to reduce any alignment. Lastly, it should be mentioned that van Reijzen has found[3] no significant differences in the $v = 0 \rightarrow v = 0$

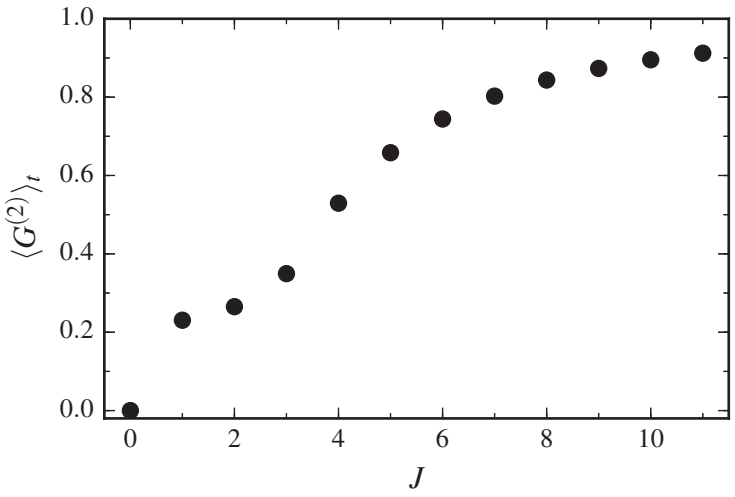

Figure 3.17 J-dependence of the time-averaged hyperfine depolarization coefficient for $I = 2$.

scattering rotational distributions derived from R- and Q-branch excitation for CH_4 scattering from Ni(111) at an incidence energy of 100 meV. This indicates that alignment of the CH_4 rotational angular momentum, at least for this low collision energy, does not play a role.

3.4.5 FM spectroscopy

Figure 3.18 shows a spectral scan of the Q-branch of the ν_3 fundamental. We recorded the spectrum by monitoring the bolometer signal while scanning the frequency of the OPO. The incident molecular beam was neat CH_4 ($p_{\text{stag}} = 3\,\text{bar}$, $T_{\text{Nozzle}} = 300\,\text{K}$), which was scattered from Ni(111) at $T_S = 673\,\text{K}$ and detected under an angle $\theta_f = 67°$.

The spectrum illustrates the exceptional spectral resolution and signal-to-noise ratio that our BILT spectrometer can achieve. However, for such wide scans (when compared to the laser linewidth of $\sim 1\,\text{MHz}$), laser intensity variations give rise to a changing base-line when the tagging laser is amplitude modulated (AM) since the amount of scattered light changes as well. Another problem are the extremely narrow linewidths of the transitions $\geq 2.5\,\text{MHz}$ and of the laser. In order to avoid strong signal attenuation due to the slow time response of the detector, the laser frequency must be scanned very slowly, which means that many hours of recording are necessary to obtain a spectrum such as the one shown in Figure 3.18. For instance, a scan rate of $2\,\text{MHz/s}$ corresponds to $0.24\,\text{cm}^{-1}/\text{h}$!

We can remove the signal response toward changes in laser intensity and increase

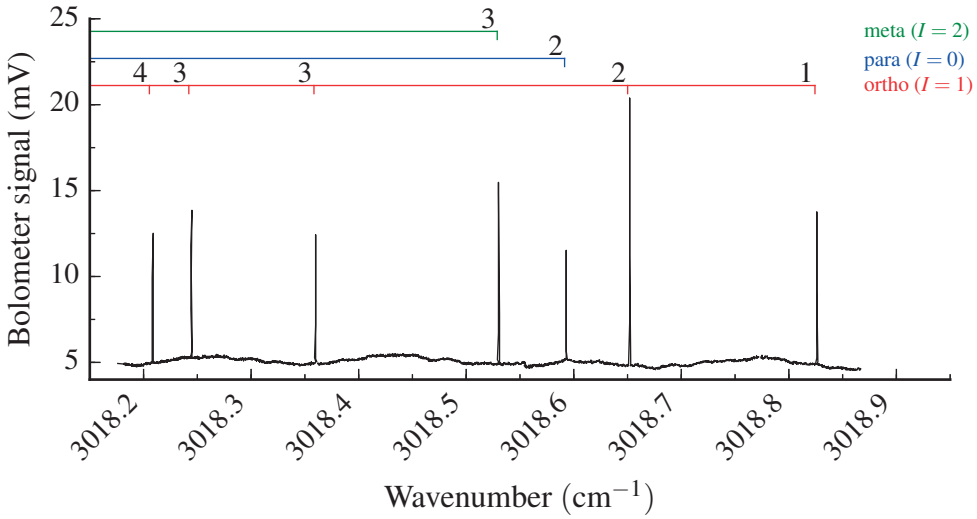

Figure 3.18 Spectral scan of the Q-branch of methane's ν_3 fundamental vibrational band using BILT detection with a chopped laser.

the scan rate by applying frequency modulation (FM) rather than amplitude modulation of our laser. Here, the lock-in effectively determines the signal difference between on- and off-resonance instead of the difference between the laser being on and off. A schematic of the laser control and data acquisition setup for FM spectroscopy is shown in Figure 3.19. In this setup, the local oscillator of the lock-in amplifier serves as the master oscillator. A sine waveform with an RMS value of $\geq 4\,\mathrm{mV}$ is produced by the lock-in at the modulation frequency f_{mod}, which has to be within the bandwidth of the bolometer. The modulation is added to a voltage ramp and a constant offset voltage by a home-built summing amplifier. The ramp rate is controlled by the transfer cavity and serves to scan the center frequency of the laser with high precision. The cavity data acquisition is synchronized with the master oscillator by triggering to a TTL synchronization pulse train from the lock-in amplifier. The modulated voltage ramp is applied to the frequency-tuning piezo of the OPO seed laser.

Figure 3.20 displays a scan of the ν_3 Q-branch similar to Figure 3.18 but this time recorded using FM spectroscopy. The peaks now have a derivative shape, as it is know for instance from Auger electron spectroscopy, where a similar technique is used. The modulation frequency was 240 Hz, the modulation amplitude $150\,\mathrm{mV_{RMS}}$ and the scan rate was $10\,\mathrm{MHz/s}$. The lock-in time constant of 300 ms caused only small skew of the absorption line profile under these conditions (see magnification in Figure 3.21). The scan was assembled from 12 individual scans as the ramp voltage supplied by the data acquisition card is limited to $+10$–$(-10)\,\mathrm{V}$ and thus needs to be reset from time to time

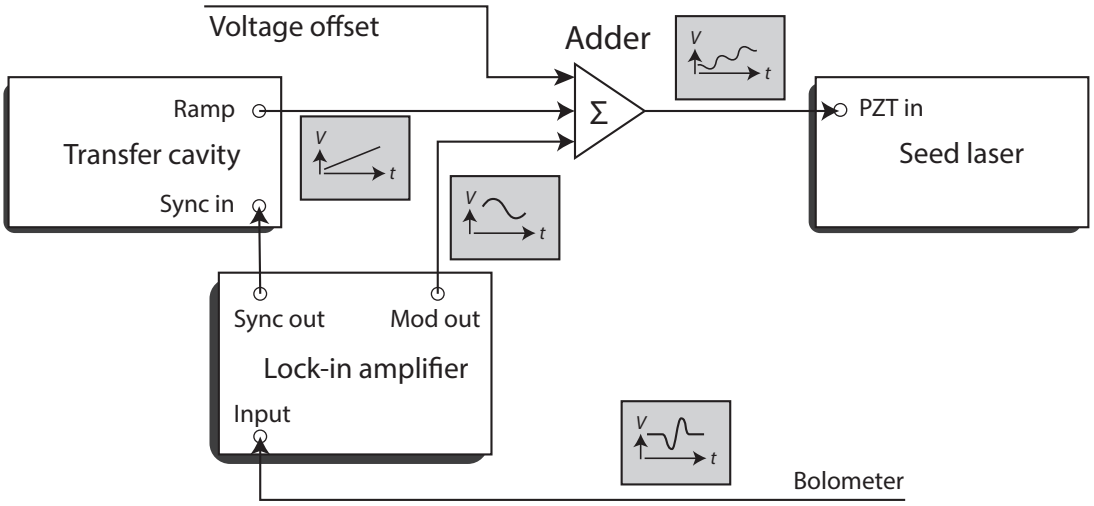

Figure 3.19 Experimental setup for frequency modulated spectroscopy.

by adjusting the voltage offset. The wavemeter recorded the absolute wavelength while scanning. To reach the desired accuracy of the horizontal axis, I fitted the wavemeter output with a linear function (linearity is guaranteed by the cavity scanning) and used the fit as wavenumber axis. I also subtracted a constant offset from the wavemeter reading by referencing the measured $Q(1)$ lineposition to the value given in the HITRAN database. The remaining linepositions indicated by the comb were directly taken from HITRAN. Note that the signal-to-noise ratio for the tallest peak ($Q(2)\mathrm{F}_2$) is about 310. Frequency modulation allows faster scan speeds because it effectively broadens the laser linewidth, thereby increasing the time during which the laser in resonance with the transition. Furthermore, the varying baseline is eliminated.

To understand the derivative lineshape, we image our setup as a system that responds to an excitation ϵ with a voltage output $U(\epsilon)$. If the excitation is modulated according to

$$\epsilon(t) = \langle\epsilon\rangle + A_{\mathrm{mod}} \sin(\omega_{\mathrm{mod}} t)\,, \tag{3.55}$$

where $\langle\epsilon\rangle$ is some average value, the system will yield a time-dependent response $U(\epsilon(t))$. This response is not necessarily of the same functional form as the sine-wave that caused the excitation. However, for a sufficiently small modulation amplitude A_{mod}, we may approximate the response by expanding $U(\epsilon(t))$ into a Taylor expansion and neglect all but the first two terms,

$$U(t) \approx U(\langle\epsilon\rangle) + \left.\frac{\mathrm{d}U}{\mathrm{d}\epsilon}\right|_{\langle\epsilon\rangle} A_{\mathrm{mod}} \sin(\omega_{\mathrm{mod}} t)\,. \tag{3.56}$$

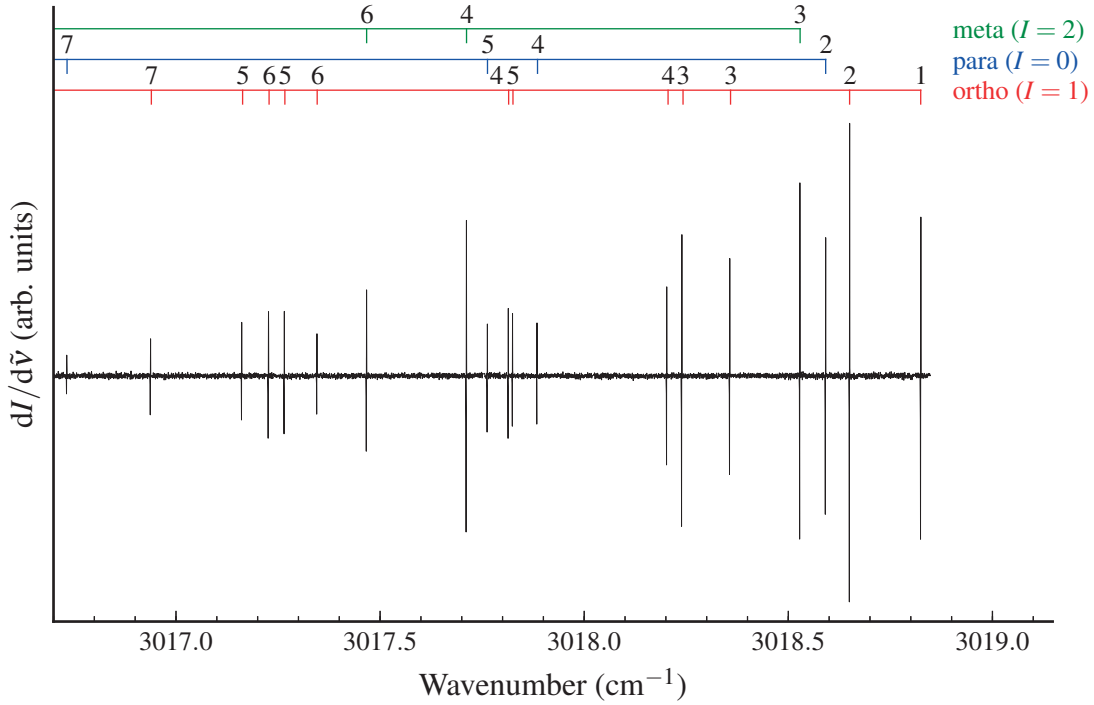

Figure 3.20 Scan of the low-J portion of the Q-branch of the ν_3 fundamental transition detected in a molecular beam of CH_4 after scattering from a Ni(111) surface. The peaks have derivative shape because the scan was carried out using frequency modulation of the tagging laser. The comb indicates the lower rotational level J''.

When this signal is phase-sensitively detected by a lock-in amplifier, the first term, which is a constant, is removed. The lock-in returns the RMS value of the first harmonic of the Fourier component at the modulation,

$$\text{Signal}_{\langle\epsilon\rangle} \approx \frac{A_{\text{mod}}}{\sqrt{2}} \left.\frac{\mathrm{d}U}{\mathrm{d}\epsilon}\right|_{\langle\epsilon\rangle}, \tag{3.57}$$

which is proportional to the derivative with respect to the excitation, in our case the absorption of laser light as a function of the laser frequency. Such a derivative spectrum is also called dispersion spectrum as the imaginary part of the refractive index (related to absorption) and its real part (related to dispersion) are linked by the Kramers-Kronig relations.

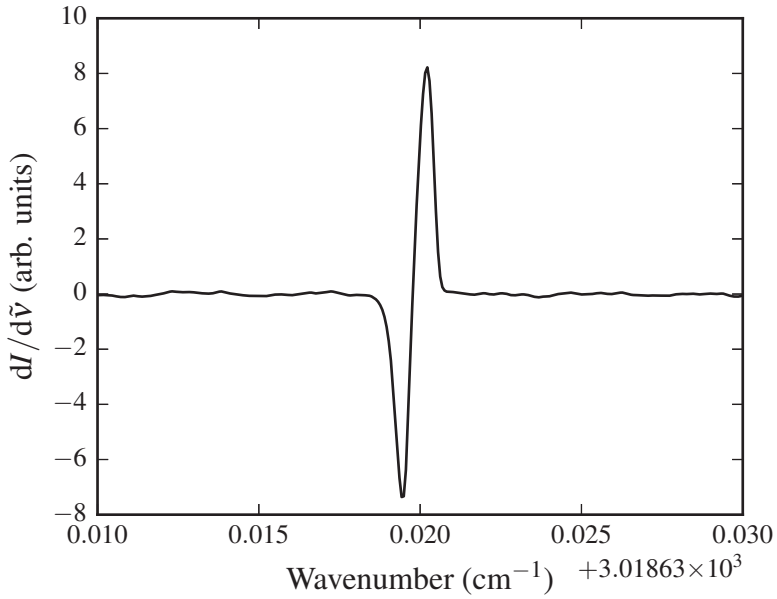

Figure 3.21 Magnified view of the Q(2)F_2 peak from Figure 3.20.

3.5 Infrared spectroscopy of CH_4

This thesis presents experimental results on the quantum-state-resolved scattering of methane from surfaces. This involves the excitation of rovibrational transitions in the infrared spectral region using lasers with very a narrow linewidth of 1 MHz. An in-depth knowledge of methane's high-resolution IR spectroscopy is thus indispensable for understanding the realization of the experiments as well as the results. Due to its wide interest in environmental science, atmospheric chemistry, astrophysics and other sciences, the microwave and infrared spectroscopy of CH_4 has been studied in great detail, see Ref. [34] and references therein. The HITRAN spectroscopic database lists more than 300 000 transitions in its latest version only for the $^{12}CH_4$ isotopologue of methane[13].

In this section, I will present the basic spectroscopic properties of CH_4 and then give a detailed account of its relevant infrared spectroscopic features. That is, the structure of rotational-vibrational (or rovibrational) transitions within the electronic ground state taking into account the fine structure that is resolved by our lasers. This excludes the hyperfine structure caused by the interaction of the nuclear spin with the molecular rotation since the corresponding line splittings are on the order of 50 – 100 kHz and thus remain unresolved[33]. However, the presence of nuclear spin in the hydrogen atoms of methane has an important effect on the rotational structure because of symmetry restrictions, which I will also discuss. This section is mostly based on the the books by Herzberg[35] and di Lauro[36] and the Ph.D. thesis of Niederer[37], which all provide excellent sources of reference. Since molecular symmetry is at the heart of methane's spectroscopic properties, the following sections rely on group theory. The reader is referred to the literature[38,39] for further information on the underlying mathematical concepts and advanced applications of group theory.

3.5.1 Structure and spectroscopic properties of CH_4

The methane molecules consist of a carbon atom at its center which is surrounded by four hydrogen atoms in a tetrahedral geometry, which means that the angle between each pair of H atoms is 109.5°. Methane's molecular mass is 16.04 u. As a tetrahedral molecule, the structure of CH_4 exhibits high symmetry. Its symmetry properties can be described by the point group T_d, which contains five irreducible representations Γ, two of which are non-degenerate, one is two-fold and two are three-fold degenerate. The character table for the T_d point group is shown in Table 3.2. The symmetry elements that form the basis for the group comprise four C_3 axes, three C_2 axes, and six σ_d mirror planes.

Table 3.2 Character table for the point group T_d. The irreducible representation E is two dimensional, whereas F_1 and F_2 are three dimensional. R and T denote the irreducible representations of the rotational and translational degrees of freedom, respectively.

$\Gamma(T_d)$	E	$8C_3$	$3C_2$	$6S_4$	$6\sigma_d$		
A_1	1	1	1	1	1		$\alpha_{xx}+\alpha_{yy}+\alpha zz$
A_2	1	1	1	−1	−1		
E	2	−1	2	0	0		$(\alpha_{xx}+\alpha_{yy}-2\alpha_{zz},\ \alpha_{xx}-\alpha_{yy})$
F_1	3	0	−1	1	−1	R	
F_2	3	0	−1	−1	1	T	$(\alpha_{xy},\alpha_{yz},\alpha_{zx})$

Due to its symmetry, methane's principal moments of inertia are equal ($I_a = I_b = I_c$) making it a spherical top. In the rigid rotor approximation, its rotational energy levels are given by the simple formula

$$E_{rot}(J) = B_v J(J+1)\,, \tag{3.58}$$

where J is the rotational quantum number that can take the values $J = 0, 1, 2, \ldots$, and where B_v is the rotational constant in the vibrational state v. For the vibrational ground state $v = 0$, the rotational constant[40] has the value $B_0 = 5.241035\ \mathrm{cm}^{-1}$. Within the rigid rotor approximation, each rotational level has a $(2J+1)^2$-fold degeneracy as there are $(2J+1)$ possible projections of the angular momentum vector with respect to an arbitrary reference axis in the molecular frame that corresponds to the K quantum number in a symmetric top. The remaining factor of $(2J+1)$ comes from the number of possible projections of the the angular momentum in the laboratory frame (space degeneracy) corresponding to the M_J quantum number and the fact that the molecule fixed reference axis can be chosen to coincide with the laboratory fixed axis. However, as I will discuss shortly, this picture is oversimplified as the $(2J+1)$ K levels are not exactly degenerate and the presence of the hydrogens nuclear spins gives rise to a more complicated situation. It is however always true that for a given J there is a total number of $(2J+1)$ sublevels and each of these sublevels is $(2J+1)$-fold degenerate due to space degeneracy since the latter can only be lifted in the presence of an external field. Before going into the finer details of the rotational structure and the discussion of nuclear spin statistics, I will summarize the vibrational mode structure for CH_4.

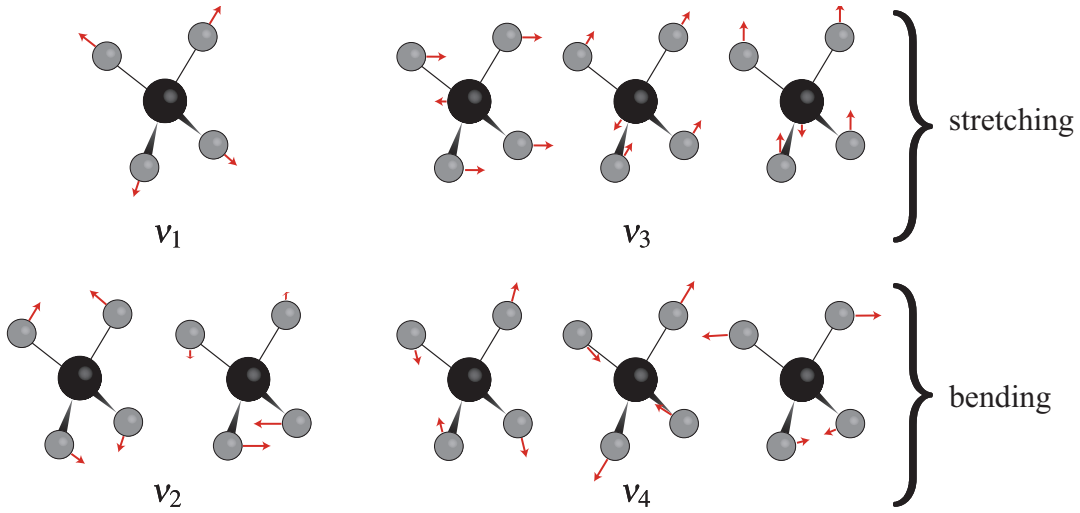

Figure 3.22 Visualization of the vibrational normal modes of CH_4 according to Herzberg[35].

3.5.2 Vibrational normal modes and polyads

Non-linear molecules posses $3N-6$ vibrational degrees of freedom. Due to its high symmetry, many of the vibrational degrees are mutually degenerate so that only four out of nine have distinct vibrational frequencies. Representations of the four normal modes of CH_4 are shown in Figure 3.22. The ν_1 mode is a symmetric C-H-stretching vibration with A_1 symmetry, the ν_2 mode is a doubly degenerate bending vibration of E symmetry, and the ν_3 and ν_4 modes are two triply degenerate anti-symmetric C-H-stretching and bending vibrations, respectively. Both ν_3 and ν_4 have F_2 symmetry. Table 3.3 summarizes the symmetries and frequencies of the four fundamental vibrations corresponding to the normal modes. The quoted term values are those of the $(v_k = 1, J = 0)$ levels, that is the rotational level J of CH_4 excited with one quantum of vibrational energy in the mode ν_k. In the zero-order picture, which assumes that any vibration can be represented by a product basis of harmonic oscillator functions, any vibrational state rigorously belongs to a set of vibrational quantum numbers (v_1, v_2, v_3, v_4) given by the number of vibrational quanta in each normal mode. In reality, the actual vibrational eigenstates that correspond to the full molecular Hamiltonian do generally not coincide exactly with product combinations of normal vibrations due to the presence of anharmonic terms in the intramolecular potential. Instead, the eigenstates are mixtures of the zero-order states. The ν_k are hence to be understood as state labels that refer to the normal modes making the largest contribution to the vibrational character of the eigenstate.

Looking at Table 3.3, one notices that methane's vibrational frequencies satisfy the

Table 3.3 Fundamental vibrations of $^{12}CH_4$ [37].

Level	$\Gamma^{\text{vib}}(T_\text{d})$	Degeneracy	Term value / cm^{-1}
ν_1	A_1	1	2916.481
ν_2	E	2	1533.332
ν_3	F_2	3	3019.493
ν_4	F_2	3	1310.761

approximate relation

$$\nu_1 \approx 2\nu_2 \approx \nu_3 \approx 2\nu_4 \approx 3000\,\text{cm}^{-1}\ . \tag{3.59}$$

This leads to a clustering of the excited overtone and combination states every $\approx 1500\,\text{cm}^{-1}$ resulting in close-lying vibrational bands, the polyads. The polyad scheme for the first five polyads is shown in Figure 3.23. Polyads are labeled with P_n where

$$n = (\nu_1, \nu_2, \nu_3, \nu_4) \cdot (2, 1, 2, 1)^T\ . \tag{3.60}$$

The name of a polyad is derived from the greek prefix corresponding to the value of n followed by -ad. The congestion of vibrational states into polyads has a profound impact on the complexity of methane's vibrational spectrum. When going to higher vibrational energy, the density of states rapidly increases, leading to a strong mixing of the close-lying levels. The spectral congestion poses a great challenge in the assignment and theoretical modeling of the IR spectrum[34]. Due to the high molecular symmetry and the resulting degenerate vibrations, the number of vibrational sublevels increases very rapidly with the polyad number. While there are only nine sublevels for the pentad (P_2), the heptacontad P_9 contains already 1746 sublevels. The vibrational symmetry species of an overtone or combination band can be found by calculating the direct product of the irreproducible representations of the vibrations that are involved. This typically yields a representation that can be further reduced to give the vibrational sublevels. For instance, the $\nu_2 + \nu_4$ combination band has two triply degenerate sublevels with F_1 and F_2 symmetry, since

$$\Gamma^{\nu_2+\nu_4} = \Gamma^{\nu_2} \otimes \Gamma^{\nu_4} = E \otimes F_2 = F_1 + F_2. \tag{3.61}$$

Attention must be paid when dealing with overtones of non-degenerate fundamentals which have a lower degeneracy compared to a combination band of two vibrations with the the same species but distinctly different frequencies. The characters of the direct

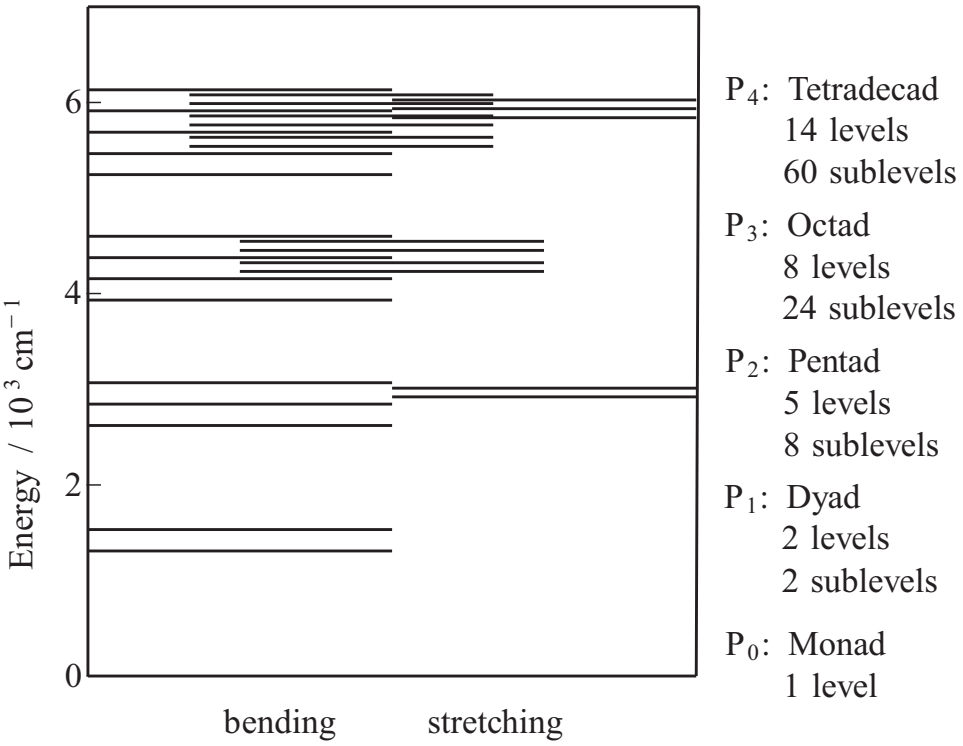

Figure 3.23 Simplified vibrational level scheme of CH_4 from the ground state up to the tetradecad. The levels are positions according to their approximate stretching and bending character. Adapted from Ref. [37].

product are then given by more complicated expressions which can be found in in the common literature, for instance in Ref. [38].

3.5.3 Nuclear spin modifications

The methane molecule contains four equivalent hydrogen nuclei, each of which has a nuclear spin of $I(H) = 1/2$ and therefore fermionic character. These individual spins can be paired in $2^4 = 16$ possible ways, where the total nuclear spin can take the values $I = 2, 1$ or 0. The corresponding nuclear spin wavefunctions are characterized[41] by the symmetry species A, F and E, respectively, in the rotational subgroup T, which contains only the symmetry elements of rotation present in T_d. The species A_1 and A_2 in T_d both belong to the species A in T, E directly corresponds to E, and F_1 and F_2 belong to F in T.

Wilson has shown[41] that the relative occurrences of the three species with A, E, and F symmetry are 5, 1 and 3, respectively. We arrive at a total of 16 spin configurations when we take into account the respective nuclear spin degeneracies of 1, 2, and 3 and sum

the resulting number of nuclear wavefunctions. Since spin state interconversion is known to be an extremely slow process, an ensemble of CH_4 molecules can be considered a composition of three practically independent "types" of CH_4 molecules with nuclear spin symmetries A, E and F. The three spin modifications are called *meta-*, *ortho-*, and *para-*methane, respectively. Table 3.4 compiles the symmetry species, statistical weights and relative abundances for the three spin modifications of CH_4. The relative abundances will be derived further below and apply in the high-temperature limit (equilibrium temperature $T \gtrsim 50$ K).

Table 3.4 Symmetry species, total nuclear spin, spin statistical weight, relative abundance and nomenclature for the spin modifications of CH_4. The relative abundances apply in the high-temperature limit ($T_{\mathrm{spin,rot}} \gtrsim 50$ K)[37].

$\Gamma(T)$	Spin statistical weight	Total nuclear spin	rel. Abundance	Prefix
A	5	2	5/16	*meta-*
E	1	0	2/16	*para-*
F	3	1	9/16	*ortho-*

3.5.4 Allowed rovibrational levels and their statistical weights

Within the Born-Oppenheimer approximation, the total wavefunction ψ_{tot} of a molecular system can be written as the product of an electronic part ψ_{el} and a nuclear motion part ψ_{nuc}. The nuclear wavefunction can be further decomposed into a product of vibrational (ψ_{vib}), rotational (ψ_{rot}) and nuclear spin (ψ_{ns}) contributions under the assumption of a zero-interaction Hamiltonian of nuclear motion, $H_{\mathrm{nuc}} = H_{\mathrm{vib}} + H_{\mathrm{rot}} + H_{\mathrm{ns}}$,

$$\psi_{\mathrm{tot}} = \psi_{\mathrm{el}}\,\psi_{\mathrm{nuc}} = \psi_{\mathrm{el}}\,\psi_{\mathrm{vib}}\,\psi_{\mathrm{rot}}\,\psi_{\mathrm{ns}} \tag{3.62}$$

For a well-defined electronic state, the symmetry species of a rovibrational wavefunction Γ^{rovib} formed by pairing a rotational wavefunction ψ_{rot} with a vibrational wavefunction ψ_{vib} is given by the direct product of their irreducible representations, $\Gamma^{\mathrm{vib}} \otimes \Gamma^{\mathrm{rot}}$. The resulting representation can be decomposed into irreducible representations giving the symmetry species of the rovibrational wavefunction.

The generalized Pauli principle stipulates that the total wavefunction of the molecular system is totally anti-symmetric with respect to the permutation of two equivalent fermionic particles. This imposes a restriction on the way that vibrational, rotational and nuclear spin wavefunction can be combined to form rovibrational wavefunctions. Here, we concern ourselves with rovibrational states within the electronic ground state,

which is totally symmetric. In the following, we therefore only need to consider the nuclear motion part ψ_{nuc}. For a rovibrational wavefunction ψ_{rovib} to comply with the Pauli principle, the product $\Gamma^{\text{rovib}} \otimes \Gamma^{\text{ns}}$ must contain the Pauli-allowed symmetry species, which in the present case are the species A_1 and A_2 [37], corresponding to the totally symmetric species A in the rotational subgroup T. Expressed in symbols, this condition reads

$$\Gamma^{\text{vib}} \otimes \Gamma^{\text{rot}} \otimes \Gamma^{\text{ns}} \supseteq A \, . \tag{3.63}$$

It is immediately clear from Equation 3.63 that not all conceivable rovibrational wavefunctions can exist for each spin modification. Using the multiplication rules of irreducible representations [38], one finds that a rovibrational wavefunction of a given species can only be paired with a spin wavefunction of the same species. For example, A_1 and A_2 symmetric rovibrational levels are Pauli-allowed only if the spin wavefunction has A symmetry. As a consequence, each spin modification has its own set of rovibrational levels and their wavefunctions are of the same symmetry (in the subgroup T) as the nuclear spin wavefunction,

$$\begin{array}{lcl} & A_1, A_2 \longleftrightarrow A & \\ \text{rovibrational symmetry} \qquad & E \longleftrightarrow E & \qquad \text{nuclear spin symmetry} \\ & F_1, F_2 \longleftrightarrow F \, . & \end{array}$$

Figure 3.24 shows the allowed rovibrational states for an A_1 symmetric vibrational state like the ground state ($v = 0$) of CH_4. Taking into account that rovibrational levels with A, E and F symmetry are non-degenerate, two-fold and three-fold degenerate, respectively, the degeneracy of $(2J + 1)$ due to the K degeneracy is recovered. It is obvious, however, that not all spin modifications can posses rotational levels for all values of the total angular momentum quantum number J. Figure 3.24 gives the partitioning of rotational sublevels among the spin modifications for the nine lowest values of J. A similar figure with rotational states up to $J = 12$ can be found in Ref. [35]. Additionally, more than one rotational sublevel can exist for a given J and symmetry. These levels appear degenerate in Figure 3.24 but in reality, high order interaction terms in the molecular Hamiltonian cause resolvable albeit very small splittings of these levels [42].

The statistical weight of a rovibrational level that belongs to a certain symmetry species is obtained by calculating the product $\Gamma^{\text{rovib}} \otimes \Gamma^{\text{ns}}$, subsequent reduction and counting the number of occurrences of the totally symmetric species in the resulting

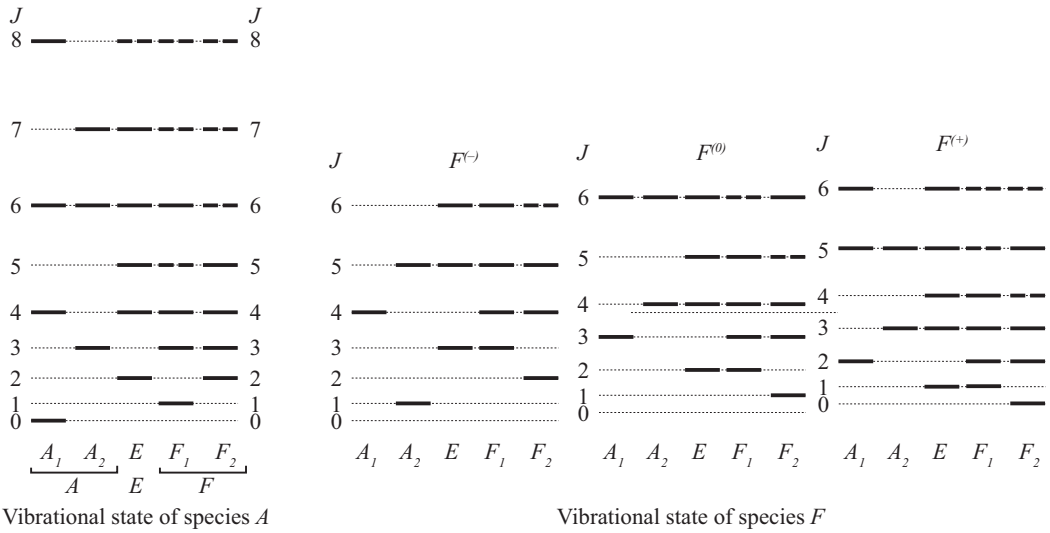

Figure 3.24 Pauli-allowed rotational sublevels of a vibrational states with A_1 (left) and F_2 (right) symmetries, respectively. Shown are the rovibrational symmetry species of the sublevels for each value of the total angular momentum J and the spin modification that they belong to. Each solid line represents an individual rovibrational state. Not all J levels exist for all spin modifications and, for higher values of J, more than one sublevel can exist for a given J and a particular rovibrational symmetry.

representation. Explicitly, we have (in the rotational subgroup T) $A_1 \otimes A_1 = A_1$, $E \otimes E = 2A + E$, and $F \otimes F = A + 2F + E$. There are 5, 1, and 3 spin functions with A, E, and F symmetry, respectively, which we can use to form these products. The statistical weights are thus 5:2:3 for rovibrational levels with A, E, and F symmetry, respectively. This is an important result because the statistical weight gives the relative chance of finding a CH_4 molecule in a rovibrational *sublevel* with a certain symmetry for a given value of J. Closer inspection reveals that the weight of 2 for E symmetry is due to parity degeneracy and not due to nuclear spin degeneracy, which can only be resolved in the presence of an external field[37]. Given the statistical weights of rovibrational levels, we can calculate the relative abundance of methane's spin modifications. In the high-temperature limit, the relative number of rovibrational sublevels with A, E and F symmetry for a given J value converges to 1:1:3. By multiplication with the statistical weights one obtains the relative abundances of $5/16$, $2/16$ and $9/16$, respectively (Table 3.4). At equilibrium temperatures lower than $\approx 50\,\mathrm{K}$, the spin modifications with the lowest available J value become favored. When an ensemble of CH_4 molecules is at equilibrium at a few Kelvin or lower, practically all molecules will be in the $J = 0$ state and therefore belong to the *meta*-modifcation.

3.5.5 Coriolis coupling in F_2 symmetric vibrational states

A further complication arises for methane's F_2 symmetric vibrations due to Coriolis forces that occur in rotating molecules and produce a coupling between mutually degenerate vibrations[35]. The origin of this coupling between vibration and rotation of the molecule lies in the fact that vibrations of polyatomic molecules generally produce a vibrational angular momentum $\boldsymbol{L}$ that can be aligned parallel or anti-parallel to the total angular momentum $\boldsymbol{J}$, thereby reducing or increasing the rotational energy by a few cm^{-1}. According to Jahn's rule[43], Coriolis coupling occurs if the product of the species of the two interacting vibrations contains the species of the rotational degree of freedom. In the scope of this work, Coriolis coupling is important in the case of methane's ν_3 vibration. For the fundamental state ($\nu_3 = 1$), the vibrational angular momentum quantum number takes the value $l = 1$ which causes a splitting of the triply degenerate vibration into three "Coriolis stacks", one of which has the original frequency and is denoted $F^{(0)}$. The other two stacks $F^{(-)}$ and $F^{(+)}$ are lower and higher in frequency, respectively. This is shown on the right hand side of Figure 3.24, which displays the allowed rovibrational states for an F_2 symmetric fundamental vibration. The coupling is called first order because the splitting increases linearly with J. Note that the number of sublevels for a given J value in all stacks combined is $(2l + 1)(2J + 1)$, consistent with the zero order picture, where the K level degeneracy is multiplied with the vibrational degeneracy. For overtones of F_2 symmetric vibrations, when l is larger than one, the Coriolis interaction splits the vibrational level into $2l + 1$ components[36].

3.5.6 IR selection rules

The general selection rule for dipole-induced IR transitions between two vibrational levels requires[38] that the product of the irreducible representations of the initial and final level and that of the dipole operator Γ^{μ} contains the totally symmetric representation,

$$A_1 \in \Gamma_f^{\text{vib}} \otimes \Gamma^{\mu} \otimes \Gamma_i^{\text{vib}} , \tag{3.64}$$

where i and f subscripts denote initial and final states, respectively. The dipole operator transform in the same way as translations $T^{(c)}$, which spans the representation F_2 (Table 3.2). Consequently, only those transitions can be excited by IR radiation for which the product representation $\Gamma_{\text{f}}^{\text{vib}} \otimes \Gamma_{\text{i}}^{\text{vib}}$ contains the F_2 species,

$$F_2 \in \Gamma_f^{\text{vib}} \otimes \Gamma_i^{\text{vib}} . \tag{3.65}$$

[(c)] Translations are denoted here in the same way as the subgroup of rotations T.

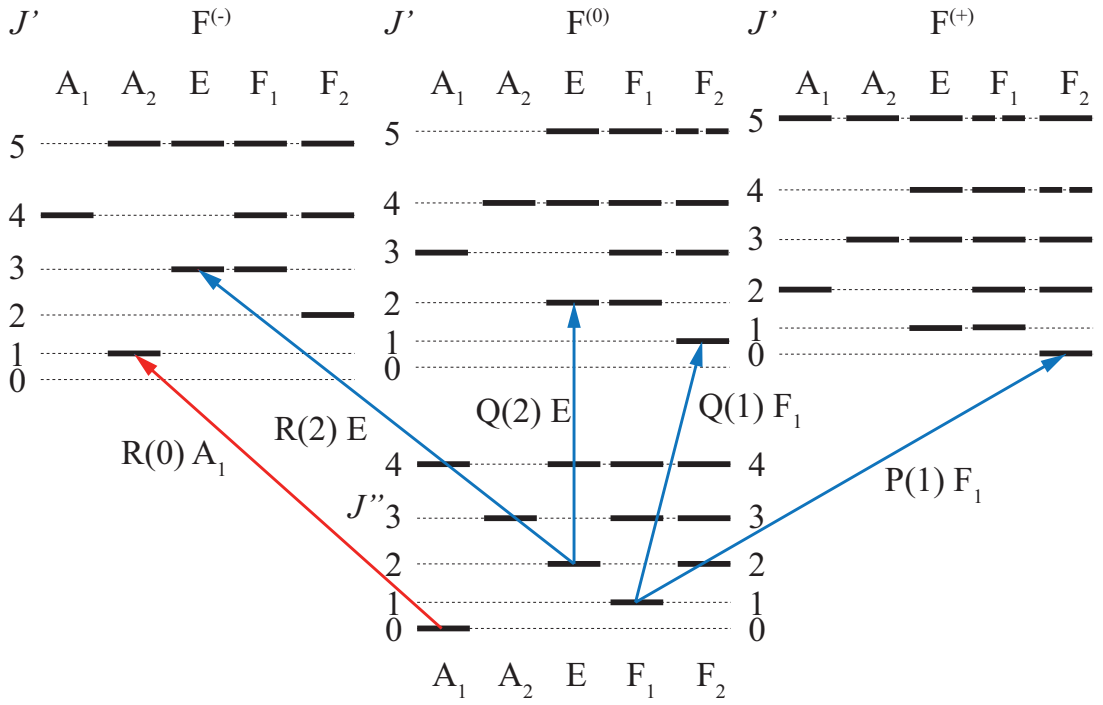

Figure 3.25 IR allowed rovibrational transitions for the ν_3 fundamental. The red arrow highlights the transition that is used to prepare methane in the $(\nu_3, J = 1)$ state. The scattering of a so-prepared methane molecular beam from Ni(111) is described in chapter 4.

For instance, only the ν_3 and ν_4 fundamental transitions are IR allowed for CH_4 since the vibrational ground state is generally totally symmetric (A_1) and $A_1 \otimes \Gamma = \Gamma$.

Rotational selection rules for one-photon transitions restrict changes in the rotational quantum number to

$$\Delta J = J' - J'' = 0, \pm 1 \tag{3.66}$$

meaning that a vibrational band consists of a P-, Q-, and R-branch corresponding to $\Delta J = -1,\ 0, \text{and} + 1$, respectively. Additionally, one finds that for a transition between rovibrational states with symmetries A_1 or A_2 and likewise F_1 or F_2 the index has to change, which in symbolic form ready

$$A_1 \leftrightarrow A_2 \qquad \text{and} \qquad F_1 \leftrightarrow F_2\ . \tag{3.67}$$

A particularly important case for the present work are transitions between vibrational states of A_1 and F_2 symmetry since our laser allows excitation of the F_2-symmetric ν_3 vibration. It can be shown[36] that R-branch transitions can only connect $F^{(-)}$ levels

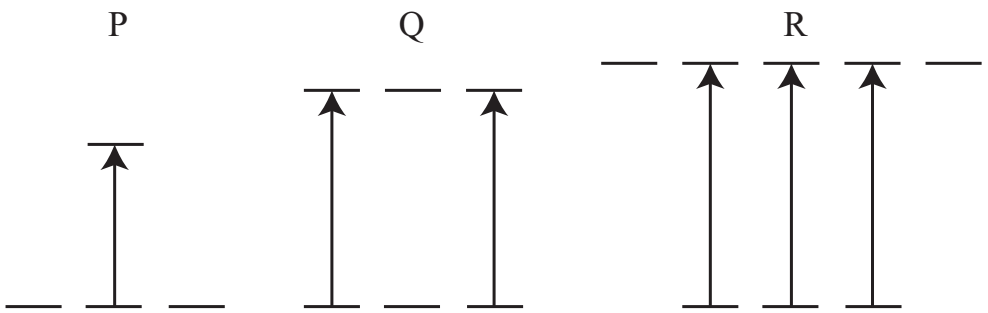

Figure 3.26 M_J-level selection rules for one-photon transitions induced by linearly polarized light in a spherical top.

with the vibrational (A_1) ground state, Q-branch transitions only $F^{(0)}$ and P-branch transitions only $F^{(+)}$ levels. This is a consequence of an additional $\Delta R = 0$ selection rule, where R is the quantum number associated with the rotational angular momentum of the molecular framework. Figure 3.25 exemplifies the selection rules by showing selected IR allowed rovibrational transitions between vibrational states of A_1 and F_2 symmetry. The $R(0)$ transition, which prepares CH_4 in the $(\nu_3, J = 1)$ excited state before scattering as described in chapter 4, is highlighted in red.

Lastly, we note the M_J-level selection rules for the excitation with linearly polarized light, $\Delta M_J = 0$, and in the case of Q-branch transitions ($\Delta J = 0$) additionally $M_J = 0 \nleftrightarrow M_J = 0$. These rules are visualized in Figure 3.26.

References

[1] M. Zen, in *Atomic and molecular beam methods, Vol. 1*, edited by G. Scoles (Oxford University Press, New York, 1988).

[2] T. E. Gough, R. E. Miller, and G. Scoles, Appl. Phys. Lett. **30**, 338 (1977).

[3] M. E. van Reijzen, *State-to-state scattering of CH_4 from Ni(111) and Gr/Ni(111)*, Ph.D. thesis, École polytechnique fédérale de Lausanne, Lausanne (2016).

[4] R. M. Stephenson and S. Malanowski, in *NIST Chemistry WebBook, NIST Standard Reference Database Number 69*, edited by P. J. Linstrom and W. G. Mallard (National Institute of Standards and Technology, Gaithersburg MD, 1987) , (retrieved January 3, 2018).

[5] D. Farias and K.-H. Rieder, Rep. Prog. Phys. **61**, 1575 (1998).

[6] L. Chen, H. Ueta, H. Chadwick, and R. D. Beck, J. Phys. Chem. C **119**, 14499 (2015).

[7] P. M. Hundt, R. Bisson, and R. D. Beck, J. Chem. Phys. **137**, 074701 (2012).

[8] B. Yoder, *Steric effects in the Chemisorption of Vibrationally Excited Methane on Nickel*, Ph.D. thesis, École polytechnique fédérale de Lausanne, Lausanne (2010).

[9] N. V. Vitanov, T. Halfmann, B. W. Shore, and K. Bergmann, Annu. Rev. Phys. Chem. **52**, 763 (2001).

[10] H. Chadwick, P. M. Hundt, M. E. van Reijzen, B. L. Yoder, and R. D. Beck, J. Chem. Phys. **140**, 034321 (2014).

[11] J. I. Steinfeld, *Molecules and radiation: an introduction to modern molecular spectroscopy*, 2nd ed. (Dover Publications, Mineola, N.Y, 2005).

[12] R. C. Hilborn, "Einstein coefficients, cross sections, f values, dipole moments, and all that," (2002).

[13] I. Gordon *et al.*, J. Quant. Spectrosc. Radiat. Transf. **203**, 3 (2017).

[14] P. M. Hundt, *Quantum-state resolved gas/surface reaction dynamics of water and methane*, Ph.D. thesis, École polytechnique fédérale de Lausanne, Lausanne (2014).

[15] Y. B. Fan, L. J. Rawluk, Y. Apelblat, and M. Keil, J. Opt. Soc. Am. B **8**, 1218 (1991).

[16] R. N. Zare, *Angular momentum: understanding spatial aspects in chemistry and physics* (Wiley, New York, 1988).

[17] A. J. Orr-Ewing and R. N. Zare, Annu. Rev. Phys. Chem. **45**, 315 (1994).

[18] M. Brouard and C. Vallance, eds., *Tutorials in molecular reaction dynamics* (Royal Society of Chemistry, Cambridge, 2012).

[19] A. C. Luntz, A. W. Kleyn, and D. J. Auerbach, Phys. Rev. B **25**, 4273 (1982).

[20] A. Kleyn, A. Luntz, and D. Auerbach, Surf. Sci. **152-153**, 99 (1985).

[21] D. C. Jacobs, K. W. Kolasinski, R. J. Madix, and R. N. Zare, J. Chem. Phys. **87**, 5038 (1987).

[22] G. O. Sitz, A. C. Kummel, and R. N. Zare, J. Chem. Phys. **89**, 2558 (1988).
[23] A. C. Kummel, G. O. Sitz, R. N. Zare, and J. C. Tully, J. Chem. Phys. **91**, 5793 (1989).
[24] A. C. Kummel, G. O. Sitz, R. N. Zare, and J. C. Tully, J. Chem. Phys. **89**, 6947 (1988).
[25] D. C. Jacobs, K. W. Kolasinski, S. F. Shane, and R. N. Zare, J. Chem. Phys. **91**, 3182 (1989).
[26] R. N. Zare, Ber. Bunsenges. Phys. Chem. **86**, 422 (1982).
[27] M. J. Weida and C. S. Parmenter, J. Chem. Phys. **107**, 7138 (1997).
[28] C. H. Greene and R. N. Zare, Annu. Rev. Phys. Chem. **33**, 119 (1982).
[29] U. Fano and J. H. Macek, Rev. Mod. Phys. **45**, 553 (1973).
[30] B. G. Perkins and D. J. Nesbitt, Proc. Natl. Acad. Sci. **105**, 12684 (2008).
[31] B. G. Perkins and D. J. Nesbitt, J. Phys. Chem. A **114**, 1398 (2010).
[32] A. Orr-Ewing, W. Simpson, T. Rakitzis, and R. Zare, Isr. J. Chem. **34**, 95 (1994).
[33] J. L. Hall and C. Bordé, Phys. Rev. Lett. **30**, 1101 (1973).
[34] S. Albert, S. Bauerecker, V. Boudon, L. Brown, J.-P. Champion, M. Loëte, A. Nikitin, and M. Quack, Chem. Phys. **356**, 131 (2009).
[35] G. Herzberg, *Infrared and Raman spectra of polyatomic molecules*, Molecular spectra and molecular structure, Vol. 2 (Krieger, Malabar, Florida, 1991).
[36] C. Di Lauro, *Rotational structure in molecular infrared spectra*, first edition ed. (Elsevier, Waltham, MA, 2013).
[37] Johannes Martin Gabriel Niederer, *The Infrared Spectrum of Methane*, Ph.D. thesis, ETH Zürich, Zürich (2011).
[38] E. B. Wilson, J. C. Decius, and P. C. Cross, *Molecular vibrations: the theory of infrared and Raman vibrational spectra* (Dover Publications, New York, 1980).
[39] D. M. Bishop, *Group theory and chemistry* (Dover, New York, 1993).
[40] G. Herzberg, *Infrared and Raman spectra of polyatomic molecules*, Molecular spectra and molecular structure, Vol. 2 (Krieger, Malabar, Florida, 1991) , p. 456.
[41] E. B. Wilson, J. Chem. Phys. **3**, 276 (1935).
[42] K. T. Hecht, J. Mol. Spectrosc. **5**, 355 (1961).
[43] H. A. Jahn, Phys. Rev. **56**, 680 (1939).

4 Vibrational energy redistribution in the scattering of $CH_4(\nu_3)$

4.1 Introduction

Previous state-resolved molecular beam studies have provided detailed evidence that CH_4 dissociation on Ni surfaces is promoted by translational and vibrational energy and that the partitioning of internal energy can influence the probability and products of the reaction[1–4]. For example, one quantum of symmetric C–H stretch excitation (ν_1) promotes the C–H bond cleavage on Ni(100) up to ten times more effectively than a quantum of anti-symmetric C–H stretch excitation (ν_3) even though the two vibrations have comparable energies of 2916 cm^{-1} and 3019 cm^{-1}, respectively[5,6]. This is shown in Figure 4.1, where the initial sticking coefficient S_0 (the reaction probability) is plotted as a function of incident translational energy and initial vibrational state. It becomes clear that the reaction probability is not simply proportional to the vibrational energy content but depends also on the very nature of the vibrational mode. This phenomenon is called mode-specificity and stands in contrast to statistical reactivity, where molecules are equally likely to react as long as they contain the same amount of internal energy. Controlling a chemical reaction's outcome by selective laser excitation has been a long-standing goal for physical chemists[7]. Most attempts, however, are impaired by fast IVR, which scrambles the vibrational energy content among all modes[8].

State-resolved molecular beam studies such as the one presented in Figure 4.1 use lasers with sufficiently narrow linewidth to prepare molecules in a single rovibrational eigenstate prior to the surface encounter. Since the so-prepared molecules are in a collision-free environment, they remain in the same eigenstate until they come into close vicinity to the surface, approximately within 10 Å. This is because the molecular eigenstate of the isolated molecule exhibits no time-dependence and radiative lifetimes are on the order of 40 ms, long compared to typical flight times of some hundred μs. However, as discussed[9] by Killelea and Utz, vibrational energy flow within the molecule-surface complex can still occur *via* surface-induced IVR once the molecule

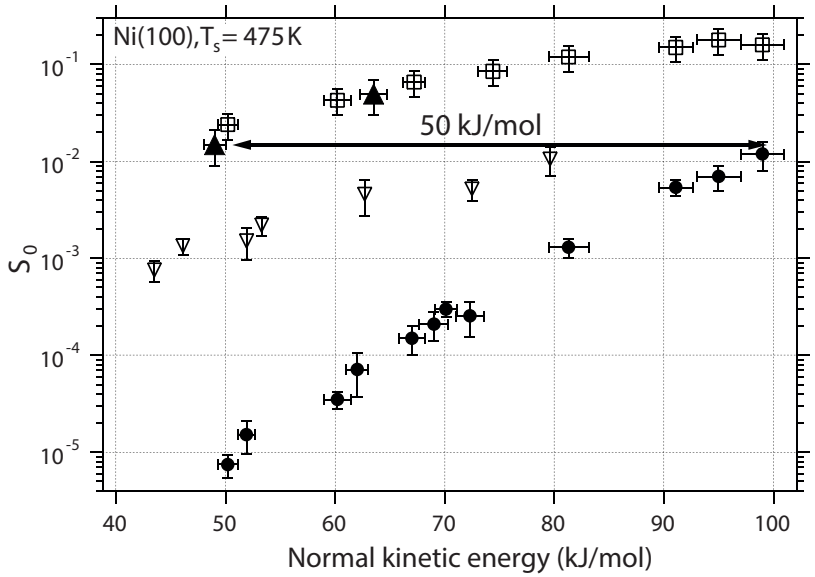

Figure 4.1 State-resolved reactivity for CH_4 in the ν_1 (filled triangles), $2\nu_3$ (open squares), ν_3 (open triangles), and ground vibrational (circles) states on Ni(100). Reproduced from Ref. [6].

approaches the surface within a few Å because the molecule-surface interaction is no longer negligible and the now-combined Hamiltonian of surface and molecule will have a different eigenstate spectrum compared to that of the isolated molecule. The original eigenstate therefore evolves into a superposition state, where the new basis is formed by the eigenstates of the molecule-surface complex. This evolution causes flow of vibrational energy within the complex because the initially prepared state is now made up of changing contributions from the original vibrational modes.

The experimental observation of mode-specificity shows that surface-induced IVR does not lead to complete scrambling of the vibrational energy in the case of CH_4 dissociation on Ni(100). Similar observations have been made[7,10,11] for the gas-phase reaction between methane and chlorine atoms to yield a methyl radical and HCl. Apparently, the vibrational spectrum of CH_4 is sparse enough for the initial vibrational excitation to remain conserved during the very short interaction time, which lasts no longer than some hundred femtoseconds. In spite of this, theoretical modeling of the dissociative chemisorption of CH_4 on transition metal surfaces such as Ni and Pt spawned hints that surface-induced vibrational mode couplings should have an important impact on the reactivity. Specifically, Jackson and co-workers have identified transitions between certain vibrational modes that aid in the conversion of the vibrational energy into translational motion along the reaction path. The extent to which surface-induced mode couplings

are treated is one of the aspects that distinguishes existing theoretical approaches[12,13]. Therefore, experimental data, which allow a more direct examination of vibrational energy flow, are desirable for benchmarking current and future theoretical approaches.

Only few scattering studies on polyatomic molecules addressing similar questions have been reported. Misewich *et al.* found that $CO_2(101)$ undergoes efficient relaxation to the ground state when scattered from a polycrystalline silver surface[14]. Similarly, the vibrational energy of C_2H_2, initially excited to the C–H-asymmetric stretch (0010^00^0), can be quenched on LiF(001)[15,16]. However, in both of these cases, vibrational relaxation occurred only for those molecules which became temporarily trapped on the surface resulting in accommodation of their internal DOF to the surface temperature. No observations of surface-induced IVR or vibrational relaxation in a direct surface collision have thus far been reported for polyatomic molecules.

With our BILT detection technique, which I introduced in chapter 3, and in combination with highly efficient IR pumping for the state-preparation of incident molecules, we now have an ideal tool to study the fate of vibrational energy in a molecule-surface collision with unprecedented detail. The question, which we want to answer in this study, is the following: What happens to the vibrational energy in a CH_4 molecule, which we initially prepared in a specific vibrational state, when it collides with a Ni(111) surface? If surface-induced IVR takes place, then this should be reflected – to some extent – in the state distributions of the scattered molecules and we should observe population in vibrational states that initially were not populated. Specifically, we prepared here the incident molecular beam of CH_4 with one quantum of the anti-symmetric C–H-stretch vibration ($v_3 = 1$). After scattering from the hot ($T_S = 673\,K$) Ni(111) surface under non-reactive conditions, we detected CH_4, both in the initially prepared state (v_3) and also in the energetically neighboring ($\Delta E_{vib} = 109\,cm^{-1}$) symmetric C–H stretch state (v_1).

The study described in this chapter has been published[17] recently in a shortened version in "Physical Review Letters"[(a)]. Here, I give a more detailed and complete description of the experimental procedure and the data analysis. I will, moreover, discuss the results in the context of our current dynamical understanding of this prototypical gas-surface system.

[(a)] The material is reprinted with permission. Copyright 2018, American Physical Society.

4.2 Experimental details

4.2.1 Molecular beam

A molecular beam of methane was generated by expanding pure CH_4 or mixtures with helium. Table 4.1 summarizes the average kinetic energies and translational temperatures for the different gas mixtures and nozzle temperatures T_{Nozzle} used in this work. The time-of-flight method was used to determine the velocity distributions of the different beams as outlined in section 2.2.1.1. In the following, the mean kinetic energy $\langle E_{\mathrm{kin}} \rangle$ of the incident beam is denoted E_i for brevity.

Table 4.1 Characteristics of the CH_4 molecular beams.

property	molecular beam characteristic		
composition	neat CH_4	3% in He	20% in He
T_{Nozzle} (K)	297	297	600
p_{stag} (bar)	3	5	3
v_0 (m/s)	1060	1650	2090
$T_{\parallel}$ (K)	14	4	39
$\langle E_{\mathrm{kin}} \rangle$ (meV)	100	230	370

4.2.2 Preparing a molecular beam of vibrationally excited CH_4

In this study, we prepared and detected *meta*-CH_4 (nuclear spin quintet), owing to its favorable statistical weight of 5. By comparison, *para*- and *ortho*-CH_4 have weights of 2 and 3, respectively. Incident CH_4 was state-prepared with one quantum of the anti-symmetric stretch vibration (ν_3) and in rotational state $J = 1$ *via* the $\nu_3 \leftarrow v = 0, R(0)$ transition at 3028.753 cm^{-1} using the idler output ($\sim 2\,\mathrm{W}$) from the Pump OPO. The IR beam was focused by a cylindrical CaF_2 lens ($f = 25$ cm) placed about 35 cm before the intersection with the incident molecular beam in order to achieve excitation by RAP. CH_4 is prepared in the excited state about 2 cm before colliding with the target surface. Yoder has shown[18] that, at this distance, hyperfine depolarization reduces the alignment in the ν_3, $J = 1$ to about half of its initial value ($A_0^2(t = 0) = -1$). Note further that in the ν_3, $J = 1$ state, it is not the actual body-rotation that gives rise to the total angular momentum of $J = 1$ but rather the vibrational angular momentum[19]. In the classical picture, we may view the associated motion as being similar to a vibrating ellipse. The hydrogen atoms are moving on the surface of the ellipsoid with undetermined absolute orientation. It is then the excited axis of the ellipse that is polarized in space due to the absorption of linearly polarized light. In the prepared state CH_4 thus has a spherically

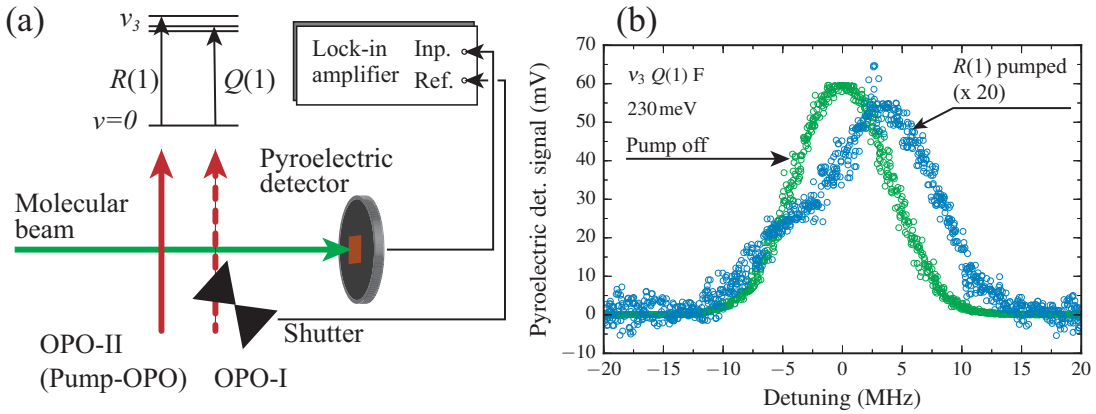

Figure 4.2 (a) Schematic of the bleaching experiment to determine the fraction of excited molecules during the pumping step. The chopped Tagging OPO beam excites the remaining population of the $v = 0$, $J = 1$ state after the Pump OPO excited the $R(1)$ F transition. Lock-in detection of the pyroelectric detector signal yields a measure of the population excited by the second (Tagging) OPO. (b) The $Q(1)$ F transition line profile recorded when the Pump beam was on (blue) and off (green). The Pump-on signal was multiplied by a factor of 20. The beam energy was 230 meV.

symmetrical rotational wavefunction but its vibrational wavefunction has a some residual polarization when the CH_4 strikes the surface. I have not further investigated the effect of reactant alignment in this study.

We can prove that inversion of population is achieved in the pumping step by performing a so-called bleaching experiment, which has been described previously in Refs. [20] and [21]. Determining the excitation efficiency is not strictly necessary because all states, which we detected in this study after scattering, are solely occupied by molecules that were initially pumped to the excited state. However, the near-inversion population transfer is a key element that makes this study possible. Moreover, the transfer cavity allows us, for the first time, to show that the excitation is efficient over the whole (residually) Doppler-broadened absorption profile.

Briefly, the pyroelectric detector monitors the vibrational energy that a second OPO adds to the incoming beam *after* the actual Pump OPO excited the beam. This is shown in Figure 4.2 (a). The detection principle is identical to our BILT scheme but instead of the cryogenic bolometer the room-temperature pyroelectric detector is used. Both, Tagging and Pump OPO are tuned to transitions, which originate from the same initial rotational level in $v = 0$. Here, only the second OPO is chopped and we measure a signal, which is proportional to the population left in the lower level while the Pump OPO is on. It is then compared to the signal when the Pump OPO is blocked, which

gives a measure of the total population in the lower state. Note that it is not possible to prove the bleaching of the $v = 0,\ J = 0$ state in this way since there is only a single allowed transition to the first excited state of ν_3. I therefore used instead the $R(1)$ and $Q(1)$ transitions of *ortho*-CH_4. If we can show that close-to-unity excitation efficiency is reached for the $R(1)$ transition, then the same must be true for $R(0)$, because both transitions have very similar A_{21} coefficients but in case of $R(1)$, the transition moments of the three M_J-levels are lower compared to the one of $R(0)$ due to the Clebsch-Gordan coefficient in Equation 3.43.

Owing to our transfer cavity, we now have the possibility to monitor the ground state depletion across the entire Doppler width of the molecular beam. For this purpose, the Tagging OPO was temporarily aligned to intersect the incoming beam before the pyroelectric detector but after the Pump OPO beam. It was chopped by a mechanical shutter at 2 Hz and the detector signal amplified by the lock-in in the same way as in our BILT experiments. Figure 4.2 (b) shows the absorption profiles obtained by scanning Tagging OPO frequency while the pump beam was either on or off. Note that the Pump-on trace is scaled by a factor of 20 for visibility. By integrating both traces and comparing the relative areas, I find that 94 ± 1 % population has been removed by pumping the $R(1)$ transition, which serves as a lower limit for the pumping efficiency when $R(0)$ is excited instead. We can further see in Figure 4.2 (b) that the bleached line profile is somewhat broader than its unbleached counterpart and moreover asymmetric. This likely comes from the fact that molecules with higher transverse velocity are more difficult to excite since they require larger Doppler detuning to achieve RAP. The asymmetry depends systematically on the pump beam alignment (not shown here) and likewise comes from difficulties in exciting certain velocity classes. Overall, however, we can see that the excited fraction is indeed close to unity. Fluence curves for the pumping step suggest that even for the highest beam energy of 370 meV, population transfer is close to complete inversion (see section 5.2).

4.2.3 Tagging scheme

Figure 4.3 displays a schematic view of the laser excitation scheme. We probed the rotational state populations of the ν_3 and ν_1 vibrational states after scattering by tagging *via* $2\nu_3 \leftarrow \nu_3$ and $\nu_1 + \nu_3 \leftarrow \nu_1$ transitions, respectively. In both cases, we used either R- or Q-branch transitions depending on transition strength and wavelength accessibility. Since these bands are not listed in the HITRAN database, we relied on predicted transition frequencies, which were kindly provided by Prof. Vincent Boudon from the *Université de Bourgogne* in Dijon, France. These line positions served as a first guess for our search

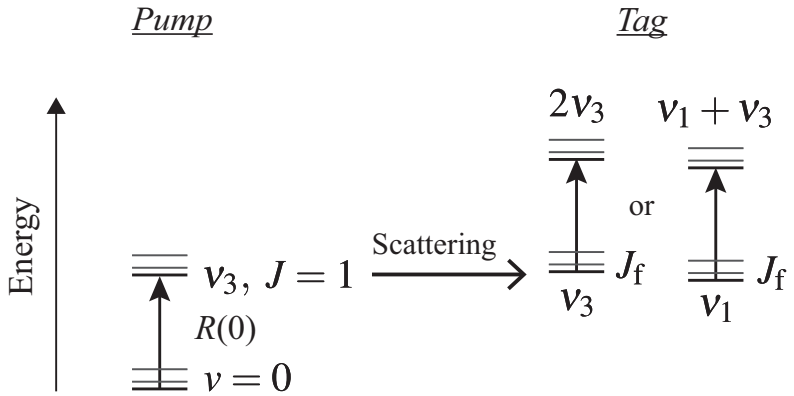

Figure 4.3 Illustration of the laser excitation scheme. $CH_4(\nu_3, J = 1)$ is scattered into final rotational states J_f and detected in either ν_3 or ν_1 by laser excitation to the first overtone of ν_3 or the $\nu_1 + \nu_3$ combination band, respectively.

and were typically not more than one tenth of a wavenumber away from the actual values. We scanned the laser frequency in the vicinity of the predicted transition frequencies, making use of transfer cavity scanning, until we found a peak in the spectrum. We then verified that the found transition belonged to a hot-band by temporarily blocking the pump laser and observing the bolometer signal decrease to the baseline, *i.e.* the scattered light level. If the transition would start from the $v = 0$ level, the signal would not depend on the presence of the pump laser. A complete list of the transitions used in this chapter can be found in appendix D together with a comparison of observed *versus* predicted line positions.

Since we used the more powerful OPO to pump the incoming molecular beam, this left us with $\sim 1\,\mathrm{W}$ of idler power from the Tagging OPO for the tagging step. Since the Einstein A_{21} coefficient for the strongest transitions of the $\nu_1 + \nu_3 \leftarrow \nu_1$ band were predicted to be on the order $10\,\mathrm{s}^{-1}$ (as compared to $25\,\mathrm{s}^{-1}$ for the ν_3 fundamental), complete saturation by RAP could not be expected. We increased the laser fluence by adding a lens with a long ($f = 1\,\mathrm{m}$) focal length about 50 cm before the cylindrical lens, which refocused the diverging laser beam to a beam diameter of 2.35 mm (FWHM) measured just before the optical access window in front of the bolometer.

Fluence curve measurements were still required for all but the strongest transitions of the $2\nu_3 \leftarrow \nu_3$ band. Specifically, we recorded only the tagging signal at the maximum available laser powers for the $R(7)$ and $R(8)$ transitions of this band because they were predicted to have high Einstein coefficient approaching $30\,\mathrm{s}^{-1}$. Moreover, the OPO was rather unstable at the corresponding wavelengths and tended to undergo mode-hopping

after a few minutes, which did not leave time to record a fluence curve. In all other cases, the curves were recorded in an automated fashion, as described in section 3.4.3.1, where the $\lambda/2$-plate was rotated in steps of 5°. Each time, we averaged the BILT signal for both flag-on and flag-off for 30 s, respectively.

We fitted the fluence curves using the empirical model based on the Landau-Zener formulation for RAP excitation. The curve asymptotes were used as a measure of state populations, thereby making a correction for transition strengths superfluous. We corrected the tagging signals only for their respective transition energies $\hbar\omega_{2\leftarrow1}$ and for the missing $M_J = 0$ population in cases where tagging occurred *via* the Q-branch. The latter correction is given by Equation 3.49, which is recalled here for the convenience of the reader,

$$P^{\text{corr}}_{J'',n''} = \frac{2J''+1}{2J''} S_{Q,J'',n''} \,, \tag{4.1}$$

where $S_{Q,J'',n''}$ is the measured signal and n'' denotes a particular rotational sublevel belonging to J''.

Rotational state distributions were recorded at an incidence angle of $\theta_i = 65°$ and an exit angle of $\theta_f = 70°$. The geometry was chosen such that it was close to specular scattering conditions but at the same time avoided the sharp specular reflection, which occurs when helium is used as a seeding gas. The surface temperature was always $T_S = 673$ K.

4.3 Results

Figure 4.4 shows the rotational state distributions after scattering of methane initially prepared in the (ν_3, $J = 1$) state and with an incidence kinetic energy of 230 meV. We observe two main scattering channels. First, the vibrationally elastic channel, where CH_4 remains in its initial vibrational state ($\nu_3 \rightarrow \nu_3$). Second, we identify a vibrationally inelastic channel, where the vibrational energy has been redistributed into the symmetric stretch vibration ($\nu_3 \rightarrow \nu_1$). For both channels, we observe significant rotational excitation upon scattering. Values of J for which no levels can exist due to the symmetry restrictions (see section 3.5) are marked by an asterisk in Figure 4.4. The rotational distributions include all existing levels from $J = 0$ through $J = 8$ except for one sublevel belonging to (ν_3, $J = 8$), which was most likely below the detection limit. We verified that there is no thermally or collisionally induced excitation from $v = 0$ to ν_1 and ν_3 by temporarily blocking the Pump OPO and observing the signal decrease to the baseline level. All observed products therefore originate solely from scattering of $CH_4(\nu_3, J = 1)$.

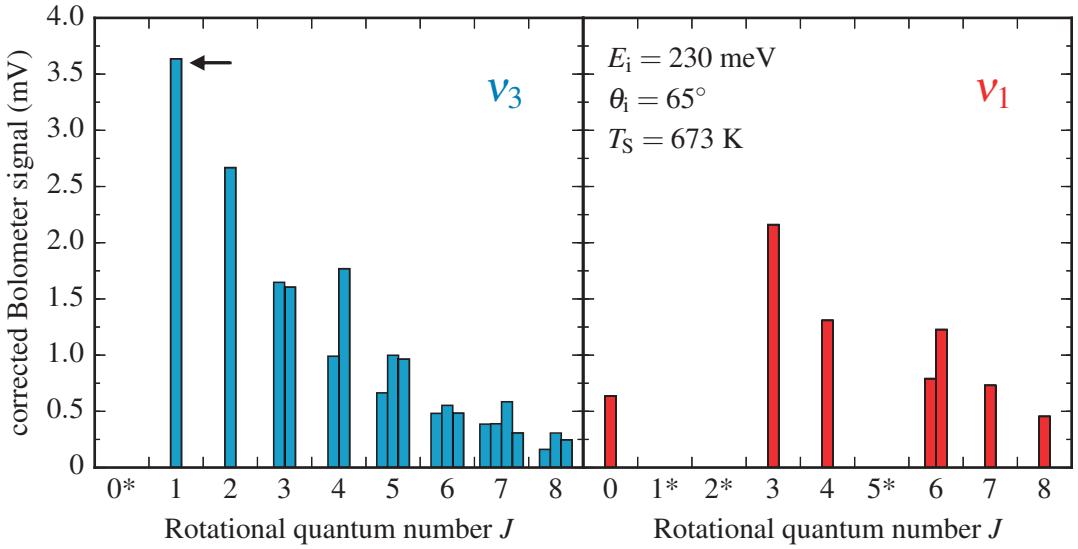

Figure 4.4 Rotational state distributions within the vibrationally elastic (ν_3) and inelastic (ν_1) channels for a molecular beam of $CH_4(\nu_3,\ J = 1)$ scattered from Ni(111) with an average incidence translational energy of 230 meV. All bars represent individual rotational sublevels. Non-existing levels are marked by an asterisk and the arrow highlights the initial state.

Before proceeding with a more detailed analysis of the scattering distributions, some remarks on measurement uncertainties are necessary. Obtaining one set of rotational distributions for both vibrational states takes several days of measurement with our current setup where most time is required for tuning of the tagging laser and recording fluence curves. It was thus not feasible to acquire a statistically meaningful number of repeated measurements before our gas mixtures would run out. However, we have repeated measurements for certain transitions like $2\nu_3 \leftarrow \nu_3,\ R(2)$ on different days and under the same conditions. Furthermore, we have multiple recordings of the rotational distributions from scattering of a beam that was formed by expanding pure CH_4 and that was in the vibrational ground state ($v = 0 \rightarrow v = 0$ scattering). Some of these data date back to the PhD work of van Reijzen and we found that the *absolute* bolometer tagging signals are reproduced within 5 % on different days. At the same time the error on repeated measurements is not below $S_{tag} = 0.1$ mV, which concerns only the most sparsely populated rotational levels. The errors reported in the remainder of this chapter are based on this repeatability and were derived by standard error propagation techniques. I believe that they provide a conservative estimate of the true measurement errors.

In Figure 4.4 we can see that for certain values of J, there is a rather large population differences between sublevels of the same J. Consider, for instance, the two $J = 4$

Table 4.2 Incidence energy dependence of the branching ratios b_{ν_1/ν_3} and the rotational excitation characterized by rotational temperatures, as well as that of the difference in mean rotational energy. The two lowest J levels were omitted in the determination of $T_{\mathrm{rot}}^{\nu_3}$ (see text).

E_{i} (meV)	b_{ν_1/ν_3}	$T_{\mathrm{rot}}^{\nu_3}$ (K)	$T_{\mathrm{rot}}^{\nu_1}$ (K)	$\langle E_{\mathrm{rot}}^{\nu_1}\rangle - \langle E_{\mathrm{rot}}^{\nu_3}\rangle$ (cm^{-1})
100	0.41 ± 0.04	153 ± 8	161 ± 14	37 ± 15
230	0.39 ± 0.06	162 ± 11	178 ± 17	40 ± 15
370	0.43 ± 0.05	181 ± 13	190 ± 20	41 ± 15

sublevels of the ν_3 state. Their relative populations differ by about 60 %. This presents a significant difference and cannot be attributed to bias in the measurement procedure. Specifically, we used R-branch transitions in both cases, ruling out an influence of angular momentum alignment in the conversion from signals to populations. Furthermore, both transitions were readily saturated and lastly, no other hot-band lines are located sufficiently close to explain an accidental misassignment. Moreover, we observe the same signal difference for all E_i. Lastly, the energy difference between the two sublevels is only about $2\,\mathrm{cm}^{-1}$, where the stronger populated level has the lower energy. It seems unlikely that this small energy gap could explain the population difference, in particular when considering $J = 3$, where the two sublevels have a similar energy gap and no significant difference in their population is observed.

I speculate that this peculiar behavior comes from incomplete scrambling of population across the three Coriolis stacks, which are present in $CH_4(\nu_3)$. The initially prepared state $(\nu_3, J = 1)$ belongs to the $F^{(-)}$ stack and the next higher state in the same stack is the more strongly populated $(\nu_3, J = 4)$ level. All other levels, which are located in between $(J = 2, 3)$, instead belong to the $F^{(0)}$ and $F^{(+)}$ stacks. The excess population in the $J = 4$ level, which belongs to $F^{(-)}$, may come from a partial conservation of the rotation-vibration coupling during the surface collision.

For all higher J-levels the differences in populations are less pronounced and potential biases for particular sublevels are less clear. We further observe a significant population difference in the two sublevels belonging to ν_1, $J = 6$, where no Coriolis coupling is at play. At this stage, I thus have to clearly mark the preceding discussion as speculative. As a last remark on this subject, I point out that the ν_3 distribution for *para*-CH_4, which was observed[22] by van Reijzen, showed similar behavior with enhanced population in the ν_3 , $J = 3$ sublevel that was initially prepared and ν_3 , $J = 5$ sublevel that belongs to the same Coriolis stack.

The rotational distributions at incidence energies of 100 and 370 meV are similar

to those at E_i = 230 meV displayed in Figure 4.4 (see appendix E). The total flux in each vibrational scattering channel is the combined intensity of all rotational sublevels belonging to the corresponding vibrational state. We define the branching ratio between the two vibrations b_{ν_1/ν_3} as

$$b_{\nu_1/\nu_3} = \frac{S^{\text{total}}_{\nu_1}}{S^{\text{total}}_{\nu_3}} = \frac{\sum_{J=0}^{8}\sum_{n\in J} S_{\nu_1,J,n}}{\sum_{J=1}^{8}\sum_{n\in J} S_{\nu_3,J,n}}\,, \tag{4.2}$$

where the second summation is respectively carried out over all sublevels n belonging to the same value of J. We find a branching ratio near 40 %, which is insensitive to E_i across the studied energy range (see Table 4.2). Based on measurements reported[22] in van Reijzen's thesis, we estimate that the probability of populating one of the bend overtone states ($2\nu_2$, $2\nu_4$) or the $\nu_2+\nu_4$ level is lower by at least a factor of five compared to that for ν_1. Furthermore, we observe no population in the fundamental bend vibrations ν_2 and ν_4 with energies of 1533 cm^{-1} and 1311 cm^{-1}, respectively.

Figure 4.5 displays a Boltzmann plot of the distributions from Figure 4.4. The distribution corresponding to ν_3 is strikingly non-Boltzmann, showing a propensity for rotationally elastic scattering. For $J \geq 3$, the distribution falls approximately on a straight line in this plot. Boltzmann analysis of the linear regimes yield rotational temperatures T_{rot} between 140 and 200 K, far below the surface temperature of 673 K. This is also observed for ν_1 and is consistent with direct scattering. It stands in contrast to a possible trapping-desorption (TD) mechanism, in which molecules become trapped for some time in a weakly bound (physisorbed) state and subsequently desorb with their DOF accommodated to the surface temperature. Hence, if the scattering were dominated by TD, rotational temperatures closer to T_S would be expected.

Table 4.2 compiles the rotational temperatures at all E_i. Rotational excitation increases slightly with E_i, which is likewise expected for direct scattering. Interestingly, rotational excitation is slightly higher for ν_1 than ν_3 in all cases. Since for the determination of the rotational temperatures, two levels of the ν_3 state had to be omitted due to the non-linearity in the Boltzmann-plot, a different quantity is required to properly characterize the difference in rotational excitation between the two vibrational channels. We therefore define the mean rotational energy as the sum of rotational level energies weighted by their relative population,

$$\langle E^{\nu}_{\text{rot}}\rangle = \frac{1}{S^{\text{total}}_{\nu}}\sum_{J=0}^{8}\sum_{n\in J} S_{\nu,J,n}(E_{\nu,J,n} - E_{\nu,J=0})\,, \tag{4.3}$$

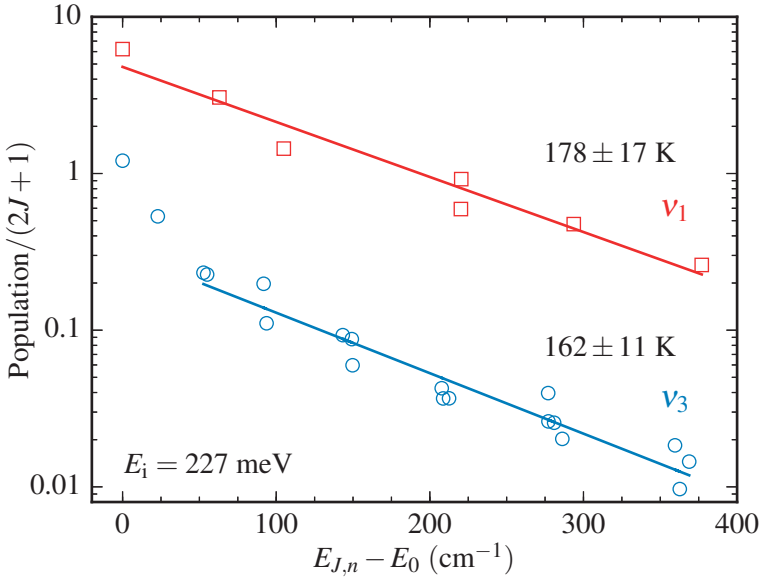

Figure 4.5 Rotational Boltzmann plot for the distributions in Figure 4.4 with ν_1 data (squares) scaled by a factor of 10 for visibility. E_0 is the energy of the lowest rotational state accessible for CH_4 in the ν_3 and ν_1 vibrational states; $J = 1$ and $J = 0$, respectively. Solid lines are linear fits to the data, where for ν_3 the two lowest rotational levels were excluded from the analysis. Indicated are the characteristic rotational temperatures T_{rot} obtained from the slopes of the fits.

where $E_{J,n}$ is the energy of the rotational sublevel (J, n) and $E_{J=0}$ is the energy of the $J = 0$ state. Since for *meta*-$CH_4(\nu_3)$ there is no $J = 0$ level, I used the energy of the $J = 0$ level that belongs to the *ortho*-modification. Figure 4.6 displays the mean rotational energy as a function of incident kinetic energy and vibrational state. Even though the ν_3 vibration was initially prepared with one quantum of angular momentum, the final mean rotational energy in the vibrationally elastic channel is significantly lower compared to the ν_1 channel. The difference in average rotational energy, $\langle E_{\mathrm{rot}}^{\nu_1}\rangle - \langle E_{\mathrm{rot}}^{\nu_3}\rangle$, accounts for nearly 40 % of the vibrational energy $\Delta E_{\mathrm{vib}} = 103\ \mathrm{cm}^{-1}$ liberated upon $\nu_3 \rightarrow \nu_1$ conversion.

Figure 4.7 shows state-resolved angular distributions for both scattering channels obtained by rotating the surface about an axis perpendicular to the scattering plane. The specular angle ($\theta_i = \theta_f$) is indicated by a vertical solid line. All distributions are narrower than a $\cos(\theta_f)$ distribution, which would be expected for a pure trapping/desorption mechanism. The predicted $\cos(\theta_f)$ curve shown in Figure 4.7 includes the convolution with the experimental geometry, which leads to a drop-off towards smaller scattering angles, where the surface assumes a parallel orientation with respect to the incident

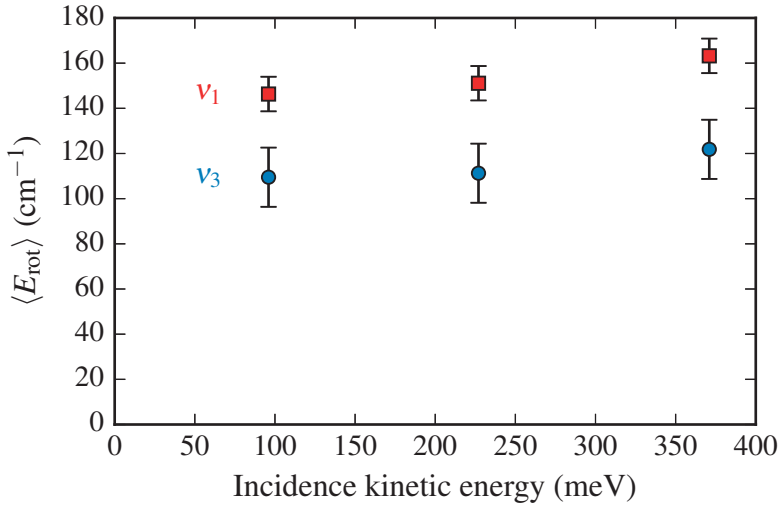

Figure 4.6 Mean rotational energy in the two vibrational scattering channels as a function of incident kinetic energy. Squares and circles represent CH_4 in the ν_1 and ν_3 vibrational states, respectively.

beam (see appendix G). The dip observed close to the specular angle at $E_i = 230$ meV comes from sensitivity reduction due to overlap with the reflected He beam. A lower He concentration and pressure was used at $E_i = 370$ meV, explaining the absence of a similar dip.

Only at $E_i = 100$ meV, we see the angular distribution shifted towards the sub-specular direction ($\theta_f < 67.5°$). This is expected because of the dominance of phonon annihilation over creation when a slow projectile is scattered from a very hot surface[23] and not necessarily a sign of trapping-desorption. With increasing E_i, the distributions become narrower and peak closer to the specular angle, consistent with direct scattering. The strong similarity of the ν_3 and ν_1 angular distributions at a given incidence energy together with the insensitivity of the branching ratio to E_i support the conclusion that, even if TD or multi-bounce trajectories were important, they exhibit no increased probability for vibrationally inelastic scattering.

We find further evidence for direct scattering in the tagging transition line shapes. They are shown in Figure 4.8 for the $\nu_1 + \nu_3 \leftarrow \nu_1$ R(3) transition and the three incident beam speeds v_0. These scans were carried out without the cylindrical lens and the long focal length lenses in place as well as with reduced laser power to avoid saturation. Here, the laser beam had a diameter of 4.7 mm measured before the optical access window. This limited transit-time broadening to < 300 kHz for a molecular velocity of 2000 m/s.

Although the spectral resolution is not sufficient to extract the final speed distributions from the line shapes, their width clearly increases with incidence speed. Since we tagged

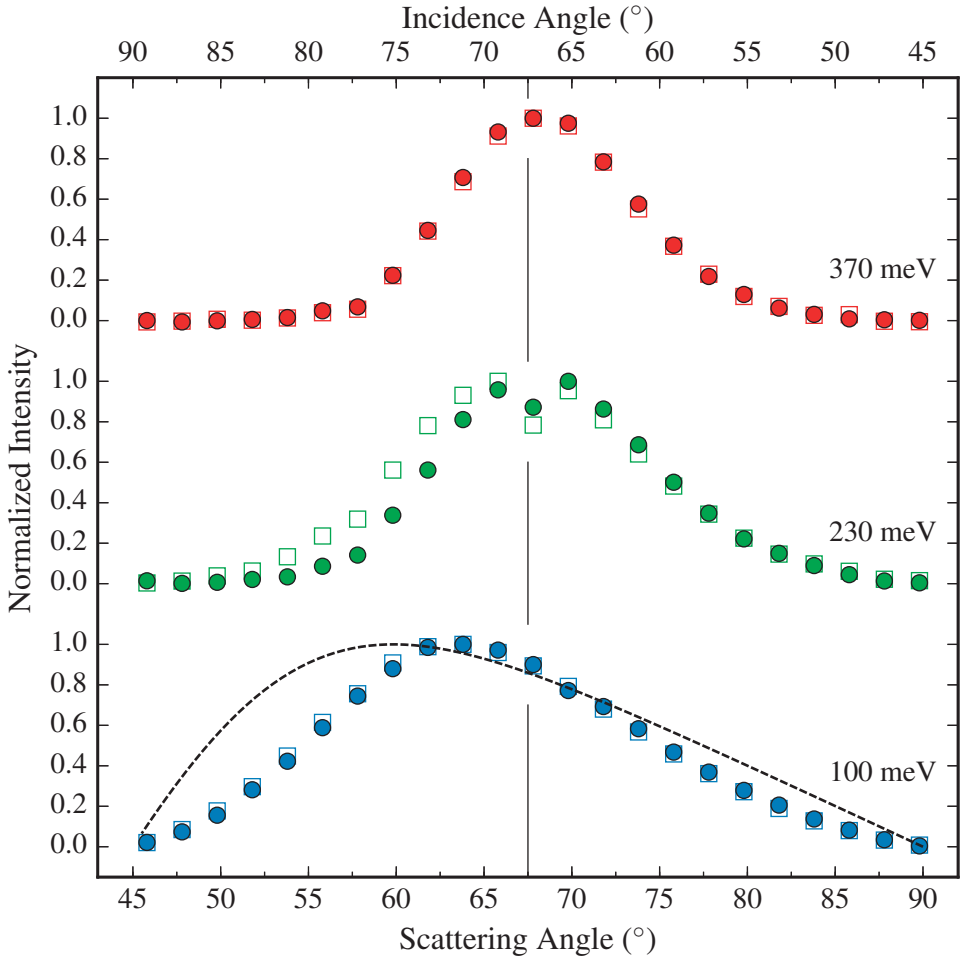

Figure 4.7 Scattering angular distributions, normalized with respect to the peak value. Open and filled symbols represent CH_4 in the $(\nu_1, J = 3)$ and $(\nu_3, J = 2)$ states, respectively. The broken vertical line depicts the specular angle and the dashed line shows the prediction for a pure $\cos(\theta_f)$ distribution.

the same transition with similar laser power, the final speed of the scattered molecules must be the reason for the broadening. The correlation between Doppler linewidth and incidence speed shows that molecules retain a memory of their initial speed. This is usually interpreted as an unambiguous sign of direct scattering based on the notion that trapping leads to a fast equilibration of the translational degrees of freedom, and thus to a rapid loss of that memory. The line shape measurements clearly indicate that trapping-desorption contributes not more than marginally to the production of $CH_4(\nu_1)$.

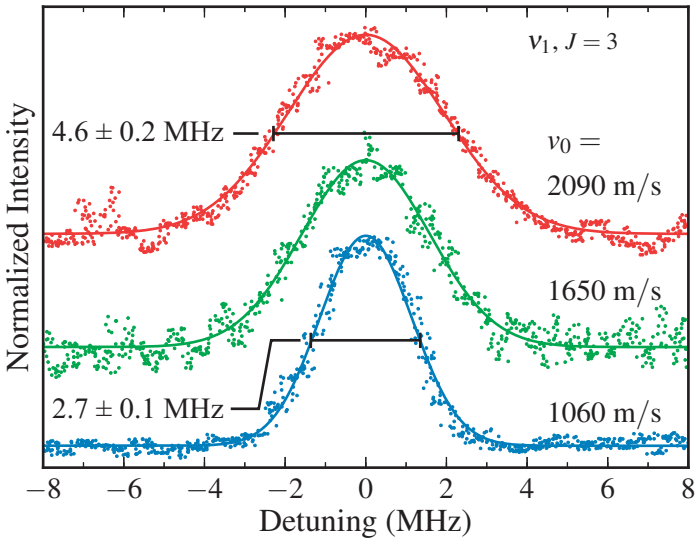

Figure 4.8 Scans of the Doppler broadened absorption profile of the $\nu_1 + \nu_3 \leftarrow \nu_1$ $R(3)$ transition at three different incidence speeds v_0, corresponding to E_i =100, 230 and 370 meV, from bottom to top. Solid lines are Gaussian fits to guide the eye. The curves are normalized with respect to the peak heights.

4.4 Discussion

The data presented above show unambiguously that the observed state distributions originate from direct scattering rather than trapping followed by desorption for both, the vibrationally elastic and inelastic channel. This is consistent with very recent data on the coherent quantum scattering of CH_4 from Ni(111) reported[24] by Al Taleb and Farías. These authors observed clear diffraction peaks in the angular distributions produced by a cold molecular beam of CH_4 scattering from Ni(111) under similar grazing incidence conditions ($\theta_i + \theta_f = 105.4°$).

Distinct diffraction features including rotationally inelastic diffraction (RID) peaks remained discernible even at incidence energies as low as 69 meV, indicating that direct scattering dominates over trapping-desorption. Unlike in their angular distributions, we do not observe sharp diffraction peaks. The difference likely comes from the low surface temperature they used (T_S = 110 K), which strongly reduces Debye-Waller attenuation, that is, inelastic scattering involving the exchange of multiple phonons. According to private communication with the authors of the aforementioned study, the coherent diffraction features disappear already at surface temperatures that are far below 673 K.

While our observations and those of Al Taleb and Farías support the conclusion that the scattering observed under the given conditions is dominated by a direct mechanism,

we should be careful in generalizing this finding to the overall scattering behavior. It should be pointed out that both experiments probe the scattering products exclusively in the scattering plane, integrating over extremely small solid angles. By placing the detector close to the specular scattering direction, we are biasing the detection toward those molecules that have undergone direct scattering because we can expect their angular distribution to be narrower and peaked more closely toward the specular angle compared to that of desorbed molecules. For the latter, we would expect a much wider distribution, which would approach $\cos(\theta_f)$ if the sticking coefficient was independent of θ_i [25]. Such a broad angular distribution leads to a rapid drop in flux with increasing distance from the surface ($\propto r^{-2}$), much faster than what can be expected for directly scattered molecules. Additionally, the direction of highest flux would be along the surface normal for desorbing molecules, while our detector samples a region closer to the specular angle. As a result, we would still expect to see mostly direct scattering even when the probability of the TD channel is comparable to or higher than that of the direct channel.

We have seen above that the rotational energy contained in molecules that undergo $\nu_3 \rightarrow \nu_1$ conversion is significantly higher compared to those remaining in ν_3. The remainder of the energy that is liberated upon $\nu_3 \rightarrow \nu_1$ conversion, ΔE_{vib}, is most likely converted into translational energy. I base this argument on previous studies that observed translational to vibrational ($T \rightarrow V$) energy transfer in the surface scattering of polyatomic molecules. Specifically, Kay *et al.* reported [26] that the ν_2 "umbrella" mode of ammonia is excited by conversion of incident translational energy when bounced off Au(111). Golibrzuch *et al.* made a similar observation [27]. They collided acetylene with Au(111) and found that excitation of the *trans*-vibration is likewise caused by "mechanical" $T \rightarrow V$ energy transfer. It is conceivable that the reverse process, $V \rightarrow T$ energy transfer, could occur as well and carry away the remainder of ΔE_{vib}.

Our results show that vibrational energy redistribution from the anti-symmetric to the symmetric C–H stretch vibration is very efficient, even though the available time-scale for this conversion is limited to less than one picosecond in an impulsive collision. We also find that production of $CH_4(\nu_1)$ dominates over all other vibrationally inelastic processes. It is well established that IVR in isolated gas phase molecules and in solution is initiated by rapid energy transfer among near resonant "doorway" states from which slower IVR channels lead to a full redistribution of vibrational energy across the whole density of states [8]. The reasoning behind this tier model of IVR [28] is that IVR rates are mainly governed by the coupling strength and energy mismatch between two vibrations. That is, the IVR rate will be the highest for states that are near-resonant

and for which the coupling order ($\Delta\nu$) is lowest. High order coupling is generally weak because corresponding coupling terms appear with much smaller magnitude in the Hamiltonian[9].

Previous studies performed by Moore and co-workers focused on the collisional deactivation of vibrationally excited CH_4 in the gas phase[29,30]. These authors deduced a rapid equilibration of population among the ν_3 and ν_1 modes before these states decay further, which is consistent with the tier model of IVR. These authors also found a four times lower stretch to bend-overtone conversion rate compared to the ($\nu_3 \leftrightarrow \nu_1$) rate, in agreement with our observations. This might seem surprising at first considering that the $2\nu_2$ bend state is only 44 cm^{-1} higher in energy than ν_3 and therefore energetically closer than ν_1. However, one might think of the difference between the two stretching modes as being due to a phase shift of two of the C–H oscillators. It is conceivable that a collision can give rise to this phase shift more readily than to a complex deformation motion. Another possible explanation is that the excess vibrational energy can be accommodated by the rotational DOF in the case of $\nu_3 \rightarrow \nu_1$ conversion, whereas $\nu_3 \rightarrow 2\nu_2$ requires energy transfer from the surface to the molecule. While the latter process is clearly possible at the elevated surface temperature we use ($k_B T_S = 478\,cm^{-1}$), it might still be less likely than the transfer of excess energy into rotation.

The fact that we could not observe population in the fundamental bend vibrations ν_2 (1533 cm^{-1}) and ν_4 (1311 cm^{-1}) can be understood when considering that about 1400 cm^{-1} of vibrational energy would need to be dissipated. In collisions between two CH_4 molecules this is possible because the process

$$CH_4(v_{stretch} = 1) + CH_4(v = 0) \rightarrow 2\,CH_4(v_{bend} = 1) \tag{4.4}$$

is near-resonant. By contrast, in the molecule-surface collision, most of the liberated vibrational energy needs to be dissipated by the surface. Assuming a surface phonon frequency[31] of *ca.* 240 cm^{-1}, we expect the energy transfer rate from the molecular vibration to phonons to be very small based on the high coupling order. On the other hand, electron-hole pair excitation could dissipate the energy. It is known that electronically non-adiabatic energy transfer can efficiently quench the vibrational energy in the case of NO and CO scattering from gold and silver surfaces, as demonstrated in detail by Wodtke and co-workers[32–36]. By contrast, non-adiabatic effects are thought to be unimportant for the interaction of polyatomic molecules, and CH_4 in particular, with metal surfaces[37–39]. Indeed, there is no experimental evidence suggesting a coupling of electron-hole pairs in the metal to the vibration of a polyatomic molecule. Moreover,

electronically adiabatic theoretical simulations have successfully reproduced most results from quantum-state-resolved reactivity experiments[4]. The lack of population in the fundamental bend states can therefore be rationalized on the basis of the tier model of IVR and by the absence of effective energy dissipation pathways.

We have seen that $\nu_3 \leftrightarrow \nu_1$ conversion is the dominant IVR process and I have drawn a parallel with general notions of IVR rates and in particular the collisional deactivation of CH_4 in the gas phase. However, our scattering product distributions are not the result of many collisions as it was the case in the bulb gas experiments. It is also remarkable that we find branching ratios b_{ν_1/ν_3} near 40 %, which is even slightly higher than the statistical expectation of $1/3$ obtained by comparing the degeneracies of the two stretch vibrations. That is, their relative populations are not quite in local equilibrium with each other. Previous quantum-state-resolved reactivity measurements have clearly shown[4] that statistical rate theories[40–43] fail in describing the rich reaction dynamics of CH_4 chemisorption on transition metal surfaces, which exhibit mode-specificity, bond-selectivity and steric effects. Our scattering results show that the outcome of the surface encounter is highly non-statistical not only in the dissociative chemisorption but also in the non-reactive scattering. We can thus conclude that the interaction, reactive and non-reactive alike, of CH_4 with Ni(111) can only be described accurately by dynamical theories.

In the remainder of this chapter, I will discuss our scattering results within the context of our current microscopic understanding of the CH_4-surface interaction. This understanding has been greatly enhanced by theoretical studies that aimed at finding a dynamical description of this particular gas-surface interaction. At the center of this discussion is the concept of surface-induced IVR, which has recently been reviewed[9] by Killelea and Utz. Figure 4.9 shows an energy level diagram of methane's pentad, in which the ν_1 and ν_3 fundamental states are located. The vertical axis shows the term energy reduced by the pure rotational energy. The fan-out structure of the rovibrational levels toward high J is due to the increasing rovibrational coupling. The color coding represents the contribution of the different zero-order states to each rovibrational eigenstate. The two stretch vibrations have almost pure (> 95 %) zero-order character up to $J = 9$ and, due to their different vibrational symmetries, do not mix. Vibrational energy transfer between these two modes requires an external perturbation that breaks the T_d symmetry. This symmetry breaking is also seen in the IR absorption spectrum of physisorbed CH_4 where both, the ν_1 and the ν_3 vibration can be observed[44]. The symmetric stretch, which in the gas phase is only Raman-active, becomes IR-active due to the reduction of symmetry when CH_4 is physisorbed. Hence, we can say that the surface-interaction

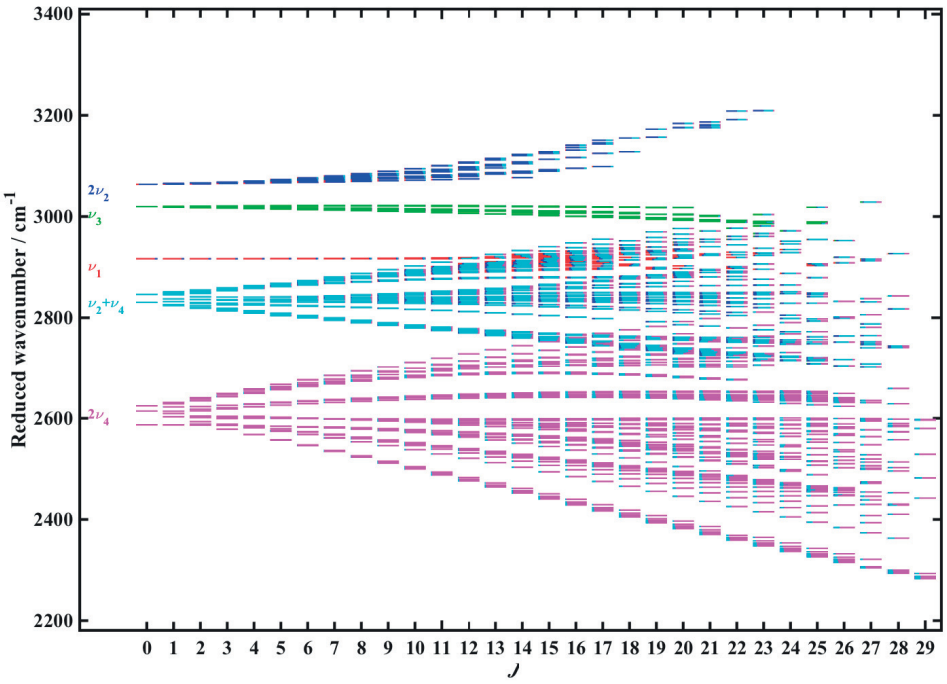

Figure 4.9 Energy level diagram showing all rovibrational levels that belong to methane's pentad up to $J = 29$. Courtesy of V. Boudon, private communication.

not only facilitates the vibrational energy transfer but enables it by altering the potential energy landscape in a way that changes the identities of the vibrational modes as the molecule approaches the surface.

The picture of surface-induced energy flow has been at the heart of the discussion of methane dissociation. Milot and Jansen performed[45] scattering calculations based on wavepacket simulations including all nine internal vibrations. They placed methane in different initial vibrational states and with certain orientation toward the surface and analyzed the vibrational and translational energy content at the end of their simulation. Their results were the first that pointed towards a mode-specific effect on surface reactivity.

Halonen *et al*. developed[46] a vibrationally adiabatic model, which treats the vibrational modes of the isolated CH_4 in a local mode basis set, including only four dimensions, and which models the surface interaction with a London-Eyring-Polanyi-Sato (LEPS) potential. By calculating the vibrational modes at different molecule-surface distances, they obtained the adiabatic normal mode evolution as the molecule approaches the surface. Their simulations predict the symmetric and anti-symmetric stretch amplitudes to become localized in the C–H bonds that are facing and pointing away from the surface,

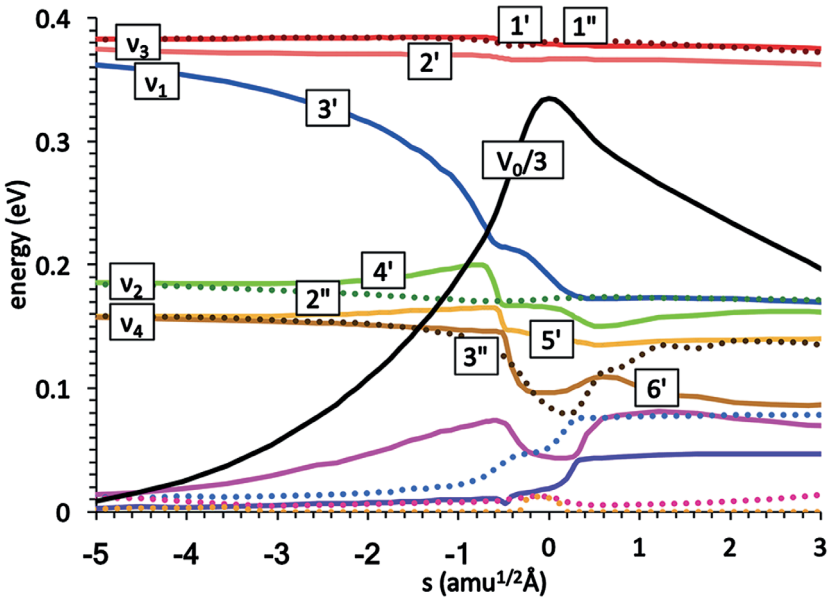

Figure 4.10 Frequencies of the 9 vibrational modes of CH_4 as a function of the distance from the transition state to dissociation on Ni(111), where s denotes the reaction coordinate. The frequencies were calculated using the reaction path Hamiltonian approach. Reproduced with permission from Ref. [47].

respectively. Based on this, they conclude that $CH_4(\nu_1)$ should be more reactive than $CH_4(\nu_3)$, which was later confirmed[6] by Maroni *et al.* for the case of Ni(100). Another implication from their simulations is that part of the $CH_4(\nu_3)$ reactivity can be explained by curve crossing to the more reactive ν_1 state. This vibrationally non-adiabatic pathway is available if the incident molecule approaches the surface with a speed above the Massey velocity, which they estimated to be about 1000 m/s based on semi-classical Landau-Zener analysis. The vibrationally non-adiabatic curve crossing provides an explanation for the production of $CH_4(\nu_1)$ observed in the current experiments. Even though the adiabatic model was based on strongly simplifying assumptions and could therefore make predictions only on a qualitative level, it provides an intuitive picture of vibrational energy flow in a gas-surface encounter.

Jackson and co-workers have developed the Reaction Path Hamiltonian (RPH) approach, a detailed dynamical treatment for the dissociative adsorption of CH_4 on transition metal surfaces[12,48–50]. The RPH method provides the most detailed insight into how energy flow between the different degrees of freedom during the encounter with the surface. Briefly, in their model, first the minimum energy path connecting reactants and products is calculated using DFT. Apart from this coordinate, the potential energy surface is approximated to be being harmonic in the remaining 14 dimensions and the

dynamics calculated by propagation wavepackets.

Figure 4.10 displays the normal mode frequency as the CH_4 molecule approaches the Ni(111) surface along the reaction path. We can see here that the enhanced reactivity of $CH_4(\nu_1)$ is largely due to mode-softening, which leads to a significant decrease of the barrier height for dissociation. The ν_3 mode, by contrast, splits into three components (1', 1", and 2') during the approach toward the surface but all three of them retain their high frequencies. The splitting is due to a reduction of the molecular symmetry because of the presence of the surface. The model also includes the possibility of vibrationally non-adiabatic curve crossing which enable conversion of vibrational energy between different modes and into motion along the reaction path. Specifically, the 2' and 3' modes are strongly coupled in the entrance channel, relatively far away from the transition state[47]. Molecules that are excited to either of these states will therefore behave similarly with respect to dissociation. This is in close analogy to the non-adiabatic curve crossing in the aforementioned model of Halonen *et al.* The coupling provides an explanation for the enhanced reactivity of $CH_4(\nu_3)$, because it enables access to the more reactive 3' mode.

In our scattering experiment, some $CH_4(\nu_3)$ molecules may undergo transition to the 3' mode due to the strong coupling with the 2' mode but their energy will be insufficient to overcome the activation barrier since the translational energy normal to the surface is very low. They will be reflected back into the gas-phase with some probability of remaining in the 3' mode. These will then be detected in the ν_1 state. What we have here, is a qualitative explanation for the conversion of $CH_4(\nu_3)$ to $CH_4(\nu_1)$.

It will be interesting to see whether theoretical models like RPH will be able to capture the relative final populations on a more quantitative level. The RPH approach is particularly promising for future scattering calculations because it does not suffer from artificial IVR by which classical or quasi-classical simulations are affected. Likewise it captures the dynamics of vibrational energy flow in an intuitive way. A fifteen-dimensional PES, which was able to reproduce CH_4 dissociation on Ni(111) with chemical accuracy, has been reported very recently[51]. It can be used as a starting point for RPH calculations aimed at obtaining vibrational state populations after scattering. I hope that the results presented in this chapter will stimulate efforts toward such calculations.

Lastly, it should be mentioned that results on the scattering of $CH_4(\nu_3, J = 1)$ from graphene covered Ni(111) presented[22] in van Reijzen's thesis show the absence of the ν_1 channel. This shows that the observed surface-induced IVR is not merely due to the presence of a surface but depends on the actual potential energy landscape.

References

[1] L. Juurlink, D. Killelea, and A. Utz, Prog. Surf. Sci. **84**, 69 (2009).

[2] R. D. Beck and A. L. Utz, in *Dynamics of Gas-Surface Interactions*, Springer Series in Surface Sciences, Vol. 50, edited by R. Díez Muiño and H. F. Busnengo (Springer, Berlin and Heidelberg, 2013) pp. 179–212.

[3] H. Chadwick and R. D. Beck, Chem. Soc. Rev. **45**, 3576 (2016).

[4] H. Chadwick and R. D. Beck, Annu. Rev. Phys. Chem. **68**, 39 (2017).

[5] L. B. F. Juurlink, P. R. McCabe, R. R. Smith, C. L. DiCologero, and A. L. Utz, Phys. Rev. Lett. **83**, 868 (1999).

[6] P. Maroni, D. C. Papageorgopoulos, M. Sacchi, T. T. Dang, R. D. Beck, and T. R. Rizzo, Phys. Rev. Lett. **94**, 246104 (2005).

[7] F. F. Crim, Proc. Natl. Acad. Sci. **105**, 12654 (2008).

[8] D. J. Nesbitt and R. W. Field, J. Phys. Chem. **100**, 12735 (1996).

[9] D. R. Killelea and A. L. Utz, Phys. Chem. Chem. Phys. **15**, 20545 (2013).

[10] S. Yoon, R. J. Holiday, E. L. Sibert, and F. F. Crim, J. Chem. Phys. **119**, 9568 (2003).

[11] H. A. Bechtel, J. P. Camden, D. J. A. Brown, and R. N. Zare, J. Chem. Phys. **120**, 5096 (2004).

[12] S. Nave, A. K. Tiwari, and B. Jackson, J. Phys. Chem. A **118**, 9615 (2014).

[13] B. Jiang, M. Yang, D. Xie, and H. Guo, Chem. Soc. Rev. **45**, 3621 (2016).

[14] J. Misewich, P. L. Houston, and R. P. Merrill, J. Chem. Phys. **82**, 1577 (1985).

[15] A. C. Wight and R. E. Miller, J. Chem. Phys. **109**, 8626 (1998).

[16] A. C. Wight, M. Penno, and R. E. Miller, J. Chem. Phys. **111**, 8622 (1999).

[17] J. Werdecker, M. E. van Reijzen, B.-J. Chen, and R. D. Beck, Phys. Rev. Lett. **120**, 053402 (2018).

[18] B. Yoder, *Steric effects in the Chemisorption of Vibrationally Excited Methane on Nickel*, Ph.D. thesis, École polytechnique fédérale de Lausanne, Lausanne (2010).

[19] W. R. Simpson, T. P. Rakitzis, S. A. Kandel, A. J. Orr-Ewing, and R. N. Zare, J. Chem. Phys. **103**, 7313 (1995).

[20] H. Chadwick, P. M. Hundt, M. E. van Reijzen, B. L. Yoder, and R. D. Beck, J. Chem. Phys. **140**, 034321 (2014).

[21] P. M. Hundt, *Quantum-state resolved gas/surface reaction dynamics of water and methane*, Ph.D. thesis, École polytechnique fédérale de Lausanne, Lausanne (2014).

[22] M. E. van Reijzen, *State-to-state scattering of CH_4 from Ni(111) and Gr/Ni(111)*, Ph.D. thesis, École polytechnique fédérale de Lausanne, Lausanne (2016).

[23] J. R. Manson, Comput. Phys. Commun. **80**, 145 (1994).

[24] A. Al Taleb and D. Farías, Phys. Chem. Chem. Phys. **19**, 21267 (2017).

[25] C. T. Rettner, E. K. Schweizer, and C. B. Mullins, J. Chem. Phys. **90**, 3800 (1989).

[26] B. D. Kay, T. D. Raymond, and M. E. Coltrin, Phys. Rev. Lett. **59**, 2792 (1987).
[27] K. Golibrzuch, J. H. Baraban, P. R. Shirhatti, J. Werdecker, C. Bartels, and A. M. Wodtke, Z. Phys. Chem. **229**, 1929 (2015).
[28] E. L. Sibert, J. T. Hynes, and W. P. Reinhardt, J. Chem. Phys. **81**, 1135 (1984).
[29] P. Hess and C. B. Moore, J. Chem. Phys. **65**, 2339 (1976).
[30] P. Hess, A. H. Kung, and C. B. Moore, J. Chem. Phys. **72**, 5525 (1980).
[31] H. Ibach and D. Bruchmann, Phys. Rev. Lett. **44**, 36 (1980).
[32] Y. Huang, A. M. Wodtke, H. Hou, C. T. Rettner, and D. J. Auerbach, Phys. Rev. Lett. **84**, 2985 (2000).
[33] Y. Huang, C. T. Rettner, D. J. Auerbach, and A. M. Wodtke, Science **290**, 111 (2000).
[34] J. D. White, J. Chen, D. Matsiev, D. J. Auerbach, and A. M. Wodtke, Nature **433**, 503 (2005).
[35] B. C. Krüger, S. Meyer, A. Kandratsenka, A. M. Wodtke, and T. Schäfer, J. Phys. Chem. Lett. , 441 (2016).
[36] R. J. V. Wagner, N. Henning, B. C. Krüger, G. B. Park, J. Altschäffel, A. Kandratsenka, A. M. Wodtke, and T. Schäfer, J. Phys. Chem. Lett. , 4887 (2017).
[37] K. Golibrzuch, N. Bartels, D. J. Auerbach, and A. M. Wodtke, Annu. Rev. Phys. Chem. **66**, 399 (2015).
[38] A. M. Wodtke, Chem. Soc. Rev. **45**, 3641 (2016).
[39] X. Luo, B. Jiang, J. I. Juaristi, M. Alducin, and H. Guo, J. Chem. Phys. **145**, 044704 (2016).
[40] V. A. Ukraintsev and I. Harrison, J. Chem. Phys. **101**, 1564 (1994).
[41] A. Bukoski and I. Harrison, J. Chem. Phys. **118**, 9762 (2003).
[42] H. L. Abbott, A. Bukoski, and I. Harrison, J. Chem. Phys. **121**, 3792 (2004).
[43] S. B. Donald and I. Harrison, Phys. Chem. Chem. Phys. **14**, 1784 (2012).
[44] L. Chen, H. Ueta, H. Chadwick, and R. D. Beck, J. Phys. Chem. C **119**, 14499 (2015).
[45] R. Milot and A. P. J. Jansen, Phys. Rev. B **61**, 15657 (2000).
[46] L. Halonen, S. L. Bernasek, and D. J. Nesbitt, J. Chem. Phys. **115**, 5611 (2001).
[47] P. M. Hundt, M. E. van Reijzen, R. D. Beck, H. Guo, and B. Jackson, J. Chem. Phys. **146**, 054701 (2017).
[48] S. Nave and B. Jackson, Phys. Rev. B **81**, 233408 (2010).
[49] B. Jackson and S. Nave, J. Chem. Phys. **135**, 114701 (2011).
[50] B. Jackson and S. Nave, J. Chem. Phys. **138**, 174705 (2013).
[51] X. Zhou, F. Nattino, Y. Zhang, J. Chen, G.-J. Kroes, H. Guo, and B. Jiang, Phys. Chem. Chem. Phys. **19**, 30540 (2017).

5 Rotationally inelastic scattering

5.1 Introduction

Rotational excitation is ubiquitous whenever rotationally cold molecular beams are collided with surfaces. It is the orientation-dependent conversion of translational into rotational motion ($T \rightarrow R$), just as if one were to bounce a (American) football on the floor and it would start spinning more or less depending on the initial angle between its long axis and the surface[1]. The possibility for a molecule to dissipate incidence kinetic energy E_i by conversion into rotational excitation can have important repercussions for surface chemistry[2–6]. The first bounce is decisive. If the molecule looses sufficient energy, it can no longer leave the potential well and thus becomes trapped. In subsequent bounces, the remaining kinetic and the temporarily stored internal energy can be dissipated by the degrees of freedom of the surface, mostly by excitation of phonons. Once the molecule is trapped there is a chance that processes such as diffusion or precursor-mediated dissociation enable further surface chemistry. The excitation of internal molecular DOFs at the expense of incidence kinetic energy can therefore have a crucial influence on chemical reactivity and becomes increasingly important as the number of internal DOFs increases.

The rotational energy distribution of directly (*i.e.* impulsively) scattered molecules can provide valuable information on the molecule-surface interaction. The magnitude of rotational excitation tells us something about the strength of the interaction's anisotropy with respect to the molecular orientation. Direct scattering generally gives rise to non-thermal rotational distributions among which so-called rotational rainbows are frequently observed[7]. A rotational rainbow corresponds to a local maximum in $J_f(\gamma_i)$, which is the classical rotational angular momentum in the scattered product as a function of initial orientation. This means that there is a range of orientations γ which yield very similar final angular momenta. If all orientations occur with the same probability, the final J distribution will then contain excess population at that particular J. The classical

singularity in the differential scattering cross-section is broadened by quantum effects and instead appears as a "bump" in the J_f distribution.

While rotational excitation in collisions with surfaces has been a field of intensive study, scattering experiments were limited almost exclusively to diatomic molecules. By contrast, only three systems have been studied so far, where the direct scatter of a non-linear polyatomic molecule was probed with rotational state resolution[6,8–11]. Moreover, only two of these studies involved a metal surface. This scarcity alone warrants further exploration of the rotationally inelastic scattering of CH_4 from Ni(111).

The previous chapter presented rotational distribution of $CH_4(\nu_3)$, which scattered from a hot ($T_S = 673\,K$) Ni(111) surface. It was established that the scattering is direct and that even if trapping-desorption takes place, we are unlikely to observe it due to our current detection geometry. We have further seen that for $\nu_3 \rightarrow \nu_3$ scattering the rotational distribution is non-Boltzmann with excess population in low-J levels and that the rotational temperature T_{rot} is far below the surface temperature. There is, however, at least one puzzling feature in these rotational distributions, which I did not address up to now. Namely that rotational excitation is surprisingly high, in particular at low incidence kinetic energies E_i. When we think of this excitation as being due to the conversion of translational energy, we usually mean by that the normal component $E_n = E_i \cos^2 \theta_i$ of the incidence translational energy since the forces during the surface encounter act primarily in this direction. Previous studies showed that in several diatomic molecule-surface systems rotational excitation indeed follows normal-energy-scaling, that is, the average final rotational energy is proportional E_n[12–15]. Consider the incidence conditions in the study from chapter 4. For $E_i = 100\,meV$ and an incidence angle of 65°, we find that only $E_n = 17.8\,meV$ are available for rotational excitation when we assume normal-energy-scaling. At the same time, the observed average rotational energy is $\langle E_{rot} \rangle = 13.4\,meV$ with population in levels extending up to $J = 10$ for which $\sim 72\,meV$ are required.

Three possible explanations for this high degree of excitation come to mind. First, the assumption of parallel momentum conservation might be wrong. Corrugation of the molecule-surface potential would lead to interconversion of normal and parallel momentum, which could also add to the torque experienced by the molecule and thereby enhance $T \rightarrow R$ energy conversion. Second, an attractive molecule-surface potential would accelerate the incident molecule and thus increase its normal kinetic energy, which can then be converted into rotational excitation. Third, the motion of surface atoms may add extra kinetic energy to the collision. Since we are performing our experiments at high surface temperatures, their thermal energy is considerable ($k_B T_S = 58\,meV$).

Rotational state-resolved angular distributions and measurements of the Doppler-

Table 5.1 Characteristics of the CH_4 molecular beams.

property	molecular beam characteristic			
composition	neat CH_4	3% in He	20% in He	3% in He
T_{Nozzle} (K)	297	297	600	600
p_{stag} (bar)	3	5	3	7
v_0 (m/s)	1060	1650	2090	2490
$T_{\|\|}$ (K)	14	4	39	13.2
$\langle E_{\text{kin}} \rangle$ (meV)	100	230	370	516

broadened transition linewidths in the scattered flux are expected to give additional insight into the rotational excitation mechanism of CH_4 scattering from Ni(111) because they allow us to infer about the translational energy contained in the scattered molecules. Unfortunately, the limited signal-to-noise ratio prevented these measurements for higher J-levels in the cases of $\nu_3 \rightarrow \nu_3$ and $\nu_3 \rightarrow \nu_1$ scattering. In this chapter, I turn to scattering of CH_4 in its vibrational ground state ($v = 0 \rightarrow v = 0$), that is, without IR pumping of the incident beam. Due to the low E_i, we expect CH_4 to remain in $v = 0$ upon scattering, which should results in less diluted state distributions and thus higher signal levels.

5.2 Experimental details

Four different molecular beam conditions covered a range of incident kinetic energies between 100 and 516 meV, where the three beams, which had the lowest energies, were identical to those in chapter 4. The beam conditions and properties are shown in Table 5.1. Despite the rotational cooling in the supersonic jet expansion, not all population will reside in the lowest rotational state but there will be some population in higher J states, depending on the expansion conditions. This means that the overall rotational distributions for CH_4 scattered in the ground vibrational state ($v = 0 \rightarrow v = 0$) will be an average with contributions from several initial rotational states J_i. As I will show below, the rotational temperature of the incident beam has a significant impact on the observed state populations after scattering. We therefore determined the fractional populations of the few lowest rotational levels in the incident molecular beam using our pyroelectric detector in combination with the Pump OPO. The laser setup was identical to that in chapter 4, apart from the fact that the Pump OPO was not used in the scattering experiments. This is shown schematically in Figure 5.1. The underlying idea of this method is the same as in the case of BILT but, due to the much slower time response of the pyroelectric detector, the OPO beam is only chopped at a frequency of 2 Hz (at 50% duty cycle).

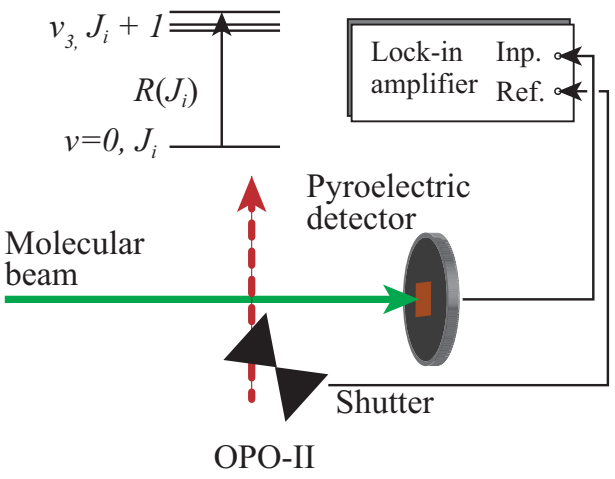

Figure 5.1 Schematic diagram of the tagging scheme for determination of the incident beam rotational populations using the pyroelectric detector.

The fractional populations in the different J_i states were determined by comparing the asymptotes of laser fluence curves with the OPO tuned to appropriate transitions of the ν_3 fundamental band. Here, we used R-branch transitions in all cases, that is $(\nu_3 = 1,\ J_i + 1 \leftarrow v = 0,\ J_i)$. Figure 5.2 shows laser fluence curves at all E_i and including J-levels up to $J = 6$ when higher nozzle temperatures were used. When the nozzle was at room temperature, populations were negligible in levels beyond $J = 4$. In all cases, population was negligible in levels with $J > 6$. We can see that saturation was achieved without exception. The relatives asymptotes of the fluence curves determined the fractional J-level populations. These are compiled in Table 5.2 together with the average rotational energies $\langle E_{\text{rot}} \rangle_0$ for each beam. Errors on the fractional populations are not larger than 1 %.

Line shape measurements were carried out with the focusing lenses removed in order to avoid line broadening due to RAP and limit transit time broadening. We measured the OPO beam spot size with the knife edge method at a position just before the optical access window to the bolometer. Figure 5.3 shows the transmitted power as a function of knife position. I fitted the data points with

$$I(x) = \frac{I_0}{2}\left[1 + \text{erf}\left(\frac{x - x_0}{w}\right)\right], \tag{5.1}$$

which is the expected functional form for a Gaussian beam, and where w is a width parameter that is related to the full width at half maximum according to FWHM = $2\sqrt{\ln 2}w$. The beam had a diameter of 4.66 mm (FWHM).

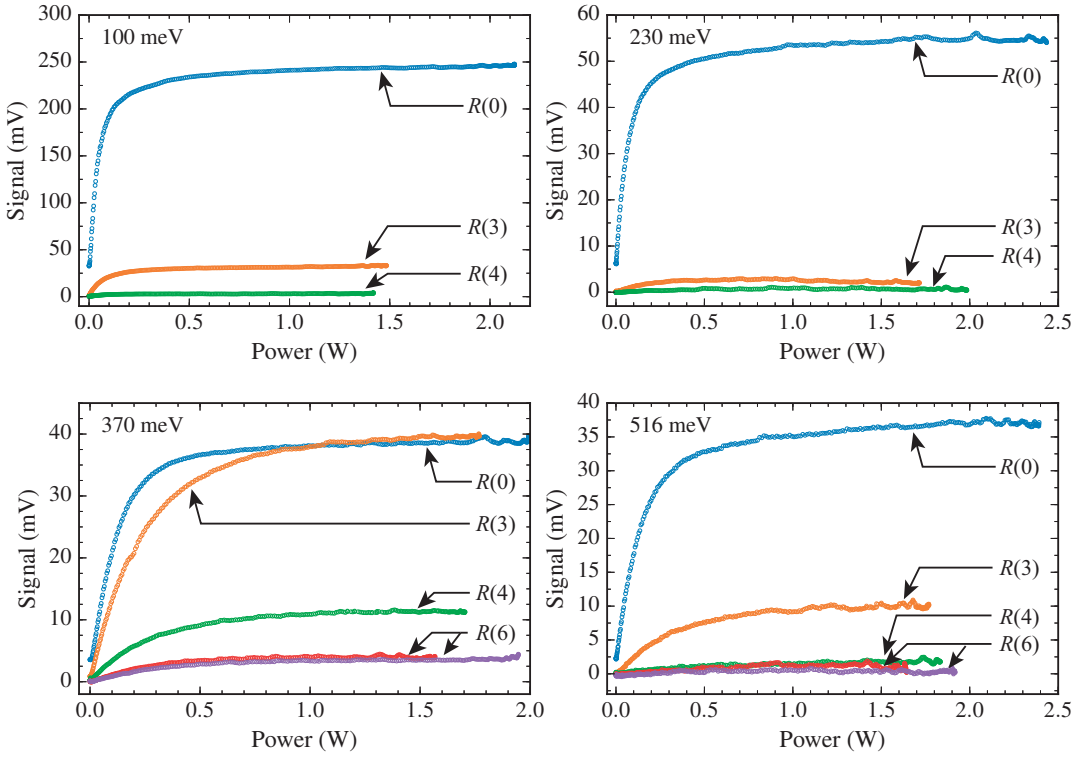

Figure 5.2 Laser fluence curves determining the incident beam rotational populations. Note that there are two distinct $v = 0$, $J = 6$ sublevels. Populations were negligible in levels with $J > 6$ in all cases.

Table 5.2 Fractional rotational populations in the incident beams and average rotational energies. A_1 and A_2 denote the rovibrational symmetries of the two distinct $J = 6$ levels.

	Incidence kinetic energy (meV)			
J	100	230	370	516
0	0.870	0.935	0.396	0.725
3	0.116	0.065	0.408	0.201
4	0.001	0	0.117	0.043
6 A_1	–	–	0.042	0.023
6 A_2	–	–	0.038	0.008
$\langle E_{\text{rot}} \rangle_0$ (cm^{-1})	8.75	4.06	55.5	24.0
$\langle E_{\text{rot}} \rangle_0$ (meV)	1.08	0.50	6.88	2.98

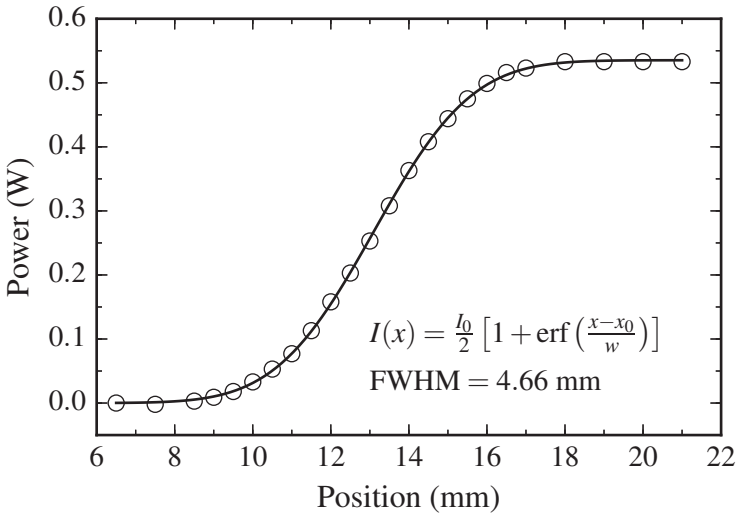

Figure 5.3 Determination of the OPO beam spot size by the knife-edge method. The transmitted laser power is monitored as a function of the knife position. This is the unfocused spot size used for line shape measurements.

We shall briefly discuss the different mechanisms that may contribute to the broadening of our absorption profiles and estimate their magnitude. Transit time broadening occurs when the time that the molecule spends in the radiation field is shorter than the natural lifetime of its excited state. For an OPO beam with a Gaussian intensity profile, the broadening can be estimated using

$$\Delta\nu_{\mathrm{transit}} = \frac{2\langle v\rangle}{\pi d}\sqrt{2\ln 2}\,, \tag{5.2}$$

where $\langle v\rangle$ is the average molecular velocity and d is the diameter of the OPO beam corresponding to the points where the electric field strength (irradiance) drops to $1/\mathrm{e}$ ($1/\mathrm{e}^2$) of its peak value. The $1/\mathrm{e}^2$ diameter d is related to the FWHM that we have determined above by $d = \mathrm{FWHM}\sqrt{2/\ln 2}$, which yields $d = 7.92\,\mathrm{mm}$. For $\langle v\rangle = 2000\,\mathrm{m/s}$, we find that transit time broadening contributes $\sim 190\,\mathrm{kHz}$ to the linewidth.

Under non-RAP conditions, power broadening is expected to influence the linewidth as well. It occurs when the fluence is high enough to cause Rabi-cycling between the upper and lower levels. This limits the lifetime of the upper level and thus causes a broadening, which is given by the Rabi frequency as defined in Equation 3.27. With the current beam diameter, a typical power of 700 mW and a transition dipole moment of $1.8 \cdot 10^{-31}\,\mathrm{Cm}$, corresponding to the $R(0)$ transition, we find a Rabi frequency of 0.9 MHz. Note that this value serves as an upper limit because the angular momentum

coupling moments, which are given by the Clebsch-Gordan coefficients in Equation 3.43, significantly reduce the transition dipole moments for all other transitions.

Doppler broadening makes the most important contribution to the linewidth in our setup, notwithstanding that our Tagging OPO crosses the scattered flux perpendicularly. The small velocity component along the OPO propagation direction, however, is sufficient to generate a measurable Doppler shift, which is given by

$$\nu_{\text{Doppler}} = \nu_{12} \frac{v \sin(\alpha)}{c} , \tag{5.3}$$

where ν_{12} is the transition center frequency, v is the final molecular velocity and α is the angle under which the molecule's flight path diverges from the surface-bolometer axis. We can estimate the largest allowed Doppler shift for a given velocity by finding the largest deflection angle α_{max} under which molecules can still pass the bolometer aperture. Using the bolometer aperture diameter of 4 mm, the surface-distance of 360 mm and a maximum molecular beam spot size on the surface of 2 mm, we find $\alpha_{\text{max}} \approx 0.48°$. For a velocity of $\langle v \rangle = 2000\,\text{m/s}$, the largest detectable Doppler shift is $\sim \pm 5\,\text{MHz}$ (at $3018\,\text{cm}^{-1}$). Note that the linewidth depends proportionally in the same way on transit time and Doppler broadening, *i.e.* the width is bilinear in v.

Lastly, we have to consider the instrumental linewidth of the OPO. The quoted instantaneous linewidth is $< 60\,\text{kHz}$ on a $500\,\mu\text{s}$ time-scale. However, frequency fluctuations on a somewhat longer time-scale will effectively broaden the linewidth. I estimate from the fluctuations seen in the transfer cavity that these are on the order of $\pm 0.3\,\text{MHz}$. Note that saturation effects act on the instantaneous homogeneous laser linewidth and are therefore negligible. I have determined the instrumental linewidth by measuring the transition linewidths in the incoming molecular beam using the pyroelectric detector (see appendix F). By varying the beam speed v_0, which I determined using the time-of-flight method, I was able to extrapolate the linewidth to $v_0 = 0$, yielding an instrumental linewidth of $1.0 \pm 0.5\,\text{MHz}$, which already includes power broadening. We can therefore assume that residual Doppler broadening limits the width of the absorption profiles.

5.3 Computational method

I performed classical trajectory calculations in order to aid interpreting the scattering rotational distributions. The scattering trajectories were calculated using the Wolfram Mathematica$^{\text{TM}}$ software with a script, which was kindly provided by A. Kandratsenka from the Wodtke group[(a)]. Park *et al.* used[8] this code to simulate the rotationally inelas-

[(a)]The notebooks can be retrieved from the location given in appendix A.

tic scattering of formaldehyde from Au(111). Here, the model was able to qualitatively reproduce the propensity for excitation of the *a*-axis, *i.e.* twirling motion, the presence of a rotational rainbow in the *a*-axis rotational distribution, and the dependence of the final rotational energy on E_i. I will briefly describe the principle of these calculations and the underlying assumptions and approximations.

Briefly, the CH_4 molecule is modeled as a rigid rotor with an equilibrium C–H bond length of 1.085 Å[16]. The surface was approximated as a flat harmonic oscillator with the mass of one nickel atom $M_{Ni} = 58$ amu and a Debye frequency of $\omega_D = k_B\theta_D/\hbar$. I adopted a value of $\theta_D = 388$ K for the Debye temperature of Ni(111), which has recently been determined[17] by Tamtögl *et al.* using helium atom scattering. Note that this corresponds to a phonon energy of 270 cm^{-1} or 33 meV.

Two simple potentials were used to model the molecule-surface interaction. First, I used a purely repulsive "hard-sphere" potential ("HS"),

$$V_{HS}(z) = a \cdot e^{-\alpha(r-r_{vdW})}\,, \tag{5.4}$$

where r is the atom-surface distance, r_{vdW} is the van der Waals radius of either hydrogen or carbon, which were taken to be 1.2 and 1.7 Å, respectively. For the adjustable parameters a and α, I chose values of 1 eV and 20 $Å^{-1}$, respectively. The second potential was a Lennard-Jones potential ("LJ") of the form

$$V_{LJ} = \epsilon_{LJ}\left[\left(\frac{r_{LJ}}{r}\right)^{12} - 2\left(\frac{r_{LJ}}{r}\right)^{6}\right]\,. \tag{5.5}$$

Here, the potential well depth ϵ_{LJ} and the well position r_{LJ} for a given atom-surface pair are approximated using the Lorentz-Berthelot rules, which read

$$\epsilon_{LJ}(AB) = \sqrt{\epsilon_{LJ}(A)\cdot\epsilon_{LJ}(B)}\,, \tag{5.6}$$

and

$$r_{LJ}(AB) = \frac{r_{LJ}(A) + r_{LJ}(B)}{2}\,. \tag{5.7}$$

Here, A and B represent an atom that constitutes the CH_4 molecule and the surface "cube", respectively. I used the Lennard-Jones parameters as defined in the UFF force field[18]. Table 5.3 compiles the relevant Lennard-Jones parameters. I determined the adsorption energy by integrating 100 trajectories for 20 ps, where the molecule was initially close to the potential well location ~ 4 Å and the surface at rest. The averaged final potential

Table 5.3 Lennard-Jones parameters used in the classical trajectory simulations. Taken from Ref. [18].

Species	r_{LJ} / Å	ϵ_{LJ} / kcal/mol
H	2.886	0.044
C	3.851	0.105
Ni	2.834	0.015

energies gave an estimate of the binding energy. An early estimate of the physisorption well depth based on temperature-programmed desorption (TPD) experiments was given by the Ceyer group, who reported[19] a value of 12 kJ/mol. Recent DFT calculations that simulated CH_4 adsorption on various Ni surfaces put forward a somewhat lower value of about 5–7 kJ/mol. These values are also in better agreement with the scattering study reported[20] by Al Taleb and Farías. I adopted here a value of 5 kJ/mol for the physisorption well depth. When using the original parameters of the force field, the potential underestimated the physisorption energy by a factor of about 15, so I rescaled the potential by the same factor.

In contrast to the work of Park *et al.*, initial excitation of the surface oscillator has to be included in order to model scattering from the hot surface. I modified the code to initialize the harmonic oscillator with random phase and an initial energy of $E_S(0) = k_B T_S$. Moreover, the initial molecular orientation was sampled randomly and the angular momentum was set equal to zero. Trajectories were started 8 Å above the surface, where the molecule-surface interaction is still negligible, and with an angle of incidence of 65°. A total of 20k trajectories were integrated over 6 ps at each E_i and $E_S(0)$.

5.4 Results

Rotational distributions of the scattered CH_4 were obtained by measuring the BILT signal for Q-branch transitions of the ν_3 fundamental band up to $J = 10$. The $R(0)$ transition probed the rotational ground state. A sample state distribution at $E_i = 230$ meV is presented in Figure 5.4. This figure compares the fractional state populations of the incident and scattered molecules, revealing that rotational excitation is significant with detectable population extending up to $J = 10$. It stands in contrast to the incident beam populations, where 93 % of all molecules reside in $J = 0$ and the highest populated state is $J = 3$.

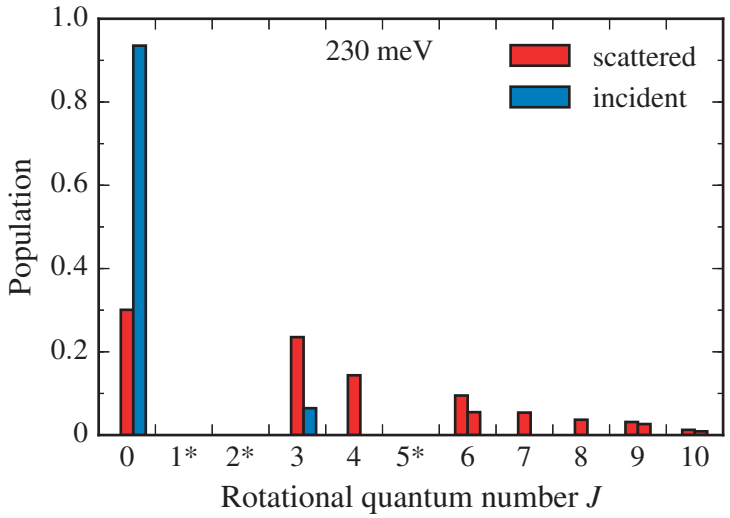

Figure 5.4 Sample rotational distributions before and after the surface collision, here at $E_i = 230\,\text{meV}$. Non-existing levels are marked by an asterisk. The two distributions highlight the contrast between the rotationally cold incident beam and the significant rotational excitation after collision with the surface.

The $v = 0$ rotational distributions obtained at the four different E_i are shown in the form of Boltzmann plots in Figure 5.5. Here, the populations are scaled by J-level degeneracies and plotted logarithmically against the rotational term value. The energy of the lowest-lying accessible state E_0 is equal to zero for *meta*-CH_4. Each subsequent data set is moreover scaled by a factor of 10 with respect to the previous one in order to enhance visibility. We can see here that all distributions are non-Boltzmann, exhibiting enhanced population in at least the lowest two J-levels. This is similar to the population distribution, which we saw in chapter 4 for $\nu_3 \rightarrow \nu_3$ scattering. Although E_i varies by more than a factor of five, all four distributions look remarkably similar. Characteristic temperatures T_{rot} describing the high-J portions of the distributions were obtained by a linear fit to the data points with $J \geq 4$. All T_{rot} are $< 250\,\text{K}$ and therefore well below the surface temperature of 673 K. If one were to assign a temperature to the $J < 4$ portion of the distributions, they would clearly be even colder, indicated by the steeper slope. We can further see that there is a trend of T_{rot} to increase with E_i, which is interrupted at 370 meV, where the highest rotational excitation is observed. Latter can be readily explained by the comparably high rotational energy already present in the incident beam at this particular E_i (see Table 5.2). Specifically, $\langle E_{\text{rot}} \rangle_0$ is more than twice that of the next "colder" incident beam.

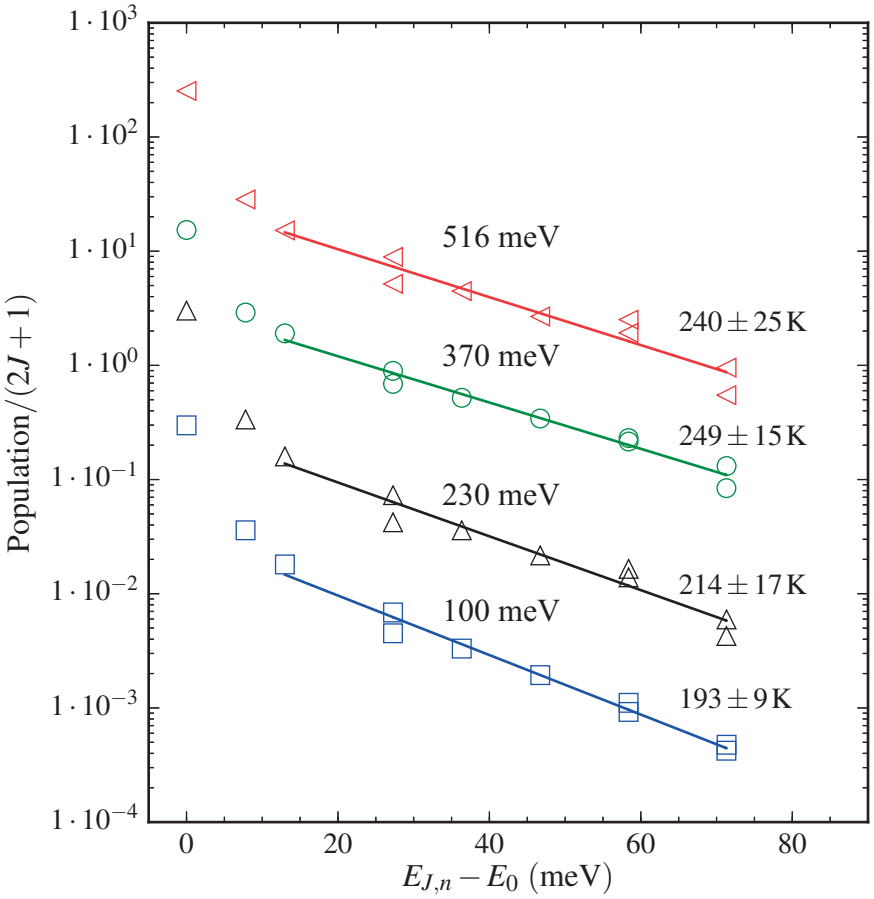

Figure 5.5 Boltzmann plot of the rotational distributions at all four E_i. Linear fits to the data points with $J \geq 4$ determined the characteristic temperatures T_{rot}, which are shown inside the graph.

Owing to the non-Boltzmann behavior, I chose to quantify rotational excitation in terms of the mean rotational energy $\langle E_{\text{rot}} \rangle$, which has been defined in Equation 4.3. The dependence of rotational excitation on E_i is shown in Figure 5.6. More precisely, this figure plots the effective rotational excitation $\langle E_{\text{rot}} \rangle_{\text{eff}} = \langle E_{\text{rot}} \rangle - \langle E_{\text{rot}} \rangle_0$ against E_n. Measurement errors of the $v = 0$ data are expected to be not larger than the symbols size. We can see that the absolute magnitude of rotational excitation and the E_n dependence is very similar in the two vibrationally elastic scattering channels. A linear fit to the $v = 0$ data yields a slope of $\mathrm{d}\langle E_{\text{rot}} \rangle_{\text{eff}} / \mathrm{d}E_n = 0.04 \pm 0.009$ and an intercept with the vertical axis at $13.7 \pm 0.6\,\text{meV}$.

We have seen that rotational excitation in $v = 0 \longrightarrow v = 0$ is indistinguishable from that in $\nu_3 \longrightarrow \nu_3$ scattering, within experimental error. We now take a closer look at the absorption line profiles measured in the scattered flux. Figure 5.7 compares the

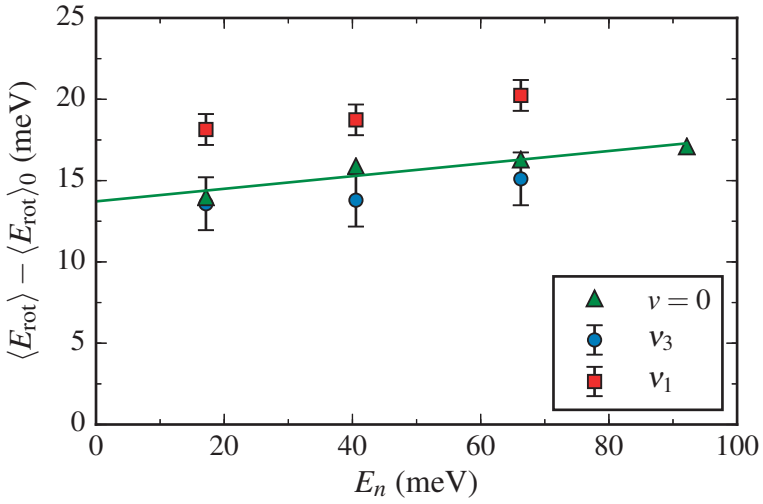

Figure 5.6 Rotational excitation as a function of normal incidence kinetic energy E_n comparing the $v = 0 \rightarrow v = 0$, $\nu_3 \rightarrow \nu_3$ and $\nu_3 \rightarrow \nu_1$ scattering channels. The data corresponding to the latter two is the same as in chapter 4. The solid green line is a linear fit through the $v = 0$ data points.

absorption line profile of the (ν_3, $J = 3 \leftarrow v = 0$, $J = 3$) obtained at four incident beam speeds v_0 indicated on the right. We see here that, as in the case of ($\nu_3 \rightarrow \nu_1$) vibrationally inelastic scattering presented in the previous chapter, the residual Doppler linewidth correlates with v_0.

The higher signal-to-noise ratio in $v = 0 \rightarrow v = 0$ scattering allowed us to measure the line profiles for a large number of J-levels. These were then treated in the following way: First, a linear baseline was subtracted from the spectral scan to compensate for drift in laser intensity. Subsequently, a Gaussian fit to the corrected profile determined the linewidth. The result of this analysis is presented in Figure 5.8. We see here that the dependence of the linewidth on the incidence speed is approximately linear. Moreover, the J-dependence of the linewidth $\Delta\nu(J)$ allows testing of our initial hypotheses. For all incidence speeds v_0, the dependence of $\Delta\nu$ is markedly insensitive to J_f. Only at the highest v_i, we can suspect a systematic drop with increasing J_f. This proves that scattering is direct. If trapping-desorption were to play a role, translational and rotational energy accommodation with the surface would have to occur to some degree. Molecules that have thermalized on the surface are expected to occupy higher J-levels (a rotational distribution at 673 K would peak at $\sim J = 6$). If the high-J states were preferentially populated because of trapping-desorption, we should also observe much lower velocities since the mean thermal velocity for methane desorbing at T_S is only $\sim 470\,\mathrm{m/s}$. We would then expect to see a much more pronounced drop in the Doppler-broadened linewidth

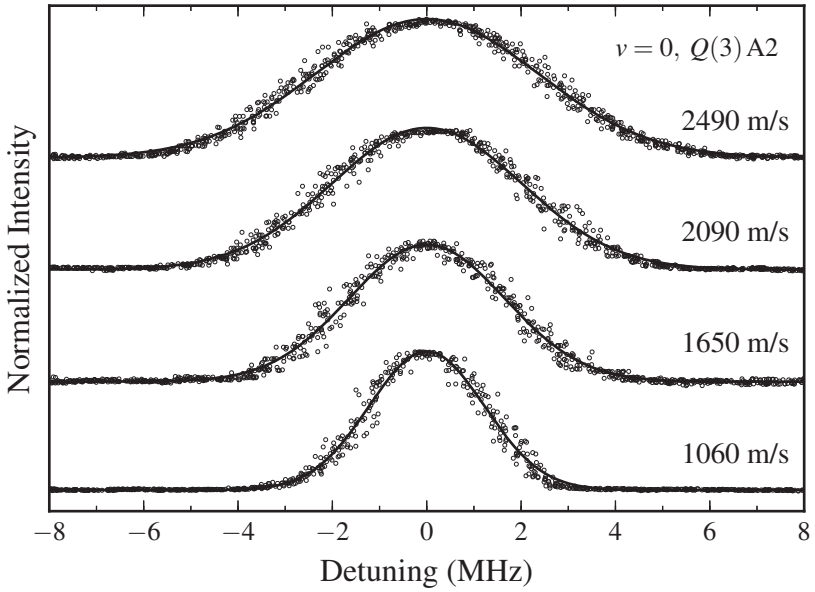

Figure 5.7 Comparison of the absorption line profile of the ν_3, $Q(3)$ transition for the four different incident beams. Numbers on the right are the incident beam speeds.

when going to higher values of J_f.

The insensitivity of $\Delta\nu$ to final rotational energy also implies that the CH_4 molecules cannot have acquired their rotational energy by conversion of incidence kinetic energy alone, especially at the lowest E_i. To highlight this aspect, I estimated the J_f-dependence of $\Delta\nu$ purely on the basis of $T \rightarrow R$ energy transfer. These are shown as dashed lines in Figure 5.8 and were calculated as follows: First, I assume that the available incidence energy is reduced due to the excitation of surface phonons. The hard-cube model is used to calculate the fraction of retained normal energy $E_{f,n}^{\mathrm{HC}}$, which is given by

$$E_{f,n}^{\mathrm{HC}} = E_n \frac{(M-m)^2}{(M+m)^2}\,, \tag{5.8}$$

with the masses M and m of Ni and CH_4, respectively. Ignoring any dependence on the scattering angle θ_f, I assume the final translational energy to be given by

$$E_f(J) = E_{i,p} + E_{f,n}^{\mathrm{HC}} - E_{\mathrm{rot}}(J)\,, \tag{5.9}$$

and the final speed as $v_f(J) = \sqrt{2E_f(J)/m}$. The predicted $\Delta\nu(J)$ is obtained by scaling

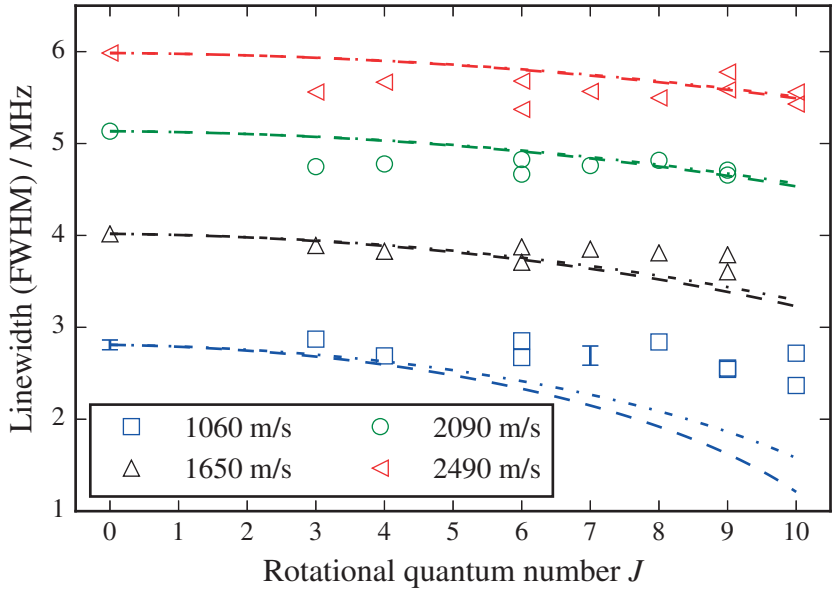

Figure 5.8 Measured linewidths (FWHM) in dependence of final rotational state J_f and incidence speed. Error bars are shown where the same profile was measured five times and the standard error of the mean calculated corresponding to the 95 % confidence interval. Also shown is a prediction of the width's J-dependence assuming pure $T \longrightarrow R$ energy transfer with (dashed dotted lines) and without an additional attractive potential (dashed lines).

$v_f(J)$ according to

$$\Delta\nu(J) = \Delta\nu(J=0)\frac{v_f(J)}{v_f(J=0)}\,. \tag{5.10}$$

We can see that this prediction fails to describe the observed $\Delta\nu(J)$ at low E_i. The kinetic energy that remains after the $T \longrightarrow R$ conversion is too low to explain the high-J linewidths, even though the model allows for the conversion of an arbitrary amount of parallel kinetic energy into rotation. Furthermore, adding an attractive potential well of $V = 5\,\mathrm{kJ/mol}$, that is,

$$E_{f,n}^{\mathrm{HC}} = (E_n + V)\frac{(M-m)^2}{(M+m)^2}\,, \tag{5.11}$$

does not change the situation significantly, as indicated by the dashed dotted lines in Figure 5.8.

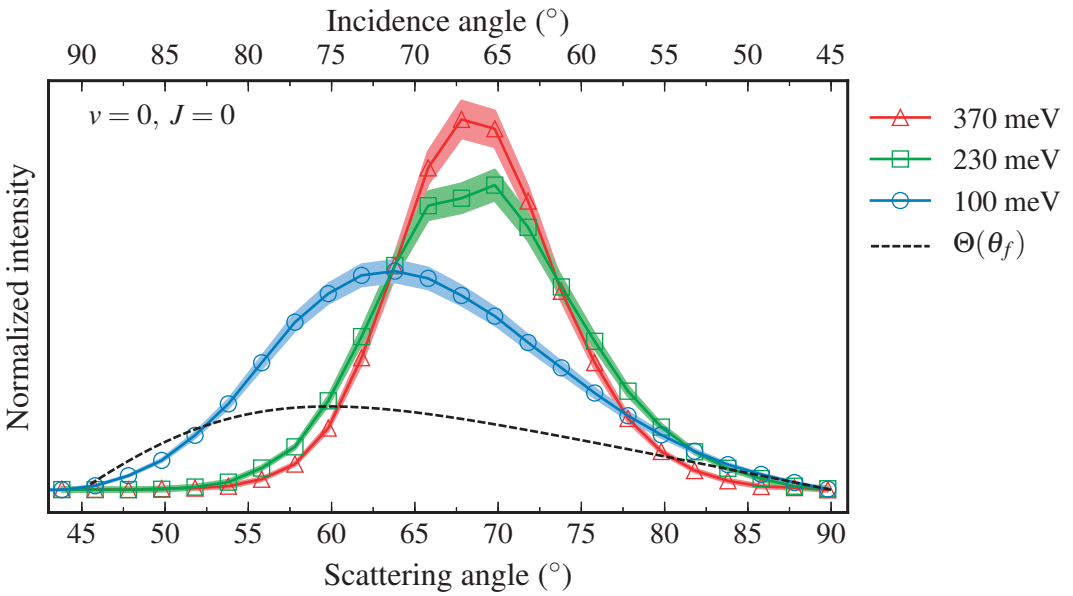

Figure 5.9 Scattering angular distributions for the $v = 0$, $J = 0$ state at different E_i. The shaded areas highlight the estimated measurement uncertainties and the dashed line indicates the predicted shape of a pure $\cos\theta_f$ distribution. Each distribution is normalized with respect to its integrated intensity.

Figure 5.9 shows state-resolved angular distributions at the three lowest E_i. BILT detection was used to single out molecules in the $J = 0$ rotational state. The angular distributions become narrower and peak closer to the specular angle $\theta_f = 67.5°$ as E_i increases. This is consistent with direct scattering, as discussed in chapter 4. The dashed line further displays the prediction for a pure $\cos\theta_f$ distribution. Its derivation can be found in appendix G.

We can understand the narrowing of the distributions as follows: The thermal energy transferred from the surface to the molecule becomes less important in determining the final momentum as E_i increases. The shift of the low-energy angular distribution toward smaller θ_f, *i.e.* toward the surface normal, can be qualitatively understood if we recall the hard-cube model. Under the assumption that parallel momentum is conserved in the surface collision, the shift in exit angle $\Delta\theta_f$ from the specular direction is determined by the loss or gain of normal kinetic energy ΔE_n. When normal energy is lost in the collision ($\Delta E_n < 0$), the scattering will be super-specular while it will be sub-specular when $\Delta E_n > 0$. We can estimate ΔE_n using Equation 5.11 and by adding an additional term, which accounts for the average thermal energy imparted by the surface atom on

the projectile[21],

$$\Delta E_n = -\frac{4mM}{(m+M)^2}(E_n + V) + \frac{m(2M-m)}{(m+M)^2} 2k_B T_S \ . \tag{5.12}$$

At $T_S = 673\,\mathrm{K}$, the last term amounts to 34 meV. Without an attractive potential V, a critical incident energy of $E_i^c = 280\,\mathrm{meV}$ is required to reach the same magnitude of "hard-cube energy loss" and make ΔE_n vanish. At lower E_i, sub-specular scattering is expected, coming from the normal momentum added by the surface atom motion. In other words, the annihilation (deexcitation) of phonons is more likely at this elevated surface temperature compared to their creation, which leads to a net energy transfer from the surface to the molecule[22,23].

While the E_i-dependent shift of the angular distribution is in qualitative agreement with our experimental observations, we see the distribution peak at the specular angle already at 230 meV. Adding the additional attractive term V results in a decrease of E_i^c. If we assume a value for V of $5\,\mathrm{kJ/mol} = 52\,\mathrm{meV}$, then ΔE_n can never become positive and only specular to super-specular scattering should be observed, which is inconsistent with the measurement. Hence, the hard-cube model does not capture the scattering dynamics quantitatively. However, this should not surprise us considering the simplifying assumptions. The atoms of relatively light metals such as Ni are strongly bound. The hard-cube model assumes that the mass of the surface is equal that of one Ni atom, but the effective mass, which the incoming molecule experiences, is most likely higher due to the strong binding of the metal atoms and the shallow incidence angle. The latter is another important factor that can lead to a breakdown of the model because we cannot expect full conservation of parallel momentum at the oblique incidence angles sampled by our experiment. Finally, we note that $T \rightarrow R$ energy conversion is also not included in the hard-cube model.

Figure 5.10 displays angular distributions for three different J_f-levels at $E_i = 370\,\mathrm{meV}$. As J_f increases, the distributions shift away from the specular angle and toward the super-specular direction. This can be rationalized by similar arguments. If part of E_n is converted into rotational energy, then this loss of normal momentum leads to a shallower exit angle. The higher J_f, the more normal energy was most likely converted into rotational energy and the larger θ_f will be. At low E_i, we encounter a different situation, as shown in Figure 5.11. Here, we see no obvious shift when comparing $J_f = 0$ and $J_f = 7$. This indicates that the energy, which is required for populating the $J_f = 7$ level, does not come from incident translational energy. The reason for the broadening of the high-J distributions in both Figure 5.10 and Figure 5.11 is not immediately clear.

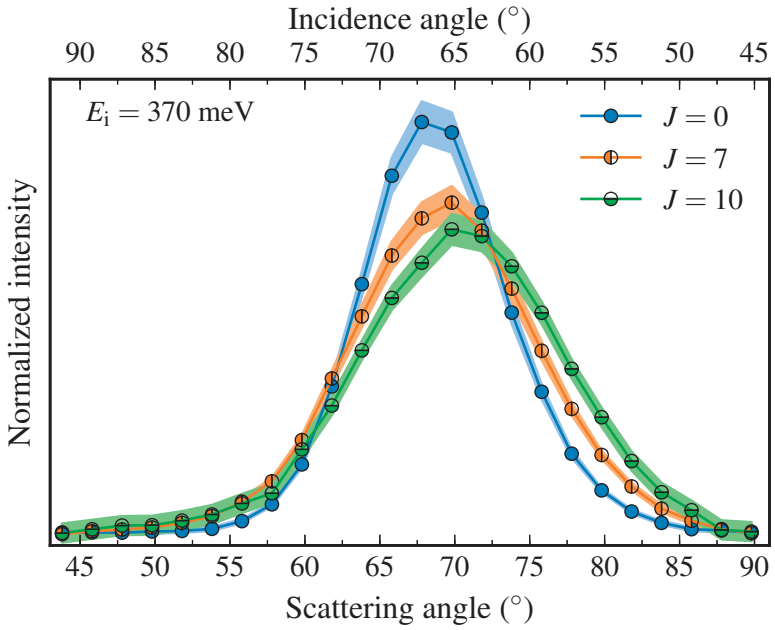

Figure 5.10 Scattering angular distributions for J-levels 0, 7 and 10 at $E_i = 370\,\text{meV}$. The shaded areas indicate the estimated measurement uncertainties.

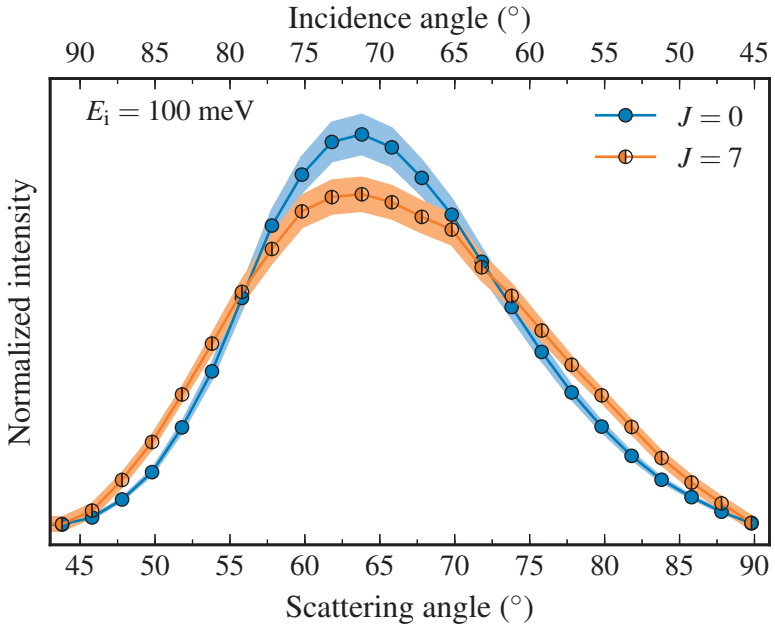

Figure 5.11 Scattering angular distributions for J-levels 0 and 7 at $E_i = 100\,\text{meV}$. The shaded areas indicate the estimated measurement uncertainties.

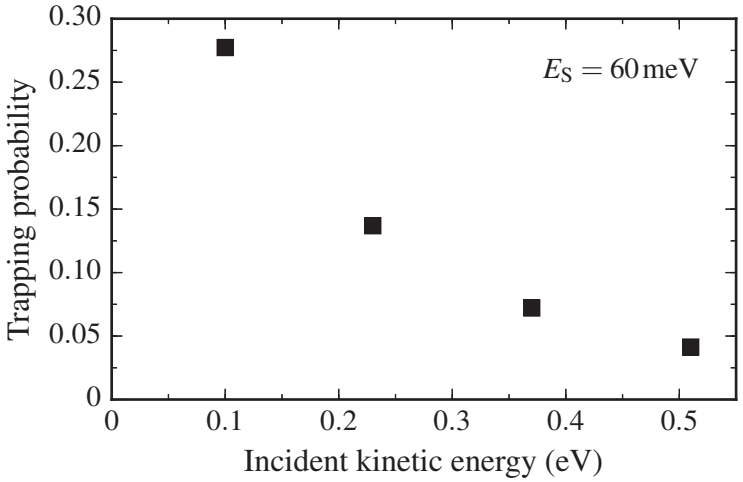

Figure 5.12 Trapping probability in dependence of E_i obtained from classical trajectory simulations using the Lennard-Jones potential and with an initial surface oscillator energy of $E_S(0) = 60\,\text{meV}$.

Taking all the experimental results together, we arrive at the following picture: At low E_i, the mean energy added by surface motion to the CH_4 molecules is comparable to or higher than their normal incidence translational energy. Here, rotational excitation is fueled by the thermal energy of the surface, while $T \rightarrow R$ conversion plays only a minor role. At higher E_i, this situation reverses and now E_n becomes high enough to excite the rotation, while the relative influence of the surface motion diminishes.

We now turn to the results of the classical scattering simulations. Since the Lennard-Jones potential allows molecules to become trapped, we first take a look at the trapping probability as a function of E_i. This is displayed in Figure 5.12, where a molecule was considered trapped if its trajectory ended up within an distance of 10 Å from the surface at the end of the integration time. Molecules, which are already further away, have left the potential well and cannot return. The initial energy of the surface oscillator was $E_S(0) = 60\,\text{meV}$, which corresponds to a surface temperature of about 700 K, similar to experiment. We see that the trapping probability is about 28 % for the lowest E_i but then drops rapidly as E_i is increased. At $E_i = 516\,\text{meV}$, merely 4 % of all molecules can be considered trapped. Our experimental results show no evidence for TD even at the lowest E_i. This is most likely due to the detection geometry, which strongly favors the detection of direct scatter over desorbed molecules, as I already discussed in the previous chapter.

In the further analysis, the "trapping trajectories" were discarded. Instead of comparing the experimentally obtained rotational state distributions with those from the simulations directly, I analyzed the trajectories in terms of their mean rotational en-

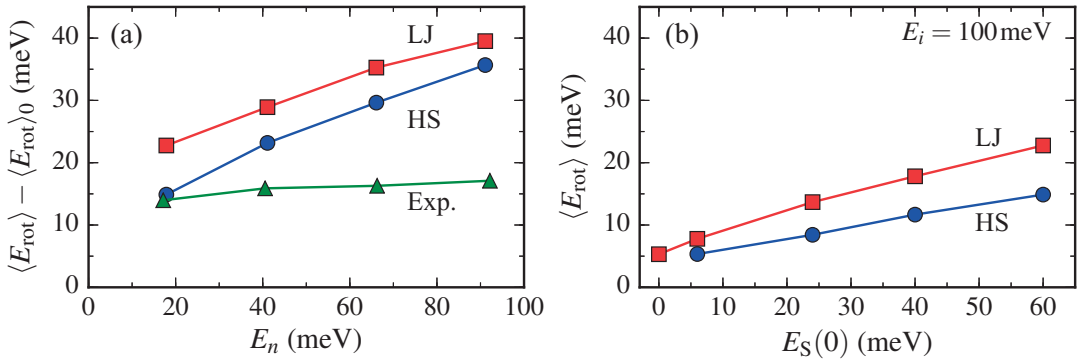

Figure 5.13 Predicted rotational excitation obtained from classical scattering trajectory simulations using a hard-sphere (HS) and an empirically scaled Lennard-Jones potential (LJ) as a function of normal incident kinetic energy (a) and initial energy of the surface oscillator (b). Experimental results are shown for comparison. Solid lines connect the points to guide the eye. The initial energy of the surface oscillator was $E_S(0) = 60$ meV in (a) and in (b) E_i was 100 meV.

ergy $\langle E_{rot}\rangle$ content after scattering. Direct comparison would overrate the predictive power of this zero-order model for several reasons: The use of classical mechanics and the assumption of a structureless surface establishes a direct relationship between exit rotational energy and final scattering angle. Although we see a difference in the angular distributions with final E_{rot}, this dependence is not nearly as strong as in the classical simulations. It is likely that motion of the surface, which is not captured in the simulations, causes additional broadening. Furthermore, no out-of-plane scattering occurs in the simulations due to the one-dimensionality of the potential. Even though it was not probed in the experiments, we can be sure that out-of-plane scattering occurs. Another important factor why a direct comparison cannot be made is the sparse and irregular occurrence of rotational quantum states, which is contrasted by the continuum of rotational energy which molecules can acquire in the classical mechanics simulations. Partitioning of the final rotational energy into individual quantum states is ambiguous.

Figure 5.13 (a) shows the dependence of $\langle E_{rot}\rangle$ on E_i for both hard-sphere and Lennard-Jones potential. Direct comparison with the experimental results is included in the figure and reveals that the simulations in either case strongly overestimate the gain in rotational energy with increasing E_n. However, we can see that the calculations predict a rather large $\langle E_{rot}\rangle$ offset at zero kinetic energy, in agreement with the experimental observation. Rotational excitation is found to be higher when the Lennard-Jones potential is used. This is not surprising because the potential energy well adds some extra energy normal to the surface, which can be converted into rotation.

In order to test the hypothesis that surface motion contributes significantly to the rotational excitation, I performed further simulations with varying initial energies of the surface oscillator. Figure 5.13 (b) shows the mean rotational energy of scattered molecules as a function of $E_S(0)$ for an incident beam energy of 100 meV. We can clearly see here that rotational excitation indeed scales with initial excitation of the surface oscillator.

5.5 Discussion

A propensity for scattering into low-J states has precedence in the surface-scattering of polyatomic molecules. Kay *et al.* reported[10] that NH_3 scatters preferentially into the lowest J-states when scattered from Au(111). They were able to explain this observation using quasi-classical scattering calculations[24], which revealed a steering effect when the NH_3 approaches the metallic surface. A strong dipole-image dipole interaction orients the molecule with its symmetry axis parallel to the surface before the collision, which causes it to scatter with low final angular momentum. This identified the observed preference for rotationally elastic scattering as a zero-energy rotational rainbow. In the case of CH_4, a similar steering effect cannot occur because CH_4 carries no permanent dipole moment.

Interestingly, Wight and Miller observed no deviation from a Boltzmann distribution when they scattered CH_4 from the presumably stronger corrugated LiF(001) surface[9]. This precludes the interpretation that the "sphericity" of CH_4 may be responsible for the preference of rotationally (near)-elastic scattering. The simplistic classical scattering calculations presented above did not reveal a similar propensity and direct comparison of the experimental and the computed rotational energy distributions is hampered by the irregular and sparse J-level occurrence in CH_4. Further theoretical modeling using a more realistic molecule-surface potential and including more dimensions is clearly needed.

The overall efficiency of translational-to-rotational energy transfer can be quantified by the slope of $\langle E_{\mathrm{rot}} \rangle$ with respect to E_n. For the scattering conditions $T_S = 673\,\mathrm{K}$, $\theta_i = 65°$ and $\theta_f = 70°$, we find a slope of $\mathrm{d}\langle E_{\mathrm{rot}} \rangle_{\mathrm{eff}} / \mathrm{d}E_n = 0.04 \pm 0.009$. This value is low when compared to recent results reported by Park *et al.* who found[8] an efficiency near 0.24 for $T \rightarrow R$ energy transfer in the direct scattering of formaldehyde from Au(111). However, due to the grazing incidence conditions in our experiments, we were able to vary E_n only over a relatively small range and it would certainly be interesting to see the effect of higher normal kinetic energies and incidence angles closer to the surface normal. Such measurements are, however, not possible with our current setup.

We also have to note that the experimentally determined rotational distributions in this work are likely to underestimate the high-J populations at higher incidence kinetic energies. This is due to the shifting and broadening of the angular distributions for increasing J_f, an effect that is observed to become more important with increasing E_i. We might thus slightly underestimate the $T \rightarrow R$ conversion efficiency as well. Ideally, one would measure angular distributions for each J and integrate them in order to derive the actual rotational distributions. Our differential measurements underestimate the total flux in scattered into J-states whose angular distributions are broader and their peak positions shifted with respect to the chosen detection geometry. Future experiments should take this effect into account.

The combined experimental and theoretical results point toward a significant contribution of the surface motion to the overall rotational excitation, explaining the previously puzzling feature of the rotational distributions, namely the high degree of excitation at low E_i. The insensitivity of the Doppler-broadened linewidths to final rotational state clearly shows that most CH_4 molecules cannot have acquired their final rotational energy on the basis of $T \rightarrow R$ energy transfer alone. Instead, thermal energy of the surface must have contributed to their rotational excitation. This is supported by the absence of a J_f-dependent shift in the angular distributions at low E_i where the surface thermal motion dominates in the rotational excitation. As E_i increases, more energy is available for conversion into rotation. Here, a shift of the angular distribution towards more glancing exit angles is observed as J_f increases, indicating the conversion of normal incidence kinetic energy into rotational excitation. Moreover, the classical trajectory calculations suggest that conversion of surface atom motion into rotational motion of CH_4 is possible and explains the large $\langle E_{\mathrm{rot}} \rangle$ intercept at $E_n = 0$. Measurements at different surface temperatures could unambiguously prove the role of surface motion. Unfortunately, problems with surface cleanliness below the T_S used here prevented such a study. However, it is possible to go to higher T_S and preliminary results indicate that rotational excitation increases upon heating.

The extent to which interconversion of normal and parallel momentum plays a role cannot be answered by the current experiments as this requires the measurement of rotational and final speed distributions at different incidence angles. However, it seems likely that, in particular at low E_i, corrugation of the surface potential should play a role for our grazing incidence conditions. The classical trajectory calculations show that complicated multi-bounce trajectories are frequent when E_i is low. Here, the molecule experiences strong rotational excitation upon the first bounce, which makes it fly parallel and close to the surface. Subsequently, the molecule becomes trapped if it can transfer

more kinetic energy to surface or it bounces back into the gas phase by converting some rotational energy back into translational energy. We can expect surface corrugation to have an influence when the molecule "skids" along the surface in such a way.

References

[1] M. A. Hines and R. N. Zare, J. Chem. Phys. **98**, 9134 (1993).
[2] M. C. Lin and G. Ertl, Annu. Rev. Phys. Chem. **37**, 587 (1986).
[3] J. Harris and A. C. Luntz, J. Chem. Phys. **91**, 6421 (1989).
[4] J. A. Stinnett, R. J. Madix, and J. C. Tully, J. Chem. Phys. **104**, 3134 (1996).
[5] J. F. Weaver and R. J. Madix, J. Chem. Phys. **110**, 10585 (1999).
[6] B. C. Krüger, G. B. Park, S. Meyer, R. J. V. Wagner, A. M. Wodtke, and T. Schäfer, Phys. Chem. Chem. Phys. **19**, 19896 (2017).
[7] A. W. Kleyn and T. C. M. Horn, Phys. Rep. **199**, 191 (1991).
[8] G. B. Park, B. C. Krüger, S. Meyer, A. Kandratsenka, A. M. Wodtke, and T. Schäfer, Phys. Chem. Chem. Phys. **19**, 19904 (2017).
[9] A. C. Wight and R. E. Miller, J. Chem. Phys. **109**, 1976 (1998).
[10] B. D. Kay, T. D. Raymond, and M. E. Coltrin, Phys. Rev. Lett. **59**, 2792 (1987).
[11] B. D. Kay, T. D. Raymond, and M. E. Coltrin, Phys. Rev. B **36**, 6695 (1987).
[12] A. W. Kleyn, A. C. Luntz, and D. J. Auerbach, Phys. Rev. Lett. **47**, 1169 (1981).
[13] A. W. Kleyn, A. C. Luntz, and D. J. Auerbach, Surf. Sci. **117**, 33 (1982).
[14] K. R. Lykke and B. D. Kay, J. Chem. Phys. **92**, 2614 (1990).
[15] K. R. Lykke and B. D. Kay, J. Phys.: Condens. Matter **3**, S65 (1991).
[16] S. Albert, S. Bauerecker, V. Boudon, L. Brown, J.-P. Champion, M. Loëte, A. Nikitin, and M. Quack, Chem. Phys. **356**, 131 (2009).
[17] A. Tamtögl, E. Bahn, J. Zhu, P. Fouquet, J. Ellis, and W. Allison, J. Phys. Chem. C **119**, 25983 (2015).
[18] A. K. Rappe, C. J. Casewit, K. S. Colwell, W. A. Goddard, and W. M. Skiff, J. Am. Chem. Soc. **114**, 10024 (1992).
[19] J. D. Beckerle, A. D. Johnson, Q. Y. Yang, and S. T. Ceyer, J. Chem. Phys. **91**, 5756 (1989).
[20] A. Al Taleb and D. Farías, Phys. Chem. Chem. Phys. **19**, 21267 (2017).
[21] E. K. Grimmelmann, J. C. Tully, and M. J. Cardillo, J. Chem. Phys. **72**, 1039 (1980).
[22] J. R. Manson, Comput. Phys. Commun. **80**, 145 (1994).
[23] A. al Taleb, G. Anemone, D. Farías, and R. Miranda, Carbon **99**, 416 (2016).
[24] M. E. Coltrin and B. D. Kay, J. Chem. Phys. **89**, 551 (1988).

6 Summary and outlook

6.1 Summary

This thesis reports experimental results on the vibrationally and rotationally resolved scattering of CH_4 from Ni(111). Methane was either incident in its vibrational ground state or prepared with one quantum of the anti-symmetric C–H stretch vibration using highly efficient IR pumping by rapid adiabatic passage. A cryogenic bolometer in combination with a modulated IR laser detected the scattered molecules resolved by rotational and vibrational quantum state. State-resolved angular distributions and the analysis of absorption line profiles delivered additional information on the scattering mechanism. This work was a continuation of the Ph.D. work of van Reijzen[1], which in turn was inspired by the ground-breaking experiments performed by Roger E. Miller and co-workers about 20 years ago[2–5]. It presents one of the first state-to-state molecular beam surface scattering studies performed on a polyatomic molecule.

In the first part of this thesis, I presented the experimental setup and procedures used throughout the rest of this work. I gave detailed account on how we combined a cryogenic semiconductor bolometer with continuous-wave single-mode mid-IR light sources in order to enable the state-selective detection of scattered molecules. I also described the improvement of a transfer cavity that constitutes another integral part of our setup because it allows laser frequency stabilization with MHz precision. Moreover, I developed an algorithm that enables quasi-continuous frequency scanning. In chapter 3, I described our state-selective detection method based on bolometric molecular beam detection with infrared laser tagging (BILT), and I illustrated its capabilities with the help of selected example data.

After having demonstrated the operating principle of our method, chapter 4 presented results on the state-so-state scattering of methane from Ni(111), where *meta*-CH_4 was initially prepared with one quantum of the anti-symmetric C–H stretch vibration (ν_3) and in rotational state $J = 1$ by IR pumping with rapid adiabatic passage. The $CH_4(\nu_3,\ J = 1)$

collided with the 673 K hot surface at an incidence angle of $\theta_i = 65°$ and at three incidence kinetic energies E_i between 100 and 370 meV. Rovibrational quantum state distributions of scattered CH_4 were obtained by means of BILT detection at an exit angle of $\theta_f = 70°$. This afforded the identification of two main vibrational scattering channels. The dominant channel corresponds to vibrationally elastically scattered CH_4. These are molecules that remain in the initially prepared ν_3 state. Second, a vibrationally inelastic channel that populates the symmetric C–H stretch vibration (ν_1) is observed. The total flux in this channel is about 40 % of that in the vibrationally elastic channel. Rotational excitation upon scattering is in all cases significant, adding between 100 and 170 cm^{-1} (12 – 21 meV) of energy this degree of freedom. The vibrationally inelastically scattered molecules bear significantly higher rotational energy, which is explained by the accommodation of excess vibrational energy that is liberated upon $\nu_3 \rightarrow \nu_1$ conversion. The branching ratio between the ν_3 and ν_1 channels is insensitive to changes in E_i, within experimental uncertainty.

Unambiguous evidence for direct scattering is found in the non-thermalized rotational distributions, which show a dependence on the molecular beam's incidence energy. Moreover, state-resolved angular distributions are narrower than $\cos(\theta_f)$ and likewise depend on E_i, where a further narrowing is observed with increasing kinetic energy. At $E_i \geq 230$ meV, the distributions peak at the specular angle, consistent with direct scattering. The fact that molecules retain a memory of the incident beam conditions is further proved by the correlation of incidence speed with the residual Doppler widths detected in the scattered beam.

Due to a lack of scattering simulations, the results were discussed in a qualitative manner based on general notions of IVR[6] and by comparing with experimental results on the collisional deactivation of CH_4 in the gas phase[7,8]. The propensity for production of ν_1 over other vibrational states is rationalized by a potentially strong coupling between these modes as the spectrum of the molecular Hamiltonian is perturbed by the interaction with the surface. The coupling is expected to be strongest among these two stretch states because of the low coupling order and the small energy mismatch.

I further discussed the results in the context of current theoretical models that aim at describing the dissociative adsorption of methane on nickel. Recent calculations performed[9] by Jackson and co-workers, who used their reaction path Hamiltonian method, suggest a strong vibrationally non-adiabatic coupling between two of the vibrationally adiabatic states that correspond to the ν_1 and one component of the ν_3 vibration of the isolated molecule. This coupling is predicted to be strong in the entrance channel of the reaction path, relatively far away from the surface. It seems likely that molecules in

our experiments, albeit their relatively low incidence energy, can sample this part of the PES. I therefore interpret the efficient production of ν_1 as a signature of vibrationally non-adiabatic coupling between the two stretch vibrations.

Chapter 5 focused on the rotationally inelastic scattering of CH_4 in its vibrational ground state ($v = 0$). We collided four different molecular beams at incidence translational energies in the range 100–516 meV with Ni(111) under the same conditions as in the previous study but without IR pumping in the incident beam. Scattered CH_4 was detected in $v = 0$ *via* BILT detection. Multiple evidences identify the scattering as direct; rotational distributions are cold and non-Boltzmann, exhibiting rotational temperatures below 250 K. Moreover, the the Doppler-broadened linewidths of tagging transitions scale roughly linearly with incidence speed, similar to the scattering of $CH_4(\nu_3)$. The state-resolved angular distributions shift towards the specular angle and become narrower as E_i is increased, which is likewise indicative of direct scattering. We note that the existence of a trapping-desorption channel cannot be excluded based on our measurements because our current scattering geometry strongly biases detection of the direct scatter.

We find a propensity for the excitation of low-J states ($J = 0$ and 3) in the scattering distributions, which is insensitive to changes in E_i. It is so far not clear as to whether this propensity signifies the presence of a rotational rainbow as it was found to be the case for NH_3 scattering from Au(111)[10].

Overall rotational excitation increases approximately linearly with E_i with a slope of $\mathrm{d}\langle E_{\mathrm{rot}}\rangle_{\mathrm{eff}}/\mathrm{d}E_n = 0.04 \pm 0.009$, where $E_n = E_i \cos\theta_i^2$ is the incident kinetic energy normal to the surface. This efficiency of translational-to-rotational ($T \rightarrow R$) energy transfer is low compared to that found for formaldehyde scattering from Au(111)[11]. In spite of the low rotational temperatures in the scattered flux, we find that rotational excitation is surprisingly high, in particular at low E_i and considering the grazing incidence condition, which significantly reduces the translational energy available in the direction of the surface normal. The widths of the tagging absorption profiles, measured as a function of final rotational state, clearly show that rotational excitation is not primarily due to $T \rightarrow R$ energy conversion, especially at low E_i. Instead, due to the high T_S used in this work, surface atom motion, *i.e.* phonon annihilation, contributes most to the population of high-J levels at low E_i. Angular distributions, which are resolved by final J-state (J_f), support this interpretation by showing no shift of the peak position as J_f increases indicating translationally elastic scattering. At higher E_i, the distributions peak more towards the super-specular direction ($\theta_f > 67.5°$) as J_f increases, suggesting that now also normal incidence translational energy contributes to rotational excitation ($T \rightarrow R$ energy conversion).

Furthermore, classical trajectory simulations were performed, treating CH_4 as a rigid rotor colliding with a flat surface, which is modeled as a harmonic oscillator with the mass of nickel. The calculations support the conclusion that surface motion plays the dominant role in the rotational excitation at low E_i. They, however, strongly overestimate the efficiency of $T \rightarrow R$ energy transfer, irrespective of whether an attractive Lennard-Jones or a purely repulsive hard-sphere potential is used. An obvious propensity for scattering resulting in small angular momentum was not obvious from the calculations, but the rotational level structure of CH_4, the particular detection geometry in our experiments, and the simplistic nature of the model render a direct comparison of J-distributions problematic. More theoretical work using a more realistic potential energy surface and less simplifying approximations is clearly merited.

More generally speaking, our results highlight that state-of-the-art mid-IR OPO light sources present a crucial improvement over previous laser technologies for the use in bolometer-assisted IR spectroscopy. They enable coherent IR pumping that achieves almost complete population inversion in a molecular beam. We have reason to believe that this maximized excitation efficiency enhances the detectability of scattered molecules by several orders of magnitude compared to previous implementations, where low-power F-center lasers were used. Thus, one important conclusion from this work is that BILT provides a universally applicable detection technique with sufficient sensitivity to allow state-to-state beam-surface scattering. This opens the possibility to systematically study the surface scattering of polyatomic molecules, a field that before was largely inaccessible to experimental study. Simple improvements of the scattering and detection geometries are expected to enhance the sensitivity by at least one order of magnitude. In the remaining sections, I will focus on future experimental improvements and give directions for further methane scattering experiments.

6.2 Experimental improvements

6.2.1 Bolometer and scattering apparatus

In this work, we have added a bolometer to an already existing molecular beam-surface science apparatus that was originally designed for state-resolved chemisorption studies[12,13]. The constraints on the bolometer incorporation due to the existing design impose several limitations on the capabilities of our BILT technique and its performance. I his thesis, van Reijzen identified[1] three major issues that currently prevent us from using the method to its full potential. There are currently efforts underway in our laboratory of constructing a new, dedicated, molecular beam-surface scattering apparatus. These

efforts are undertaken in close collaboration with Prof. Daniel Auerbach. I have been involved in the proposal of this new machine and the early design stages. The design process addresses all of the current shortcoming, which I will discuss in the following paragraphs. The new apparatus will allow measurements to be performed with enhanced sensitivity over a wider angular range. Higher sensitivity means higher chances for discovering small effects as well as reduction of measurement time, resulting in higher throughput.

Bolometer UHV compatibility The first and probably most important drawback concerns the bolometer itself. As discussed in chapter 2, the bolometer purchased from Infrared Laboratories is not entirely UHV compatible. We suspect that it is the use of certain adhesives in the construction of the liquid nitrogen cooled radiation shield that causes most of the hydrocarbon contamination, which we observe in the background of our scattering chamber. Moreover, some materials used in the assembly of the actual bolometer itself cannot undergo the baking procedure that is typically required to achieve UHV conditions. A modified version of the bolometer has been ordered for the new apparatus. A more careful selection of materials and fixing of some construction design flaws, as the use rubber O-ring seals for instance, will result in better UHV compatibility. The new bolometer will also be equipped with a temperature sensor for monitoring the temperature during bake-out, and provisions were made for cooling the bolometer sensor. A cleaner vacuum environment would allow scattering at lower surface temperatures, where Debye-Waller attenuation is strongly reduced, yielding narrower angular distributions, lower surface-induced rotational excitation, and the possibility to observe diffraction in the scattering angular distribution[14].

Detection geometry The second limitation of our current setup is given by the scattering geometry. The angle of 135° between incident beam and bolometer only allows for grazing incidence angles, which means low normal incidence kinetic energies. The highest translational energy with respect to the surface normal achieved in this work is 91 meV (or 8.8 kJ/mol) in a geometry that is close to specular. Considering the $\sim 95\,\mathrm{kJ/mol}$ activation barrier, higher energies are desirable as the molecule could then sample parts of the PES closer toward the transition state. This could allow the observation of a larger number of energetic pathways, which convert translational or initial vibrational energy into degrees of freedom that are closely coupled to the reaction coordinate. It would also be interesting to investigate vibrational excitation induced by $T \rightarrow V$ energy transfer[15,16] or by coupling to electron-hole pairs of the metal, as it has previously been

observed in the case of some diatomic molecules[17–24].

The currently fixed geometry moreover prevents measuring the scattering angular distributions independently from the incidence angle. Also, the angular range covered by rotation of the crystal is limited to 45°. The situation is further complicated by the fact that the molecule beam no longer fully hits the surface when the incidence angle exceeds 75°. The new apparatus will feature a rotatable bolometer, which will be able to probe the angular distribution independently of θ_i. The smallest angle between incident and scattered beam will be about 15°.

Moreover, the large surface-to-bolometer distance of 36 cm reduces the solid angle under which scattered products can be detected to $9.7 \cdot 10^{-5}$ sr. In the new scattering setup, this distance will decrease more than threefold, thereby increasing the attainable signal-to-noise ratio by about one order of magnitude. The likewise reduced angular resolution can always be improved by placing an aperture in front of the detector at the expense of sensitivity, if needed.

However, sensitivity improvements due to an increase in the detected beam flux will likely bring about some new challenges. As I have shown in chapter 3, the build-up of condensible gases on the bolometer has a deteriorative effect on its responsivity. While a somewhat reduced sensitivity due to cryofrost formation might be tolerable and be outweighed by the overall improved sensitivity, it is mostly the change of sensitivity with time that would pose a problem. In order to quantitatively determine the populations of quantum states using BILT, the sensitivity must be stable on the time-scale of hours. I have shown in section 3.2 that dephasing and bolometer sensitivity are related. A dual-phase lock-in amplifier, such as the one we are already using, measures the amplitude *and* the phase of a modulated signal at the same time. In cases where the time-dependent reduction of sensitivity is a problem, I suggest obtaining a calibration function, sensitivity = $f(\phi)$, which relates sensitivity to phase. During the measurements, both phase and amplitude are recorded, and the signal amplitude is subsequently corrected by means of this calibration.

Doppler velocimetry The third improvement that should be made is the addition of a means for measuring the final speed distribution. While the time-response of the bolometer is too slow to allow time-of flight measurements, the narrow linewidth of our OPOs lends itself to the implementation of the Doppler velocimetry (or sometimes Dopplerimetry) technique[25,26]. It has already been successfully employed in surface scattering in the work of Miller and co-workers[2–4], which inspired the present work, as well as by Perkins and Nesbitt, who measured the final speed distributions of CO_2

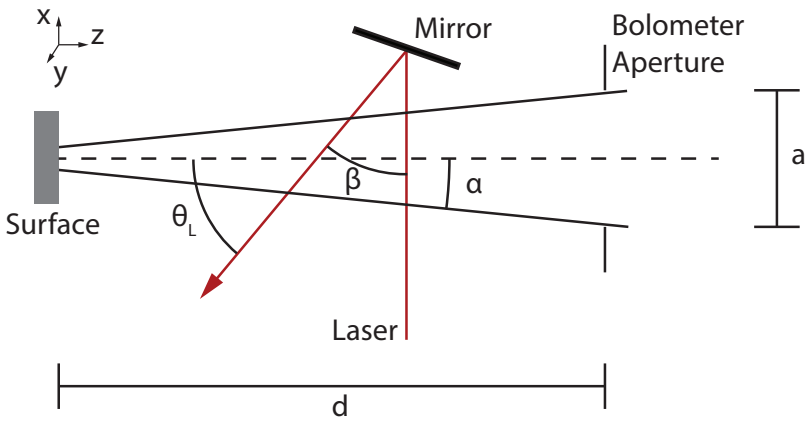

Figure 6.1 Experimental layout for Doppler velocimetry. The diverging beam of molecules coming from the surface after scattering is intersected twice by a narrow linewidth laser beam before hitting the bolometer detector. The angle β between the two laser crossing leads to two absorption features due to the different Doppler shifts.

scattering from a liquid surface[27–33].

In its most simple form, the technique is realized as shown in Figure 6.1. The scattered beam travels towards the bolometer detector located at a distance d from the surface. Molecules, which pass through the circular bolometer aperture of diameter a will contribute to the signal. The tagging laser beam is arranged such that there are two crossings with the flight path of the scattered molecules. In the first crossing, the laser propagation direction and the scattered beam are orthogonal. The laser beam is reflected by a mirror under an angle β in the plane defined by the incoming laser beam and the scattered molecular beam.

I have simulated the expected Doppler profiles using the arrangement shown in Figure 6.1 for the detection geometry of the new apparatus using Monte-Carlo sampling of molecular trajectories[(a)]. Here, I will only show the simulated spectral scan for CH_4 molecules that arrive at the detector with two distinctly different speed distributions. One of the distributions is a thermal Maxwell-Boltzmann distribution at $T = 300\,\mathrm{K}$, similar to what we would expect in the case of trapping followed by desorption from a room-temperature surface. The other one is a narrow, hyperthermal distribution described by a shifted Maxwell-Boltzmann distribution with a mean speed of $\langle v \rangle = 1000\,\mathrm{m/s}$, as we can expect it for direct scattering. The result is shown in Figure 6.2.

Consider the histogram for $\beta = 12°$ in blue. We see here three distinct features. The tallest peak at zero-detuning is the absorption coming from the laser beam that crosses

[(a)]The corresponding MATLAB^{TM} code and a summary of the simulations can be retrieved from the location given in appendix A.

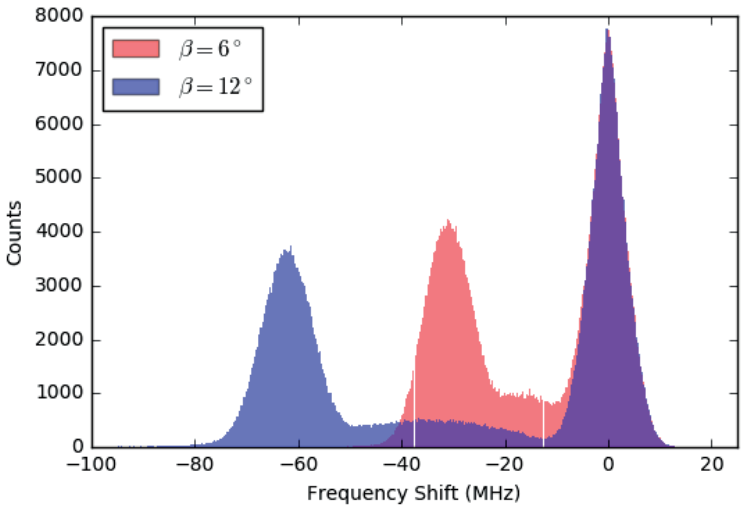

Figure 6.2 Monte-Carlo simulation of the absorption profile as it would appear in a Doppler velocimetry setup. The simulated velocity distribution contains a hyperthermal and a thermal component, which give rise to a narrow strongly shifted and a broad less shifted absorption feature, respectively. Both histograms contain the same total number of samples (N = 500k).

the molecules' flight path perpendicularly. It provides reference for the quantitative analysis of the Doppler shifted absorption feature, which here is observed at negative detuning. There, we see two distinct components, which correspond to the two velocity distributions. The narrow peak at ~ -62 MHz is due to the hyperthermal component, while the broad shoulder comes from the thermal component. This highlights that one will be able to distinguish trapping-desorption from direct scattering by means of their different Doppler shifts. It gives the possibility to study both channels under the same conditions and, furthermore, opens up the possibility of probing the time-scales at which energy accommodation happens on the surface by analyzing the trapping-desorption component as a function of surface residence time. Golibrzuch *et al.* have shown[34] in a recent paper how final velocity selection can help in elucidating the trapping-desorption kinetics on surfaces. In our case, we would not be able to study the residence time on the surface but the degree of accommodation of the molecule's DOF as a function of residence time. The latter can be tuned by changing the surface temperature, which in turn changes the time-scale for desorption. Lastly, I add that the future scattering geometry with its smaller surface-detector distance will facilitate the detection of such a trapping-desorption channel compared to the present setup.

6.2.2 Laser setup

Also the laser setup imposed some limitation on the current experiments. The Tagging OPO system approaches 10 years of operation and shows some deficiencies. Due to a drop in the available output power from the fiber amplifier, which was observed already prior to our scattering experiments, the original idler output coupler in the OPO cavity was replaced by a highly-reflective mirror. This reduced the oscillation threshold and with it the available idler power. One problem, which is related to this switch and which gave us considerable troubles, was the fact that the oscillation threshold was now so low for certain wavelength that single-mode operation of the OPO was no longer possible without greatly reducing the pump power. Moreover, multimoding was observed far more frequently than it is the case for the Pump OPO system. I thus suggest that the Tagging OPO system be refurbished and fitted with an output coupler of appropriate reflectivity. While high idler power is an important factor in our BILT scheme, frequency stability is even more important owing to the duration of the experiments.

Moreover, wavelength tuning can be improved. I have shown that our transfer cavity enables wavelength scanning with MHz precision. Currently, the tuning range is limited by the $10-(-10)\,\mathrm{V}$ output of the digital-analog converter. This limitation is purely given by our electronics setup but can be solved in the very near future. A high-voltage amplifier capable of driving the seed laser piezo in combination with a high dynamic range DAC would be sufficient to enable cavity-controlled tuning over the entire range available by tuning of the seed laser.

In addition to the previous point, wavelength tuning of Argos OPOs can be automated, as shown by the Douberly group[35]. A fully automated BILT spectrometer can therefore be realized and would present another step toward a more user-friendly implementation.

6.3 Future directions in methane scattering

In the remainder of this thesis, I will suggest some future scattering experiments that could make use of our BILT technique. Considering our limited understanding of the dynamics of polyatomic molecules at surfaces and the vast number of systems, which are now accessible by means of BILT detection, this can only be a selection based on personal interests. The reader should bear in mind that BILT is practically universally applicable, not only to poly- but also to many, albeit heteronuclear, diatomic molecules.

In the following, I will limit myself to describing a few promising subjects for future scattering experiments with methane only, going beyond of what was presented in this thesis and that of van Reijzen. In addition to the suggestions below, it is obvious that apart from Ni(111) a large variety of different metals with varying surface structures and orientations can be investigated.

Coriolis effects in the scattering of $CH_4(\nu_3)$ In chapter 4, I presented results that indicated a possible propensity for vibrationally elastic scattering into the same Coriolis stack when CH_4 was initially prepared in the $F^{(-)}$ stack of the ν_3 fundamental state. Further experiments should be performed to clarify whether this effect is indeed real. One way of doing so is to prepare incident CH_4 in different Coriolis stacks of the ν_3 fundamental state *via* excitation of *P*- and *Q*-branch transitions. The effect is real if the final distributions show a similar propensity for scattering into the same stacks. This subtle effect would present a new challenge for theoretical modeling.

Vibrational relaxation and excitation One of the main initial goals of our state-to-state experiments was to find decisive evidence for or against the influence of electronically non-adiabatic effects in the interaction of methane with metal surfaces. Two experiments are feasible to be performed with our setup; first, the vibrational excitation of ground state CH_4 and second, the vibrational relaxation of initially excited CH_4. Signatures of electronically non-adiabatic energy transfer can be found in the surface temperature dependencies of these processes[17,36].

So far, we have not been able to obtain a decisive result. The reasons for this failure are at least twofold: electronically non-adiabatic effects are expected to be small for CH_4. Hence, the probabilities for vibrational excitation in the direct scattering of methane are probably so low that the corresponding state populations are below our detection limit. The fact that, unlike in diatoms, the number of vibrational subbands increases dramatically for polyatomics, does not help. Furthermore, due to our grazing incidence conditions, kinetic energies normal to the surface are low and we may speculate that molecules cannot travel far enough into regions of higher electron density, where electron-hole pair interaction would be more probable. Vibrational relaxation may occur with a higher probability but its detection suffers likewise from the large number of states that are available. I suggest that the search for non-adiabatic effects be continued using the new scattering apparatus, which will provide more favorable scattering geometries and improved sensitivity.

Steric effects Yoder has shown[37,38] that the dissociation of vibrationally excited CH_4 on nickel depends on the initial alignment of the C–H stretch amplitude with respect to the surface. The fact that a steric effect is measurable in the dissociation reaction means necessarily that a corresponding effect must be detectable in the fraction of molecules that underwent non-reactive scattering. BILT has the capability of probing angular momentum polarization, as I have outlined in section 3.4.4. In this work, however, conditions were chosen such that the effects of alignment and/or orientation on the measured state distributions were minimized. A future study of the stereodynamics could prepare the incoming CH_4 in an aligned or oriented state and the resulting angular momentum polarization of the scattered molecules could be probed using BILT. In this type of experiment, one usually measures the rotational state populations using two different laser polarizations, *e.g.* parallel and perpendicular with respect to the surface normal. The signal difference between the two polarizations could be measured directly in our BILT scheme by sending the laser beam through a Pockels cell before interrogating the scattered molecules. Periodic polarization switching and lock-in amplification of the bolometer signal at the switching frequency directly gives a measure of that difference, as shown by Perkins and Nesbitt[31].

Rotational excitation Isotopologues of methane can be used to explore more aspects of the molecule-surface PES that relate to rotational excitation during scattering. Up to now, there are only two rotationally resolved (metal) surface scattering studies with molecules that are neither spherical tops nor linear, ammonia[10] and formaldehyde[11]. In both cases, a propensity for axis-specific rotational excitation was reported.

References

[1] M. E. van Reijzen, *State-to-state scattering of CH_4 from Ni(111) and Gr/Ni(111)*, Ph.D. thesis, École polytechnique fédérale de Lausanne, Lausanne (2016).

[2] T. W. Francisco, N. Camillone III, and R. E. Miller, Phys. Rev. Lett. **77**, 1402 (1996).

[3] A. C. Wight and R. E. Miller, J. Chem. Phys. **109**, 1976 (1998).

[4] A. C. Wight and R. E. Miller, J. Chem. Phys. **109**, 8626 (1998).

[5] A. C. Wight, M. Penno, and R. E. Miller, J. Chem. Phys. **111**, 8622 (1999).

[6] D. R. Killelea and A. L. Utz, Phys. Chem. Chem. Phys. **15**, 20545 (2013).

[7] P. Hess and C. B. Moore, J. Chem. Phys. **65**, 2339 (1976).

[8] P. Hess, A. H. Kung, and C. B. Moore, J. Chem. Phys. **72**, 5525 (1980).

[9] P. M. Hundt, M. E. van Reijzen, R. D. Beck, H. Guo, and B. Jackson, J. Chem. Phys. **146**, 054701 (2017).

[10] B. D. Kay, T. D. Raymond, and M. E. Coltrin, Phys. Rev. Lett. **59**, 2792 (1987).

[11] G. B. Park, B. C. Krüger, S. Meyer, A. Kandratsenka, A. M. Wodtke, and T. Schäfer, Phys. Chem. Chem. Phys. **19**, 19904 (2017).

[12] M. P. Schmid, P. Maroni, R. D. Beck, and T. R. Rizzo, Rev. Sci. Instrum. **74**, 4110 (2003).

[13] M. Schmid, *Interaction of Highly Excited Molecules with Solid Surfaces*, Ph.D. thesis, École polytechnique fédérale de Lausanne, Lausanne (2003).

[14] A. Al Taleb and D. Farías, Phys. Chem. Chem. Phys. **19**, 21267 (2017).

[15] B. D. Kay, T. D. Raymond, and M. E. Coltrin, Phys. Rev. B **36**, 6695 (1987).

[16] K. Golibrzuch, J. H. Baraban, P. R. Shirhatti, J. Werdecker, C. Bartels, and A. M. Wodtke, Z. Phys. Chem. **229**, 1929 (2015).

[17] C. T. Rettner, F. Fabre, J. Kimman, and D. J. Auerbach, Phys. Rev. Lett. **55**, 1904 (1985).

[18] R. Cooper, I. Rahinov, Z. Li, D. Matsiev, D. J. Auerbach, and A. M. Wodtke, Chem. Sci. **1**, 55 (2010).

[19] R. Cooper, C. Bartels, A. Kandratsenka, I. Rahinov, N. Shenvi, K. Golibrzuch, Z. Li, D. J. Auerbach, J. C. Tully, and A. M. Wodtke, Angew. Chem. Int. Edit. **51**, 4954 (2012).

[20] T. Schäfer, N. Bartels, K. Golibrzuch, C. Bartels, H. Köckert, D. J. Auerbach, T. N. Kitsopoulos, and A. M. Wodtke, Phys. Chem. Chem. Phys. **15**, 1863 (2013).

[21] K. Golibrzuch, A. Kandratsenka, I. Rahinov, R. Cooper, D. J. Auerbach, A. M. Wodtke, and C. Bartels, J. Phys. Chem. A **117**, 7091 (2013).

[22] K. Golibrzuch, P. R. Shirhatti, J. Altschäffel, I. Rahinov, D. J. Auerbach, A. M. Wodtke, and C. Bartels, J. Phys. Chem. A **117**, 8750 (2013).

[23] P. R. Shirhatti, J. Werdecker, K. Golibrzuch, A. M. Wodtke, and C. Bartels, J. Chem. Phys. **141**, 124704 (2014).
[24] J. Werdecker, P. R. Shirhatti, K. Golibrzuch, C. Bartels, A. M. Wodtke, and D. J. Harding, J. Phys. Chem. C **119**, 14722 (2015).
[25] K. Bergmann, W. Demtröder, and P. Hering, Appl. Phys. **8**, 65 (1975).
[26] U. Hefter and K. Bergmann, in *Atomic and molecular beam methods, Vol. 1*, edited by Giacinto Scoles (Oxford University Press, New York, 1988).
[27] B. G. Perkins, T. Häber, and D. J. Nesbitt, J. Phys. Chem. B **109**, 16396 (2005).
[28] B. G. Perkins and D. J. Nesbitt, J. Phys. Chem. B **110**, 17126 (2006).
[29] B. G. Perkins and D. J. Nesbitt, J. Phys. Chem. A **111**, 7420 (2007).
[30] B. G. Perkins and D. J. Nesbitt, J. Phys. Chem. A **112**, 9324 (2008).
[31] B. G. Perkins and D. J. Nesbitt, Proc. Natl. Acad. Sci. **105**, 12684 (2008).
[32] Perkins and D. J. Nesbitt, J. Phys. Chem. B **112**, 507 (2008).
[33] B. G. Perkins and D. J. Nesbitt, J. Phys. Chem. A **114**, 1398 (2010).
[34] K. Golibrzuch, P. R. Shirhatti, J. Geweke, J. Werdecker, A. Kandratsenka, D. J. Auerbach, A. M. Wodtke, and C. Bartels, J. Am. Chem. Soc. **137**, 1465 (2015).
[35] A. M. Morrison, T. Liang, and G. E. Douberly, Rev. Sci. Instrum. **84**, 013102 (2013).
[36] D. Matsiev, Z. Li, R. Cooper, I. Rahinov, C. Bartels, D. J. Auerbach, and A. M. Wodtke, Phys. Chem. Chem. Phys. **13**, 8153 (2011).
[37] B. L. Yoder, R. Bisson, and R. D. Beck, Science **329**, 553 (2010).
[38] B. L. Yoder, R. Bisson, P. Morten Hundt, and R. D. Beck, J. Chem. Phys. **135**, 224703 (2011).

Appendices

A Additional files and documentation material

I have placed experimental data, additional program code, and documentation material, which I created during my doctoral work, on the group's intranet data server (Surface folder). The following list points to the respective locations under which these can be found. Paths are given relative to the group folder.

- Experimental data
  `/all data/Results/Machine 1`
- Laboratory notebook (MS OneNote™)
  `/all data/Results/Other Results/Machine 1 Logged Data/Notebooks`
- Spectral data from the Dijon group
  `/Joern/Scattering/CH4 Spectroscopy/Dijon files`
- Mathematica™ notebook for the classical scattering calculations (cf. section 5.3)
  `/Joern/Scattering/Simulations/Rotational Inelasticity/...`
  `...final notebooks`
- Python library for the BILT analysis
  `/Joern/Scattering/pylib/BoloLib`
- Python library for searching the Dijon spectral data files and spectrum simulation
  `/Joern/Scattering/pylib/DijonReader`
- Python library for searching the HITRAN spectral data files and spectrum simulation
  `/Joern/Scattering/pylib/pyTRAN`
- MATLAB™ scripts for TOF analysis
  `/Joern/Other projects/TOF fitting programs`
- Doppler velocimetry simulations (cf. paragraph 6.2.1)
  `/Joern/Other projects/Doppler Velocimetry Scattering Machine`
- Python script evaluating the Ciddor equation (cf. section 2.4.4.4)
  `/Joern/Other projects/C module Transfer Cavity/air index`
- Model for calculating the fraction of the molecular beam hitting the surface (cf. appendix G).
  `/Joern/Writeups/molecular_beam_profile`
- Bolometer noise measurement documentation (cf. section 2.3)
  `/Joern/Other projects/Bolometer Noise Measurement`

B Conversion of helium pressure to temperature

Conversion of helium partial pressure to absolute temperature is defined by the international temperature scale ITS-90 according to the formula

$$T_{90}/K = A_0 + \sum_{i=1}^{9} A_i \left(\frac{\ln(p/\mathrm{Pa}) - B}{C} \right)^i . \tag{B.1}$$

The coefficients valid in the range from 1.25 to 5.0 K are compiled in Table B.1.

Table B.1 Coefficients for the conversion of ^{4}He partial pressure to absolute temperature according to the ITS-90 temperature scale.

coefficient	^{4}He 1.25 – 2.1768 K	^{4}He 2.1768 – 5.0 K
A_0	1.392 408	3.146 631
A_1	0.527 153	1.357 655
A_2	0.166 756	0.413 923
A_3	0.050 988	0.091 159
A_4	0.026 514	0.016 349
A_5	0.001 975	0.001 826
A_6	−0.017 976	−0.004 325
A_7	0.005 409	−0.004 973
A_8	0.013 259	0
A_9	0	0
B	5.6	10.3
C	2.9	1.9

C Details of the transfer cavity software

The overall program layout follows a producer/consumer architecture using several queues to transmit data in between independently running loops. The most important ones are the data acquisition loop, which executes with a fixed timing given by the configured clock frequency f_{rep} and the main data analysis loop, which performs the peak picking, fitting, and generates the correction voltage output. The photodiode signals are transferred from the acquisition to the analysis loop by means of a queue. The analysis loop executes whenever new data becomes available in the queue. If one iteration of the analysis loop takes longer than $1/f_{\mathrm{rep}}$, the older data will be discarded and only the data from the latest acquisition used. The behavior is changed when the "Robust mode" is enabled, then all elements remain in the queue. This, however, can lead to a lag between acquisition and analysis, which can increase if analysis time consistently exceeds acquisition time. This mode should thus only be used in rare cases. The LabVIEW block diagram contains a number of comments, which serve to make the code more readable.

C.1 Description of the stabilization algorithm

Figure C.1 shows a flow diagram of the IR fitting and PID stabilization procedure. Several comments are merited. The scanning functionality of the algorithm requires simultaneous fitting of two IR peaks during certain times. There are two "channels", which perform fitting of the peaks independently. Whenever a new peak is found by the peak picking algorithm, a logic function (IR peak distributor VI) assigns this peak to the channel that is currently not fitting. If no fitting was performed, then the first peak that is detected is assigned to channel 1. If the fitting is successful in at least one channel (i.e. the peak position is within the allowed range `lower/upper limit`), stabilization may be activated by the user. The current IR peak position relative to the HeNe is then stored as setpoint and the PID control activated. The setpoint can be changed by the user (scanning). There are two independent PID loops, one for each fitting channel. During stabilization, one of them is active and derives an output from the process variable and the setpoint. The second one is set to "manual" mode. Here, its output is set to the output of the other PID (its last value from the previous iteration). In the case of a switchover, this avoids a sudden jump of the output voltage. In the case that one peak can no longer be fitted (e.g. because it is now outside of the allowed range), a logic inside the Lock PID VI switches the formerly passive PID to active and sets the formerly active PID to "manual". Also the output is switched from one PID to the other.

The peak switchover procedure requires a change of the PID setpoint since now a

different peak is responsible for stabilization. The following variables are used to keep track of the frequency detuning:

- Setpoint x_S: The desired IR-HeNe distance, which serves as the input for the active PID.
- Offset x_{Offset}: Total offset from the initial stabilization point.
- Offset compensation x_{comp}: Stores the accumulated offset starting from the initial setpoint (when the lock was activated the first time) each time a peak switchover occurs.

Initially, when the stabilization is activated, we have $x_{\text{comp}}(0) = 0$, $x_{\text{Offset}} = 0$, and $x_S = x(0)$. When the user changes the offset x_{Offset} (detunes the laser), the setpoint becomes $x_S = x(0) + x_{\text{Offset}}$. When the nth switchover takes place, we set $x_{\text{comp}} = x_{\text{Offset}}$ and the new setpoint is given by $x_S = x(0,n) + x_{\text{Offset}} - x_{\text{comp}}$, where $x(0,n)$ is the relative peak position at the moment the peak takes over for stabilization.

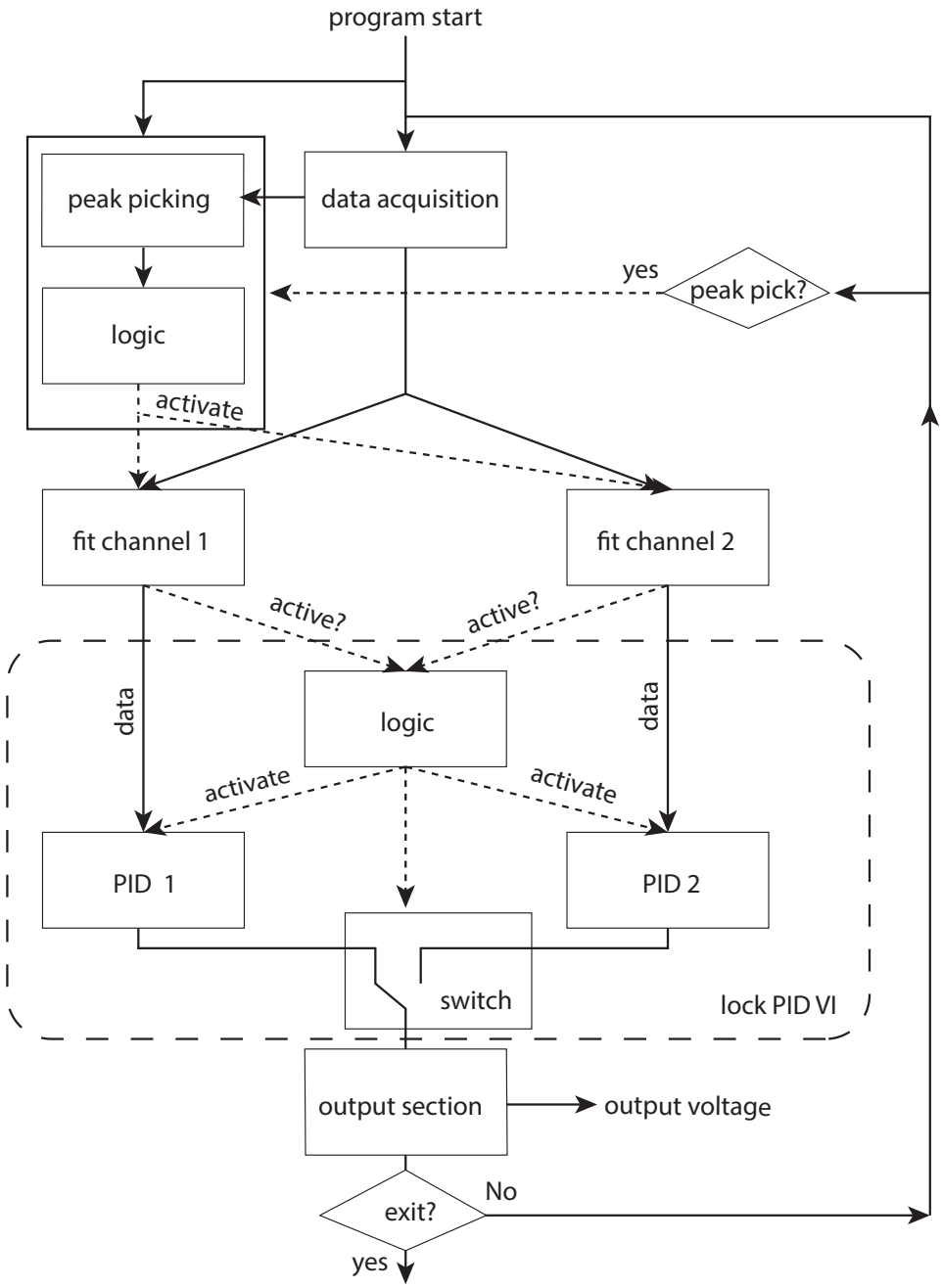

Figure C.1 Flow diagram of the overall IR fitting and PID stabilization loop. Solid lines represent flow of data and depict the sequence of events. Dashed lines indicate controlling actions.

Stabilization algorithm in pseudocode

```
program IR_stabilization;
    search_for_peaks := True; // search for peaks during first iteration
    while program_running do
        signal_waveform = obtain_data(); // obtain latest waveform from data queue
        if (search_for_peaks == True) then
            IR_peak_positions := IR_peak_picking(); // peak picking
            if (new peak found) then
                // IR  peak distributor VI
                assign_peak_to_avilable_fitting_channel();
                set_active_flag(available_channel); // activates the fitting channel

        // perform fitting of IR peaks if channel is active
        // Fit Single Gaussian VI
        position_1 := perform_fit(signal_waveform, active_flag_1);
        position_2 := perform_fit(signal_waveform, active_flag_2);

        check_if_fit1_is_valid();  // Check if peaks within lower and upper limits
        check_if_fit2_is_valid();

        // check if user can be allowed to activate stabilization loop
        if (at least 1 channel has a valid fit) then
            allow_stabilization := True;
        else:
            allow_stabilization := False;

        // Lock PID VI
        if stabilization_active() then  // activated by user
            determine_fitting_state(); // # of peaks found, which channels are active?
            if state_changed then   / e.g. because a peak went outside limits
                if (no PID output was active) then
                    enable_PID_output;
                    setpoint := position_#
                else if (PID output was active) then
                    switch_to_other_PID();
            else
                do nothing;

            if (PID 1 active) then
                PID_1_output := update_PID1(position_1, setpoint);
                PID_2_output := update_PID2(last_PID1_output);
                generate_voltage_output(PID_1_output);
            else if (PID 2 active) then
                PID_1_output :=update_PID1(last_PID2_output);
                PID_2_output :=update_PID2(position_2, setpoint);
                generate_voltage_output(PID_2_output);

        // Check if Peak Picking should be performed on next iteration.
        // X is the range corresponding to the setting parameters
        // "Search for 2nd peak if 1st is...  "
        // Check Peak Pick VI
        if (fitted peak is outside X) or (no peak fitted) then
            search_for_peaks := True;
        else
            search_for_peaks := False;
    end.
end.
```

C.2 Documentation of configuration parameters

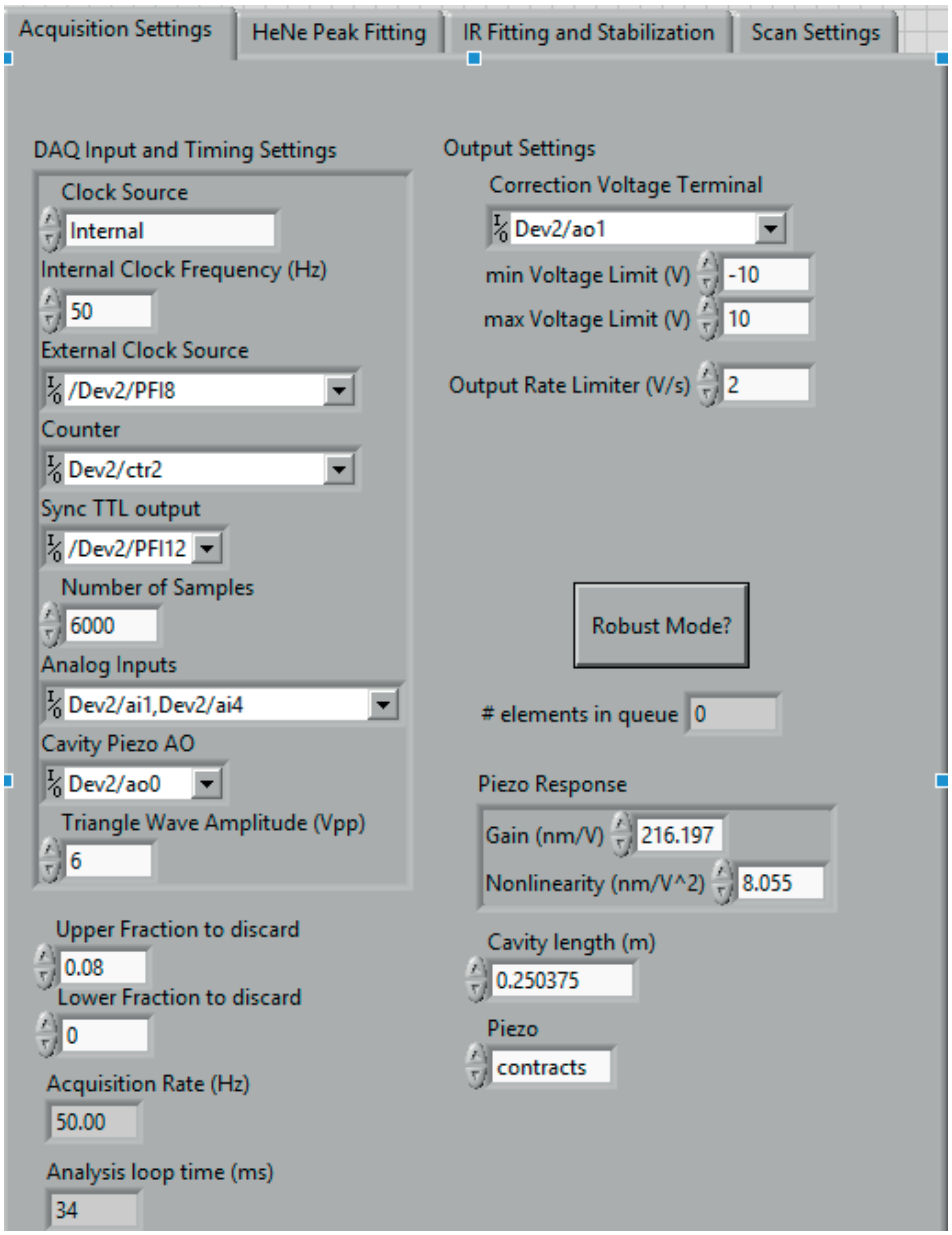

Figure C.2 "Acquisition Settings" panel of the transfer cavity GUI. Refer to Table C.1 for a description of the parameters.

Table C.1 Description of configuration parameters of the transfer cavity in the "Acquisition Settings" panel (cf. Figure C.2).

Parameter	Description
Clock Source	Selects the master oscillator that triggers each acquisition and analysis cycle. Possible values Internal: Uses the DAQ card on-board clock. External: Trigger to TTL pulse applied to the PFI terminal specified in External Clock Source.
Internal Clock Frequency	Repetition rate f_{rep} of the cavity in Hz.
External Clock Source	DAQ input terminal for external trigger.
Counter	Counter used to generate the internal time reference or the TTL output.
Sync TTL output	Sync TTL output terminal in case the internal clock is used
Number of samples	Number of samples n acquired per second for each, HeNe and IR. Note that $2f_{\mathrm{rep}} \cdot n$ cannot exceed the maximum sampling rate of the DAQ card.
Analog Inputs	Specifies the photodiode input terminals. The first entry corresponds to the HeNe signal.
Cavity Piezo AO	Output terminal for the triangle wave that scans the cavity PZT.
Triangle Wave Amplitude	Maximum voltage of the triangle wave (peak-to-peak Voltage).
Upper/lower fraction to discard	Fraction of the acquired photodiode waveforms that should be discarded.
Correction Voltage Terminal	Analog output terminal for the seed laser PZT voltage.
min/max Voltage Limit	Limits for the correction voltage.
Output Rate Limiter	Maximum rate at which the correction voltage is ramped to zero when the stabilization is turned off or when it fails.
Piezo response	Cavity calibration parameters as described in section 2.4.4.2. Gain and Nonlinearity are the a_1 and a_2 coefficients in Equation 2.19, respectively. They have to be determined beforehand for a given repetition rate and triangle wave amplitude.

continues on next page ...

Table C.1 continued ...

Parameter	Description
Piezo contraction/extension	Specify whether the cavity piezo contracts or extends when the driving voltage is increased.
Robust mode	Activation of this mode gives the analyzing algorithm more time to process the waveforms at the expense of precision. Can be used if the IR fringe is noisy. Care must be taken that the analysis queue does not become too long. If this mode is off, the queue elements are evaluated immediately and no lag builds up.

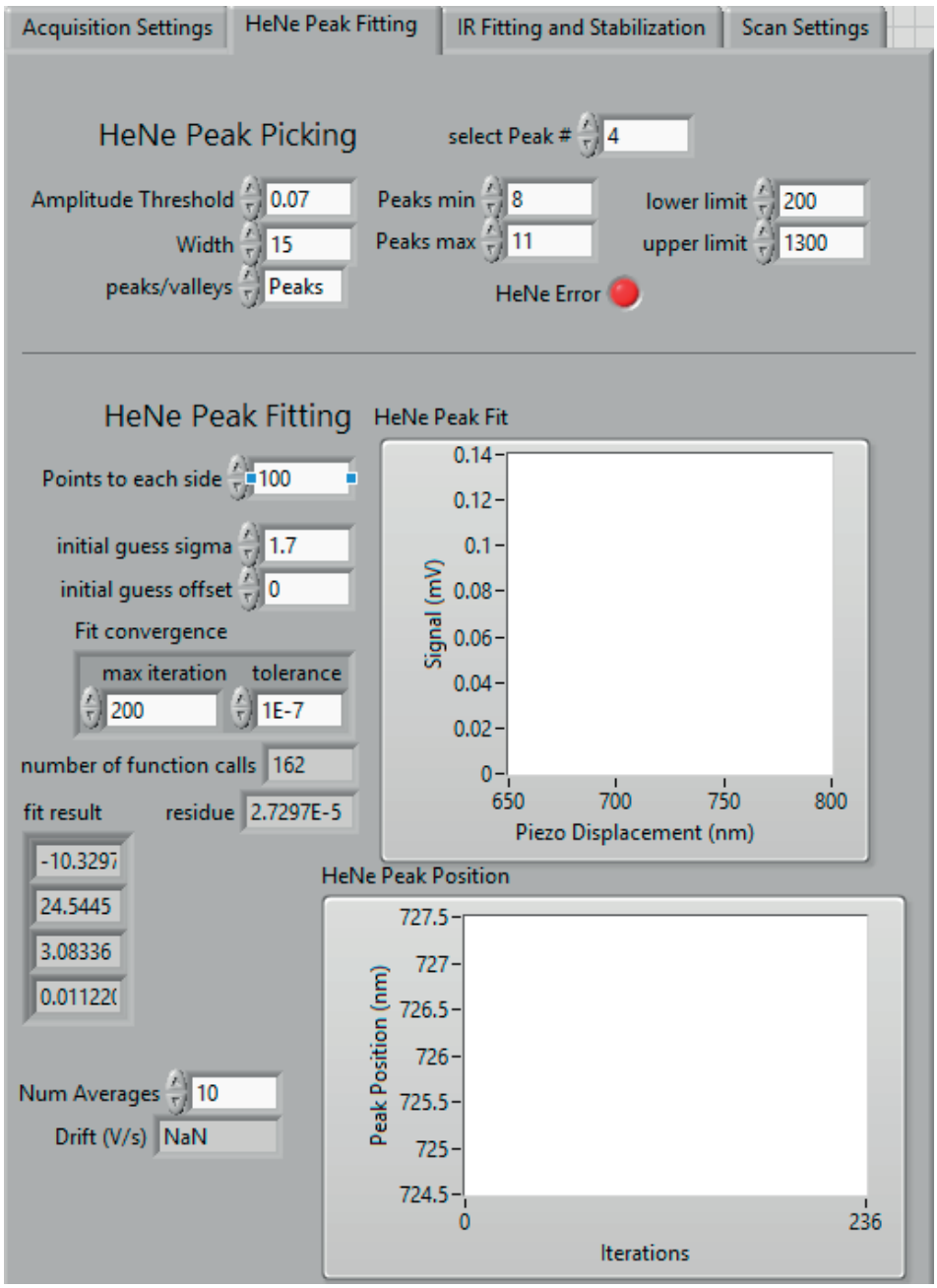

Figure C.3 "HeNe Peak Fitting" panel of the transfer cavity GUI. Refer to Table C.2 for a description of the parameters.

Table C.2 Description of configuration parameters of the transfer cavity in the "HeNe Peak Fitting" panel (cf. Figure C.3).

Parameter	Description
select Peak #	Selects which HeNe peak is chosen as reference (counted from the left).
Amplitude threshold	Considers only peaks with amplitudes larger or equal to this value in the initial peak picking.
Width	Width parameter used in the initial peak picking in terms of number of samples.
peaks/valleys	Select whether fringes are negative or positive with respect to the baseline.
Peaks min/max	Minimum and maximum number of expected fringes.
lower/upper limit	The reference peak is only fitted as long as it is within these limits. If it drifts outside, HeNe error will be raised and the IR stabilization stopped.
Points to each side	Select number of data points to each side from the peak center to be taken into account in the fitting.
initial guess sigma/offset	Initial guesses for the width and vertical offset in the first round of the fitting.
Fit convergence	Convergence criteria for the nonlinear least squares fitting. If max iteration is exceeded, the fit fails and HeNe error will be raised.
fit result	Shows the current best fit parameters. From top to bottom: Peak position (nm), width (sigma of the Gauss function), amplitude, vertical offset.
Num Averages	Length of the moving average of the HeNe peak position. Only used for determining the drift.

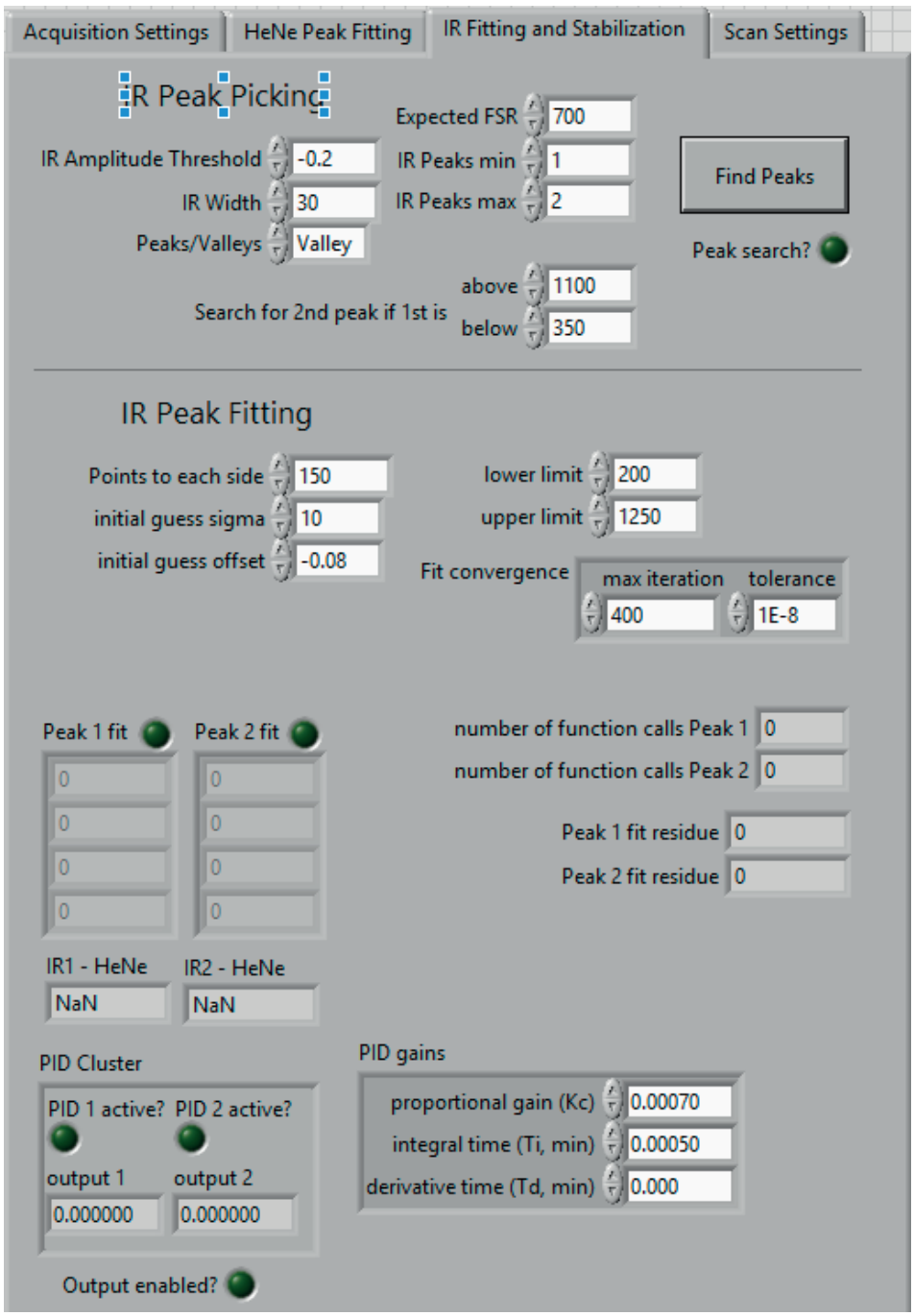

Figure C.4 "IR Fitting and Stabilization" panel of the transfer cavity GUI. Refer to Table C.3 for a description of the parameters.

Table C.3 Description of configuration parameters of the transfer cavity in the "IR Fitting and Stabilization" panel (cf. Figure C.4).

Parameter	Description
Peak picking parameters	Same meaning as for HeNe (cf. Table C.2).
Expected FSR	Expected spacing between two IR peaks in nm. This setting is important in the search for a second IR peak.
Search for 2nd peak if 1st is ...	Sets limits from which IR position the algorithm looks for a second IR peak. This range must be well within the upper/lower limits defined below in the fitting section but the range must also be larger than the corresponding FSR.
Find Peaks	Press to stop fitting and perform a new peak search.
Peak search?	Indicates whether peak picking is performed.
Peak fitting parameters	Same meaning as for HeNe (cf. Table C.2). Number of iterations limit can be increased if the IR fringes are noisy and the fitting fails.
Peak 1/2 fit	Shows the IR peaks which are currently being fitted (green LED) and the resulting fit parameters with the same meaning as for the HeNe. Also shown is the distance to the reference HeNe peak. Same meaning as for HeNe.
PID cluster	Shows which PID loop is active and what the current voltage output is.
Output enabled?	Lights up if stabilization is enabled.
PID gains	Sets the PID parameters for the correction voltage output. The shown values are applicable for the old seed laser used with the C module where the correction voltage is supplied to the seed after a : 2 voltage divider.

D Linepositions of CH_4 hot-band transitions

I report here the line positions of the hot-band transitions used for product state tagging in chapter 4. A constant frequency offset caused by slight misalignment of the laser beam into the wavemeter was subtracted by measuring the line position of the $\nu_3 \leftarrow v = 0$ $R(0)$ fundamental transition and referencing to the value given in the current version of the HITRAN database [I.E. Gordon *et al.*, J. Quant. Spectrosc. Radiat. Transf. **203**, 3 (2017)] (3028.75226 cm^{-1}). The line position for the $2\nu_3 \leftarrow \nu_3$ and the $\nu_1 + \nu_3 \leftarrow \nu_3$ band are summarized in Tables D.2 and D.1, respectively. The uncertainties are ± 0.002 cm^{-1}. The tables also include the predicted transition frequencies that were kindly provided by the group of Prof. Vincent Boudon from the *Université de Bourgogne* in Dijon, France. The assignments of the rotational quantum numbers J'' and J' as well as of the sublevel identifiers n'' and n' is moreover based on their line list. Figure D.1 additionally displays the difference of the experimentally observed and predicted line positions in vacuum-wavenumbers for both hot-bands.

Table D.1 Experimentally determined line positions $\nu_{exp.}$ of rovibrational transitions in the $\nu_1 + \nu_3 \leftarrow \nu_1$ band in vacuum-wavenumbers. Calculated frequencies ν_{Dijon} provided by the Dijon group are included as well.

Assignment	J''	n''	J'	n'	$\nu_{exp.}$ /cm^{-1}	ν_{Dijon} /cm^{-1}
$R(0)$	0	2	1	15	2956.851	2956.965
$R(3)$	3	5	4	44	2991.699	2991.588
$R(4)$	4	6	5	49	2991.274	2991.287
$Q(6)$	6	7	6	57	2942.158	2942.147
$Q(6)$	6	8	6	52	2943.515	2943.457
$Q(7)$	7	9	7	61	2942.956	2943.007
$Q(8)$	8	10	8	69	2940.079	2940.321

Table D.2 Experimentally determined line positions $\nu_{\text{exp.}}$ of rovibrational transitions in the $2\nu_3 \leftarrow \nu_3$ band in vacuum-wavenumbers. Calculated frequencies ν_{Dijon} provided by the Dijon group are included as well.

Assignment	J''	n''	J'	n'	$\nu_{\text{exp.}}$ /cm^{-1}	ν_{Dijon} /cm^{-1}
$R(1)$	1	3	2	29	3006.261	3006.266
$R(2)$	2	4	3	40	3013.967	3013.966
$Q(3)$	3	4	3	40	2984.232	2984.233
$Q(3)$	3	6	3	32	2983.386	2983.386
$Q(5)$	5	6	5	59	2983.396	2983.406
$R(5)$	5	7	6	72	3089.939	3089.937
$Q(6)$	6	8	6	71	2985.094	2985.090
$Q(6)$	6	9	6	66	3021.788	3021.780
$Q(6)$	6	10	6	65	2981.202	2981.205
$R(7)$	7	8	8	83	3068.168	3068.105
$Q(7)$	7	9	7	80	2981.831	2981.819
$R(7)$	7	10	8	91	3068.482	3068.468
$Q(7)$	7	11	7	73	2981.891	2981.912
$R(8)$	8	9	9	94	3074.681	3074.610
$R(8)$	8	11	9	99	3078.346	3078.420
$Q(8)$	8	12	8	85	3015.850	3015.857

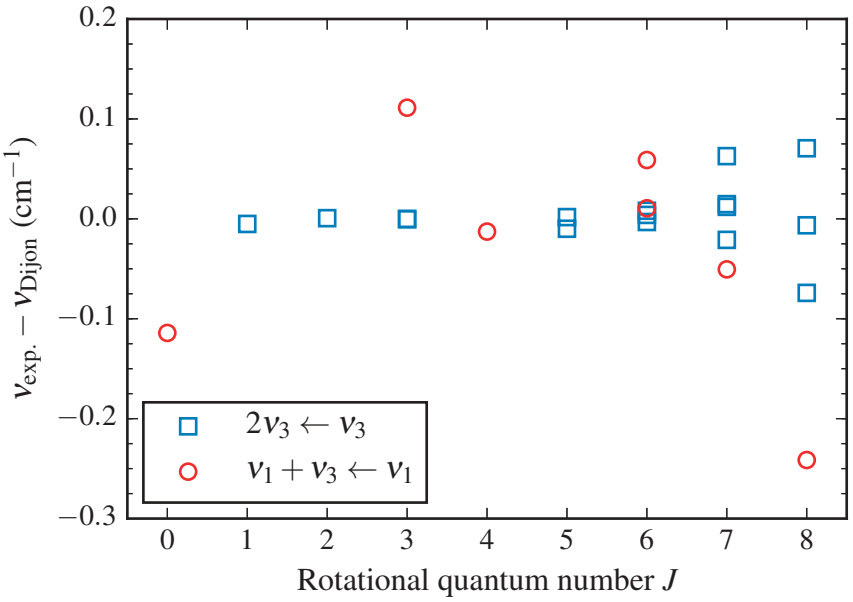

Figure D.1 Difference of experimentally observed and predicted line positions in vacuum-wavenumbers for both hot-bands.

E Supplementary rotational distributions

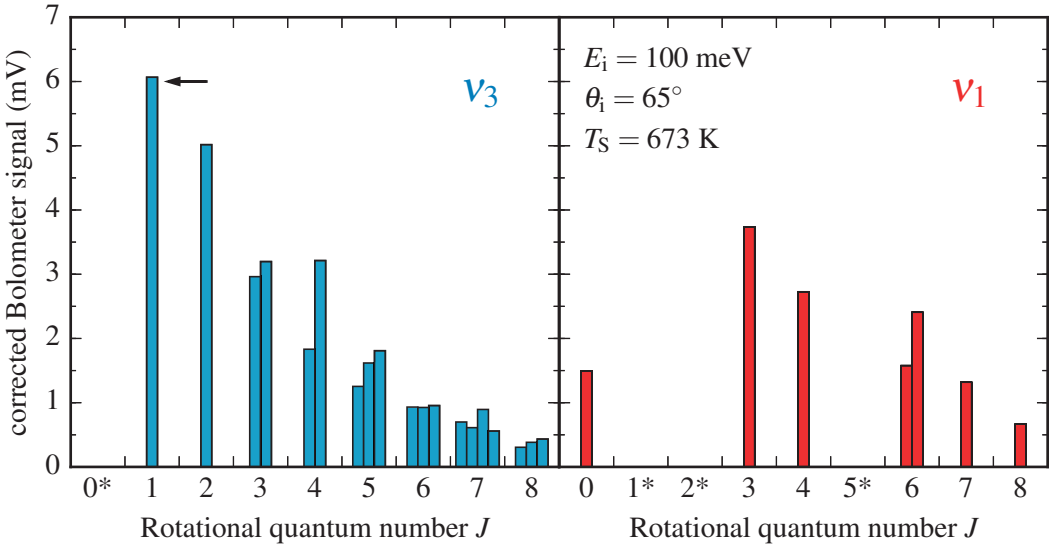

Figure E.1 Rotational state distributions within the vibrationally elastic (ν_3) and inelastic (ν_1) channels for a molecular beam of $CH_4(\nu_3,\ J = 1)$ scattered from Ni(111) with an average incidence translational energy of 100 meV.

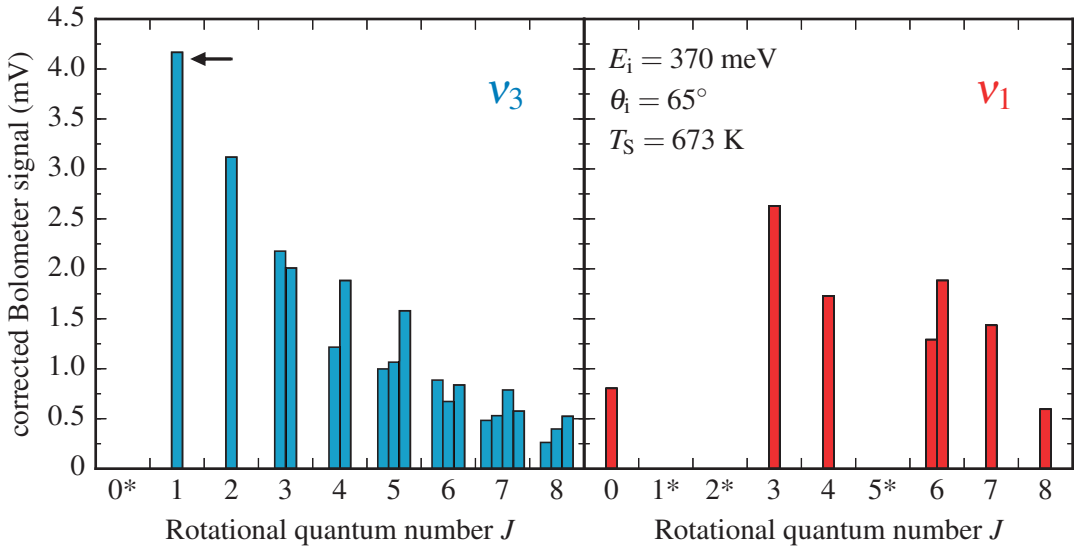

Figure E.2 Rotational state distributions within the vibrationally elastic (ν_3) and inelastic (ν_1) channels for a molecular beam of $CH_4(\nu_3,\ J = 1)$ scattered from Ni(111) with an average incidence translational energy of 370 meV.

F Determination of the instrumental linewidth of the tagging OPO

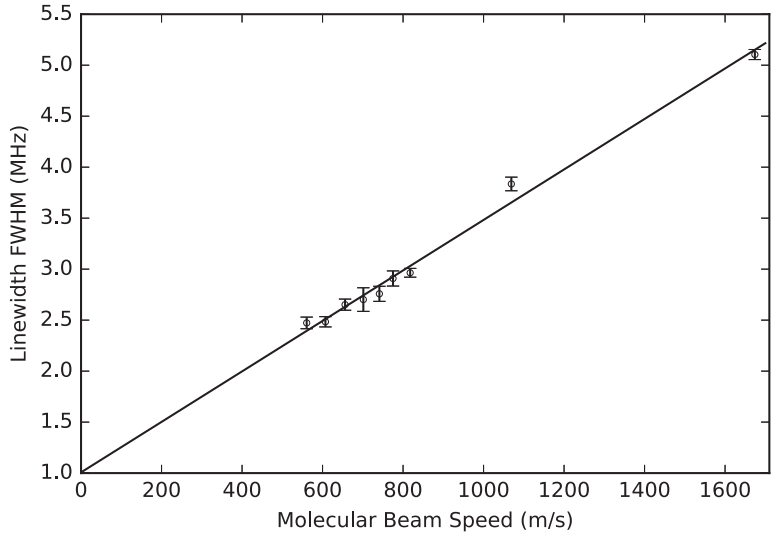

Figure F.1 Linewidth of the ν_3 $Q(1)$ transition measured in the incoming molecular beam using the Tagging OPO in combination with the pyroelectric detector in order to determine the OPO's instrumental linewidth. Error bars represent the 95 % confidence interval based on 5 individual measurements at each incidence speed. See text for experimental details.

The instrumental linewidth of the Tagging OPO was determined as follows: The OPO was aligned to intersect the incoming molecular beam and the pyroelectric detector was positioned to measure the vibrational energy, which the chopped OPO added to the incoming beam. The OPO was tuned to the $Q(1)$ transition of the ν_3 fundamental and chopped at 2 Hz. The pyroelectric detector signal was lock-in amplified with a time constant of 300 ms. The absorption profile was scanned at 0.1 MHz/s for varying molecular beam speeds, which were achieved by seeding CH_4 in helium or argon and by changing the nozzle temperature. TOF measurements of the direct beam yielded the average incidence speeds. Scans were repeated five times for each molecular beam speed. Each line profile was background corrected and a Gaussian fit determined its width. Figure F.1 shows the dependence of the measured FWHM on the incidence speed. A linear fit to the data gives an intercept with the vertical axis of 1.00 ± 0.08 MHz, which still includes homogeneous line-broadening due to power broadening. However, transit time and residual Doppler-broadening are removed by the extrapolation procedure since the final linewidth is bilinear in the widths corresponding to these two contributions.

G Estimation of the molecular beam fraction hitting the surface

Our angular distributions have to be corrected for the fraction of the incident beam that misses the surface when the incidence angle θ_i approaches 90°. The apparent $\cos\theta_f$ distribution can be written as the product

$$\Theta(\theta_f) = f(135^\circ - \theta_f) \cdot \cos\theta_f \tag{G.1}$$

where $f(135^\circ - \theta_f)$ is the fraction of the beam that actually hits the surface at the incidence angle $\theta_i = 135^\circ - \theta_f$. This fraction is calculated as follows: For simplicity, I assumed the flux distribution in the incident beam to be Gaussian, that is,

$$I(r) = I_0 \exp\left(-\frac{r^2}{w^2}\right), \tag{G.2}$$

where $r = x^2 + y^2$ is the transverse distance from the beam center. It can be shown that the flux distribution projected onto a surface, which is tilted by an angle θ_i about the z

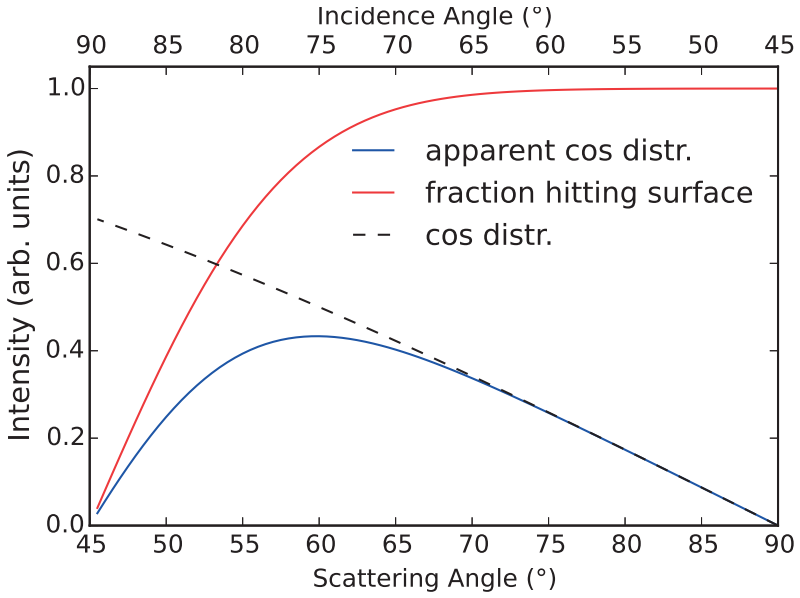

Figure G.1 Fraction of the molecular beam hitting the surface (red) as a function of incidence angle θ_i obtained by evaluating Equation G.5 assuming a molecular beam spot size of 2 mm (FWHM). The bottom blue curve is the apparent $\cos\theta_f$ distribution given by the product of the red curve and the dashed $\cos\theta_f$ curve.

axis, is given by

$$I(x_S, y_S; \theta_i) = I_0 \exp\left(-\frac{x_S^2 \cos^2\theta_i}{w^2}\right) \exp\left(-\frac{y_S^2}{w^2}\right) \cos\theta_i \,, \tag{G.3}$$

where x_S and y_S are the projections of x and y onto the surface plane. The fraction of molecules $f(\theta_i)$ that hits the surface at an angle of incidence θ_i can then be calculated according to

$$f(\theta_i) = \frac{\iint_{\text{surface}} I(x_S, y_S; \theta_i)\, \mathrm{d}x_S\, \mathrm{d}y_S}{\iint I(x_S, y_S; \theta_i)\, \mathrm{d}x_S\, \mathrm{d}y_S} \tag{G.4}$$

$$= \frac{1}{I_0 \pi w^2} \int_{-r_t}^{r_t} \int_{-\sqrt{r_t^2 - x_S^2}}^{\sqrt{r_t^2 - x_S^2}} I(x_S, y_S; \theta_i)\, \mathrm{d}y_S\, \mathrm{d}x_S \,, \tag{G.5}$$

where r_t is the surface radius. I assumed a beam FWHM of 2 mm, in agreement with deposition spot sizes reported in Hundt's thesis using the same skimmer and aperture dimensions. Figure G.1 displays how the fraction of the molecular hitting the surface drops as θ_i is increased beyond 65°. Also shown is the apparent $\cos\theta_f$ distribution, which takes the θ_i-dependence of the incident flux into account.

A full documentation for simulating the molecular beam intensity distribution on the tilted surface can be found on the group's data server (see appendix A). A simple Matlab code example is provided below.

MATLAB code

```
surface_radius = 5; % set the radius of the target surface in mm
fwhm = 2;           % set FWHM of the incident beam in mm
w = fwhm/(2*sqrt(log(2)));
y_min = @(x) - sqrt(surface_radius^2 - x.^2);
y_max = @(x) sqrt(surface_radius^2 - x.^2);
int_distr_circle = @(theta) integral2(...
    @(x, y) exp(-x.^2*cos(degtorad(theta))^2/w^2).*exp(-y.^2/w^2)*cos(degtorad(theta))
        ,...
    -surface_radius, surface_radius, y_min, y_max);

% interate over angles
fractions = [];
theta = 0:0.5:89;
for ang = theta
    fractions = [fractions int_distr_circle(ang)/(pi*w^2)];
end

plot(theta, fractions);
xlabel('Incidence Angle')
ylabel('Fraction of molecules hitting the Surface')
```

H List of LabVIEW projects

Table H.1 Overview of LabVIEW projects developed during this doctoral work.

Project	Description
Auger	New VIs for AES measurements, automated sample movement, and AES peak analysis tools.
Beam Flag Control	Enables controlling the AML UHV stepper motor *via* RS232 interface and remote control using a client/server architecture.
Bolometer Acquisition	A collection of VIs used for acquiring BILT data including fluence curves and angular distribution measurements.
Bristol Wavemeter	Self-developed driver for the Bristol wavemeter interfaced *via* USB.
Experiment Monitor	Contains a VI for displaying the most important experimental parameters (UHV pressure, laser power, bolometer temperature) and webcam live stream. Also contains the temperature and humidity logging VI.
gentec powermeter	Readout VI for the gentec SOLO-PE power meter *via* USB interface.
LHe Pumpdown	VI that automates the initial pump down procedure of the bolometer. Also ships the necessary drivers to readout the Pfeiffer pressure gauge controllers.
Pressure Monitor	Reads the Pfeiffer pressure gauge controllers and displays and logs the pressure data.
RGA 200	Incomplete library of VIs to interface the SRS RGA 200 residual gas analyzer.
SR830 Additional VIs	VI library for remote control of the SRS 830 Lock-in amplifier.
Transfer Cavity	Libraries and executables for the transfer cavities. There are two separate libraries for the C- and the A-module cavities, respectively.

List of Figures

List of Tables

Acknowledgements

Looking back on my PhD, I am astonished by how quickly 4 years in Lausanne have passed, and I realize what an unbelievable luck I had in having ended up here, not least because of the many great people I met. It is now time for me to thank all of them and in particular those who guided and accompanied me on this incredible journey.

First of all, I want to thank my supervisor Prof. Rainer Beck for accepting me in the "Group for Gas-surface Dynamics" and for providing the outstanding conditions under which we are able to work in this laboratory. Thank you for giving me the opportunity to work on such a challenging project and for providing everything that was necessary to make it a success. Moreover, I thank you for your trust, your advice and your support.

I also want to thank Prof. Alec Wodtke, who agreed to be the co-advisor of this thesis work and without whom none of this would have happened. Thank you for the enthusiasm and creativity that made me pursue this exciting field of science.

Moreover, I would like to thank Dr. Anne-Sophie Chauvin and Dr. Wolfgang Harbich for having agreed on serving as members of my PhD exam jury. Special thanks go to Prof. Dan Auerbach and Prof. Fleming Crim for serving as members of the jury and, moreover, for the many insightful discussion during your visits to EPFL.

I want to particularly thank the former and current members of the Surface Group, who I had the pleasure to call my colleagues and, in some cases, my friends. Special thanks to Dr. Maarten van Reijzen for the friendly and productive working atmosphere. It has been a pleasure working with you, even during the longest "bolometer days" (and nights). Thanks as well to Dr. Helen Chadwick; it was always nice to discuss scientific or non-scientific topics with you guys over a beer after work or outside of EPFL. I would also like to thank Ana Gutiérrez for the nice and friendly atmosphere that she brings to the lab and for the awesome trip to NYC. Thanks also to Bo-Jung Chen, who has been a great help in the lab during the final stages of my PhD and for bearing me in moments of stress. I am confident that you will do a great job in bringing this line of research to the next level.

Furthermore, I want to thank Prof. Thomas Rizzo, the head of the LCPM group for his helpful feedback, especially during group meeting presentations. I also thank all members of the LCPM group. In particular, I would like to mention: Dr. Morten Hundt, Dr. Lucy Voronina, Dr. Oleg Aseev, Dr. Mike Kamrath, Dr. Andreas Osterwalder, Ahmed Ben Faleh, Valeriu Scutelnic, Verónica Oliver, Andrew Clark. Thank you all for the nice atmosphere and the good times I had with you inside and outside EPFL. A very special thank you goes to Dr. Justin Jankunas for the evenings that we spent playing billard or eating pizza. You are truly missed ...

I also thank Dr. Marcel Drabbels for the opportunity to teach our EPFL students some Physical Chemistry, and Stéphane Thonney for his assistance in the TP.

My gratitude goes to our current secretary, Angeles Alarcon, who is a great help and whose friendliness and kindness enriches the group. A very warm thanks is reserved for Marianne Dang Bridel, one of the most caring people I have met. In particular, I want to thank you for taking so much care after I arrived in Switzerland with not much more than an awfully big suitcase.

This brings me to two people to who I owe a lot because they welcomed me into their home without reserves and treated me as if I belonged to their family. Chers Claude et Bernard, un grand merci pour votre hospitalité, générosité et votre amitié. Vous faites partie de ma familie.

Vielen Dank an meine lieben Eltern, Ingrid und Helmut. Ihr habt mich dazu ermutigt diesen Schritt zu gehen und ich danke Euch von Herzen für die Unterstützung, die Ermutigung und die langen Wege, die Ihr immer wieder auf Euch genommen habt, um euren Sohn zu besuchen, der es selber viel zu selten geschafft hat die Reise anzutreten. Und ich danke Euch besonders dafür, dass Ihr letzteres versteht.

The last thank you goes to my beloved Chiara. Thanks for being on my side at all times, for traveling with me to the other side of the planet, exploring new places, and for climbing Dent de Jaman with me each year in July. Thank you for the constant encouragement and for the little surprises that sharing my life with you brings to me each day and, most of all, for your love. Grazie mille!

Lausanne, 18th February 2018

Jörn Werdecker

Chemin de Rionza 5
1020 Renens
Switzerland
✉ *jwerdec@gmail.com*
Nationality: German

Education

2014–2018 **Swiss federal institute of technology, Lausanne (EPFL), Switzerland.**
Ph.D. in Physical Chemistry

Supervisors: Prof. Rainer D. Beck (EPFL) and Prof. Alec M. Wodtke (Max-Planck Institute for Biophysical Chemistry, Göttingen, Germany)

Thesis title: *Vibrationally and Rotationally Inelastic Scattering of Methane from Ni(111)*

2011–2013 **University of Göttingen, Germany**
Master's Degree in Chemistry

Final diploma awarded with distinction. Mark for the thesis: 15/15.

2008–2011 **University of Göttingen, Germany**
Bachelor's Degree in Chemistry

Publications

[1] J. Werdecker, M. E. van Reijzen, B.-J. Chen, and R. D. Beck. *Vibrational Energy Redistribution in a Gas-Surface Encounter: State-to-State Scattering of CH_4 from Ni(111).*
Phys. Rev. Lett. **120**(5), 053402 (**2018**).

[2] K. Golibrzuch, J. H. Baraban, P. R. Shirhatti, J. Werdecker, C. Bartels, and A. M. Wodtke. *Observation of Translation-to-Vibration Excitation in Acetylene Scattering from Au(111): A REMPI Based Approach.*
Z. Phys. Chem. **229**(10-12), 1929 (**2015**).

[3] K. Golibrzuch, P. R. Shirhatti, J. Geweke, J. Werdecker, A. Kandratsenka, D. J. Auerbach, A. M. Wodtke, and C. Bartels. *CO Desorption from a Catalytic Surface: Elucidation of the Role of Steps by Velocity-Selected Residence Time Measurements.*
J. Am. Chem. Soc. **137**(4), 1465 (**2015**).

[4] J. Werdecker, P. R. Shirhatti, K. Golibrzuch, C. Bartels, A. M. Wodtke, and D. J. Harding. *Electronically Nonadiabatic Vibrational Excitation of N_2 Scattered from Pt(111).*
J. Phys. Chem. C **119**(26), 14722 (**2015**).

[5] P. R. Shirhatti, J. Werdecker, K. Golibrzuch, A. M. Wodtke, and C. Bartels. *Electron hole pair mediated vibrational excitation in CO scattering from Au(111): Incidence energy and surface temperature dependence.*
J. Chem. Phys. **141**(12), 124704 (**2014**).

Awards

2017 **Best Poster Presentation Award**
at the Gordon Research Conference on Dynamics at Surfaces, Newport (RI), USA.

2017 **Chemistry Travel Award**
by the Swiss Academy of Natural Sciences (SCNAT) and the Swiss Chemical Society (SCS).
1000 CHF towards attending the *International Symposium on Molecular Beams 2017.*

Languages

German:	Native	French:	Intermediate
English:	Fluent	Italian:	Basic